Rho GTPase Dynamics in the Regulation of Cellular Signaling and Migration

Christopher M. Welch

A dissertation submitted to the faculty of the University of North Carolina at Chapel Hill in partial fulfillment of the requirements for the degree of Doctor of Philosophy in the Department of Pharmacology

Chapel Hill
2011

Approved By:

Klaus Hahn, PhD

Keith Burridge, PhD

Adrienne Cox, PhD

David Siderovski, PhD

Ken Jacobson, PhD

Teresa Tarrant, MD

ABSTRACT

CHRISTOPHER MICHAEL WELCH: Rho GTPase Dynamics in the Regulation of
Cellular Signaling and Migration
(Under the direction of Dr. Klaus M. Hahn)

Cell migration is critical to the development and maintenance of higher

organisms, and is required for the patterning of the nervous system, for the development

of organs, and for responses to wounds or sites of inflammation. Because cell migration

is so widely utilized, it must be very tightly controlled, as is apparent when the process

goes awry, such as in cancer cell metastasis or chronic inflammation.

Growth factors and other cues mediate the activation of a variety of pathways that

induce cell migration. Despite these many pathways, a family of proteins called Rho

GTPases are universally engaged to cause changes in the cellular cytoskeleton, leading to

cell migration. Because Rho GTPases are so critical to cell migration, yet can be used to

mediate many different types of cellular responses, they must be precisely controlled. In

most cases, it is the timing and placement of Rho GTPase activity that defines cellular

behaviors in response to specific signals. However, tools to investigate the

spatiotemporal dynamics of Rho GTPase activity in live cells have only recently been

developed. I this work, I characterize the spatial and temporal dynamics of the Rho

GTPases in cell migration through the development of sensors for Rho GTPase activity

for live cell imaging. I establish the spatial and temporal dynamics of RhoA, Rac1, and

Cdc42 at the leading edge of migrating cells, and the role of RhoG in its ability to precisely position and activate Rac1 at the leading edge of cells. This work provides the first thorough characterization of the roles of these GTPases at the leading edge relative to one another and the mechanisms by which they are regulated. This work also demonstrates preliminary studies on the roles of these GTPases during leukocyte transendothelial migration.

It is critical to gain an understanding of the mechanisms by which cells control cell migration via the Rho GTPases.   Aberrant signaling through the GTPases leads to a variety of disease processes. Thus, a better understanding of normal Rho GTPase signaling will provide a framework for understanding how cell migration goes awry and how it can be potentially treated.

ACKNOWLEDGEMENTS

Never in the work that I will describe in this thesis have I worked alone. Without those who have taught me, encouraged me, corrected me, and loved me, none of this work would have been possible. First, I would like to thank my advisor, Dr. Klaus Hahn. Dr. Hahn has graciously given me the support I needed to pursue my work and freedom to explore a variety of scientific questions, which have greatly improved my scientific abilities. His instruction and guidance have been vital in my development as an experimentalist and scientist, and for this I am thankful. Additionally, I would like to thank my co-mentor, Dr. Keith Burridge, for involving me in his laboratory. Through interactions with his group and him, I have gained invaluable biological perspectives, and a number of these projects in this dissertation have been the result of working directly with members of his laboratory.

I would also like to thank the advice and support from the rest of my thesis committee members, Drs. Adrienne Cox, David Siderovski, Ken Jacobson, and Terri Tarrant. Through their unique points-of-view, each of the members has taught me about the myriad ways to ask scientific questions, and they have all shown me where my weaknesses lie, helping me to address them and improve them, for which I am grateful.

The time I have spent in the lab also would not have been the same without those I have worked closely with over the years. I thank Dr. Akash Gulyani for training me during my rotation through the laboratory, and Dr. Louis Hodgson for his patience in

PREFACE

Parts of Chapters Three and Five of this dissertation have been previously published. Authorship rights to the following articles remain with the authors and thus these articles can be reproduced here in a modified format, as provided by Nature, the Journal of Cell Biology, and the American Society for Cell Biology:

Machacek, M.*, Hodgson, L.*, Welch, C.M.*, Elliott, H., Pertz, O., Shen, F., Abell, A., Johnson, G.L., Hahn, K.M., Danuser, G. (2009) Coordination of Rho GTPase activities during cell protrusion. *Nature.* 2009 Sep 3;461(7260):99-103.

Koivusalo M, Welch C, Hayashi H, Scott CC, Kim M, Alexander T, Touret N, Hahn KM, Grinstein S. Amiloride inhibits macropinocytosis by lowering submembranous pH and preventing Rac1 and Cdc42 signaling. *J Cell Biol.* 2010 Feb 22;188(4):547-63.

Samson T, Welch CM, Monaghan-Benson E, Hahn KM, Burridge K. Endogenous RhoG is Rapidly Activated after EGF Stimulation through Multiple GEFs. *Mol Biol Cell.* 2010 May 1;21(9):1629-42. Epub 2010 Mar 17.

TABLE OF CONTENTS

xvi

LIST OF TABLES

LIST OF FIGURES

LIST OF ABBREVIATIONS

Δt: Change in Time

2D: Two-dimensional

3D: Three-dimensional

aPKC: Atypical Protein Kinase C

Ar/Kr: Argon/Krypton

Arf6: ADP-ribosylation Factor 6

ARNO: Cytohesin-2/ARF Nucleotide Binding-site Opener

Arp2/3: Actin-Related Proteins 2 and 3

BAEC: Bovine Aortic Endothelial Cells

BAI-1: Brain-specific Angiogenesis Inhibitor 1

BDNF: Brain-derived Neurotrophic Factor

β-Pix: p21-activated Kinase [Pak]-interacting Exchange Factor

BiFC: Bimolecular Fluorescence Complementation

BSA: Bovine Serum Albumin

Ca^{2+}: Calcium Ion

CAAX: Cysteine Aliphatic Aliphatic Any

CAM: Cellular Adhesion Molecule

CaMKIIα: Calmodulin Kinase II α

cAMP: Cyclic Adenosine Monophosphate

CBD: WASP Cdc42 Binding Domain

CCD: Charge-coupled Device

CD: Cellular Determinant

Cdc42: Cell Division Control Protein 42 Homolog

CED-10: Cell Death Abnormality, Protein 10

CFP: Cyan Fluorescent Protein

cGMP: Cyclic Guanosine Monophosphate

CMV: Cytomegalovirus

CRIB: Cdc42/Rac1 Interactive Binding

CtBP/BARS: C-terminal Binding Protein/Brefeldin A-ADP Ribosylated Substrate

CyPet: Cyan Fluorescent Protein for Energy Transfer

D: Distance

D-TOPO: directional topoisomerase

Dbl: Diffuse B-Cell Lymphoma GEF

DCX: Doublecortin (DCX)

DH: Dbl Homology

DIC: Differential Interference Contrast

DMEM: Dulbecco's Modified Eagle Medium

DNA: Deoxyribonucleic Acid

dNTP: Deoxynucleotide Triphosphate

Dock180: Dedicator of Cytokinesis

DPBS: Dulbecco's Phosphate Buffered Saline

DsRed: Discosoma Red Fluorescent Protein

EGF: Epidermal Growth Factor

EGM-2: Endothelial Growth Medium 2

EIPA: Ethylisopropylamiloride

ELMO: Engulfment and Cell Motility

ErbB: Erythroblastic Leukemia Viral Oncogene

ESAM: Endothelial Cell-selective Adhesion Molecule

FA: Focal Adhesion

FACs - Fluorescence Activated Cell Sorting

FAK: Focal Adhesion Kinase

FBS: Fetal Bovine Serum

FCS: Fluorescence Correlation Spectroscopy

FGF: Fibroblast Growth Factor

FLIM: Fluorescence Lifetime Microscopy

FRET: Fluorescence Resonance Energy Transfer

GAP: GTPase Activating Protein

GBD: ELMO1 RhoG Binding Domain

GDI: Guanine Dissociation Inhibitor

GEF: Guanine Nucleotide Exchange Factor

GFP: Green Fluorescent Protein

GPCR: G-protein Coupled Receptor

Grb2: Growth Factor Receptor-bound Protein 2

GS: Glycine Serine

GTP: Guanosine Triphosphate

GTPase: Guanosine Triphosphatase

H: Hours

HeCd: Helium/Cadmium

HeLa: Henrietta Lacks

HEPES: 4-(2-hydroxyethyl)-1-piperazineethanesulfonic Acid

Hg: Mercury

HOE-694: (3-methylsulphonyl-4-piperidinobenzoyl)guanidine Methanesulphonate

HQ: High Quality

HUVEC: Human Umbilical Vein Endothelial Cells

ICAM-1: Intracellular Adhesion Molecule 1

IgG: Immunoglobulin G

IQGAP: IQ Motif-containing GTPase Activating Protein

IRSp53: Insulin Receptor Tyrosine Kinase Substrate p53

ITLGMDELYK: Isoleucine Threonin Leucine Glycine Methionine Glutamic Acid Leucine Tyrosine Lysine

JAM: Junctional Adhesion Molecule

KD: Knockdown

kDa: Kilodalton

LARG: Leukemia Associated Rho GEF

LDEV: Lactose Dehydrogenase-Elevating Virus

LFA-1: Lymphocyte Function-associated Antigen 1

LPA: Lysophosphatidic Acid

M199: Medium 199

MAC1: Macrophage Antigen 1

MADCAM1: Mucosal Vascular Addressin Cell-adhesion Molecule 1

MAPK: Mitogen Activated Protein Kinase

MCS: Mutliple Cloning Site

mDia: Mammalian Diaphanous Protein

MEF: Mouse Embryonic Fibroblast

MeroCBD: CBD (see above) Labeled with Merocyanine Dye

$MgCl_2$: Magnesium Chloride

Mig-2: Abnormal Cell Migration, Protein 2

MILO: Mdia Interactor in fiLOpodia or Mammalian vIlse homoLOgue

min: minutes

mKO: Monomeric Kusabira Orange

MLK3: Mixed Lineage Kinase 3

MMP-MT1: Membrane Type 1 Metalloprotease

N: Number

NaCl: Sodium Chloride

NF-κB: Nuclear Factor κB

NHE: Na+/H+ Exchangers

NIH: National Institutes of Health

NO: Nitric Oxide

Opti-MEM: Optimum Modified Eagle's Medium

pAd-DEST: Adenoviral Destination plasmid

PAK: p21-Activated Kinase

Par3: Partioning Defective Protein 3

Par6: Partitioning Defective Protein 6

PBD: p21 Activated Kinase Rac1 Binding Domain

PCR: Polymerase Chain Reaction

PDGF/VEGF: Platelet-derived Growth Factor/Vascular Endothelial Growth Factor

PECAM1: Platelet/endothelial-cell Adhesion Molecule 1

PH: Pleckstrin Homology

pH: Concentration of Hydrogen Ions

PI3K: Phosphatidylinositol-3 kinase

PIP3: Phosphatidyl Inositol (3,4,5)Phosphate$_3$

PIP2: Phosphatidyl Inositol (4,5)Phosphate$_2$

PKC: Protein Kinase C

PKA: Protein Kinase A

PLA$_2$: Phospholipase A$_2$

PLC: Phospholipase C

PLD: Phospholipase D

PLEKHG6: Pleckstrin Homology Domain Containing, Family G Member 6

PMSF: Phenylmethanesulfonylfluoride

Por-1: Mitochondrial Porin 1

POSH: Plenty of SH3s

PSGL1: P-selectin Glycoprotein Ligand 1

PTEN: Phosphatase and Tensin Homolog

Puro: Puromycin

Rac1: Ras-related C3 Botulinum Toxin Substrate 1

Rab: Ras-like GTP-binding protein

Rap1: Ras-proximate-1 or Ras-related Protein 1 GTP-binding Protein

Ras: Rat Sarcoma GTP-binding Protein

Rho: Ras Homology GTP-binding Protein

RhoGIP122: RhoG Inhibitior Protein 122 kDa

RBD: Rhotekin RhoA Binding Domain

RNAi: Ribonucleic Acid (RNA) Interference

ROCK: Rho Kinase

RTK: Receptor Tyrosine Kinase

S: Seconds

S3: Serine 3

S/N: Signal to Noise

SEM: Standard Error of the Mean

SGEF: Src Homology 3 Domain-Containing Guanine Nucleotide Exchange Factor

SGLRSELGS: Serine Glycine Leucine Arginine Serine Glutamic Acid Leucine Glycine Serine

shRNA: Short Hairpin RNA

siRNA: Short Interfering Ribonucleic Acid

SNX: Sorting Nexin

Src: Sarcoma

TC: Transmigratory Cup

tdmCh: Tandem mCherry

tdYPet: Tandem YPet

TEM: Transendothelial Migration

TEM4: Tumor Endothelial Marker 4

Tiam-1: T-cell Invasion and Metastasis

TIRF: Total Internal Reflection Microscopy

TNFa: Tumor Necrosis Factor α

TRAF3: TNF-receptor Associated Factor 3

Tris: Tris(hydroxymethyl)aminomethane

Toca-1: Transducer of Cdc42-dependent Actin Assembly

UV: Ultraviolet

VASP: Vasodilator-stimulated Phosphoprotein

VCAM-1: Vascular Cellular Adhesion Molecule 1

W: Watt

WASP: Wiskott-Aldrich Syndrome Protein

WSP-1: Wiskott-Aldrich Syndrome Protein, *C. elegans*

WAVE: WASP and Verprolin Homology

WVE-1: WASP and Verprolin Homology, *C. elegans*

WT:Wild Type

YFP: Yellow Fluorescent Protein

YPet: Yellow Fluorescent Protein for Energy Transfer

ZDC: Zero-drift Compensation

CHAPTER ONE: INTRODUCTION

1.1 Introduction to Cell Migration

A Historical Perspective:

Cell migration is clearly critical to most physiological and pathological organismal processes, playing necessary roles in embryogenesis, neural cell migration and brain cortical development, inflammatory responses, wound healing, and cancer cell metastasis. While we understand this clearly today, this knowledge has been long in development.

Since the invention of the microscope in the early 17th century, scientists have been able to examine the world of living organisms in more detail, in particular the world of the very small living things that had theretofore gone unnoticed by the naked human eye. A bewildering variety of new structures and particles were seen by early luminaries such as Hooke, Leeuwenhoek, Kircher, and Swammerdam, with Hooke being the first to use the term "cell" as he visualized the cell walls of the components of cork. These early experiments also noted the movement of cells within their samples, as Leeuwenhoek saw and described motility in bacteria and spermatozoa (Ford 1995). However, it was almost 200 years later that "cell theory," or the idea that all living things are composed of cells as a fundamental unit, was proposed by Schleiden (Schleiden 1838) and Schwann (Schwann 1839). In addition, the cell was also recognized as the fundamental unit of disease processes, as stated in Virchow's works on cellular pathology (Mazzarello 1999),

which became the standard for the approach to disease pathology until molecular pathology was developed in the following century. In parallel with these studies, the microscope was also improved and advanced, with achromatic lenses in the 1800s pushing the field forward and allowing better visualization of cellular structures at higher magnification. However, further technological advances were needed to study the movements and migration of metazoan cells. In the late 1800s, Ernst Abbe and Carl Zeiss developed several technologies that enabled progress in visualizing thin, low-contrast objects: apochromatic lenses, the Abbe condenser for oblique and darkfield imaging, and a new theory of image formation in microscopy (Dunn and Jones 2004). Among the first observations of metazoan cell migration was that by Ilya Metchnikoff, who studied motile cells in transparent starfish larvae. By the introduction of small thorns into the larvae to see if the cells would defend against intruders, he observed the accumulation of cells around the sites of injury, single-handedly discovering leukocyte chemotaxis and engulfment (Tauber 2003). However, it was not until Ross Harrison, in 1907, plated frog neural tissue explants in clotted lymph and observed cells migrating out of the tissues, that it was confirmed with certainty that cells from tissues could move, and that cells from tissues could be cultured (Harrison 1907). Further developments in photography and interference contrast microscopy all enhanced scientists' abilities to visualize and record such cellular movements.

What still remained to be identified were the molecular components of the cellular machinery. Through development of antibodies for cytoskeletal components, scientists were able to identify the structure and location of actin and tubulin in fixed cells (Lazarides and Weber 1974) but these cells were not moving. In the late 1970s, D.

Lansing Taylor and Yu-Li Wang revived the use of the microscope by injecting fluorescently labeled actin into live cells and visualizing its dynamics (Taylor and Wang 1978). With the advent of the laser-scanning confocal microscope (Amos and White 2003) and the cloning and expression of green fluorescent protein (GFP) (Prasher et al. 1992), the usefulness of fluorescent microscopy massively expanded, and scientists were then able to tag multiple components of cellular machinery and observe their dynamics in both space and time as cells moved or were perturbed.

In parallel, the methodological barriers to studying cell migration were being overcome as well, with scientists developing methods for visualizing chemotaxis, mechanical forces, and signaling pathways. As research on the GFP molecule has advanced, the field of cell migration has been provided with a myriad of tools to allow for visualization of protein localization, protein dynamics, protein activity, diffusion of molecules at steady-state, and lifetimes of expressed proteins (Newman et al. 2011). Similar work has also provided novel tools that allow for the ability to tune and activate proteins by light in living cells (Levskaya et al. 2009; Wu et al. 2009), enabling specific manipulation of protein activity in time and space to study how cellular behaviors are then changed. Lastly, with new microscopy techniques, such as total internal reflection microscopy (TIRF) (Lanni et al. 1985), fluorescence correlation spectroscopy (FCS) (Schwille et al. 1999), and multiphoton fluorescence microscopy (also known as two-photon fluorescence microscopy) (Zipfel et al. 2003), scientists can now examine cellular dynamics from a variety of angles at a variety of time-scales and depths, even permitting imaging of protein dynamics in large living organisms such as mice (Condeelis and Segall 2003). With these tools, cell biology seems poised to better understand the

complexity of the amazing integrative signal processing device that is the cellular cytoskeleton, with all its myriad components. However, much work remains to be done and hopefully the work presented here will unravel just a very small part of this complexity.

The Role of Cell Migration in Development, Homeostasis, and Disease:

In nearly all organisms, cell migration is critical for development and normal homeostatic function. The ways in which organisms guide neuronal development, target immune cells appropriately for their development, guide neural crest cells to their wide range of physical locations during development, respond to wounds, or respond to infections all involve precise regulation of cell migration (Franz et al. 2002). A wide array of research has probed the various areas of development in which cell migration is crucial. For example, due to the ability to visualize and perturb many proteins involved in cell migration, studies of development in *Drosophila melanogaster* have provided great insight into how cell migration is controlled through the observation of defects. The process of migration in development has been broken down into a number of questions. What causes cells to initiate their movement? How do they move? How are cells guided? How do cells know when to stop migrating? In *Drosophila* border cells, it has been shown that local paracrine signaling helps define which cells will migrate (Silver and Montell 2001), and then ecdysone, a hormone, specifies the timing of their migration (McDonald et al. 2003), and as the cells migrate, they are guided to the appropriate sites by ligands for the epidermal growth factor (EGF) and platelet-derived growth factor/vascular endothelial growth factor (PDGF/VEGF) receptors (Duchek et al. 2001). Each of these pathways leads to engagement of the machinery required for

4

alteration of the actin cytoskeleton, including the Rho guanosine triphosphatases (GTPases), and in particular Rac1 in *Drosophila* (Bianco et al. 2007).

Similarly, the role of migration in the targeting of immune cells to sites of infection for homeostatic maintenance has been intensively studied. In response to inflammation, endothelial cells upregulate the expression of a number of chemokines and adhesion molecules. As leukocytes flow by in the bloodstream, engagement of the selectins on the surface of the endothelium causes the leukocytes to slow down (Kansas 1996), whereupon they can be stimulated by chemokines on the surface of the endothelium (Middleton et al. 1997), telling the leukocytes to "activate." Once activated, the leukocyte can engage other upregulated receptors on the endothelium and come to a full stop (Kinashi 2005), whereupon the leukocyte will engage its machinery to reorganize the actin cytoskeleton and transmigrate into tissues to the site of infection (Springer 1995; Ley et al. 2007). Thus, cell migration is absolutely critical to these normal processes of development and homeostasis.

If cell migration becomes dysregulated, a number of disorders and diseases may result, depending on the cell type and location affected. Cell migration must be exquisitely controlled, not just by the migrating cell itself, but also in the ways that tissues surrounding the migrating cells interact with them. Aberrant migration is a hallmark of cancer cell metastasis, inflammatory disease, neuronal developmental disorders, and many other diseases, whether as a cause or a consequence of the disease. For example, in cancer cell metastasis, cells must disseminate from the primary tumor, invade into those local tissues, invade into the lymphatic or vascular system, extravasate from those systems, and colonize distant tissues, all of which require cell migration

behaviors (Bos et al. 2009). To accomplish these movements, cancer cells take on highly migratory and invasive capabilities due to changes in gene expression and function, often through the epithelial-to-mesenchymal transition (Yilmaz and Christofori 2009). Once these capabilities are acquired, cells can migrate by a number of different paradigms, including amoeboid, mesenchymal, and collective migration modes, all of which require reorganization of the actin cytoskeleton and force generation to move through tissues (Nurnberg et al. 2011). Many studies have been targeted at understanding and inhibiting the changes that occur that drive cancer cell migration, but due to the plasticity of cancer cells, attempts to inhibit cell migratory pathways have often failed because cells simply engage other available signaling pathways to continue cell migration (Sanz-Moreno et al. 2008), though there have been some promising studies (Shan et al. 2005).

A lack of cell migration in tissues can also lead to significant impairments and disease. Perhaps one of the richest fields for the study of disorders due to aberrant cell migration is neuronal development. A number of proteins and signaling pathways have been identified that when disrupted lead to defective cell migration and defective patterning of the brain. To achieve proper structuring and patterning of the brain, neuronal cells must divide (Valiente and Marin 2010), develop a leading process, move along radial glial cells to their proper position, stop their migratory program, and polarize appropriately for the formation of cell-cell contacts. Mutations have been discovered that impact nearly every stage of this process. For example, proteins regulating cell polarity and centrosome progression have been found to be defective in lissencephaly, with the classical Lis1 protein and dynein both being required for centrosome progression and nucleokinesis. Similarly, doublecortin (DCX), when lost, leads to aberrant dynamics of

6

microtubules which are normally utilized by the Lis1 protein to regulate nucleokinesis and centrosome positioning (Grabham et al. 2007; Sapir et al. 2008). Recent studies have also identified mutations in both the α and β tubulin genes that cause a variety of neuronal disorders in humans (Jaglin et al. 2009). Cell migration also appears to play a role in some more complicated disorders, such as Alzheimer's disease and schizophrenia, where the disease causative factors are still unclear. In these diseases, it has been shown that genes encoding Neuregulin-1, a growth factor, and Disc-1,which regulates dynein function, both contribute to the development of these diseases through the dysregulation of neuronal cell positioning, especially later in life. However, these findings have largely been ignored from a clinical standpoint (Flames et al. 2004; Kamiya et al. 2005; Duan et al. 2007). Thus, gaining an understanding of the molecular mechanisms that contribute to the proper cell migration, and of the mechanisms that are engaged when this process goes awry, is essential for the development of therapeutics targeted to either enhance or suppress the signaling pathways that control cell migration.

1.2 Overview of Signaling Pathways Involved in Regulating Cell Migration

Cell migration has long been a visually-oriented field of study. It is upon this backdrop that the signaling pathways that regulate cell migration have been investigated. However, before the development of probes for visually studying protein activity in living cells, biochemical methods and fixed-cell observations have been the preferred techniques for the investigation of the signaling pathways leading to cell migration.

The individual players in the signaling processes that regulate cell migration have been and are being discovered rather rapidly, and how they regulate cell migration is only slightly behind. However, the understanding of the integrative and combinatorial functions of the cytoskeleton as a complete signaling network are only starting to be understood, though it is clear that cell migration is a coordinated process in both time and space. The space needed to cover all the signaling pathways studied and their relevance for cell migration would be prohibitive, and many excellent review articles are available that cover the field exceptionally well (Lauffenburger and Horwitz 1996; Ridley et al. 2003; Burridge and Wennerberg 2004; Yilmaz and Christofori 2009; Nurnberg et al. 2011). Thus, what will be covered here is a more broad-scale view of cell migration signaling that will eventually focus on the role of the Rho GTPases in cell migration, as these molecules are at the core of the work contained within this dissertation.

Rho GTPases as Coordinators of Cell Migration:

The Ras superfamily of small (21–25 kDa) GTPases is subdivided into five branches, namely Rho, Ras, Rab, Ran, and Arf. To date, 20 members of Rho family GTPases (Figure 1.1) and 36 Ras family members are known (Wennerberg et al. 2005).

The best characterized of the Rho GTPases are RhoA, Rac1, and Cdc42. However, it should be noted that unique roles have been identified, some cell-type specific, for the other GTPases as well, and the cell migratory behaviors discussed above are not solely the domain of RhoA, Rac1, and Cdc42.

These GTPases cycle between an active GTP-bound and an inactive GDP-bound state, acting as molecular switches in a variety of signalling pathways regulating many diverse cellular processes. When converted to the active, GTP-bound state, the GTPases develop high affinity for downstream effectors via conformational changes in switch I and switch II, and this process is tightly controlled. Inactivation to the GDP-loaded state is tightly controlled as well, since GTPases have low intrinsic hydrolytic activity. The molecules involved in this process of GTP-loading and hydrolysis to GDP are guanine exchange factors (GEFs), GTPase activating proteins (GAPs), and guanine dissociation inhibitors (GDIs). GEFs catalyze the exchange of GTP for GDP, leading to activation of the GTPase. GAPs enhance the intrinsic hydrolytic rate of the GTPase, inactivating the GTPase. Lastly, GDIs sequester the GTPase, binding to the prenyl moiety on the C-terminus and stabilizing the GDP-bound state. Regulation of the GTPases is very context-dependent and varies from cell-line to cell-line depending on the composition of regulatory molecules present. However, these GTPase molecules are often defined as the master regulatory molecules of cell migration, serving as integration nodes for cellular signaling pathways to effect coordinated changes in the cellular cytoskeleton leading to cell migration (Burridge and Wennerberg 2004).

Signaling Pathways Leading to Cellular Morphological Polarization:

Traditionally, cell migration has been broken down into a series of physical events, each utilizing distinct signaling pathways: cellular polarization, lamellipodial protrusion, establishment of cell-substrate contacts, contractility and force generation, and release of rearward attachments (Lauffenburger and Horwitz 1996; Ridley et al. 2003). Figure 1.2 summarizes these steps and the critical signaling molecules in each step. The first event in this process is the response of the cell to some form of polarized extracellular cue, such as chemokines or growth factors, but also including extracellular matrix proteins, mechanical force, and electrical gradients. These signals cause morphological polarization of the cell, which is required for directional extension of actin-rich lamellipodial structures via the activity of actin-polymerizing proteins discussed shortly. These cues (both intracellular and extracellular) activate many downstream pathways leading to cell polarization, but most converge on the master regulator of polarity, Cdc42. Activation of Cdc42 recruits the Par3/Par6/aPKC complex and serves as a central regulatory node for crosstalk between Rac1, RhoA, and Cdc42 (Etienne-Manneville and Hall 2003), for centrosome reorientation, for microtubule stabilization, and for membrane trafficking to the leading edge for the maintenance of polarity (Etienne-Manneville and Hall 2002; Rodriguez et al. 2003). Cdc42 activation leads to recruitment of the GEF βPix to the leading edge for activation of Rac1 (Koh et al. 2001), while simultaneously activating Rac1 via Tiam-1 recruitment to the Par3/Par6/aPKC complex, in addition to stabilizing microtubules at the leading edge via the same complex (Nishimura et al. 2005; Pegtel et al. 2007). Cdc42 not only facilitates actin polymerization for lamellipodial protrusion via Rac1, but also stabilizes

microtubule "highways" such that molecules needed for further signaling at the leading edge are added and replenished, maintaining a signaling polarity (Osmani et al. 2010). This leading edge activation of Cdc42 (Li et al. 2003) and Rac1 (Kraynov et al. 2000) also appears to be important for antagonizing RhoA activity at the leading edge, leading to activation of RhoA at the rear of cells to further polarize the cell and to define the leading and retracting edges of the cell required for efficient cell migration (Xu et al. 2003). In contrast, if RhoA is activated at the leading edge, which has been described in numerous studies (Pertz et al. 2006; Ridley 2006; Machacek et al. 2009; Tkachenko et al. 2011), Rho kinase (ROCK) can then phosphorylate Par3, leading to the disruption of Cdc42 effects through Par3 and Rac1 recruitment to the edge (Nakayama et al. 2008; Simoes Sde et al. 2010), thus antagonizing Cdc42 and Rac1 activities. Thus, these are but several of the many mechanisms which can lead to polarization of the cell during motility (Burridge and Wennerberg 2004).

Signaling Pathways Regulating Lamellipodium Formation:

Once polarity is generated, lamellipodia must be extended and stabilized by the eventual formation of new cellular contacts. At the leading edge, phospholipid signaling pathways appear to play a significant role in the extension of lamellipodia by converging on the Rho GTPases and defining, critically, where the GTPases are active, particularly Rac1 (Welch et al. 2003). In chemotaxis, it has been shown that by their non-overlapping distributions, PI3K (phosphatidylinositol-3 kinase) can generate $PtdIns(3,4,5)P_3$ (PIP_3) at the edge in response to extracellular cues, while PTEN at non-leading-edge locations tends to degrade PIP_3 into $PtdIns(4,5)P_2$ (PIP_2) to create a gradient of PIP_3 which can

activate Rac1 and a subsequent positive feedback loop that stimulates massive polymerization of actin and lamellipodial extension (Devreotes and Janetopoulos 2003; Huang et al. 2003; Merlot and Firtel 2003). Additionally, it has been shown that phospholipase A_2 (PLA$_2$), phospholipase C (PLC), and phospholipase D (PLD) all contribute to the modulation of this gradient and the activation of parallel pathways (Kolsch et al. 2008), such as the inhibition of cofilin (Edwards et al. 1999), which enhance Rac1 activity and actin polymerization downstream of extracellular cues . These parallel pathways also seem to be critical for the direction-finding component of cell migration, suppressing lateral lamellipodia, while the PI3K pathway predominantly affects the velocity of the migration (Wessels et al. 2007). Additionally, a myriad of feedback amplification pathways are present for both Rac1 and Cdc42 (Sasaki et al. 2007)in this process such that even extremely shallow chemoattractant gradients can be amplified into very strong signals that cause directed cell migration (Andrew and Insall 2007). Ultimately, lamellipodial protrusion is generated when Rac1 and Cdc42 bind to WASP homology domain containing proteins such as N-WASP and WAVE which subsequently activate Arp2/3, which directly polymerizes actin (Ridley et al. 2003; Burridge and Wennerberg 2004). Further, Cdc42 is also well known for generating another protrusive structure, filopodia, via interaction with an additional actin nucleating protein, mDia2, and these structures may even extend from lamellipodia and serve sensory functions during protrusion (Mellor 2009; Lee et al. 2010b). Rac1 and Cdc42 both can bind and activate the PAK kinases which phosphorylate and activate LIM kinase (Bokoch et al. 1998), which in turn phosphorylates and inactivates cofilin, which normally severs actin filaments, permitting actin filament growth (Wang et al. 2007).

RhoA at the leading edge can also polymerize actin, which was a surprising finding, even though biochemical and colocalization data both show that RhoA can bind and activate mDia (Lammers et al. 2008) at the leading edge to nucleate and polymerize actin (Kurokawa and Matsuda 2005; Pertz et al. 2006; Machacek et al. 2009; Tkachenko et al. 2011). Collectively, these signaling pathways lead to the extension and stabilization of actin-rich lamellipodia.

Signaling Pathways Involved in the Stabilization of Extended Lamellipodia:

Once a lamellipodium is extended, it needs to form new contacts with the substrate to stabilize the extension. At this step, perhaps more than others, integrins play a large role. Integrins serve as links or tethers between the extracellular matrix and cellular components, and are activated by inside-out cellular signaling which permits them to attach to extracellular substrates. Their binding, clustering, and conformational changes lead to a variety of intracellular signals, including formation and strengthening of focal adhesions, cytoskeletal changes through the Rho GTPases, and alterations in cell polarity (Hood and Cheresh 2002; Geiger et al. 2009). Where these integrins interact with the extracellular matrix, molecular complexes called focal complexes and focal adhesions often form . These structures, in many cell types, appear to require the GTPases to form, with Rac1 and Cdc42 stabilizing the formation of smaller focal complexes (Ridley et al. 2003), while RhoA activity and actomyosin contractility are required for the larger focal adhesions to develop (Chrzanowska-Wodnicka and Burridge 1996; Worthylake et al. 2001). These focal adhesions are extremely dense with signaling proteins, which enter and exit at varying times during the development of the adhesions.

13

Over 180 proteins have been identified within these complexes (Zaidel-Bar et al. 2007), and a thorough review of adhesion signaling is well beyond the scope of this introduction. Very recent work using superresolution microscopy has also shown that the proteins present in adhesions are very precisely stratified to either anchor other signaling proteins or transduce signals further within the cell (Kanchanawong et al. 2010). Suffice to say that these adhesions serve as anchor points for the cell for generation tractional forces for movement, and for mechanosensation by the cell. At this point in the migration cycle, the cell has stretched and extended a lamellipodium which has become anchored, through which it can sense adhesion via mechanical forces exerted on these new adhesive contacts.

Signaling Pathways Involved with Retraction of the Cell Tail with Body Translocation:

How force is generated underlies the final stage of cell migration: the cell rear retraction event. First, adhesion attachment sites have to be severed, and this is mediated by pathways involving FAK, Src, intracellular Ca^{2+}, and various proteases including calpain (Hendey et al. 1992; Lee et al. 1999; Glading et al. 2002). Once these adhesions are weakened, the forces exerted on the cell cause detachment of adhesions at the rear of the cell to allow retraction of the tail and propulsive forward movement of the cell. This force is generated by the interaction of myosin II with actin filaments anchored at adhesion sites (Chung et al. 2001). Myosin is a motor protein whose activation causes increased tension generation on the actin filaments to which it is adhered. It in turn is activated by a number of mechanisms, perhaps most prominently by RhoA via Rho kinase (ROCK), which activates myosin light chain kinase and inactivates the myosin

light chain phosphatase to increase myosin activation (Riento et al. 2003). It is curious to note that the severing of adhesion sites at the cellular rear appears to have a stimulatory effect on leading edge protrusion, perhaps through generation and transmission of hydrostatic pressure, starting the protrusion-adhesion cycle anew (Ridley 2006).

Specific Role of RhoG Signaling in Cell Migration:

While most of the small GTPase literature has focused on the canonical GTPases RhoA, Rac1, and Cdc42, 20 other Rho GTPases have been identified. One particularly interesting GTPase for this work is RhoG. RhoG is a Rac-family GTPase with 72% sequence identity to Rac1, and was identified in a screen looking for early gene expression induced during cellular growth by stimulation with growth factors (Vincent et al. 1992). RhoG is a ubiquitously expressed, evolutionarily conserved GTPase, with homologs identified in *C. elegans*, *D. melanogaster*, *M. musculus*, and others. Further, RhoG appears to play a critical role in the evolutionarily conserved processes of phagocytosis and apoptotic cell clearance via the GEF Trio (deBakker et al. 2004). However, its importance in cellular signaling has been debated given that RhoG knockout mice display only minor defects in immune cell function and no gross pathological changes (Vigorito et al. 2004).

Further, given its homology to Rac1, many have sought to determine its role in other forms of cytoskeletal rearrangement, such as lamellipodial protrusion during cell migration. RhoG is thought to act upstream of both Rac1 and Cdc42 (Gauthier-Rouviere et al. 1998; Katoh et al. 2000; Hiramoto et al. 2006; Katoh et al. 2006) and in parallel (Wennerberg et al. 2002). With regard to effectors, it is unclear the variety of effectors

that RhoG engages; for example, RhoG does not bind IRSp53, WASP, Por-1, POSH, or PAKs (Gauthier-Rouviere et al. 1998; Wennerberg et al. 2002), but does bind MLK3, IQGAP, and PLD1, as well as kinectin, and the fragment RhoGIP122 which appears to map to a sequence from TRAF3 Interacting protein. It has also been shown that at least in *C. elegans* axon guidance, RhoG (Mig-2) interacts with WASP (WSP-1), whereas Rac1 (CED-10) interacts with WAVE (WVE-1), suggesting an ability to polymerize actin via the Arp2/3 complex, but this interaction or the interaction of RhoG with Sra1 has not been tested fully in higher organisms (Shakir et al. 2008). Later studies manipulating RhoG and Rac1 in fibroblasts have shown that RhoG is dispensable for cell spreading and only contributes to cell migration in the absence of Rac1 (Meller et al. 2008), suggesting minimal capacity for RhoG to signal on its own. In contrast, the key factors regulating RhoG activation of Rac1 were identified to be ELMO1 and DOCK180, an unconventional Rac1 GEF (Katoh and Negishi 2003), and this pathway was shown to play a role in cell migration (Katoh et al. 2006). Thus, the true downstream effects of RhoG still remain poorly understood.

Similarly, the upstream regulation of RhoG is also poorly defined. To date, only two growth factors have been shown to activate RhoG, EGF (Samson et al. 2010) and FGF (Elfenbein et al. 2009), and in a related fashion phosphatidylserine via the BAI-1 receptor (Park et al. 2007), and ICAM-1 via LFA-1 (van Buul et al. 2007a). Similarly, only a few GEFs have been shown to activate RhoG, among them Trio/Kalirin, Vav2, Vav3, SGEF (Ellerbroek et al. 2004), PLEKHG6 (D'Angelo et al. 2007), and Ephexin4 (Hiramoto-Yamaki et al. 2010). Among the other regulators of GTPases, to date no GAP has been identified for RhoG, but two GDI molecules, GDI-1 and GDI-3, have both been

shown to bind to RhoG (Zalcman et al. 1996; Olofsson 1999; Michaelson et al. 2001; Brunet et al. 2002; Elfenbein et al. 2009). Thus, piecing together a coherent picture of what RhoG does in cells is a bit difficult. Based on localization and function studies, RhoG appears to be trafficked along microtubules in vesicles, as regulated by its effector kinectin, and these vesicles likely contain caveolin-1 (Prieto-Sanchez and Bustelo 2003) and Trio (Prosser et al. 2010). RhoG is also present at the cell membrane where it can be activated by extracellular cues via GEFs and subsequently engage ELMO1 and DOCK180 to activate Rac1. Beyond this, functionally, little is known. Loss of RhoG is known to reduce EGF-stimulated macropinocytosis in A431 cells (Samson et al. 2010), to block phagocytic engulfment of apoptotic cells (deBakker et al. 2004), to reduce dorsal ruffling in some cell types (Wennerberg et al. 2002), and to potentially alter the velocity of cell migration (Katoh et al. 2006; Monypenny et al. 2009), or migration in cancer cells (Hiramoto-Yamaki et al. 2010). Given the ability of RhoG to modulate other GTPases and potentially affect the actin cytoskeleton in so many ways, it is of importance to better understand its functional role in cellular behaviors, particularly in migration where its role remains most controversial (Meller et al. 2008).

Conclusion:

It is important to note, however, that while cells share most aspects of these migration behaviors, the actual details may vary dramatically from cell type to cell type and from one environment to another. Fibroblasts clearly migrate in a manner strikingly different from leukocytes, and cells migrating in a 3-dimensional culture migrate very differently from those migrating on a 2-dimensional culture dish (Wolf and Friedl 2006;

Wolf et al. 2009). Some cells can even modify their modes of migration dramatically in response to extrinsic challenges (Sahai and Marshall 2003). All of these curiosities we wish to better understand so that we can better understand how normal and pathological cell migration disorders develop and how they can be treated.

1.3 Introduction to Growth Factor Signaling and the Regulation of Cytoskeletal Dynamics:

A Broader Perspective:

To respond to environmental changes, cells must have mechanisms by which they can sense those environmental changes and translate them into changes in cellular behavior. Broadly speaking, the ability of cells to respond to extracellular cues is conferred by the expression of a variety of receptors that are incorporated into the plasma membrane and bridge the extracellular and intracellular environments. Many classes of receptor exist, including G-protein coupled receptors (GPCRs), receptor tyrosine kinases (RTKs), cellular adhesion molecules (CAMs), integrins, and many others. Many of these receptors respond to molecules known as growth factors, which were discovered as components of serum that caused cellular proliferation. In addition to their ability to cause cellular proliferation, many of these growth factors are also known to cause cell migration, or chemotaxis, toward the growth factor.

Among these extracellular growth factors known to stimulate and regulate cell migration is the extracellular ligand epidermal growth factor (EGF). The fact that a number of different therapeutic attempts have been made to target EGF signaling in metastatic breast cancer and other diseases indicates the importance of this signaling pathway not only in normal physiological development, but in pathological cellular responses as well.

EGF Signaling in the Regulation of Cell Migration:

The EGF signaling pathway is evolutionarily very highly conserved, but attains great complexity in higher organisms. In fact, it is the combinatorial nature of the

19

components of the EGF signaling pathway that determine specific contextual and cellular responses to EGF ligands, rather than simple activation of the pathway itself (Figure 1.3). EGF binding to EGF receptors promotes hetero- or homodimerization of the four major EGF receptors (ErbB1-4), which are receptor tyrosine kinases, and induces autophosphorylation of the receptor. In turn, this autophosphorylation generates docking sites on the cytoplasmic tail of the receptor that allow for the binding of adaptor proteins and scaffolds. From this point, many signaling proteins interact with the adaptor proteins, initiating downstream signaling cascades dependent on the particular proteins recruited to the receptor. Common to all EGF signaling is the activation of the mitogen-activated protein kinase (MAPK) pathway, the PI3K/Akt pathway, and the p70S6 kinase pathway, which lead to cellular responses such as apoptosis, migration, growth, adhesion, and differentiation (Rubin and Yarden 2001; Yarden and Sliwkowski 2001).

With the early work of Ridley and Hall (Ridley and Hall 1992; Ridley et al. 1992; Nobes and Hall 1995; Nobes et al. 1995), it was established that the Rho GTPase family could be activated downstream of growth factor signaling, and that led to a number of changes in the actin cytoskeleton that were visibly prominent, including membrane ruffling and stress fiber formation. How these morphological changes are mediated has been the subject of a large body of work since those seminal studies. The GTPases can all be stimulated downstream of growth factor receptors, including lysophosphatidic acid (LPA), bombesin, endothelin-1, vascular endothelial growth factor (VEGF), and EGF (Figure 1.4) (Burridge and Wennerberg 2004). The activation of Cdc42 and Rac1 downstream of EGF receptor signaling is perhaps most clear. For both Rac1 and Cdc42, the GEF Vav2 is recruited to the receptor and phosphorylated, causing its activation and

subsequent activation of both Rac1 and Cdc42 (Liu and Burridge 2000). Additionally, there are many other pathways leading to Rac1 activation downstream of the EGF receptor, predominantly mediated by the PI3K pathway (Nobes et al. 1995). Through this pathway, as mentioned above, phosphoinositides are generated, particularly PI$_3$P, at the leading edge, leading to recruitment of a variety of Rac1 GEFs including Tiam-1, P-Rex, and others (Kolsch et al. 2008). In turn, both Cdc42 and Rac1 can bind to and activate PI3K generating a feedback loop that further stimulates the production of leading edge phosphoinositides for signaling and actin polymerization. In addition, RhoA is apparently inactivated at first by EGF stimulation, giving further credence to the mutual antagonism of Rac1/RhoA (Sander et al. 1999; Nimnual et al. 2003), but is activated at later stages, perhaps to assist in productive cell migration by retraction of the trailing edge (Burridge and Wennerberg 2004).

EGF Signaling in the Regulation of Macropinocytosis:

In addition to its effects on cell migration pathways mediated through the Rho GTPases, EGF stimulation in many cell lines also engages the Rho GTPases to rearrange the actin cytoskeleton for the purposes of macropinocytosis. Macropinocytosis is a non-selective fluid-uptake process. Most cells do not demonstrate constitutive macropinocytosis, but rather macropinocytose in response to growth factor signaling, such as in fibroblasts which respond potently to both PDGF and EGF (Mellstrom et al. 1988; West et al. 1989; Anton et al. 2003). The macropinocytosis process is very similar to phagocytosis and requires rearrangement of the actin cytoskeleton on the dorsal surface to engulf and enclose extracellular fluid. Typically, cells form cup-shaped ruffles

on the dorsal surface which are actin-based, and eventually the cup closes in a similar fashion to phagosome formation (Swanson and Watts 1995). Because of its dependence on actin-based dynamics, a number of actin-regulatory proteins have been identified in these structures, including the GTPases Rac1 and Cdc42 (Cox et al. 1997; West et al. 2000; May and Machesky 2001). The phosphoinositides again play a role in macropinocytosis, particularly in the closure of the macropinosomes (Araki et al. 1996) (Swanson JCB 1996). Further, PI3K in particular appears critically important in growth-factor induced macropinosomes (Wennstrom et al. 1994; Kotani et al. 1995), functioning upstream of Rac1 to regulate the actin cytoskeletal changes needed for cup formation in some cell lines, while becoming more important for macropinosome closure in others such as A431 cells. The reasons for these differences remain unclear, but are likely due to the different composition of signaling proteins downstream of EGF signaling. For example, it was recently reported that PLEKHG6 is a GEF that binds to ezrin on the dorsal surface of cells to mediate dorsal ruffling and in its absence, EGF-induced macropinocytosis through membrane ruffling is inhibited (Samson et al. 2010). Further, PLEKHG6 was identified as a specific GEF for RhoG, which can subsequently activate Rac1 through the ELMO1/DOCK180 pathway. How the ezrin/PLEKHG6 complex is activated is uncertain, but appears to involve a RhoA-mediated pathway through PI4,5K that increases PIP_2 concentration and recruits ezrin to the membrane for microvillus formation (Hirao et al. 1996; Matsui et al. 1999). Further, work by Araki et al. (Araki et al. 2007) is in line with these observations, demonstrating that PIP2 is elevated first and is required for the formation of ruffles, but is rapidly degraded with the formation of PIP3, and that this is closely correlated with actin depolymerization and macropinosome

22

closure. However, signaling through ezrin is complex and may activate a number of

GTPases, so the full context is not clearly understood. However, it is clear that the Rho

GTPases are activated by EGF in the process of growth-factor induced macropinocytosis,

and much remains to be understood about their spatiotemporal regulation, in particular

their ability to affect both the formation of macropinocytic cups, and the closure of those

macropinosomes.

1.4 Overview of Fluorescent Biosensors for Protein Activity

Introduction:

Dynamic cellular responses and behaviors, such as cell migration described above, are encoded by the complex spatial and temporal dynamics of a variety of signaling networks. A major challenge is to delineate the precise spatial and temporal behaviors of each of the signaling molecules and second messengers in these networks and how they relate to one another in both space and time. To this end, a large body of work has been devoted to observing the formation, localization, activation, and turnover of a vast number of these signaling molecules. Many techniques have been developed to observe the activity of these molecules over a large population of cells with biochemistry, or single molecules in single cells, both with and without spatial and temporal resolution. Recently, fluorescence-based methodologies have become among the most widely used methods to monitor these cellular events. Biosensors, probes designed to detect changes in protein or second messenger activity or concentration, have been developed to achieve these goals, and they provide the exquisite spatial and temporal resolution needed for analysis of signaling pathways within single cells. However, researchers have long sought to observe more than one molecule's activity in cells at the same time, such that correlative analyses can be made more accurately. As the fluorescent protein and dye palette has expanded, new biosensors and imaging technologies have been designed to observe multiple protein activities within live cells, known as multiplexing or multiparameter imaging. In tandem with the expansion of the available biosensors, analysis of biosensor data has become increasingly complex as well, allowing better analysis of signaling pathways from complex imaging data. In this section, I will

24

highlight the developments that have led to the ability to image signaling activity within cells, the development of probes for the study of intracellular signaling, and some of the current approaches and challenges to the study of intracellular signaling by imaging.

Development of Fluorescent Proteins and Chemical Dyes:

Fluorescence as a biophysical phenomenon has been used for many years to visualize cellular structures and targets, typically by labeling antibodies with small organic dyes, fixing cells or samples of interest, and then adding the antibody which can be subsequently visualized via fluorescence. However, these techniques were highly invasive and gave little information about cellular dynamics due to fixation. Later, dyes were developed that could recognize some cellular structures and molecules, such as DNA or intracellular ions, in living cells, but these are fewer in number and limited in their utility overall. The true revolution in fluorescence technology came with the discovery and development of fluorescent proteins, the first of which were phycobiliproteins isolated from cyanobacteria (Oi et al. 1982). Despite their excellent brightness properties, these fluorescent proteins have remained somewhat limited in their usefulness given their large size (> 200 kDa) and the need to supply bilin chromophores for their functionality. While discovered earlier, green fluorescent protein (GFP) was not cloned until a few years after the phycobiliproteins were used. Clearly the cloning and expression of GFP and its variants has revolutionized the whole of biology (Prasher et al. 1992; Chalfie et al. 1994), allowing for the visualization of molecules within living cells with minimal invasiveness and simplicity of use. In those early days following the cloning and expression of GFP, numerous papers were published simply by tagging a

25

protein with GFP and observing its dynamics and localization. As years went by, the

complexity of such studies gradually increased. In parallel, much work has been devoted

to improving and expanding the "base" GFP molecule, yielding advances in protein

folding efficiency, brightness, photostability, monomericity, and spectral diversity

(Shaner et al. 2004; Shaner et al. 2007; Shaner et al. 2008; Newman et al. 2011).

Through these advances, the ease of use of fluorescent proteins through either

transfection of plasmid DNA or transgenic methods for expression has brought them to

the forefront of imaging studies of protein dynamics.

Biosensors for Monitoring Protein Movement and Translocation:

One of the first uses of the GFP molecule was to examine protein localization,

function, or activity simply by labeling the target molecule with a fluorophore, which acts

as the "affinity reagent," and monitoring the movement or translocation of the target

(Newman et al. 2011). This background information cannot begin to cover all the

examples of fluorescently tagged proteins used for localization studies, as there are now

hundreds, if not thousands, of examples, but we provide a few examples of "activity"

probes using tagged proteins. For example, the treadmilling of actin and the dynamic

polymerization/depolymerization of microtubules have been studied extensively by the

introduction of small quantities of fluorescently-labeled actin or tubulin (< 0.5%) to

reveal significant information about the structure of the cytoskeleton and its dynamics

(Waterman-Storer et al. 1998; Watanabe and Mitchison 2002; Danuser and Waterman-

Storer 2006). Similarly, a variety of proteins and second messengers are known to

translocate to various cellular compartments, such as GTPases to the plasma membrane

in response to growth factors, phosphoinositide-binding proteins to sites of inositide production (Akt, ARNO, GRP1, PLC) (Stauffer et al. 1998; Gray et al. 1999; Hirose et al. 1999; Meili et al. 1999; Oatey et al. 1999; Watton and Downward 1999; Servant et al. 2000), and transcription factors to the nucleus, such as NF-κB (Nelson et al. 2004), and these have been observed through imaging of single fluorophores (O'Rourke et al. 2005). Observation of combinations of such probes simultaneously is relatively trivial today given the available range of bandpass filters, dichroic mirrors, and spectrally separable fluorophores, and has been applied to a variety of high-throughput methodologies for the examination of signaling pathways, of which category a particularly elegant study was recently published (Taylor et al. 2009). However, these single protein fluorescent fusions can only reveal a limited amount of information when it comes to localization or translocation. In particular, for many enzymes or signaling proteins, simply observing localization does not reflect when and where the protein is active, which likely represents the truly functional form of the protein. Thus, sensors that could detect the active form of proteins were soon developed via the use of fluorescence resonance energy transfer (FRET) principles.

FRET-Based Biosensor Design and Usage:

In the field of biosensor development, a myriad of sensors for the detection or identification of signaling protein or second messenger function, activity, or concentration has been generated for use in live-cell imaging. The majority of these probes are based upon Förster Resonance Energy Transfer, or FRET. These probes are particularly advantageous because of their ability to reveal cellular behaviors with a high

degree of spatial and temporal resolution. Probe designs have been extensively covered

in several excellent review articles (Zhang et al. 2002; Miyawaki 2003; Lalonde et al.

2005; Tsien 2005; VanEngelenburg and Palmer 2008) and here I will broadly cover

common designs, methods for their use, and their advantages and disadvantages in

multiplexing.

In general, biosensors come in two basic "flavors": target/substrate-modified

sensors or endogenous sensors. Either format contains an "affinity reagent," which is

either a sensing or substrate element that is modified or bound upon signaling molecule

activity/concentration change within the cell, resulting in a change in FRET or associated

fluorophore intensity/wavelength. See Figure 1.5 for general biosensor design and

possible variations. Here I will discuss several categories of these sensors and their use

in the evaluation of signaling molecule behaviors or activities within cells.

The range of available FRET probes has expanded greatly since the first

demonstrated use of FRET between two fluorescent proteins in an intracellular probe,

which observed the protease-mediated cleavage of a peptide flanked by BFP (blue

fluorescent protein) and GFP (green fluorescent protein) (Mitra et al. 1996). The current

list is almost too exhaustive to list but general classes of sensors can be defined. In

general, there are three categories of probe activity detection methods: activity or ligand-

binding causes 1) FRET between two fluorescent proteins to change, or 2) spectral

properties of a single fluorophore to change, or 3) translocation of a fluorophore.

Translocation sensors and single fluorophore sensor designs are typically simpler than the

FRET-based sensors. The most common examples of these types of sensors are the

phosphoinositide binding domains from a number of proteins, such as Akt, ARNO, Grb2,

28

and others (O'Rourke et al. 2005; Newman et al. 2011). Single fluorophore probes that

change spectrally have been designed based on a critical understanding of the chemistry

of the fluorophore itself, often designing the fluorophore to be more sensitive to pH, ions,

redox status, or even adding domains to the fluorophore that cause the fluorophore to

change its spectral properties. In contrast, FRET-based sensors are much more complex,

usually consisting of multiple domains and flexible linker regions connecting the

fluorophores to the activity-detecting segment, or "affinity reagent." Three basic designs

of these probes exist, with many variants: the sensors separate two fluorescent proteins

with 1) a cleavage-sensitive linker, 2) an affinity reagent that undergoes conformational

change (phosphorylation motif, binding of the molecule of interest, etc.), or 3) an affinity

reagent in addition to the molecule that binds the affinity reagent on the same molecule or

on separate molecules (intramolecular versus intermolecular FRET). These three broad

classes cover most available FRET probes published to date. For design variants that fall

within these classes, see Figure 1.5. For prototypical examples of these probe designs,

the different classes of molecules that can be studied with them, and representative

references, see Table 1.1.

One additional way these sensors can be modified is to alter their targeting. In

many cases, cellular signaling is compartmentalized, and thus it is of interest to better

understand the signaling within that compartment or region. To this end, sensors have

been modified with a number of cellular targeting signals, including, but not limited to

the K-Ras4b membrane targeting sequence for plasma membrane targeting, an ER lumen

targeting sequence, nuclear localization sequences, and Golgi lumen targeting sequences

(VanEngelenburg and Palmer 2008; Palmer et al. 2011). In a number of cases, by

compartmentalizing sensors, multiple sensors can be introduced into cells in different

compartments to allow visualization of subsets of the protein of interest, or to allow study

of two proteins simultaneously, which will be discussed in more detail below.

FRET-Based Biosensors for the Rho GTPases:

Of particular interest to this work, most Rho GTPase FRET probes fall under the

intramolecular FRET sensor design, wherein the affinity reagent and the molecule of

interest are both contained within the probe, in addition to the two fluorophores. Much

optimization has been undertaken to obtain GTPase probes that change their FRET signal

when in the active versus inactive states. In chapter two, I will discuss the design and

optimization of these probes, as well as new advances in this area generated by the Hahn

lab.

Selection of Fluorescent Proteins for Optimal FRET:

In addition to the design of the probe, a key to the development of a sensitive,

useful FRET sensor is to select fluorophores that are optimal for FRET. For a suitable

FRET pair, the following criteria should be met as laid out by Campbell et al. (Campbell

2009): 1) Spectral overlap, donor quantum yield, and acceptor extinction coefficient

sufficient to provide a proper Förster radius; 2) minimal direct excitation of the acceptor

at the wavelength used to excite the donor; 3) sufficient separation of the emission peaks

for ratiometric imaging with bandpass filters; 4) sufficient quantum yield ($\varphi_A > 0.5$) or in

FRET-FLIM, an extinction coefficient, ε_A, greater than 50000 M^{-1} cm^{-1}; 5) and closely

matched values for maturation in both donor and acceptor in the case of fluorescent

proteins (if the acceptor is slow to mature, FRET will be reduced). Additionally, 6) each

FRET pair must be excited using wavelengths that do not excite the other FRET pair, or

the microscope should be able to collect emission from each pair where the other FRET

pair does not fluoresce, or the FRET pairs must be targeted to non-overlapping

subcellular regions. Finally, 7) longer excitation wavelengths are preferred as they cause

significantly less photodamage to the cells under study, permitting shorter intervals

between each image acquisition, and autofluorescence is reduced in the longer

wavelengths, thus reducing background and enhancing signal-to-noise ratio.

When used ratiometrically, these probes consume the greatest amount of spectral

bandwidth, requiring the use of both the donor and acceptor emission and excitation

spectra. Many fluorophores, particularly fluorescent proteins, are problematic in that

they have broad excitation and emission spectra, are relatively dim compared to dyes, and

the resultant FRET signal is relatively small. Thus, only a few fluorophores fit the

criteria above, with most FRET probes largely developed using the fluorophores CFP and

YFP, because they meet all the criteria listed above (Tsien and Miyawaki 1998; Campbell

2009), and can be genetically encoded. Other pairs, such as BFP/CFP and EGFP/DsRed,

have also been used for FRET probes (even before CFP/YFP), but each of these pairs has

significant excitation and emission overlap with the other available pairs, preventing their

simultaneous use in live cells for ratiometric imaging when the probes are present in the

same location. This has prevented the ability of researchers to achieve imaging of

multiple signaling molecule activities/changes simultaneously.

The available palette of FRET fluorophores can be broadened if one considers

dyes in addition to fluorescent proteins. A number of dyes have been used in the

31

literature to effect FRET, and these have been covered in previous reviews (Berney and Danuser 2003; Wallrabe and Periasamy 2005). In addition to these previously used dyes, environmentally-sensitive dyes that change intensity in response to local conformational changes may be used to detect protein activity quantitatively when the change is ratioed against a non-responding fluorophore such as EGFP (Nalbant et al. 2004). Dyes are often much brighter than fluorescent proteins, though less photostable, and there are a number of dyes which extend further into red wavelengths than fluorescent proteins, permitting a greater number of ratiometric FRET pairs, which was taken advantage of to simultaneously image the activities of both RhoA and Cdc42 GTPases using a CFP/YFP FRET pair in addition to an environmentally sensitive long-wavelength dye ratioed against Alexa750 (Machacek et al. 2009). In the case of dyes, there are some limitations. First, the probe must be labeled with the dye in an appropriate location that detects the activation/change in the molecule of interest. For some affinity reagents which can be labeled on a lysine or the N- or C-termini of the protein to detect target changes, dye-coupling is easier and more efficient. However, if the dye is to be coupled to a specific position internal to the affinity reagent, alteration of a number of residues to allow coupling of the dye and testing of the response may be necessary before generating an appropriate construct for experimental use. Dye use also requires protein purification, which is not tractable for all probes. Further, the protein must then be reintroduced into cells at an appropriate level, either by shear-loading, cell-penetrating peptides, endocytic uptake, or by microinjection, all of which will perturb cellular dynamics to a degree. However, there are methods for labeling proteins within cells, such as the FlAsH/ReAsH system, which is dependent upon a tetracysteine motif tagged onto the protein of interest,

32

and a biarsenical dye, which has been previously used for FRET studies (Van Engelenburg et al.; Martin et al. 2005). Such methods for labeling endogenous proteins are still few in number, but will likely expand as time goes on and will permit easier use of dyes for multiplex imaging studies (Hinner and Johnsson 2010).

A third fluorescent protein-based intracellular signal detection technique which has many useful applications, but does not fall under the realm of FRET, is bimolecular fluorescence complementation (BiFC) (Hu et al. 2005; Kerppola 2006; Kerppola 2009; Robida and Kerppola 2009). This technique has the advantage of detecting protein interactions similar to FRET, while only using a single fluorescent protein. However, this technique suffers from irreversibility and the necessity of tagging two proteins with fragments of the fluorescent protein to be complemented. Thus, this technique is primarily useful for detecting protein interaction, but not the dynamics of these interactions. However, it has been used to effect in multicolour studies (Vidi et al. 2008; Kodama and Wada 2009).

Less useful for many applications, intensiometric changes have been measured for FRET or single fluorophore probes. While such intensiometric changes are helpful in assessing relative changes in activity or concentration, they are not truly quantitative and make comparisons between cells and between labs difficult, if not impossible and thus we will not cover these extensively here. Campbell et al. (Carlson and Campbell 2009) have written an excellent review for examining such uses.

Progress toward the ability to use two FRET pairs simultaneously and thus detect

two intracellular signaling activities for correlation studies has been one of the key goals

of FRET-based biosensor work. However, this goal has been limited by the lack of

fluorophores for novel FRET pairs that are genetically encodable, spectrally distinct,

bright, monomeric, photostable, and do not overlap with the common CFP/YFP pair.

The development of the red fluorescent protein from *Discosoma,* DsRed, initially brought

much hope toward the development of a second FRET pair (Matz et al. 1999), but

development of red-shifted fluorescent proteins for sensitized FRET emission that meet

the criteria defined above has been difficult. Only recently have there been significant

advances in the improvement of the photostability, brightness, and quantum yield of red-

shifted fluorescent proteins (Ouyang et al.; Shaner et al. 2004; Shaner et al. 2008), though

the current red-shifted fluorescent proteins are still not as useful for FRET as the

previously developed FRET pairs, given their poorer photostability and lower quantum

yield (Ai et al. 2008). Here we will briefly cover the fluorophores that have been used to

effect in multiparameter imaging experiments.

True emission ratiometric multiplex FRET imaging experiments provide the

greatest quantitative measurements of the spatial and temporal behaviors of the molecules

of interest and thus are preferable to other techniques. For a current list of published

multiplex FRET experiments, see Table 1.2. We will highlight a few illustrative

examples here. In perhaps the most complex multiplex methodology to date, Piljic et al.

(Piljic and Schultz 2008) performed a series of experiments using two spatially resolved

CFP/YFP FRET probes with another probe converted to an mOrange/mCherry FRET

34

pair, along with Fura red to sense Ca^{2+} levels. They achieved resolution of FRET signal, corrected for bleedthrough, despite mCherry being a poor FRET acceptor due to its low quantum yield (Wallrabe and Periasamy 2005; Ai et al. 2008). In that work, the authors were able to relate temporally the relationship among Ca^{2+} changes, PKC and CaMKIIα activity, and Annexin A4 assembly down to a temporal resolution of seconds from imaging data. Further, Ouyang et al. (Ouyang et al. 2010) have recently demonstrated use of mOrange2/mCherry as a second FRET pair to examine both Src and MMP-MT1 simultaneously within cells, showing dramatically different spatiotemporal patterns for each molecule, with Src activity being fast and dispersed downstream of EGF stimulation, whereas MMP-MT1 was slow and predominantly membranous, despite the fact that Src activates MMP-MT1. In contrast to these studies utilizing currently available orange and red fluorescent proteins for novel FRET pairs, Ai and others (Ai et al. 2008) sought to generate a second FRET pair that would better meet the criteria above than mOrange/mCherry combinations and developed an mTeal/YFP and mAmetrine/tdTomato combination which they used to image nucleus-targeted and nucleus-excluded caspase-3 activity sensors simultaneously within the same cell. mAmetrine is a unique fluorophore with a large Stokes shift that allows effective separation of the two FRET pairs but suffers from the need to irradiate cells with near-UV-wavelength light (405 nm). Otherwise, this unique set of FRET pairs best fits the properties laid out above and should be considered for use where cells can tolerate the near-UV-wavelength light irradiation. Additional fluorophores have recently emerged in the violet excitation and emission ranges that permit multiplex imaging, but again, these suffer from the need to illuminate cells with damaging near-UV light (Niino et al. ; Niino

et al. 2009; Tomosugi et al. 2009). A graphical representation of the spectra of fluorophores used in known ratiometric multiplex FRET experiments is illustrated in Figure 1.6.

Perhaps the largest and most successful set of multiplexing experiments has been performed using a CFP/YFP FRET sensor with a ratiometric Ca^{2+} sensor such as Fura-2, Fura red, or Indo-1 (Violin et al. 2003; Palmer et al. 2004; Landa et al. 2005; Harbeck et al. 2006; Newman and Zhang 2008; Wier et al. 2008). In particular the study by Wier et al. examining Ca^{2+} levels via Fura-2, and a CFP/YFP biosensor for MLCK, performs particularly careful experiments addressing spectral crosstalk between the two probes while permitting simultaneous imaging of Ca^{2+} levels and MLCK activity in mouse small arteries. Other groups have suggested that Indo-1 may have less spectral interference than Fura-2 (Tay et al. 2007), while recently Fura red was used with a blue-shifted FRET sensor for cGMP (Cygnus), and a CFP/YFP sensor for cAMP (Niino et al. 2010).

Other groups have developed other methods to expand the range of useful FRET biosensors. Several groups have used additional FRET pairs such as CFP/tHcRed or mTagRFP/mPlum for fluorescence lifetime imaging (FLIM) (in parallel with YFP/tHcRed FLIM or CFP/YFP emission ratiometric imaging) which is highly quantitative, but these FLIM-based multiplexing experiments require tradeoffs in temporal resolution or spatial resolution, depending on the variable measured, not seen with ratiometric imaging. Homo-FRET can also be used with changes in fluorescent polarity being the readout, and this technique only uses a single wavelength, but the emantating signals are often very weak. Additional red-shifted sensors have been used to detect Ras activation via TagRFP/mPlum in FLIM (Grant et al. 2008), and T-

Sapphire/DsRed to detect cGMP (Niino et al. 2009), in addition to a CFP/YFP FRET pair in each study.

Appropriate Probe Use and the Potential for Perturbation of Signaling Dynamics:

As researchers load cells with multiple activity sensors for multiplex imaging, one might hypothesize that cellular perturbation might be an even greater concern than simple spectral separation of the sensors. It is difficult to study a system without perturbing said system. However, we believe that the higher the dynamic range of the sensor, the better, as it allows lower expression levels of the sensor to visualize the same target changes, preventing perturbation of intracellular signaling. In general, the sensitivity or dynamic range of a sensor should be great enough to detect normal, constitutive signaling behaviors within the range of cells' endogenous changes. As we consider a few cases, we can imagine the different ways in which FRET sensors might alter the system they are measuring. When one considers available Ca^{2+} sensors, introduction of these sensors necessitates the binding of some of the cellular Ca^{2+} to the sensor itself. As cellular concentration of the FRET probe increases, binding of Ca^{2+} will increase, thus depleting the cellular pool of Ca^{2+} and potentially blunting or altering intracellular signaling cascades (Berlin et al. 1994; Helmchen et al. 1996). Some calcium-sensing probes were even shown to significantly affect other proteins in the cell, though modification of the sensor to a unimolecular construct abrogated this problem (Miyawaki et al. 1999; Miyawaki 2003). Similarly, substrate sensors, such as phosphorylation sensors, may simply sense active kinase within the cell when expressed at low levels, but as one

37

increases the amount of sensor, the sensor may compete with the endogenous substrate for phosphorylation, thus blunting or altering intracellular signaling cascades.

In the case where the enzyme of interest is contained within the sensor, the cell may be swamped by the addition of this extra enzymatic activity. In the case of GTPase sensors, where the GTPase itself is present within the sensor, comparison of both unimolecular and bimolecular designs is illustrative. In the case of an intramolecular GTPase sensor, it has been shown previously that the sensor is unable to interact effectively with downstream effectors (Pertz et al. 2006), but it is still capable of interacting with GEFs, GAPs, and GDI. As one increases the amount of sensor, the interaction with these proteins increases, and thus the sensor can behave as a dominant negative. Overexpression of GTPases also depletes the available GDI within cells, thus increasing the activity and altering the normal function of many other GTPases dependent on GDI1 (Boulter et al. 2010). In intermolecular GTPase sensors, the same GAP, GEF, and GDI interactions occur, along with additional interactions with downstream effectors. Overexpression of this sensor type can cause it to behave either as a dominant negative or a signal amplifier if allowed to interact with downstream effectors, depending on the circumstances. Massive overexpression of the intermolecular sensor may allow the sensor to act on downstream effectors more easily and activate downstream signaling pathways. However, the dynamic range may be as great as 600% due to low FRET in the "off" state (Welch and Hahn, unpublished observations) with such intermolecular sensors, allowing the expression levels to be titrated much lower than with intramolecular sensors while still obtaining usable FRET signal, reducing the possibility of perturbation. One commonly used method to determine whether GTPase biosensor expression has

perturbed cellular signaling is to monitor for morphological changes or changes in migratory behavior (Kraynov et al. 2000) .

A final consideration in the use of multiple sensors and their potential impacts on cellular signaling should discuss where in signaling cascades these probes should be used in order to reveal the greatest amount of information. Several authors (Miyawaki 2003; O'Rourke et al. 2005; Schultz et al. 2005) have proposed that sensors should be applied to major signaling cassettes, or nodes, where use of a single sensor could reveal the behavior of the entire cassette. Further, they argue that the sensors should be introduced into nodes where the sensor will be buffered or hidden by greater amounts of the endogenous target, thus preventing significant perturbation of the signaling pathway. Indeed, as discussed above with Ca^{2+} sensors, and with other work on GTPases, researchers have addressed how probe expression compares to endogenous molecule concentration. Lastly, if one expresses two sensors that are within the same signaling pathway, perturbations may thus be multiplicative, rather than if two sensors in separate pathways are used, where the perturbation to a pathway is affected by a single sensor rather than two. Thus, careful consideration should not only be given to selection of the available fluorophores for imaging, but also to expression levels and potential impacts on cellular signaling.

1.5 An Introduction to Leukocyte Transendothelial Migration

Blood leukocytes play a critical role in immune surveillance and the host response to foreign antigens. This surveillance is rapid and efficient and involves the routine trafficking of leukocytes from blood to tissue, to lymph, and back to the blood (Springer 1994). In inflammation, an inflammatory stimulus or antigen causes the extravasation of leukocytes to the site of the stimulus or antigen. Extravasation of these leukocytes into tissues is the critical process of transendothelial migration (TEM), and excessive TEM is seen in a variety of inflammatory disorders, including ischemia-reperfusion injury after heart attack, atherosclerosis, and asthma (Jones et al. 2000; Worthylake and Burridge 2001; Hordijk 2006; Galkina and Ley 2007), among others.

Inflammation and Endothelial Adhesion Molecules in the Pathogenesis of Disease:

Many of these disease processes, including atherosclerosis, asthma, rheumatoid arthritis, and others, are chronic inflammatory diseases characterized by the formation of inflammatory lesions at different sites within the body. These lesions are comprised of a myriad of cells, including numerous inflammatory cells which undergo TEM to reach these lesions. The continued presence of these lesions can lead to vessel occlusion causing ischemic damage to the heart (Hansson and Libby 2006), or can cause long-term damage to tissues surrounding the lesions.

Inflammation is also important in the events that occur after an event such as a myocardial infarct caused by an occlusive atherosclerotic plaque, leading to ischemia-reperfusion injury. It is thought that a major mechanism by which the heart is damaged following an infarct is the intense inflammatory response that occurs after reperfusion of

40

the ischemic tissue. This inflammation causes additional damage in the area around the ischemic heart, resulting in an enlarged lesion. However, the central tenet in all of these issues is the recruitment of leukocytes into the tissues and their continued presence at those sites. Thus, a better understanding of the signals that lead to leukocyte recruitment at those sites would offer potential therapeutic mechanisms for preventing these diseases. The only issue with this approach is how one targets pathological inflammation without causing immunosuppression by blocking the ability of leukocytes to be recruited appropriately to sites of infections or other external threats.

Adhesion Molecules and the Initiation of Signaling Events during Leukocyte TEM:

In an effort to modulate inflammatory signals and leukocyte recruitment to reduce disease burden, TEM has been studied intensively. In the endothelium of the vasculature, tight and adherens junctions restrict the passage of fluid and macromolecules into tissues, so to effect inflammation leukocytes must cross this barrier by undergoing TEM. Historical models are based on leukocyte TEM occurring at endothelial cell-cell junctions with junctional breakdown, termed the paracellular TEM route. The possibility that leukocytes traverse endothelial cells, or the transcellular TEM route, was ignored until recently, despite numerous studies (Williamson and Grisham 1961; Faustmann and Dermietzel 1985; Raine et al. 1990) showing that the transcellular route contributes significantly to TEM. Even higher frequencies of transcellular TEM are observed *in vivo*, especially in the microvasculature (Wekerle et al. 1991; McMenamin et al. 1992; Greenwood et al. 1994; Engelhardt and Wolburg 2004; Yang et al. 2005; Hordijk 2006; Nieminen et al. 2006; Carman et al. 2007).

The paradigm of leukocyte TEM signaling divides the process into three steps: rolling adhesion, firm adhesion, and TEM, illustrated with its major molecular players in Figure 1.7. In rolling adhesion, selectins on the leukocyte bind weakly to carbohydrate ligands on the endothelial surface. Next, leukocytes encounter endothelial-bound chemokines which in turn activate leukocyte integrins, facilitating firm adhesion through binding and clustering of the leukocyte integrins $\alpha_4\beta_1$ and $\alpha_{L/M}\beta_2$ to the endothelial ligands VCAM-1 (vascular cellular adhesion molecule 1) and ICAM-1 (intracellular adhesion molecule 1), respectively (Springer 1994). This process is facilitated by signaling processes within endothelial cells with the endothelium responding in a complex fashion to leukocyte adhesion via VCAM-1 and ICAM-1 (van Buul et al. 2007b). Interestingly, mouse models predisposed to atherosclerosis demonstrate that disruption of endothelial cell adhesion molecule interactions reduces the development of atherosclerotic plaques (Lichtman et al. 1996; Lutters et al. 2004; Galkina and Ley 2007). ICAM-1 in particular is critical for leukocyte adhesion in TEM, and is upregulated by inflammatory stimuli (Ross 1999; Cybulsky et al. 2001). Blockade of ICAM-1 and genetic deficiency both reduce the development of atherosclerotic plaques (Sligh et al. 1993; Bourdillon et al. 2000; Hansson and Libby 2006) and significantly attenuate myocardial necrosis in ischemia reperfusion injury (Entman et al. 1991; Smith et al. 1991; Jones and Lefer 2000; Jones et al. 2000), in addition to alleviating a number of other inflammatory diseases such as Crohn's disease and multiple sclerosis (Miller et al. 2003; Sandborn and Yednock 2003; Dalton et al. 2004).

After adhesion to ICAM-1 or VCAM-1, one mechanism by which the endothelium responds is the formation of "transmigratory cups" (TCs), which are actin-

rich processes that form around the adhered leukocyte (Barreiro et al. 2002; Carman et al. 2003; Carman and Springer 2004; Millan et al. 2006). Finally, in the actual process of TEM leukocytes migrate across the endothelium by either passing *between* adjacent ECs (paracellular TEM) into the tissues or by crossing *through* endothelial cells (transcellular TEM). TCs may be involved in guiding leukocyte TEM, as they appear to organize leukocyte β_2- and α_4- containing integrins into linear patterns oriented in the direction of TEM, and have been observed to form regardless of the route of TEM taken (Carman et al. 2003; Carman and Springer 2004; Dejana 2006). However, while paracellular TEM mechanisms are better understood, the signaling pathways involved in TC formation and transcellular TEM, and how the cell decides between the two routes, remain mostly unknown.

Endothelial Cell Signaling During TEM:

A great deal of work has been done examining leukocyte signaling during TEM and in establishing the transmigration paradigm, but it has become apparent that the endothelium plays more than a passive role in TEM. Current knowledge of TEM signaling suggests that leukocyte adhesion to the endothelium begins with engagement of the selectins which induces the recruitment of a variety of proteins that affect actin, including FAK, filamin, α-actinin and others (Millan et al. 2006; Ley et al. 2007). Next, the leukocyte binds endothelial ICAM-1 and VCAM-1 via the integrins $\alpha_{L/M}\beta_2$ and $\alpha_4\beta_1$, leading to the RhoA-mediated clustering of the receptors and actin stress fiber formation (Thompson et al. 2002). Upon ICAM-1 and VCAM-1 clustering, these molecules are incorporated into lipid rafts with other molecules such as tetraspanins from which they

43

form a scaffold to initiate signaling within the endothelial cell (Rohlena et al. 2009). Among the pathways activated include phosphoinositide signaling pathways, release of intracellular Ca^{2+}, and phosphorylation of actin-binding proteins (Etienne et al. 1998; Adamson et al. 1999; Etienne-Manneville et al. 2000). Ultimately, each signaling pathway converges on the Rho GTPases Rac1, RhoG, and RhoA to cause cytoskeletal rearrangement in the endothelium in response to the adherent leukocyte. Interestingly, it is from these clustered ICAM-1 patches that dorsal ruffles often form and lead to the formation of microvillous cup-like structures that embrace the migrating leukocytes within minutes. ICAM-1 signaling is clearly important in TEM since the cytoplasmic tail is required for the formation of these cups and leukocyte TEM (van Buul et al. 2007b; van Buul and Hordijk 2009; Fernandez-Borja et al. 2010). These pathways are summarized in Figure 1.8.

It is at this point in TEM that clarity in cellular behaviors begins to fade. It is clear that in some cases, adherence of the leukocyte and formation of these "cups" causes the endothelium to engulf the leukocyte and passage it to the basolateral surface via "transcellular" transmigration. The precise mechanisms leading to this behavior remain obscure, but do use the GTPases described above (Barreiro et al. 2002; Carman and Springer 2004; Dejana 2006). In contrast, many leukocytes are known to pass between cells, or the "paracellular" transmigration pathway (Springer 1994; Ley et al. 2007). Compared to transcellular migration, the signaling pathways involved in paracellular transmigration are better characterized. First, leukocyte adhesion to ICAM-1 and VCAM-1 causes the disassembly of tight and adherens junctions between endothelial cells (Fernandez-Borja et al. 2010). It accomplishes this by a RhoA-dependent

phosphorylation of VE-Cadherin, one of the junctional proteins, leading to junctional instability and separation of endothelial cells (Allingham et al. 2007). VE-Cadherin also couples to the actin cytoskeleton, and it is likely that actomyosin contractility via RhoA pulls on these contacts to further assist in the separation of the cellular junctions (Saito et al. 1998). In addition, downstream of VCAM-1, Rac1 is activated and binds to the NADPH oxidase system to produce reactive oxygen species which indirectly induce phosphorylation of components of the adherens and tight junctions, further impairing cell junction stability (van Wetering et al. 2002; van Wetering et al. 2003). This paracellular pathway is clearly important, as most leukocytes appear to pass through endothelial monolayers by this mechanism (70-100%) (Dejana 2006). Thus, by investigating these signaling pathways further, we hope to identify novel targets for inhibition that may more selectively prevent leukocyte recruitment and transendothelial migration at sites of pathological inflammation.

Therapeutic Strategies in Inflammatory Diseases:

The general paradigm for leukocyte TEM has provided a great wealth of information on which molecules are involved at different stages of TEM. As a result, many attempts have been made to selectively block the different steps of TEM to prevent disease. Most of the attempts to generate therapeutics have focused on the first two steps, rolling adhesion and firm adhesion. Some of the first studies focused on rolling adhesion as a target to prevent inflammatory cell recruitment, with double knockout mice for P-selectin and E-selectin having no leukocyte rolling and virtually no recruitment in response to an inflammatory insult (Mayadas et al. 1993; Bullard et al. 1996; Frenette et

al. 1996). A commercially available compound, fucoidan, was an excellent blocking

agent for both selectins, but in systematic assessment of its use, a number of issues were

raised, chief among them that nearly 95% inhibition of rolling had to be achieved before

leukocyte adhesion could be affected (Kubes et al. 1995). Further, some blood vessels

did not even respond to the fucoidan treatment. Continued investigations into using

selectin inhibitors have been performed, but nearly all have been unsuccessful (Harlan

and Winn 2002). Curiously though, studies have indicated that the timing of anti-selectin

therapy may be critical (Staite et al. 1996), demonstrating that for the first two hours after

an insult, selectins are important for leukocyte recruitment, and treatment works at this

stage, but after two hours, treatments have no impact (Hwang et al. 2004).

Attention has also been turned to the cellular adhesion molecules and their

associated binding partners, the leukocyte integrins. One of the first targets was the

CD18 receptor (Arfors et al. 1987; Harlan and Winn 2002), with many positive studies

suggesting potential therapeutic effects by blocking it (Doerschuk et al. 1990; Kurose et

al. 1994; Issekutz et al. 1996). However, clinical trials with agents designed to target the

CD18 receptor have largely failed (Kelly et al. 2007), with the exception being

Efazulimab, which targets the co-receptor CD11a and is used in moderate to severe

psoriasis (Papp et al. 2001; Jullien et al. 2004). It is suspected that it may be of value in

some inflammatory conditions to inhibit CD18, but it has become apparent that

leukocytes simply bypass the need for CD18 and selectins in adhesion by using α_4

integrins to bind VCAM-1 and subsequently firmly adhere (Alon et al. 1995). Indeed,

clinical trials using an antibody against α_4 integrin have shown promise against multiple

sclerosis, Crohn's disease, and ulcerative colitis (Ghosh 2003; Miller et al. 2003;

Sandborn and Yednock 2003; Dalton et al. 2004). While there is some promise in these studies, they suggest that either combinatorial therapy or targeting of new signaling molecules will be necessary for the treatment of inflammatory diseases. Thus, we anticipate looking at other targets, starting with those involved in endothelial cell signaling, particularly as it pertains to the Rho GTPases.

1.6 Figures and Legends

Figure 1.1: Rho Family of Small GTPases.

Summary of all known Rho family small GTPases and their phylogenetic relationships.

Figure 1.1
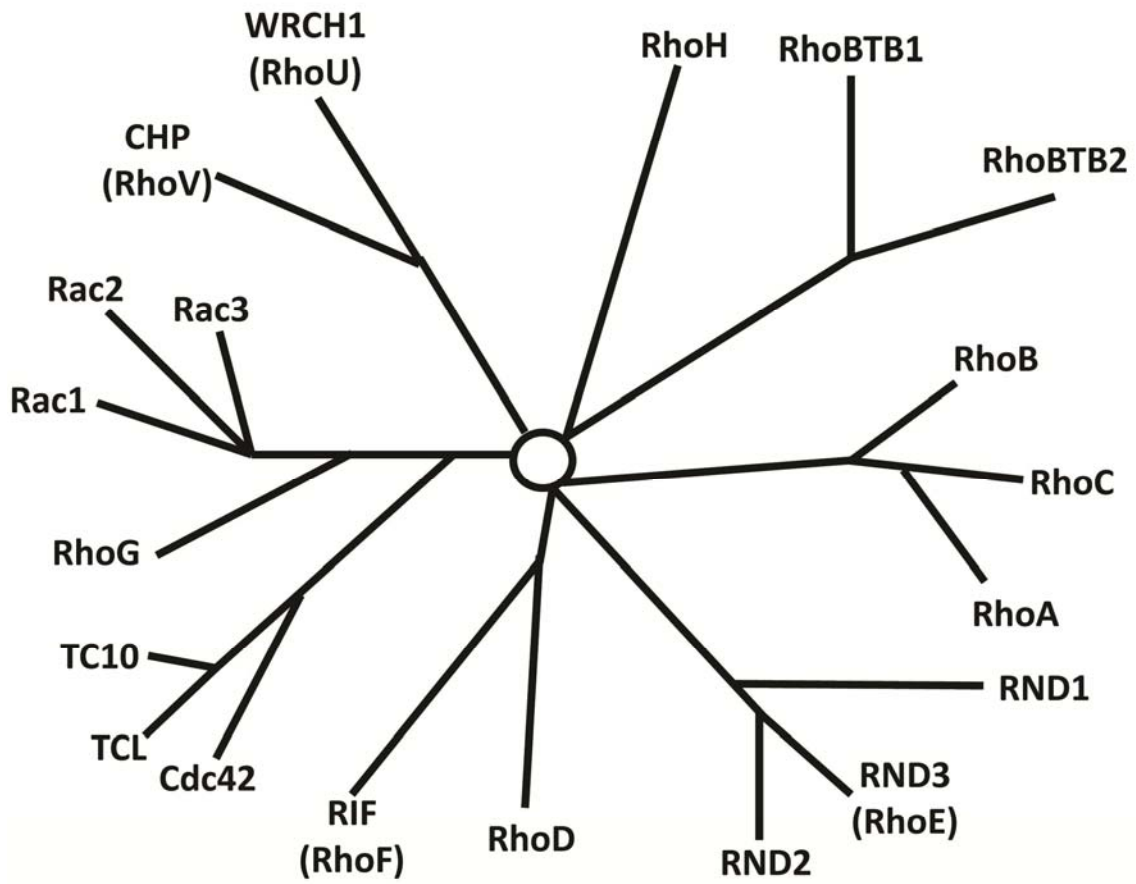
Adapted from Heasman and Ridley, Nat Rev Mol Cell Bio *2008;9:690-701*

Figure 1.2: Distinct Steps in the Cell Migration Cycle.

A depiction of the three major steps in cell migration and associated signaling proteins.

(A) Cell Polarization: the first step is morphological polarization, mediated largely by generation of phosphoinositides at the leading edge, activation of Cdc42, and alteration of microtubule/Golgi polarity.

(B) Cell Protrusion: the second step combines protrusion and adhesion formation, with protrusion mediated largely by actin polymerization through Rac1/Cdc42, potentially RhoA, and actin regulators, and adhesion also mediated by Rac1/Cdc42, but also via integrins and other focal adhesion proteins.

(C) Tail Retraction: the last step is adhesion disassembly and rear retraction, mediated by FAK, actomyosin contractility (RhoA-Myosin II), Ca^{2+}, and proteases. Each of these steps is critical to the cyclical nature of cell migration.

Figure 1.2

(A) Cell Polarization
Regulators of Polarity

Side/Rear	Leading Edge
PTEN	aPKC/Par3/Par6
Myosin	Microtubules
	Integrins
	Rac1.GTP and Cdc42.GTP
	Phosphoinositides

Microtubules
MTOC
Nucleus
Leading Edge
Actin Stress Fibers
Vesicles
Adhesions

(B) Cell Protrusion
Regulators of Protrusion

Adhesion Formation	Actin Polymerization
Integrins	mDia
Talin	Arp2/3
Rap1	ADP/Cofilin
Rac1.GTP, Cdc42.GTP, RhoA.GTP	
ENA/VASP	

New Adhesions
Protrusion

(C) Tail Retraction
Regulators of Retraction

Adhesion Disassembly/ Force Generation
Calpain
FAK
RhoA.GTP
Myosin II
Ca^{2+}

Translocation

Adapted from A. J. Ridley et al. Science 2003;302:1704-1709.

Figure 1.3: Combinatorial Nature of Growth Factor Signaling Networks.

(A) A variety of growth factors and ligands are capable of binding to a variety of cell surface receptors. EGF, for example, and its related growth factor ligands such as NRG bind to a combination of the dimers of the four EGF receptor tyrosine kinase subtypes, initiating a variety of downstream signals.

(B) The signal-processing layer is activated by particular combinations of the receptor homo- and hetero-dimers after ligand binding, and depending on the spatial and temporal dynamics of the signals, initiates a variety of cellular signaling cascades, a few of which are illustrated here.

(C) Upon engagement of a variety of cellular signaling cascades, a variety of cellular behaviors can be initiated depending on the context of the stimulus, leading to behaviors as varied as migration, adhesion, growth, apoptosis, and differentiation.

Figure 1.3
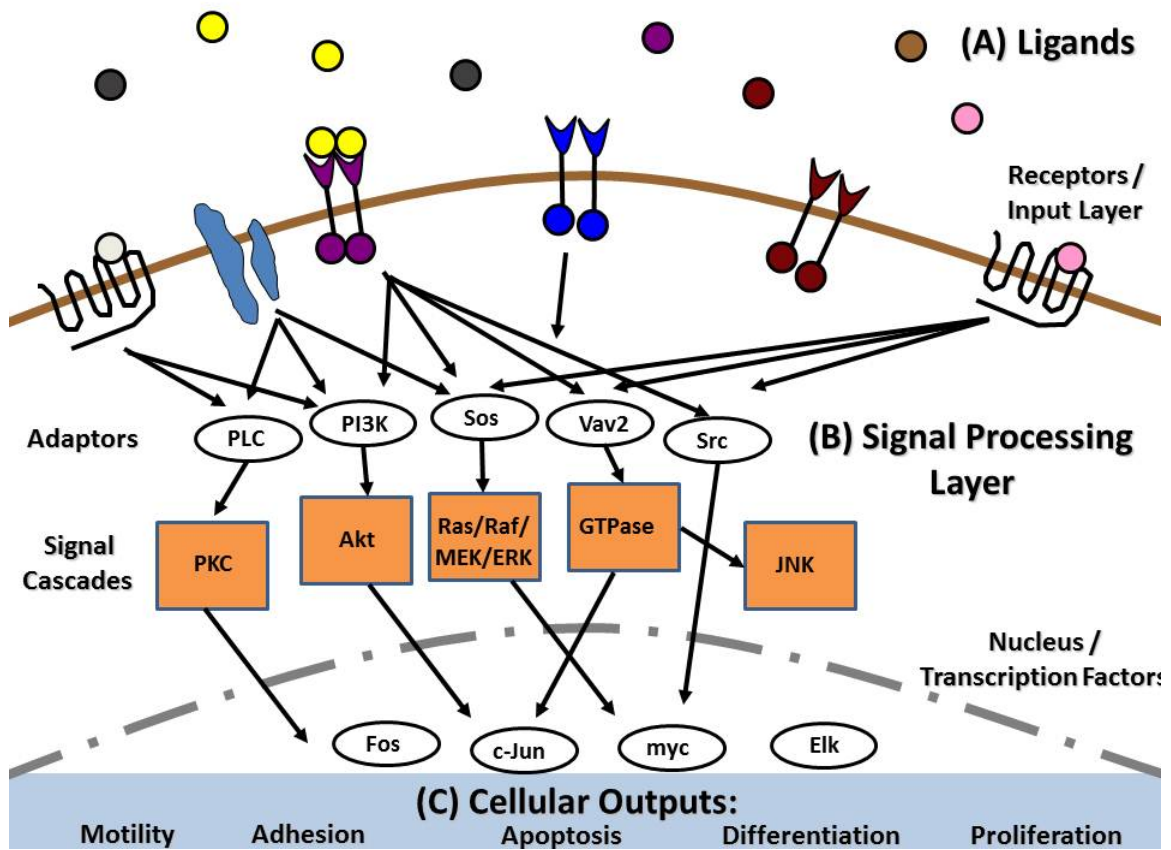
Figure adapted from Yarden and Sliwkowski Nat Rev Mol Cell Bio *(2001);2(2):127-37.*

Figure 1.4: Regulation of Rho GTPases Downstream of Growth Factors.

Summary of known signaling pathways activated by growth factor signaling that lead to regulation of the major Rho GTPases Rac1, RhoA, and Cdc42 for actin cytoskeleton rearrangement. Both stimulatory and inhibitory pathways exist downstream of these factors.

Figure 1.4
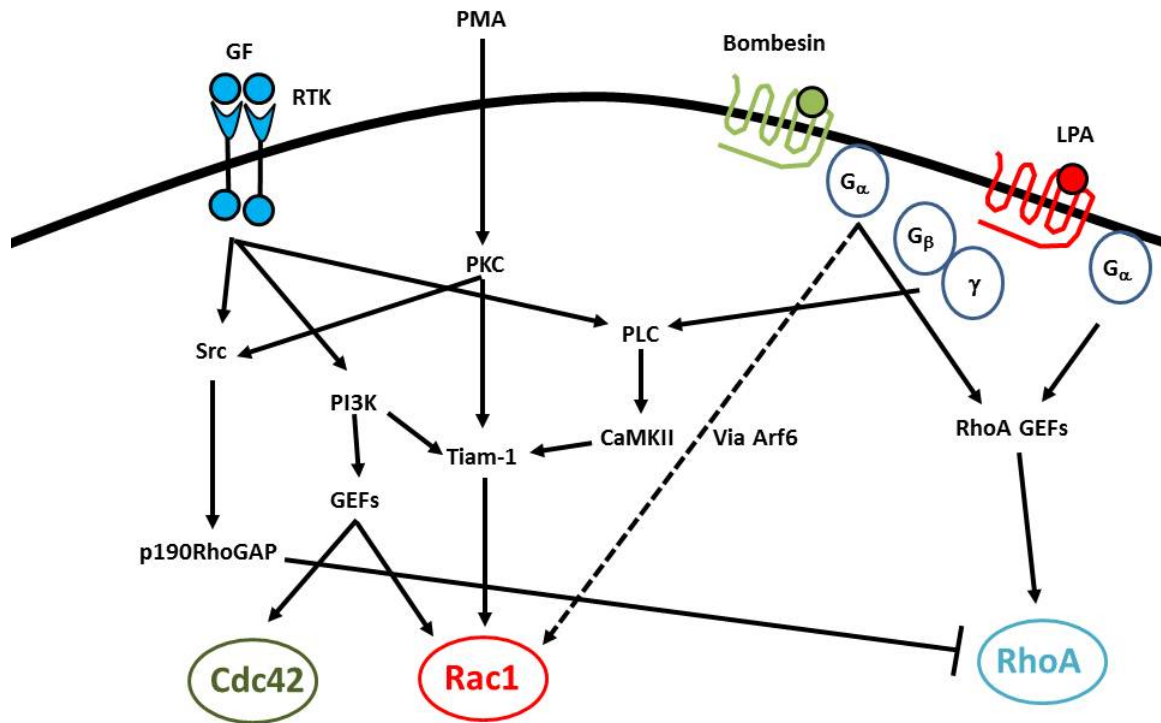
Figure adapted from Burridge and Wennerberg, Cell. *2004;116(2):167-79.*

Figure 1.5: Common Designs for Intracellular Signaling Probes.

Biosensors for intracellular signaling come in a variety of designs, for sensing both (A)

the regulation of the endogenous protein, and (B) the endogenous protein itself.

Figure 1.5
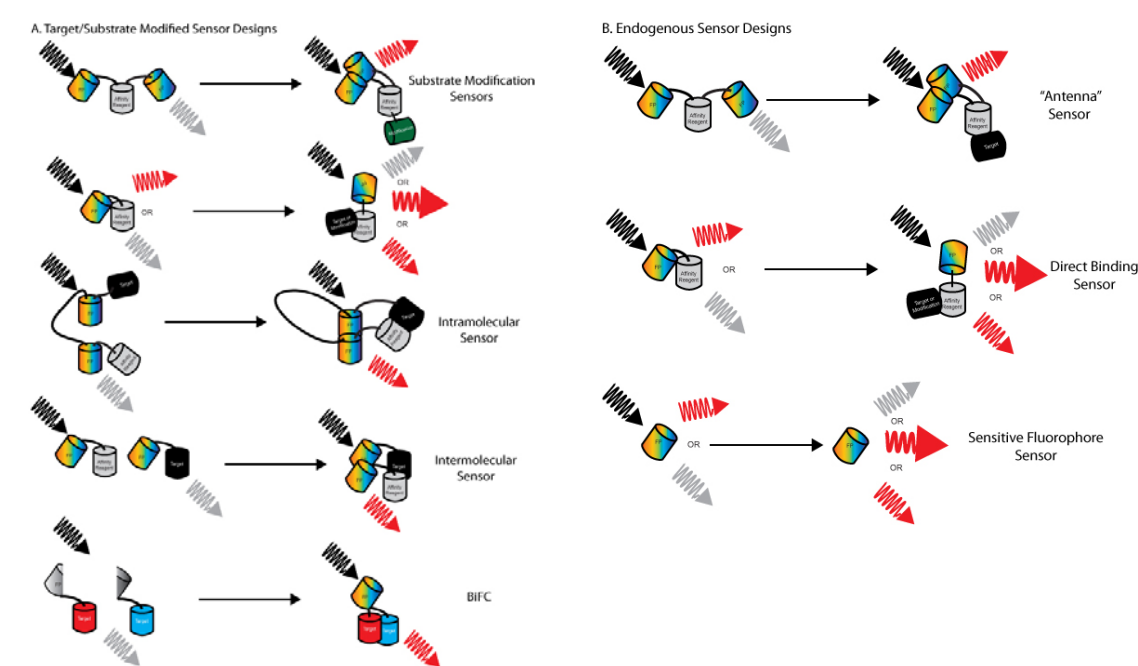
Figure 1.6: Spectra of Fluorophores Used in Ratiometric FRET Multiplex Experiments.

Four major "groups" of fluorophores have been utilized to perform ratiometric imaging

of two FRET probes simultaneously. These orthogonal FRET pairs are (A) EBFP/ECFP

and mOrange/mCherry, (B) ECFP/EYFP and mOrange2/mCherry, (C)

mAmetrine/tdTomato and mTeal/YFP, and (D) T-Sapphire/DsRed and ECFP/EYFP.

Figure 1.6
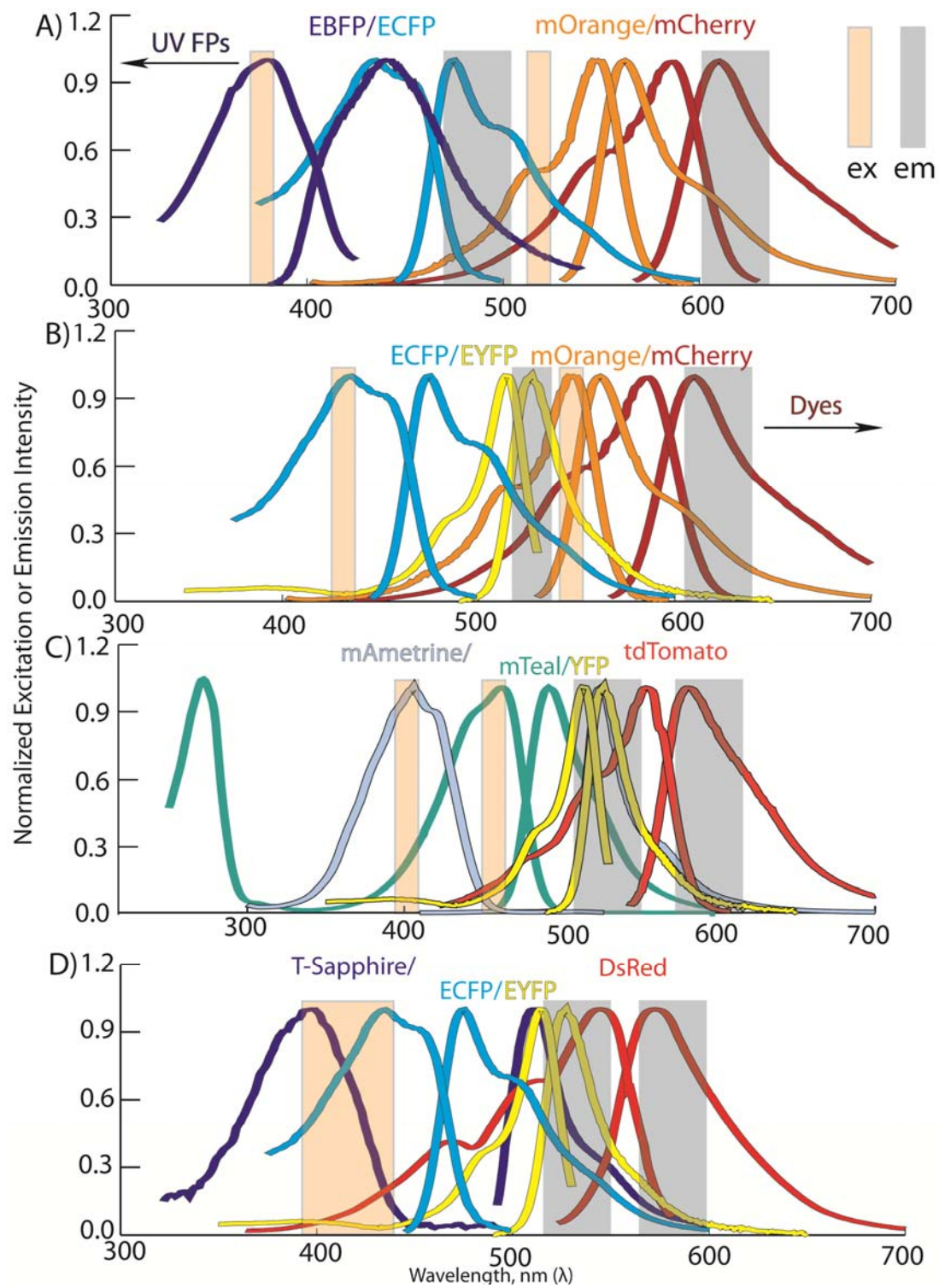
Figure 1.7: Leukocyte Adhesion and Signaling Cascade.

For leukocytes to respond to sites of inflammation, they must interact with the inflamed endothelium to receive the appropriate signals to stop and transmigrate. The first interaction with the endothelium is rolling, mediated largely by selectins. The leukocyte is then activated (integrins, specifically) by chemokines on the surface of the endothelium as it rolls across the endothelium, leading to arrest of the leukocyte via integrin-endothelial cell adhesion molecule interactions. Additional steps have been described, such as tethering and slow rolling mediated by selectins, adhesion strengthening and intravascular crawling mediated by a variety of signaling pathways, and paracellular and transcellular transmigration mediated by signaling processes in both the leukocyte and the endothelium. Key molecules involved in each step are indicated in boxes.

Figure 1.7
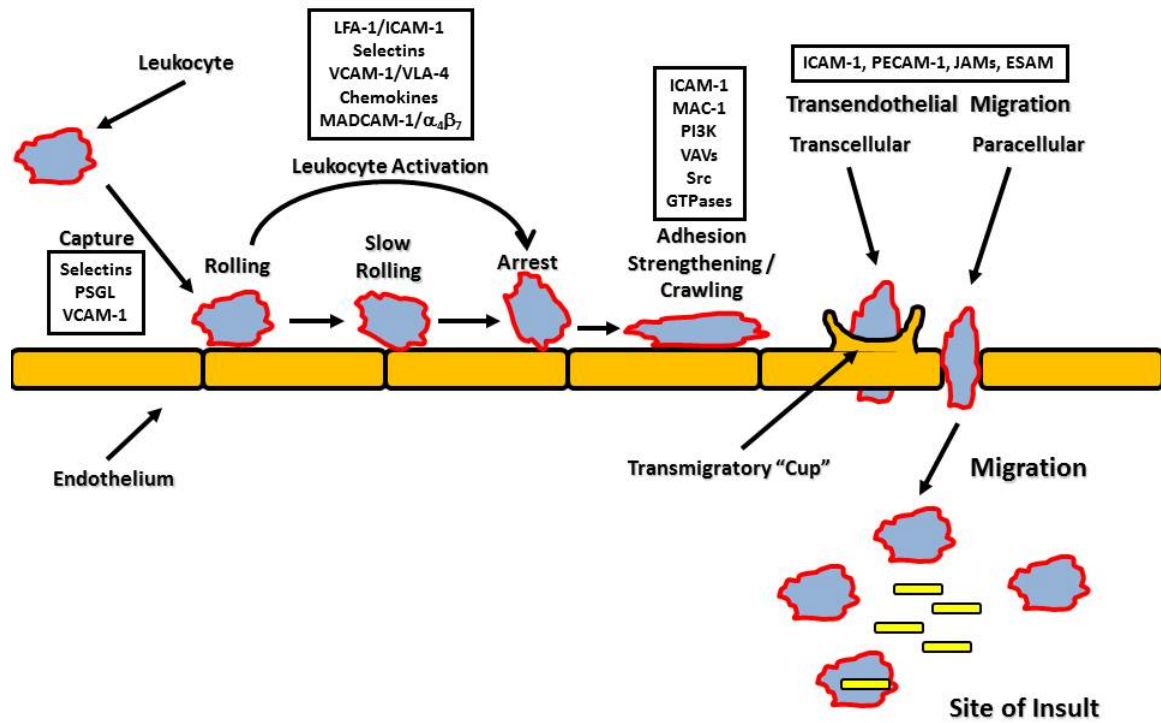
Figure adapted from Ley, K et al. Nat Rev Immunol *2007;7(9):678-89.*

Figure 1.8: Proximal Signaling Events in the Endothelium Leading to Formation of Endothelial Docking Structures Induced Upon Firm Adhesion of Leukocytes via ICAM-1.

Overview of signalling events leading to the formation of endothelial docking structures, due to firm leukocyte adhesion. Ligation and clustering of ICAM-1 leads to activation of GEFs, which activate a subset of Rho GTPases that lead to formation of the docking structure via cytoskeletal rearrangement. RhoA appears to be involved in clustering ICAM-1and stiffening the cell, whereas RhoG and Rac1 mediate membrane ruffling and actin dynamics that lead to formation of the docking structure.

Figure 1.8
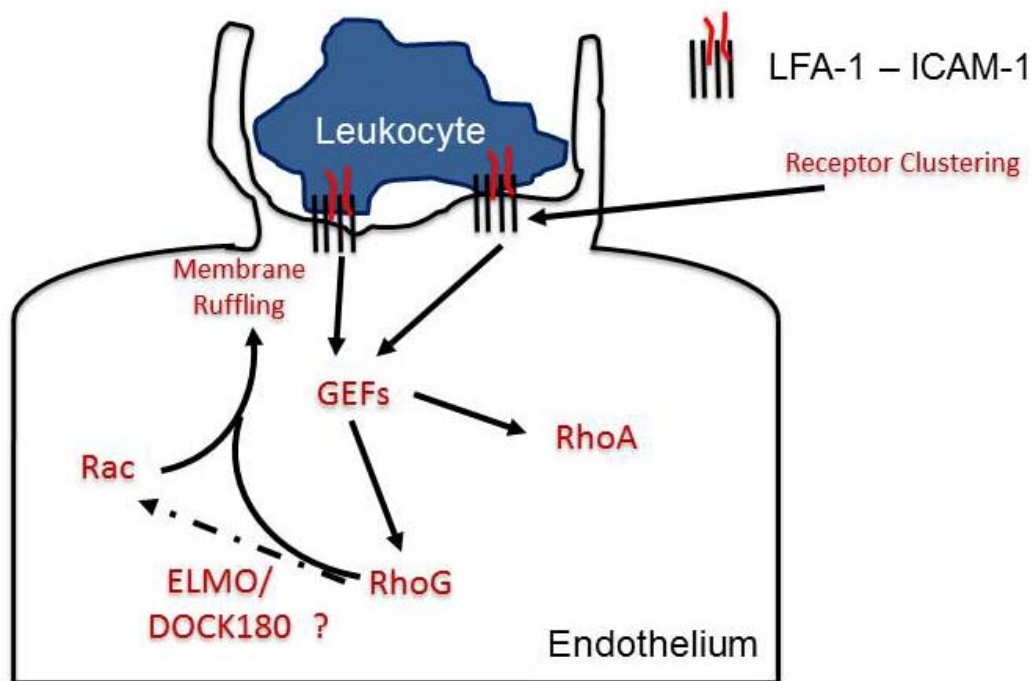
Figure adapted from Fernandez-Borja M et al. Cardiovasc Res *2010;86(2):202-210.*

Table 1.1: Fluorescent Biosensors for Intracellular Signaling Pathways

A list of available targets for study of intracellular signaling pathways with representative

biosensor examples for each.

Reporter For:	Types of Sensors:	Sensor Examples:	References:
Transcriptional activity	Single fluorophore, color-changing fluorophores	DsRed-Timer, EGFP-MODC	(Li et al. 1998; Terskikh et al. 2000; Bogdanov et al. 2009)
Protein turnover	Fluorescent proteins, FLASH/ReAsH	Fluorescent timers, FLASH/ReAsH labeled proteins	(Gaietta et al. 2002; Patterson and Lippincott-Schwartz 2002)
PI(4,5)P$_2$ Dynamics	Localization-based, FRET-based	CYPHER, Pippi-PI(4,5)P$_2$, FP-PH$^{PLC\delta1}$	(Violin et al. 2003; Varnai and Balla 2006; Nishioka et al. 2008)
PI(3,4,5)P$_3$ Dynamics	Localization-based, FRET-based	FP-PH^{GRP1}, FP-PH^{ARNO}, Fllip	(Sasaki et al. 2003; Varnai and Balla 2006)
3'PI Dynamics	FRET-based	InPAkt	(Ananthanarayanan et al. 2005)
Absolute [IP$_3$]	FRET-based	FIRE-1,-2,-3, IRIS-1	(Tanimura et al. 2004; Matsu-ura et al. 2006; Kapur et al. 2007)
Diacylglycerol Dynamics	FRET-based	DAGR, DIGDA; (PKCβII)	(Violin et al. 2003; Nishioka et al. 2008)
Phosphatidylserine Dynamics	Localization-based	GFP-Lact-C2	(Yeung et al. 2008)
Phosphatidic Acid Dynamics	FRET-based	Pii-DK (based on DOCK2)	(Nishioka et al.)
Halide Ions	Intensity-based, FRET-based	YFP(H148Q), Clomeleon, Cl-Sensor	(Jayaraman et al. 2000; Kuner and Augustine 2000; Galietta et al. 2001; Markova et al. 2008)
Intracellular pH	Intensity-based, Ratiometric single fluorophore, FRET-based	EGFP, EYFP, SuperEcliptic pHluorin, ratiometric pHluorin, YFpH	(Kneen et al. 1998; Llopis et al. 1998; Miesenböck et al. 1998; Awaji et al. 2001)
Redox Status and Redox Species	Intensity-based, Ratiometric single fluorophore	rxYFP^N_C, roGFP, roGFP 1-iX, HyPer, mt-cpYFP	(Ostergaard et al. 2001; Dooley et al. 2004; Hanson et al. 2004; Belousov et al. 2006; Cannon and Remington 2006; Wang et al.

			2008)
$\Delta[Ca^{2+}]$	Intensity-based	Camgaroo-2, GCaMP3, flash-pericam	(Griesbeck et al. 2001; Nagai et al. 2001; Tian et al. 2009)
Absolute $[Ca^{2+}]$	FRET-based	Cameleon3, split cameleon, D3cpv	(Miyawaki et al. 1997; Palmer et al. 2006)
Absolute [cAMP]	FRET-based	ICUE3, PKA-camps, PKA^{RII}-ECFP/PKA^{Cat}-EYFP	(Zaccolo and Pozzan 2002; Nikolaev et al. 2004; Allen et al. 2006)
Δ[cGMP]	Intensity-based	FlincGα or β	(Nausch et al. 2008)
Absolute [cGMP]	Ratiometric single fluorophore, FRET-based	Cygnet-2.1, cGi family, cGS-DE5	(Honda et al. 2005; Lohse 2006; Russwurm et al. 2007)
NO	FRET-based	FRET-MT, Piccell	(Pearce et al. 2000; Sato et al. 2006)
Absolute [ATP]	FRET-based	Ateam-1.03/3.10	(Imamura et al. 2009)
[ATP]/[ADP]	Ratiometric single fluorophore	Perceval	(Imamura et al. 2009)
Extracellular [glutamate]	FRET-based	FLIPE-Y, SuperGluSnFR	(Okumoto et al. 2005; Hires et al. 2008)
Absolute [sugar]	FRET-based	FLIPglu-Y, FLIPmal-Y, FLIPrib-Y	(Lager et al. 2003; Deuschle et al. 2005)
Absolute $[Zn^{2+}]$	FRET-based	eCALWY, Cys_2His_2, His_4	(Dittmer et al. 2009; Vinkenborg et al. 2009)
Membrane Potential	Intensity-based, FRET-based	FlaSh family, Flare, VSFP2.3, Mermaid, SPARCS	(Siegel and Isacoff 1997; Ataka and Pieribone 2002; Guerrero et al. 2002; Dimitrov et al. 2007; Tsutsui et al. 2008)
Small G-Protein Activity	FRET-based	Raichu series, FLAIR (Rac1), RhoA, Cdc42, Ral, Ras, Rap probes	(Kraynov et al. 2000b; Mochizuki et al. 2001; Chiu et al. 2002; Itoh et al. 2002; Yoshizaki et al. 2003; Nalbant et al. 2004a; Fujioka et al. 2006; Pertz et al. 2006b; Machacek et al. 2009)
Kinase Activity	FRET-based	Akind (Akt), Miu2 (ERK), GFP-PDK1-	(Gavet and Pines ; Kurokawa et al.

		RFP (PDK1), DKAR (PKD), CKAR (PKC), AKAR (PKA), Phocus-2pp (InsR Kinase), Srcus/Src reporter, Picchu (RTK), Picchu-Z (EGFR), ATOMIC (ATM), Aurora B kinase, Cyclin-B1, Histone H3 phosphorylation,	2001; Violin et al. 2003; Lin and Ting 2004; Sato and Umezawa 2004; Schleifenbaum et al. 2004; Itoh et al. 2005; Wang et al. 2005; Fujioka et al. 2006; Calleja et al. 2007; Johnson et al. 2007; Kunkel et al. 2007; Fuller et al. 2008)
Calcineurin Phosphatase	FRET-based	CaNAR1	(Newman and Zhang 2008)
O-glycosyl-transferase	FRET-based	O-GlcNAc Sensor	(Mahal 2008)
Proteases	FRET-based	Caspase-3, Caspase-3/6, MT1-MMP	Luo Y Nuc Acids Res 1998, He L Cytometry A 2006, Ouyang M JBC 2008
Histone Modification	FRET-based	K9, K27, Histac	Yoshida M PNAS 2009, Singh PB Bioessays 2000
Cell Cycle Progression	Intensity-based	Fucci series	Miyawaki Cell 2008
Neutrophic Factor [BDNF]	FRET-based	Becell	Umezawa Y ACS Chem Bio 2008
Mechanical Force	Intensity-based, FRET-based	TSMod, stFRET, PriSSM	511, 512, 513, Schwartz MA Nature 2010, Sachs F FEBS 2008, Uyeda TQ PNAS 2008

Table 1.1

Table adapted from Newman et al., Chem Rev. 2011 May 11;111(5):3614-66.

Table 1.2: Known Multiplex Imaging Experiments

A list of known multiplex imaging experiments with the fluorophores and analysis techniques used.

FRET Multiplex Experiments	Reference	Fluorophores Used	Methods Used for Imaging
	(Abad et al. 2004; Galperin et al. 2004; He et al. 2004; He et al. 2005; Wu et al. 2006)	CFP/YFP/mRFP1	Three-color, Ratiometric FRET x2 on same probe
	(Kawai et al. 2004; Kawai et al. 2005)	CFP/DsRed with YFP/DsRed	Intensiometric FRET x2
	(DiPilato et al. 2004)	CFP/YFP	Spatial separation, Ratiometric FRET x2
	(Brumbaugh et al. 2006)	CFP/YFP	Ratiometric FRET x2 on same probe
	(Piljic and Schultz 2008)	CFP/YFP, mOrange/mCherry, Fura Red	Ratiometric FRET x2, Spatial separation, Ratiometric FRET x2 + Intensiometric FRET + Calcium Sensor
	(Ai et al. 2008)	mTFP1/YFP, mAmetrine/tdTomato	Ratiometric FRET x2
	(Tomosugi et al. 2009)	Sirius/mseCFP, Sapphire/DsRed	Ratiometric FRET x2
	(Niino et al. 2009)	mSapphire/RFP CFP/YFP	Single wavelength excitation, Ratiometric FRET x2
	(Machacek et al. 2009)	CFP/YFP, Dyes: Mero87/Alexa750 pair	Ratiometric FRET + Ratiometric dye change
	(Niino et al. 2010)	mTagBFP/sREACh, CFP/YFP, Fura Red	Ratiometric FRET x2 + Ca^{2+}
	(Ouyang et al. 2010)	CFP/YFP, mOrange2/mCherry	Ratiometric FRET x2
	(Peyker et al. 2005)	FLIM: CFP/tHcRed and YFP/tHcRed	FLIM FRET
	(Grant et al. 2008)	CFP/YFP and FLIM: mTagRFP/mPlum	Ratiometric FRET + FLIM FRET
	(Kwok et al. 2008)	FLIM: mRFP/GFP, mStrawberry/GFP, mRFP/Venus, mStrawberry/Venus, and mDarkVenus/mGFP	FLIM FRET

Table 1.2

CHAPTER TWO: RATIONAL DESIGN AND DEVEOPMENT OF RHO GTPASE BIOSENSORS FOR LIVE CELL IMAGING

2.1 Abstract

Numerous FRET-based biosensors have been developed for the study of intracellular signaling. One of the classes of intracellular targets whose understanding has grown greatly from development of these tools has been the Rho GTPases. Rho GTPase biosensors have largely taken two forms: intramolecular (single-chain) FRET sensors and intermolecular (dual-chain) FRET sensors based on CFP/YFP FRET pairs. Traditionally, single-chain sensors have been preferred given their ease of use due to equimolar expression of donor and acceptor fluorophores, and their assumed inability to interact with downstream effectors. However, these sensors exhibit significant FRET in the "off" state and dynamic ranges are not large. Here we improve upon existing dual-chain and single-chain sensors, and compare and contrast their sensitivity and dynamic ranges, their tendencies to exhibit artefacts, and their ability to perturb downstream signaling pathways.

In addition, we develop new sensors utilizing FRET pairs orthogonal to CFP/YFP, and also a new construct design that allows for equimolar expression of dual-chain sensors from a single plasmid. Our results indicate that both single-chain and dual-chain sensors are highly useful depending on the particular experiment, and that through the use of new expression and analysis techniques, dual-chain sensors, due to their high dynamic range, are the preferred choice for many experiments.

2.2 Introduction

As discussed in the background materials, the Rho GTPases are biochemical switches that bridge the gap between extracellular stimuli and changes in intracellular signaling and cellular morphology. The GTPases couple a variety of extracellular receptors to a host of cellular processes, including gene transcription, phagocytosis, cell migration, cell-cycle progression, vesicular trafficking, and others. That these GTPases can selectively control so many responses indicates that these molecules are very tightly controlled both spatially and temporally. Thus, to tease apart these different signaling pathways, researchers have long sought to examine the activity of these GTPases in living cells.

Previous Methods for Assessing Rho GTPase Activity:

As molecular switches, Rho GTPases cycle between an "on" and "off" form, dictated by their GTP-loading status. When bound to GTP, Rho GTPases are "on," and when bound to GDP, Rho GTPases are "off." Guanine Exchange Factors (GEFs) are molecules that catalyze the exchange of GDP for GTP and activate the GTPases, while GTPase Activating Proteins (GAPs) catalyze the hydrolysis of GTP to GDP, turning the GTPases "off." Only when the GTPases are in the "on" state do they interact with downstream effectors, and this state of the protein is the one that scientists are interested in, as it catalyzes the myriad cellular events controlled by the Rho GTPases. Accessing the activity status of Rho GTPases, however, has been a difficult process over the years. Early studies used proxy indicators for Rho GTPase activation, such as the presence of stress fibers, as an indicator of RhoA activation. Biochemical assays were also

69

developed to examine the activation status of the GTPases, first by adding $^{32}P_i$-orthophosphate to cell media, allowing its incorporation into GTP, immunoprecipitating the Rho GTPase, and then using thin layer chromatography to separate GDP and GTP (Gibbs 1995) as an indicator of Rho GTP loading status. Next, other researchers developed the "pull down" assay whereby the GTPases were immunoprecipitated by the use of a GST-fused binding domain that selectively bound the active form of the GTPase (Taylor and Shalloway 1996; de Rooij and Bos 1997).

Slowly, these concepts pushed their way into imaging studies, where fluorescently labeled forms of the GTPases were observed for changes in localization (Kranenburg et al. 1997; Michaelson et al. 2001). Others utilized fluorescently tagged versions of the binding domains used in the pull down studies as an indicator of where the active forms of the GTPases were located (Kim et al. 2000; Cannon et al. 2001; Srinivasan et al. 2003). While the biochemical assays showed excellent sensitivity and selectivity, they simply averaged what was going on in large populations of cells, in contrast to the ability of imaging to identify processes in single cells. However, the imaging studies were not very sensitive or specific. Thus, FRET-based sensors which were both sensitive and specific were developed to examine GTPase activity status in live cells (Kraynov et al. 2000b; Mochizuki et al. 2001). Over the course of development of these FRET-based sensors, a handful of basic designs have come to the front in terms of usefulness, but each sensor type must be used with a full understanding of the caveats of each.

Comparison of Basic Rho GTPase Biosensor Design:

The basic sensor designs that have arisen from studies attempting to discern Rho GTPase activation by FRET are: 1) intermolecular (dual-chain) and 2) intramolecular (single-chain) designs as illustrated in Figure 1.5. Within the intramolecular class of sensors, two basic flavors exist as well, the GTPase-effector fusion and effector domain-only designs (Itoh et al. 2002; Seth et al. 2003). These sensor designs have been used for a variety of other intracellular targets as well (Miyawaki 2003; Newman et al. 2011). Due to the lack of specificity and sensitivity inherent in the effector domain-only designs, these sensors are rarely used today, given the better characteristics of the other sensor formats. Basic differences in these sensor designs unfold in the acquisition and processing of the imaging data. Intermolecular FRET sensors consist of two components which often distribute differentially within the cell at different expression levels, so bleedthrough correction must be performed to correct for contributions due to localized accumulation of one domain or the other. In contrast, bleedthrough correction has typically been ignored for single-chain sensors as both donor and acceptor fluors are present in the same place at the same time, reducing these artefacts. Such differences are largely responsible for the differences in their frequency of usage and popularity in scientific studies.

Comparison of Usage of Intramolecular and Intermolecular Rho GTPase FRET Biosensor Designs:

As mentioned above, intramolecular FRET sensors typically require less intensive image acquisition and processing techniques in order to obtain an informative FRET signal, and typically generate a fairly large FRET signal due to proximity of the

fluorophores. Further, it has been argued that intramolecular FRET sensors typically interact less with other cellular components since it is likely that once the GTPase becomes activated, it is immediately bound by the associated binding domain, preventing interaction with endogenous effectors and thus perturbing intracellular signaling to a smaller degree (at least as demonstrated for the cameleon sensors) (Miyawaki et al. 1999; Miyawaki 2003). These lines of reasoning have largely driven the use of intramolecular FRET sensors for the GTPases.

While there is some evidence that these concerns are true of the intramolecular Rho GTPase sensors (Pertz et al. 2006), these sensors could as a result behave as dominant negative constructs, sequestering upstream regulators such as GAPs, GEFs, and GDI. Indeed, recent work suggests that overexpression of Rho GTPases alters intracellular signaling by a mechanism different than expected: alterations in the expression of endogenous GTPases due to derangement of GTPase/GDI ratios in cells (Michaelson et al. 2001; Boulter et al. 2010). Interestingly, it has been shown recently that use of dual-chain and single-chain RhoA FRET sensors produced the same results in a thorough quantitative assessment of the role of RhoA activation at the leading edge of cells, suggesting that sensor design does not significantly influence the detection of GTPase activation dynamics in live cells (Machacek et al. 2009). Additionally, it is known that intermolecular FRET sensors, while requiring more extensive image processing, generate larger dynamic ranges due to lower FRET in the off state, perhaps permitting their expression at lower levels in cells (Pertz and Hahn 2004; Hodgson et al. 2008). This property could be exploited to detect smaller changes in intracellular signaling if the intermolecular sensors are used appropriately.

72

Thus, in light of the lack of comparative data on different Rho GTPase sensors and sensor designs, our aim was to generate new and improved versions of our Rho GTPase sensors utilizing dual-chain and single-chain sensor designs. Through comparison of these designs, we are able to show that sensitivity and dynamic range of these GTPase sensors can be improved through several new strategies. Additionally, we show that both dual-chain and single-chain sensors suffer from artefacts that must be considered when selecting probes for imaging, that dual-chain sensors are more sensitive than single-chain sensors and can be analyzed by different methods compared to single-chain sensors, that both dual-chain and single-chain sensors perturb cellular signaling at high expression levels, that expression levels of dual-chain sensors can be normalized through utilization of a novel expression cassette, and that new red-shifted FRET pairs can be utilized in these sensors that are orthogonal to the traditional CFP/YFP pair so commonly used. This work thus provides a quantitative comparison of Rho GTPase sensor designs and enables researchers to better select and interpret data generated by these probes, in addition to providing new sensors for use.

2.3 Results

Comparison of Sensitivity and Cellular Perturbation with Intramolecular and Intermolecular GTPase Activity FRET Sensors:

Over the past decade, a variety of FRET-based probes to monitor signaling protein activity have emerged, particularly targeting kinase and GTPase activities (Newman et al. 2011) (See Table 1.1). These probes have enabled a much greater understanding of the spatial and temporal dynamics of intracellular signaling. One of the more prevalent Rho GTPase probe designs has been the intramolecular, or single-chain, design, which contains both donor and acceptor fluorophores, in addition to the affinity reagent and often the target GTPase, on the same protein to allow for simple ratiometric analysis of activity (Figure 2.1A). A similar but less frequently used sensor type is the "dual-chain" or intermolecular FRET sensor, in which the GTPase is tagged with the donor fluorophore and expressed separately from the binding domain, which is tagged with the acceptor fluorophore (Figure 2.1B).

While the construction and validation of these different sensor types can be difficult and time-consuming, FRET signal analysis and interpretation for each type of sensor is even more critical. First, a major difference between single-chain and dual-chain sensors is the quantity of FRET present in the "off" state. For single-chain sensors, since the fluorophores are constrained together within the construct, there is always FRET at baseline, regardless of GTPase activity status. If single- and dual-chain sensors are constructed missing the binding domain/recognition motif, single-chain sensors still exhibit FRET at baseline, whereas the dual-chain sensor shows no FRET in this case (Figure 2.1C). In using this truncated single-chain construct, fluctuating patterns of RhoA are still observed, presumably reflecting stochastic FRET changes due to

74

movements of the fluorophores in space at any point in time within a voxel of cellular space, in addition to bleedthrough from the donor fluorophore. Visually, these signals can mislead one into observing changes in FRET that appear "real" due to activation of the sensor. In fact, validation of the RhoA.SC sensor in its truncated state illustrates that the probe can still respond to interaction with p50RhoGAP and RhoGDI-1 with changes in FRET, though to significantly smaller degree than the wild-type sensor (Figure S2.1A). Quantitation of linescans at the cell edge where it has been previously shown that RhoA is activated during protrusion demonstrated that the change in intensity is diminished in the RBD truncation mutant (Figure 2.1D). Thus, when examining small changes in FRET or subcellular FRET changes, single-chain sensors can be more prone to false-positive signals, resulting in the presumption of activity changes where none exist.

In the converse, dual-chain sensors may have difficulty in showing FRET where minimal activity exists due to minimal activation of the endogenous GTPase, making these sensors prone to false-negative issues. For example, in HeLa cells, which have low but biochemically detectable RhoA activity, a single-chain sensor for RhoA shows significant activity, but a dual-chain sensor fails to detect RhoA activity (Figure S2.1B). In contrast, in mouse embryonic fibroblasts, which have higher baseline levels of RhoA activity biochemically, both single- and dual-chain FRET sensors detect significant RhoA activity (Figure S2.1B).

Lastly, we note that in some cases, dual-chain sensors can be "shielded" from the affinity reagent by interactions with endogenous proteins or subcellular localizations that prevent interaction with the fluorescently labeled affinity reagent, as shown in Figure

S2.1C. Thus, choice of sensor and interpretation of the resultant FRET signal will vary based on the particular experiment being performed. The risks and benefits of using each sensor design must be considered.

However, there are methods that can be used to overcome this apparent lack of signal for dual-chain sensors. Since dual-chain sensor exhibit virtually no FRET in the "off" state, any FRET signal indicates activity, though not activity per unit molecule as the FRET ratio provides. By analyzing the raw, or total, FRET signal from these sensors, conclusions can be made about the total activity present at subcellular locations in the cell. Thus the total FRET observed will reflect a combination of local changes in FRET and diminishing amount of target protein available to FRET in the thinner parts of the cell. Analyzing total FRET by linescan analysis and comparing the total FRET signal with ratiometric FRET and the donor signal by both widefield and TIRF microscopy (Figure 2.1E) demonstrates that the total FRET signal differs from the ratiometric FRET signal (Figure 2.1G). By using total FRET, significant increases in FRET are observed at the leading, protrusive edge, in addition to significant amounts of FRET from regions associated with endomembranes, both in widefield and TIRF. By contrast, when using of a modified form of the Rac1.DC sensor C-terminus with a K-Ras4b polybasic region and CAAX motif which membrane anchors the probe, this same analysis demonstrates that the total FRET signal perfectly parallels the FRET ratio. In addition to demonstrating this total FRET is a viable method for measuring FRET signal, especially in cases where signal is too low to measure ratiometric FRET, these results also show that Rac1 is activated in regions other than the plasma membrane such as the cytosol and

endomembranes, consistent with previous reports (Del Pozo et al. 2002; del Pozo et al. 2004).

Comparison of Sensitivity and Cellular Perturbation with Intramolecular and Intermolecular GTPase Activity FRET Sensors:

One of the greatest challenges in the development of probes for signaling molecule activity is to avoid perturbing the system under study. As others have noted, this is difficult, if not impossible (Miyawaki 2003; O'Rourke et al. 2005), but a few guiding principles aid us in choosing molecules for study. For example, central nodes in cell signaling pathways that have a sizable buffering capacity are the preferred choice for study. Thus, researchers need probes that have high sensitivity so that expression levels can be kept low while still observing subtle changes within the system. Traditionally, single-chain sensors have been favored because they often give high FRET signal compared to dual-chain sensors (Figure 2.2A), but the dynamic ranges are often much smaller for single-chain sensors due to significant FRET at baseline. Thus, we attempted to determine whether we could detect leading edge activation of RhoA with decreasing amounts of single-chain or dual-chain RhoA FRET probe. Figure 2.2B demonstrates that a RhoA dual-chain sensor can be expressed at much lower levels than the single-chain sensor and still detect at minimum a twenty percent increase in leading edge activation of RhoA, suggesting much greater sensitivity for dual-chain sensors. This is further confirmed in fluorescence lifetime (FLIM) FRET analysis of these probes, which is not subject to artifacts due to cellular thickness or uneven distribution of the two fluorophores in dual-chain sensors. By use of FLIM, for a single-chain RhoA sensor the low FRET and high FRET states demonstrate FRET efficiencies of 9.4% and 35.4%

77

(2.28 ns to 2.10 ns lifetime shift), respectively, whereas for a dual-chain Rac1 sensor, the low and high FRET states demonstrate FRET efficiencies of 1% and 30.6% (2.45 ns to 2.10 ns lifetime shift), indicating a much greater dynamic range for the dual-chain sensor and thus enhanced sensitivity (Figure 2.2C) due to lower FRET in the "off" state.

Knowing that the dual-chain sensor is more sensitive to cellular signaling behaviors, we attempted to determine whether expression of dual-chain and single-chain sensors had differential impacts on downstream signaling in cells. Previous studies have implied that single-chain sensors tend to interact with downstream effectors less than dual-chains and thus are preferable. However, it has been shown that overexpression of GTPases leads to dysregulation of endogenous GTPases via saturation of the binding capacity of RhoGDI (Boulter et al. 2010). To determine the effects of both dual-chain and single-chain RhoA and Rac1 sensors on downstream signaling, we examined the levels of cofilin phosphorylation before and after serum stimulation in the presence of low or high levels of sensor expression. Cofilin phosphorylation is influenced by both Rac1 and RhoA activity (Wang et al. 2007), allowing us to compare the effects of these sensors. Figure S2.2 shows that at high levels of sensor expression, both dual-chain and single-chain RhoA sensors appear to alter downstream signaling through cofilin slightly, whereas at low levels, little change in cofilin phosphorylation is observed. Similar effects are observed for both dual-chain and single-chain Rac1 sensors. Given recent reports demonstrating that overexpression of GTPases does not just influence effector interactions, but also the pool of available GDI-1 (Boulter et al. 2010), these results are not unexpected. Typical imaging experiments use expression levels more closely corresponding to the "low expression" condition for the sensor types used. Thus, these

results demonstrate that dual-chain sensors are more sensitive to changes in cellular signaling, and in addition, do not perturb cellular signaling to any greater degree than single-chain sensors. Thus, this argues for use of dual-chain FRET sensors where possible.

Comparison of C-terminal Modifications in GTPase Activity FRET Sensors:

One additional consideration when selecting a sensor for use and interpreting the resultant FRET signal is that a number of modifications are used to target the sensors to different subcellular regions. For example, Rho GTPases are often lipid-modified to allow for their insertion into the plasma membrane to permit activation by GEFs and downstream signaling. It has been held that GTPases are membrane-bound in the active state, but cytostolic in the inactive state due to sequestration by RhoGDI. To test whether regulation of the GTPase cycle by GDI-1 affects apparent activity, we generated sensors mutated from the wild-type form by swapping the poly-basic region and CAAX box for the K-Ras4b sequence, or by truncating this region entirely (see Figure 2.3A for sequence alignment). As anticipated, truncation of the tail grossly affected both localization and activity patterns (Figure 2.3B, bottom panel) for the Rac1.DC sensor. Without a prenylation sequence, Rac1 strongly localizes to the nucleus in addition to the cytosol (Michaelson et al. 2008), and activity patterns are dramatically different. In the tail truncation mutant, activation appears to occur only near membranes, suggesting that transient diffusion of the GTPase to the membrane may bring it in proximity to GEFs for activation, but this activation does not persist past the very leading edge of the cell, in contrast to wild-type Rac1. However, there are no significant activity pattern differences seen when the C-terminus is replaced with the K-Ras4b sequence (Figure 2.3B), but

localization is altered. When K-Ras modified, virtually all Rac1 is present at the peripheral membrane, and the GTPase is lost from the perinuclear region and other internal membranes (Figure 2.3C). Interestingly, even though the activity patterns do not change for Rac1 (Figure 2.3B), Rac1 activity appears biased towards higher levels and the K-Ras modified sensor does not respond to GDI-1 as expected (Figure 2.3D), suggesting that GDI-1 plays a significant role in preventing the activation of the sensor, particularly at the leading edge. To confirm that these localization differences occur for other GTPases as well, a RhoA dual-chain sensor was C-terminally modified with the KRas-4b sequence. Localization patterns again show that K-Ras modification causes loss of the GTPase from internal membranes and localization to the plasma membrane only (Figure 2.3E). Additionally, when analyzing this RhoA dual-chain sensor for FRET by FLIM, the high FRET state had a FRET efficiency of 38.4%, consistent with our previous results showing that K-Ras modification biases the sensors toward higher activity.

Thus, we conclude that utilizing C-terminal sequences other than the wild-type sequence may alter the ability of the sensor to properly sense endogenous signaling pathways by either modulating the placement of the GTPase (Michaelson et al. 2001; Prior et al. 2001; del Pozo et al. 2004; Michaelson et al. 2008; Osmani et al. 2010), or altering how it is regulated.

Rational Development and Improvement of Intramolecular and Intermolecular GTPase Activity FRET Sensors:

Seizing upon the issues with both single-chain and dual-chain FRET sensors, we sought to develop new probes and upgrade existing probes for the GTPases. To design these probes, most effort has been expended determining the proper orientation and

positioning of the fluorophores and recognition elements through the use of linker sequences. In the process of improving and upgrading our biosensor library, we found that the linker, or hinge region, between the two fluorophores (Figure 2.1A) greatly affected the ability of sensors to respond appropriately to upstream regulators. In generating a single-chain Rac1 activity FRET sensor, we tested linker lengths increasing by 18 amino acids (1L = 18 amino acids) and found that while the Rac1 sensor could be activated to its maximum by GEFs at all linker lengths tested, GDI interactions were greatly impacted by linker length both in terms of activity (Figure 2.4A) and localization (Figure 2.4B), perhaps due to steric block within the sensor itself preventing GDI-1 access.

Next, we found that the choice of assay used for sensor validation influenced whether the sensor was determined to respond appropriately to regulators. For example, when validating the Rac1 single-chain sensor with the GEF Tiam-1, we noted that in fluorometry assays using cell suspensions previously used to validate a number of FRET-based GTPase biosensors (Pertz et al. 2006), Tiam-1 appeared to have no ability to activate the Rac1 sensor since no increase in FRET was seen (Figure 2.4C). In contrast, if FRET responses to Tiam-1 expression were tested in adherent cells, robust activation of the sensor was observed (Figure 2.4C), suggesting adherence of cells may be required to properly localize cellular signaling components for the activation of these sensors. As a consequence, construction and validation of single-chain FRET sensors can be a difficult process, requiring testing and consideration of a great number of factors.

We have also explored the development and improvement of intermolecular (dual-chain) FRET sensor designs. Typically in these probe formats, the target is tagged

with a donor fluorophore, and the affinity reagent is expressed separately, tagged with an acceptor fluorophore. In the process of testing these probes, it was determined that fluorophore orientation was critically important for these probes (Figure 2.4D). In testing a binding domain of constant length, placement of the fluorophore at one terminus versus the other yielded significant differences in FRET. Similar to the single-chain sensors, the length of linkers also influenced the resultant FRET signal. Using binding domains increasing in length by 5 amino acids, which shifts the acceptor fluorophore in space roughly 5 amino acids in length, we showed that there was an optimal placement of the acceptor fluorophore in space (Figure 2.4E). Linkers that were too short or too long resulted in suboptimal FRET. Lastly, based on recent work showing that the presence of two acceptor fluorophores in a FRET system results in greater than additive FRET transfer (Koushik et al. 2009), we tested the use of tandem acceptor constructs and their ability to increase FRET. Independent of the increase in molecular brightness, we showed that use of tandem YPet as an acceptor for CFP nearly doubles the apparent FRET signal (Figure 2.4F), enhancing the dynamic range of these dual-chain FRET probes.

Generation of Orthogonal Red-Shifted FRET Probes for Use with CFP/YFP FRET Probes:

Particularly intriguing questions in the field of GTPase signaling involve the study of cross-talk between different GTPases. Currently, no genetically encodable FRET probe pairs for the GTPases are available to simultaneously study two GTPases in the same cell at the same time. Recent studies have either used dye-labeled probes or have used computational methodologies reliant upon a common fiduciary marker to

cross-correlate different GTPase activities in cells (Tsukada et al. 2008; Machacek et al. 2009). To overcome this issue, we have generated single-chain and dual-chain FRET probes that rely upon FRET between orange and red fluorescent proteins and that are spectrally distinct from currently available CFP/YFP probes. As shown in Figure 2.5A, these probes are constructed using similar designs as the new probes we generated in Figures 2.1A and 2.1B, but using mKO and mCherry (or tandem mCherry in Figure 2.5A) as donor and acceptor, respectively. In constructing these probes, we noted that mKO possessed a different C-terminal sequence than most of the EGFP variants. In an attempt to restore roughly the same orientation as that found in the original CFP/YFP sensors, we modified the C-terminus to contain the amino acid sequence ITLGMDELYK found at the C-terminus of the GFP variants. By adding this sequence to the end of mKO, we were able to increase the resultant FRET significantly. However, as shown in Figure 2.5B, and as reported by others (Ai et al. 2008), mCherry is a fairly poor acceptor and thus the FRET signal is reduced compared to donor signal in red-shifted single-chain sensors compared to CFP/YFP probes. However, as we have shown that dual-chain sensors are more sensitive than single-chain sensors, we attempted to improve red-shifted FRET signal by generating a tandem mCherry acceptor which, as shown in Figure 2.5C, enhances the resultant FRET signal significantly, almost to levels seen for CFP/YFP variants as shown in Figure 2.5C. even after bleedthrough correction. We also tested tandem acceptors in red-shifted single-chain sensors, but this appeared to decrease expression levels and increase the susceptibility of these probes to aggregation and degradation as was also the case for CFP/tdYFP single-chain variants (data not shown). A summary of new and updated probes is provided in Figure S2.3.

Generation of a Novel Expression Cassette for Dual-Chain FRET Sensors:

Even though we have demonstrated that dual-chain sensors are very sensitive, two of the greatest hindrances to the use of dual-chain sensors have been 1) uneven expression and differential localization of the donor and acceptor components, and 2) difficulties in correctly determining FRET signal due to the need for bleedthrough correction because of point (1). While bleedthrough correction will be required for all dual-chain sensors, we can attempt to alleviate some of the difficulty in point (1) by normalizing expression of the two sensor components in a population of cells. The design of such a new Rac1 dual-chain sensor cassette is shown in Figure 2.6A. Through the use of a short viral sequence, the A2 sequence (Das and Piccirilli 2005; Trichas et al. 2008), that causes co-translational cleavage of a protein product, we have generated an auto-cleavable construct that expresses both components of the sensor at roughly equal levels from a single plasmid with no contaminating uncleaved product (Figure 2.6B). As shown in Figure 2.6C, use of the wild-type A2 sequence yields expression of two separable bands that are reactive with anti-GFP antibody by western blot. Replacement of the A2 sequence with a poly-GS linker of equivalent length, or mutation of the critical final two amino acid residues of the A2 sequence to alanine both result in a much larger band representing the uncleaved product (Figure 2.6C). That there is no uncleaved sensor product in the WT A2 linker condition is critical since any uncleaved product would contaminate the signal from the actual sensor. Further, in live cells, we can show that the autocleavable sensor normalizes the relative expression of the two components compared to manual selection of cells during imaging (Figure 2.6D). We also show that in live cells, use of the WT A2 linker results in differential distribution of the sensor

components as expected (Figure 2.6E), whereas when the final two residues of the A2 sequence are mutated to alanine as above, the two sensor components are both membrane-localized (Figure 2.6E). Quantitation of these localization differences is demonstrated in the linescans for both the GTPase and binding domain fragments in Figure 2.6F. Most importantly, Rac1 activity patterns appear identical between both the normal dual-chain and this autocleavable dual-chain, with prominent activity seen in the lamellipodium upon protrusion, indicating that this sensor behaves normally in adherent cells (Figure 2.6G). Initial experiments to incorporate this construct into *Drosophila melanogaster* indicate that this autocleavage process remains intact in living organisms, and that the subcellular distribution of the two components is properly maintained. Further, generation of stable *Drosophila* lines incorporating this construct enables the uniform expression of the two components in contrast to insertion of the donor and acceptor independently into the genome (data not shown). Thus, this novel expression cassette allows for the use of dual-chain sensors in a variety of experimental conditions by overcoming one of the major hurdles to their use: uneven expression of the donor and acceptor components of the sensor.

2.4 Discussion

Development of New and Updated Rho GTPase Biosensors:

Rho GTPases are molecular switches that serve as central integrators and regulators of a host of cellular functions downstream of extracellular receptors. Given that these GTPases very specifically control certain cellular functions in response to very specific cellular cues, it is clear that significant spatial and temporal control is exerted on these GTPases to regulate their functions. Understanding these controls has been largely inaccessible until the development of biosensors that could examine Rho GTPase activity in live cells (Kraynov et al. 2000b; Mochizuki et al. 2001; Yoshizaki et al. 2003; Nalbant et al. 2004a; Pertz et al. 2006b; Kitano et al. 2008). However, despite the value of these probes, there has been an endless drive to improve these sensors (Seth et al. 2003; Yoshizaki et al. 2003), much as has been done for other sensors (Miyawaki et al. 1997; Miyawaki et al. 1999; Truong et al. 2001; Palmer et al. 2006) to obtain improvements in brightness, in dynamic range, and in sensitivity without perturbation of cellular signaling. Additionally, as our microscopes and computational abilities improve, researchers seek to study the relationship between two GTPases simultaneously in the same cell (Schultz et al. 2005; Ai et al. 2008; Piljic and Schultz 2008; Machacek et al. 2009).

To this end, in the present study, we demonstrate the development of novel dual-chain FRET biosensors for the GTPases Cdc42, RhoG, RhoA, and Rac1, along with a new single-chain sensor for Rac1 which maintains GDI regulation. Through this development process, we illustrate some of the difficulties in building and testing biosensors, such as the choice of linker regions and proper positioning of binding domains and fluorophores, and the choice of assays performed for validation of the

sensors. Additionally, we show that by use of a tandem acceptor cassette, tdYPet, we can further enhance the dynamic ranges of dual-chain sensors, based on the reports of anomalous surplus FRET energy transfer in the presence of multiple acceptors (Koushik et al. 2009). Additionally, we report the conversion of these sensors to red-shifted varieties that can be used simultaneously with CFP/YFP FRET pairs. Drawing upon our experience in the development of a tdYPet acceptor, we find that development of a tdmCherry acceptor similarly improves the dynamic range of dual-chain red-shifted FRET sensors.

Artefacts Inherent to Biosensor Imaging:

Many arguments have been made that favor the use of single-chain sensors for protein activity in live cells, particularly that single-chain sensors perturb intracellular signaling to a lesser degree, and that they exhibit higher amounts of FRET which are easier to detect in live-cell imaging. However, little data that supports these points is available for the Rho GTPase sensor field from a comparative standpoint with dual-chain sensors (Pertz and Hahn 2004). Because we consistently saw higher dynamic ranges for dual-chain sensors during probe development, we set out to compare the value of dual-chain and single-chain sensors in live cell imaging.

Through these comparative analyses, we find that dual-chain sensors indeed have larger dynamic ranges than single-chain sensors, and exhibit higher sensitivity, permitting lower expression levels of dual-chain probes compared to single-chain probes to observe the same intracellular signals. Further, both sensors display imaging artefacts that must be understood when using them. Single-chain sensors are prone to exhibit FRET where

none exists, or false positive signals. Dual-chain sensors are prone to exhibit false negative signals, or lack of FRET where activation of GTPase does occur. Thus, a careful understanding of these risks is required during their use.

Additionally we demonstrate that both sensor designs perturb downstream signaling to the same degree, presumably from effects not only on interactions with effectors, but also due to effects on GDI-1 binding and saturation. Lastly, we show that due to the design of the dual-chain probes, we can analyze FRET in low signal situations by the study of total FRET with certain caveats.

Lastly, we examine a number of modifications used to enhance cellular signals during imaging, such as the use of different C-terminal modifications, and their effects on FRET interpretation. As expected, loss of the C-terminal tail greatly disrupts patterns of activation seen in live cells. Modification by constitutive membrane-tagging using the K-Ras4b sequence is more subtle. Grossly, FRET patterns are intact, but the probes localize very differently, with loss of cytosolic and endomembrane localization for the Rac1-KRas4b sensor and placement of the sensor at locations different than where some of its regulators exist. Additionally, we show that Rac1 activity seen in these locations with the wild-type sensor is lost by use of the K-Ras modified version. Such modifications are useful in certain circumstances, but must be used with an understanding of their caveats. For example, for a number of GTPases it has been shown that vesicular trafficking is key to their regulation, and that in the case of Rac1, activation occurs on endosomes via the GEF Tiam-1 (Palamidessi et al. 2008; Osmani et al. 2010). Indeed, use of a K-Ras modified sensor would fail to detect such activation events. However, if utilized properly, these sensors can be targeted to specific subcellular regions to enhance the

contrast of FRET detected in those regions, such as on endomembranes or at focal adhesions.

Overcoming Hurdles to the Use of Dual-Chain Sensors:

As we have shown, dual-chain sensors have higher sensitivity and dynamic range than single-chain sensors, and can be extremely valuable for detecting small changes in intracellular signaling with low expression of the probe such that intracellular signaling is not perturbed. However, the two biggest hurdles to their use, practically, are the need for bleedthrough correction, and the uneven control of expression of the two sensor components. To circumvent the issues with uneven expression of the two sensor components, an autocleavable cassette has been developed which normalizes the expression of both components from a single plasmid, yielding roughly a 1:1 expression ratio for the two components. Our hope is that this will enable broader use of these probes in cells in tissue culture, and eventually in organisms. Achieving equal and even expression of two exogenously expressed proteins in living organisms is notoriously difficult, making the use of dual-chain sensors quite difficult. However, with the ability to express a dual-chain sensor from a single plasmid gene, the use of these sensors could be eased significantly. Thus, use of a more sensitive dual-chain sensor in live organisms could permit the study of much smaller changes in intracellular signaling.

Concluding Remarks:

In closing, we have attempted to further the field of genetically encodable FRET sensors for Rho GTPases by performing a quantitative comparison of biosensor development and design with an eye to their use in the study of intracellular signaling.

Our findings indicate that, while infrequently used in the literature, dual-chain FRET probes for the Rho GTPases are of significant value. Also, as is the case for any experimental setup, a solid understanding of the advantages and disadvantages to the use of both single-chain and dual-chain FRET probes is needed when selecting a probe to use in the study of intracellular signaling pathways. Such an understanding is critical for the appropriate analysis and interpretation of FRET signals and Rho GTPase activation during cellular signaling.

2.5 Materials and Methods

Materials and Reagents:

Lipofectamine was purchased from Invitrogen (Carlsbad, CA), Fugene6 from Roche (Basel, Switzerland). All other chemicals were from Sigma. Anti-GFP antibody (Clone JL-8) was from Clontech, Inc. Anti-Cofilin, Anti-phospho-Cofilin (S3), anti-p42MAPK, and anti-phospho-p42/44MAPK antibodies were from Cell Signaling. Anti-actin antibody was from Millipore. Anti-mouse and anti-rabbit secondary antibodies were from Amersham/GE Health Sciences.

Cell culture and Constructs:

The Rac1 dual-chain FRET biosensor was reported previously (Kraynov et al. 2000b; Machacek et al. 2009). The new dual-chain Cdc42 biosensor uses an intermolecular design as reported by several groups (Itoh et al. 2002; Seth et al. 2003; Tzima et al. 2003; Hoppe and Swanson 2004), but here is further optimized by the use of different fluorescent proteins and of a Cdc42-binding domain from Neuronal Wiskott Aldrich Syndrome Protein (N-WASP), a fragment shown to provide good selectivity for activated Cdc42 in previously developed biosensors with a different design(Nalbant et al. 2004; Frantz et al. 2007; Koivusalo et al. 2010). The new RhoA dual-chain sensor is based upon a previous RhoA dual-chain sensor (Machacek et al. 2009), but is modified to extend the Rho binding domain by 10 amino acids, and the acceptor construct was modified to generate a trandem YPet construct fused to the C-terminus of the Rho binding domain. The red-shifted variants of these sensors were generated by replacing CFP or CyPet with mKO, and YFP or YPet with mCherry. The autocleavable Rac1

91

sensor was generated by cloning the previously described Rac1 sensor into a pTriEx plasmid with the cleavable sequence described in (Das and Piccirilli 2005; Trichas et al. 2008) sandwiched between the two sensor components.

Each of the dual-chain biosensors was generated by first constructing plasmids encoding either Rac1, RhoA, or Cdc42 fused to the C terminus of CyPet, a CFP variant optimized for FRET (Nguyen and Daugherty 2005), and either the CRIB domain from p21-activated kinase (PBD) published previously (Machacek et al. 2009), the Cdc42-binding CRIB domain from WASP (CBD), amino acids 230–314, or amino acids 7-99 from Rhotekin (RBD) fused to the C terminus of YPet, a YFP variant optimized for FRET (Nguyen and Daugherty 2005) for PBD and CBD, or the N-terminus of YPet for RBD. The EGFP coding region from the EGFP-C1 vector (Clontech, Inc.) was replaced with a PCR product containing the CyPet or YPet coding regions flanked by an NcoI restriction site and a SGLRSELGS linker containing a BamHI restriction site. The PCR products of the Rac1, RhoA, Cdc42, PBD, and CBD coding sequences were inserted between the BamHI restriction site in the SGLRSELGS linker and an EcoRI restriction site in the downstream multiple cloning site of the vector. The RBD-YPet construct were generated by inserting the PCR product for YPet via the EcoRI and XhoI restriction sites in the pTriEx-4 backbone. Then, the PCR product for amino acids 7-99 of RBD were then cloned in via the restriction sites NcoI and BamHI in the pTriEx-4 backbone. To generate the RBD-tandem-YPet construct, the PCR product for a second YPet was cloned between the BamHI and EcoRI sites in the pTriEx-4 backbone, flanked by a GSGS linker sequences on both sides. To generate the red-shifted forms of these sensors, the same

constructs were used, except that mKO and mCherry replace CyPet and YPet, respectively.

For the single-chain biosensor designs, the RhoA single-chain FRET biosensor is used as described previously (Pertz et al. 2006b; Machacek et al. 2009). For the Rac1 single-chain sensor, a similar GTPase-effector fusion design is used. The YPet-PBD fragment was generated by PCR from the dual-chain acceptor DNA template and inserted into the pTriEx-4 backbone via the NcoI/HindIII restriction sites in the MCS. This was followed by a 4x repeated linker based on the linker described previously for the RhoA single-chain sensor (Pertz et al. 2006) inserted between the restriction sites HindIII and NotI. Monomeric Cerulean (A206K) was generated from template by PCR, as was wild-type Rac1, and the two were fused via overlapping PCR with a GSG linker sequence between them. This fragment was subsequently cloned into the pTriEx-4 vector via the NotI and XhoI restriction sites in the MCS. To generate the red-shifted forms of these sensors, the same constructs are used, except that mKO and mCherry replace CFP and YFP, respectively. For mKO, the C-terminus differs slightly from EGFP-based fluorophores and we found that this mattered in single-chain constructs, so the C-terminus was extended to match the EGFP C-terminus by using the amino acid sequence ITLGMDELYK.

To generate the K-Ras4b variants of the sensors, the Rac1, RhoG, and RhoA fragments were amplified by PCR from amino acids 1-176 for Rac1 and RhoG, and 1-178 for RhoA with flanking BamHI or EcoRI and HindIII restriction sites, excluding the prenylation sequence and poly-basic region. Primers were ordered that corresponded to the K-Ras4b poly-basic region and prenylation sequence containing flanking restriction

sites of HindIII and EcoRI or XhoI and were annealed. This fragment was then ligated to the Rac1, RhoG, or RhoA fragments, with subsequent ligation into the sensor vector constructs (both single-chain and dual-chain) described above. The C-terminal truncation variants were generated by amplifying Rac1, RhoG, and RhoA by PCR from amino acids 1-176 for Rac1, and 1-178 for RhoA with flanking BamHI or EcoRI and EcoRI or XhoI restriction sites with subsequent ligation into the sensor vector constructs (both single-chain and dual-chain) described above.

To generate the autocleavable Rac1 dual-chain construct, YPet-PBD was amplified from template by PCR and ligated in to the pTriEx-4 vector via NcoI and NdeI restriction sites. CyPet-Rac1 was amplified from template by PCR and ligated in to the pTriEx-4 vector via NheI and XhoI restriction sites found in the MCS. Primers were generated corresponding to the 18 amino acid A2 viral sequence (Das and Piccirilli 2005; Trichas et al. 2008), annealed, and subsequently ligated in to the pTriEx-4 vector via NdeI and NheI restriction sites.

For regulators tested with each sensor, the Vav2, Tim, Ect2, and Tiam-1 GEF DH/PH domains, Rho GDI-1, and p50RhoGAP were used as described previously (Pertz et al. 2006).

Plasmids were transfected into Cos-7 cells or HeLa cells using Lipofectamine or Fugene6. Cos-7 cells and HeLa cells were maintained in DMEM (Mediatech, Manassas, VA) supplemented with 10% FBS, penicillin/streptomycin, and 2 mM glutamine (Invitrogen, Carlsbad, CA).

<u>*Generation of Stable Cell Lines:*</u>

For production of mouse embryonic fibroblasts (MEF) stably incorporating the biosensor DNA, we used the tet-OFF MEF/3T3 cells (Clontech.com). The biosensor components were cut out as cassettes from the pCyPet/pYPet or pTriEx cloning constructs at NcoI/EcoRI sites for CyPet-RhoA, and NcoI/XhoI sites for RBD-YPet. Digested fragments were treated with Klenow fragment of the DNA polymerase I in the presence of 33μM dNTP for 15 minutes at room temperature to perform the end filling reaction of the 5'-overhangs to produce blunt ends. The pBabe-sin-Puro-tet-CMV was cut at an HpaI site to produce blunt ends and ligated with the blunt-ended inserts. Bacterial colonies were screened using polymerase chain reaction (PCR) for the proper directional incorporation of the biosensor DNA. For detection of RhoA activity using the previously described RhoA single-chain sensor, MEF/3T3 cells were stably transduced using a retroviral system with the RhoA biosensor under the control of a tet-inducible promoter and FAC sorted for low expressors, as described in (Pertz et al. 2006) . Cells were kept under 1 μg/ml Doxycycline in the culture medium to repress biosensor expression. Forty eight hours before experiments Doxycycline was removed from the medium. These cells did not exhibit migration behaviors different from non-transfected MEF/3T3 cells.

<u>*Fluorometry Assays for Validation of RhoA, Rac1, and Cdc42 Biosensors:*</u>

To validate the various sensors constructed in this assay, 293 cells were transfected with low levels of each of the sensors and co-transfected with a panel of regulators to assess the ability of each sensor to respond appropriately to endogenous regulators. In brief, 293 cells were plated on poly-L-lysine coated wells of a 6-well dish

36 hours before the assay was run. The following morning, 24 hours before the assay

was run, the 293 cells were transfected with Lipofectamine according to the

manufacturer's instructions. A total of 650 ng of DNA was transfected per well,

consisting of 100 ng of sensor donor, 100 ng of sensor acceptor, or in the case of single-

chain sensors, 100 ng of sensor, and the balance consisted of various regulators or blank

vector DNA. Each experimental condition was set up in triplicate. The following

morning, the cells were checked for appropriate brightness, washed once with DPBS,

gently trypsinized using 400 μL trypsin which was removed after 15 seconds, and then

resuspended in 500 μL cold DPBS. 400 μL of cell suspension was then loaded into a

spectrophotometer cuvette. Using a SPEX Fluorolog sensitive spectrophotometer to

assess CFP/YFP FRET, the cell suspension was excited at 433 nm, the excitation of

CyPet, and the emission was monitored from 450 nm to 600 nm at 3 nm intervals to

monitor the emission spectrum of YPet. For each test, a sample transfected with YPet

only and monitored for emission with CFP excitation as above to account for differences

in brightness and thus bleedthrough by direct excitation of the acceptor fluorophore. This

reading was subtracted from each measurement. For the calculation of FRET ratio, after

bleedthrough correction, each sample was normalized such that the peak of CFP emission

(475 nm) was set as an intensity value of 1.0. The FRET emission peak (525 nm) was

then divided by the CFP peak for each sample, and the samples were averaged for each

condition. For mKO/mCherry FRET, the cell suspension was excited at 540 nm, near the

excitation of mKO, and the emission was monitored from 550 nm to 700 nm at 3 nm

intervals to monitor the emission spectrum of mCherry. For each test, a sample

transfected with mCherry only was monitored for emission upon mKO excitation as

above to account for differences in brightness and thus bleedthrough by direct excitation of the acceptor fluorophore. This reading was also subtracted from each measurement. For the red-shifted FRET ratio, each sample was normalized such that the peak of mKO emission (560 nm) was set as an intensity value of 1.0. The FRET emission peak (610 nm) was then divided by the mKO peak for each sample, and the samples were averaged for each condition. FRET ratios could then be compared between each condition. Statistical significance between conditions was assessed by two-tailed student's t-test assuming unequal variance.

Rac1, RhoG, and RhoA Adherent Cell Activity Assays:

Cos-7 cells were transfected with Rac1, RhoG, and RhoA dual-chain and single-chain sensors, separately, with the regulators also used for the fluorometry assays described above using FuGene6. The following day, the cells were transferred to fibronectin-coated glass coverslips, and conditioned in Ham's F-12K without phenol red (Invitrogen, Carlsbad, CA) with 2% FBS and 15 mM HEPES (Mediatech, Manassas, VA). The cells were then placed in a closed chamber (Warner Instruments, Hamden, CT) and immediately transferred to a heated stage for imaging. Cells were chosen for medium expression levels so that cellular morphology did not change noticeably. FRET imaging was performed as described below in "Imaging the Activity of One Rho GTPase per Cell."

Whole-Cell FRET Analysis:

To calculate whole-cell average FRET ratio, photobleach-corrected FRET ratio (FRET/CFP) time-lapse image stacks acquired and processed as described above were loaded into Metamorph, thresholded to generate masks for each cell, and regions were drawn around each cell using the mask. From these regions, a number of parameters, including average pixel intensity, could be measured and recorded. Average FRET ratio was calculated for three separate time points, averaged, and recorded for each cell.

Imaging the Activity of One Rho GTPase per Cell:

Activation levels of Rac1, RhoA, and Cdc42 assessed by dual-chain sensors were measured in living cells by monitoring the ratio of FRET (CyPet to Ypet transfer) to CyPet emission, and corrected for bleed-through from CyPet and YPet species as detailed below. Time-lapse sequences were acquired on an Olympus IX81 inverted epifluorescence microscope, using an Olympus 40x UPlan FLN1.3 N/A DIC lens, CoolsnapES^2 CCD camera (Roper Scientific) and Metamorph software (Universal Imaging). For emission ratio imaging, the following filter sets were used (Chroma): CFP: D436/20, D470/40; FRET: D436/20, HQ535/30; YFP: HQ500/20, HQ535/30. A dichroic mirror ("Quad-Custom" Lot# 511112038) was custom manufactured by Chroma Technology Corporation for compatibility with all of these filter sets. Cells were illuminated with a 100 W Hg arc lamp through an ND 1.0 neutral density filter. At each time point, three images were recorded with the following exposure times: CFP (1.2 s), FRET (excitation of donor, observation of acceptor emission) (1.2 s), YPet (0.4 s) at binning 2x2. We routinely changed the order of acquisition for all experiments, varying

between the order CyPet, FRET, YPet, or FRET, CyPet, YPet. The image sets were taken at 10s intervals. Ratio calculations to generate activity images were performed following bleed-through correction methods described previously. Briefly, Metamorph software was used for image alignment and ratiometric calculation of activation signals. All images were shading-corrected and background-subtracted. Binary masks with values equal to 1 inside the cell and 0 elsewhere were extracted by applying a threshold to the CyPet image, because it had the largest signal-to-noise ratio. Control cells expressing either CyPet alone or YPet alone were used to obtain bleed-through coefficients, α and β in the following equation:

$$FRET\ Ratio = \frac{FRET - \alpha \cdot CyPet - \beta \cdot YPet}{CyPet} \quad \text{(Eq. 1)}$$

where R is the Ratio, FRET is the total FRET intensity as measured, α is the bleed-through of CyPet into the FRET signal, β is the bleed-through of YPet into the FRET signal and CyPet and YPet are the total CyPet and YPet intensities as measured through the CyPet and YPet filter sets, respectively. The bleed-through parameter α is given by the slope of the linear relationship between FRET and CyPet intensities upon CyPet excitation of cells expressing only CyPet. Similarly, the bleed-through parameter β is given by the slope of the linear relationship between FRET and mYPet intensities of cells expressing only the mYPet. The α parameter was found to be 0.4~0.5 and the β parameter was ~0.2. Both were dependent on the particular optical configuration of the microscope used. With these parameters, the ratio of corrected FRET over CyPet was calculated and used as a measure of Rac1 and RhoG activation. In time-lapse experiments, CyPet and YPet typically bleach at different rates. Therefore, the ratio was corrected for photobleaching as described in (Nalbant et al. 2004; Hodgson et al. 2006).

For Rac1 and RhoA activites assessed by single-chain sensors, since both donor and acceptor fluorophores are present on the same molecule, no bleedthrough correction was required. At each time point for RhoA, two images were recorded with the following exposure times: CFP (1.2 s) and FRET (0.6 s) using illumination from a 100 W Hg arc lamp through an ND 1.0 neutral density filter. The FRET ratio was calculated as the ratio of FRET/CFP after image processing as described above.

For visual representations of ratio images, a linear pseudocolor lookup table was applied to all ratio images and the ratio values were normalized to the lower scale value, which was chosen to exclude the bottom 5% of the total histogram distribution, avoiding spurious low intensity pixels. In each experiment, all images were carefully inspected to verify that all portions used to create the ratio image had a sufficiently high signal/noise ratio. We targeted at least 300 gray level values (12 bit dynamic range) above background in the lowest intensity regions within the cell ($S/N > 3$). This was especially important in thin parts of the cell where fluorescence was low and where beads typically adhered. Furthermore, we routinely reversed the order of image acquisition to confirm that the effects of motion artifacts associated with sequential image acquisition were not significant. We have used this approach previously to show that the order of data acquisition did not affect the measured ratio (Nalbant et al. 2004; Pertz et al. 2006).

Confocal Imaging:

To obtain images of the distributions of wild-type Rac1 and K-Ras-4b-modified Rac1, live cell imaging was performed on an Olympus Fluoview FV1000MPE Multiphoton laser scanning confocal microscope outfitted with a zero-drift compensation

(ZDC) device for active focal plane maintenance. The cells were kept in Ham's F12K medium supplemented with 10% FBS and 15 mM HEPEs buffer (to create CO_2-independent medium at 37° C by means of a Prior on-stage incubation chamber. Automated image acquisition was performed using Olympus Fluoview software. Z-stacks were acquired for single cells at sufficient intervals to satisfy Nyquist sampling requirements.

Biochemical Measurement of Biosensor Perturbation of Downstream Signaling:

To measure cofilin phosphorylation as a readout of downstream signaling perturbation due to expression of low or high levels of dual-chain and single-chain sensors, we performed western blotting. Briefly, HeLa cells were starved for 6 hours in DMEM supplemented with glutamine (Gibco), and then one set of each treatment condition was stimulated using 20% serum in DMEM for 20 minutes at 37°C. Cells were then washed twice with Dulbecco's phosphate buffered saline (Mediatech) and then lysed in lysis buffer (50 mM Tris, pH 7.4, 10 mM $MgCl_2$, 150 mM NaCl, 1% Triton X-100, 1 mM PMSF, and 10 μg/ml each of aprotinin and leupeptin). Lysates were cleared by centrifugation at 14,000 g for 5 min. Lysates were then immunoblotted for total cofilin, S3-phospho-cofilin, p42MAPK, phospho-p42/44MAPK, biosensor expression (GFP), and actin.

2.6 Acknowledgments

2.7 Figures and Legends

Figure 2.1: Comparison of FRET Signal Measurement in Intramolecular and Intermolecular GTPase Activity FRET Sensors.

(A) Single-chain probe design: a schematic representation of the intramolecular FRET activity biosensor. GTP: guanosine triphosphate, GDP: guanosine diphosphate, CFP: cyan fluorescent protein, YFP: yellow fluorescent protein.

(B) Dual-chain probe design: a schematic representation of the intermolecular FRET activity biosensor. GTP: guanosine triphosphate, GDP: guanosine diphosphate, CFP: cyan fluorescent protein, YFP: yellow fluorescent protein.

(C and D) Representative images and quantitation of effects of binding domain truncation on the FRET/CFP emission ratio (RhoA activity) in both single-chain and dual-chain sensors. Red outline in panel at far right indicates location of cell. Heat map indicating dynamic range scaling is shown for each cell. Data are represented as means $\pm$ 95% confidence intervals at $\alpha = 0.05$.

(E) Representative images of the FRET ratio, total bleedthrough corrected FRET signal, and CyPet-Rac1 or CyPet-Rac1/K-Ras4b modified as acquired by widefield epifluorescence or total internal reflection microscopy. Red lines indicate linescans used for analysis in panel (F).

(F) Representative linescans of the normalized intensities for FRET ratio, total bleedthrough corrected FRET signal, and CyPet-Rac1 or CyPet-Rac1 (K-Ras4b modified) as acquired by widefield epifluorescence or total internal reflection microscopy.

Figure 2.1
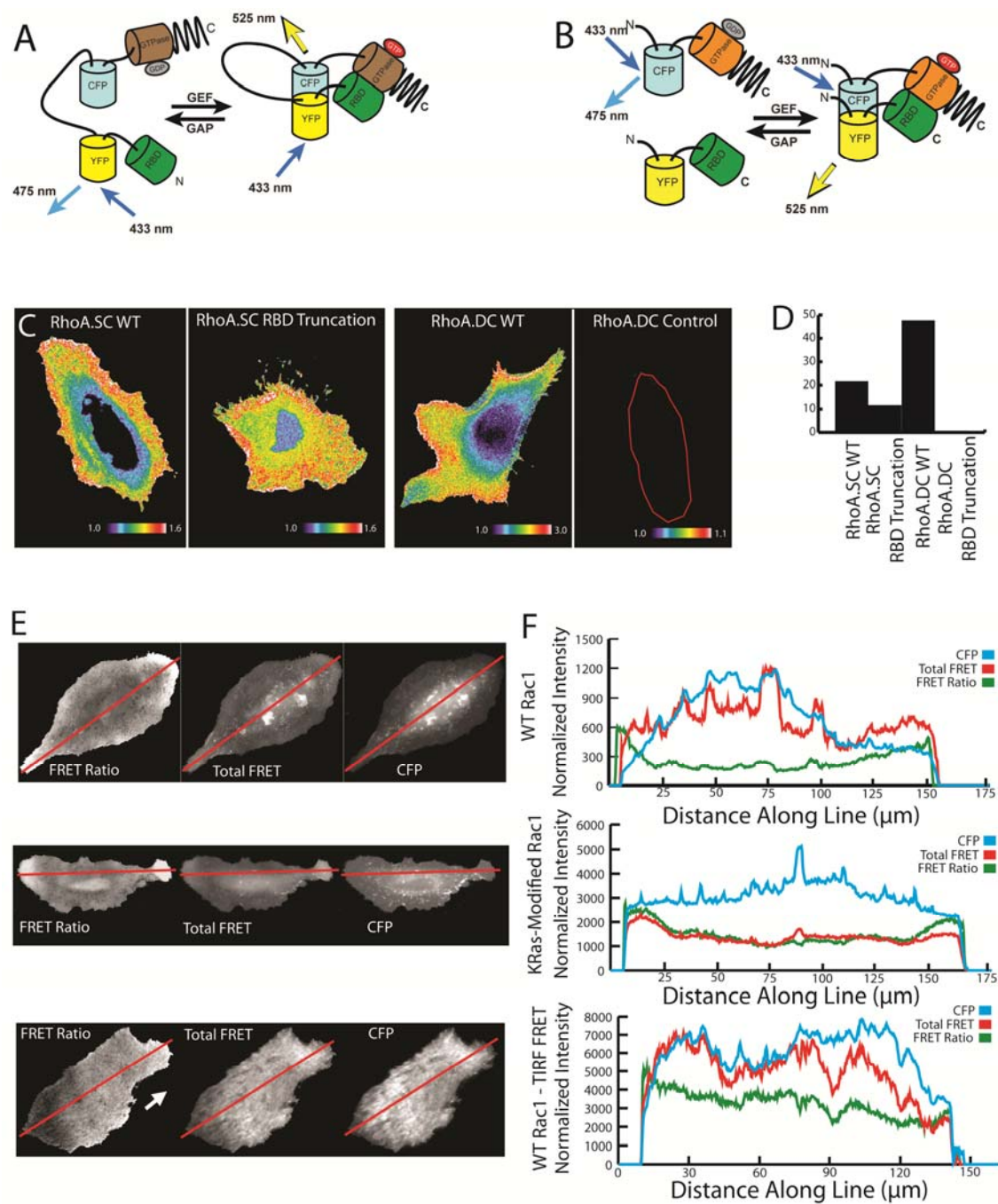
Figure 2.2: Comparison of Sensitivity of Intramolecular and Intermolecular GTPase Activity FRET Sensors.

(A) Quantitation of raw FRET emission intensity in dual-chain versus single-chain RhoA sensors as assessed in adherent mouse embryonic fibroblasts at equivalent expression levels.

(B) Quantitation of detection of a 20% increase in RhoA FRET signal at the leading edge of protrusions compared to cell center in migratory mouse embryonic fibroblasts expressing varying concentrations (as assessed by CFP Intensity) of a dual-chain or single-chain RhoA sensor. Black data points indicate presence of a 20% increase, red data points indicate absence of a 20% increase. Solid red lines indicate means of CFP intensity where there was absence of a 20% increase, with dashed red lines indicating confidence intervals at $\alpha = 0.05$.

(C) Quantitation of FRET efficiency as determined by fluorescence lifetime microscopy (FLIM) in Cos-7 cells expressing either a dual-chain Rac1 sensor or a single-chain RhoA sensor in either non-stimulated ("Free") or stimulated ("Bound") states. Data are represented as means.

Figure 2.2
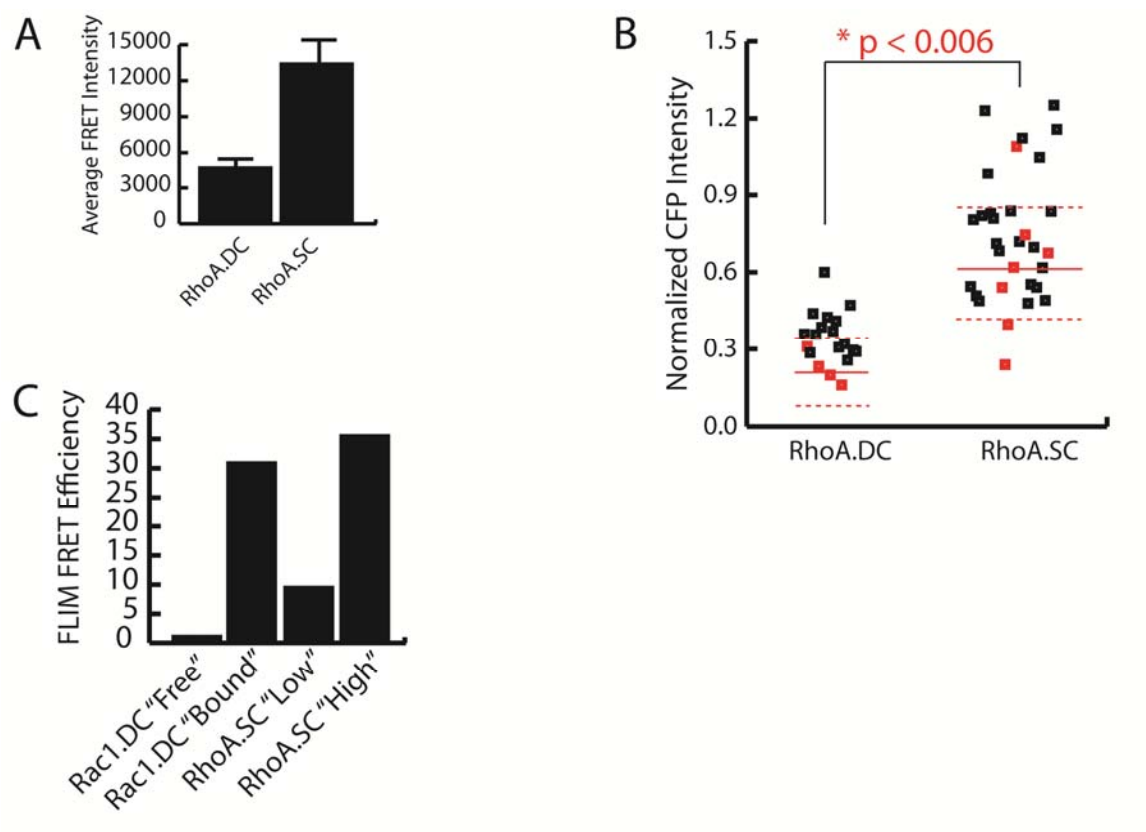
Figure 2.3: Comparison of C-terminal Modifications in GTPase Activity FRET Sensors.

(A) Alignment of C-termini of Rac1 components used to generate wild-type, no-tail, and K-Ras-modified dual chain probes. K-Ras sequence appended to Rac1 is highlighted in red.

(B) Representative images of effects of C-terminal tail modification in Rac1 dual-chain sensors on FRET/CFP emission ratio (Rac1 activity, left panel) and localization (right panel). Heat map indicating dynamic range scaling is shown for each cell.

(C) Representative images of effects of C-terminal tail modification of a Rac1 dual-chain sensor on localization to membranes (a), with quantitation of relative intensity of internal membranes and cytosol (cell center) versus the plasma membrane (b). Data are represented as means ± 95% confidence intervals at $\alpha = 0.05$.

(D) Effects of C-terminal tail modification of a Rac1 dual-chain sensor on normalized FRET/CFP emission ratios representing Rac1 activity. Biosensor responses were assessed with wild type and K-Ras modified dual-chain Rac1 biosensors in 293 cell suspension assays in the presence of the GEF Vav2, control DNA, or RhoGDI-1. Data are represented as means ± 95% confidence intervals at $\alpha = 0.05$.

(E) Representative images of effects of C-terminal tail modification of a RhoA dual-chain sensor on localization to membranes and the golgi (indicated by the red arrow in the wild-type condition).

Figure 2.3

A

WT Rac1	QRGLKTVFDEAIRAVLCPPPVKKRKRKCLLL
No-Tail Rac1	QRGLKTVFDEAIRAVL
KRas Rac1	QRGLKTVFDEAIRAVLGKKKKKKSKTKCVIM

B   Rac1 Activity (FRET)   Rac1 Localization (CFP)

Rac1.DC WT

Rac1.DC KRas

Rac1.DC No-Tail

C   (a)   Rac1.DC WT   Rac1.DC K-Ras

(b)
% Change in Intensity (Cell Center/Membrane)

D
Normalized FRET Ratio (FRET/CFP)
+GEF WT +GDI   +GEF WT +GDI
Rac1.DC WT   Rac1.DC KRas

E   RhoA WT   RhoA KRas

Figure 2.4: Rational Development and Improvement of Intramolecular and Intermolecular GTPase Activity FRET Sensors.

(A) Effects of linker length on normalized FRET/CFP emission ratios representing Rac1 activity. Biosensor responses were assessed with a wild type single-chain Rac1 biosensor in 293 cell suspension assays. Biosensor response was assessed in the presence or absence of the GEF Vav2 or RhoGDI-1. Data are represented as means ± 95% confidence intervals at $\alpha = 0.05$.

(B) Representative images of effects of linker length on Rac1 single-chain sensor localization. Left panel illustrates continued membrane localization in the presence of GDI with a 1L linker, but increasing to a 4L linker causes all Rac1 to be cytosolic in the presence of GDI (middle panel). Right panel illustrates membrane localization of sensor in the presence of the GEF Vav2.

(C) Effects of assay type on normalized FRET/CFP emission ratios representing Rac1 activity. Biosensor responses were assessed with a wild type single-chain Rac1 biosensor in 293 cell suspension assays and in adherent Cos-7 cells in the presence or absence of constitutively active Tiam-1. Data are represented as means ± 95% confidence intervals at $\alpha = 0.05$.

(D) Effects of fluorophore positioning on normalized FRET/CFP emission ratios representing RhoA activity. Biosensor responses were assessed with a wild type dual-chain RhoA biosensor in 293 cell suspension assays in the presence of a RhoA binding domain from Rhotekin tagged at either the N- or C-terminus with YPet. Data are represented as means ± 95% confidence intervals at $\alpha = 0.05$.

(E) Effects of binding domain length on normalized FRET/CFP emission ratios representing RhoA activity. Biosensor responses were assessed with a wild type dual-

chain RhoA biosensor in 293 cell suspension assays in the presence of RhoA binding domains from Rhotekin of increasing length tagged at the C-terminus with YPet. Data are represented as means $\pm$ 95% confidence intervals at $\alpha = 0.05$.

(F) Effects of increasing the number of acceptor fluorophores on normalized FRET/CFP emission ratios representing RhoA activity. Biosensor responses were assessed with a wild type dual-chain RhoA biosensor in 293 cell suspension assays in the presence of RhoA binding domains from Rhotekin tagged at the C-terminus with either one or two YPet acceptors. Data are represented as means $\pm$ 95% confidence intervals at $\alpha = 0.05$.

Figure 2.4
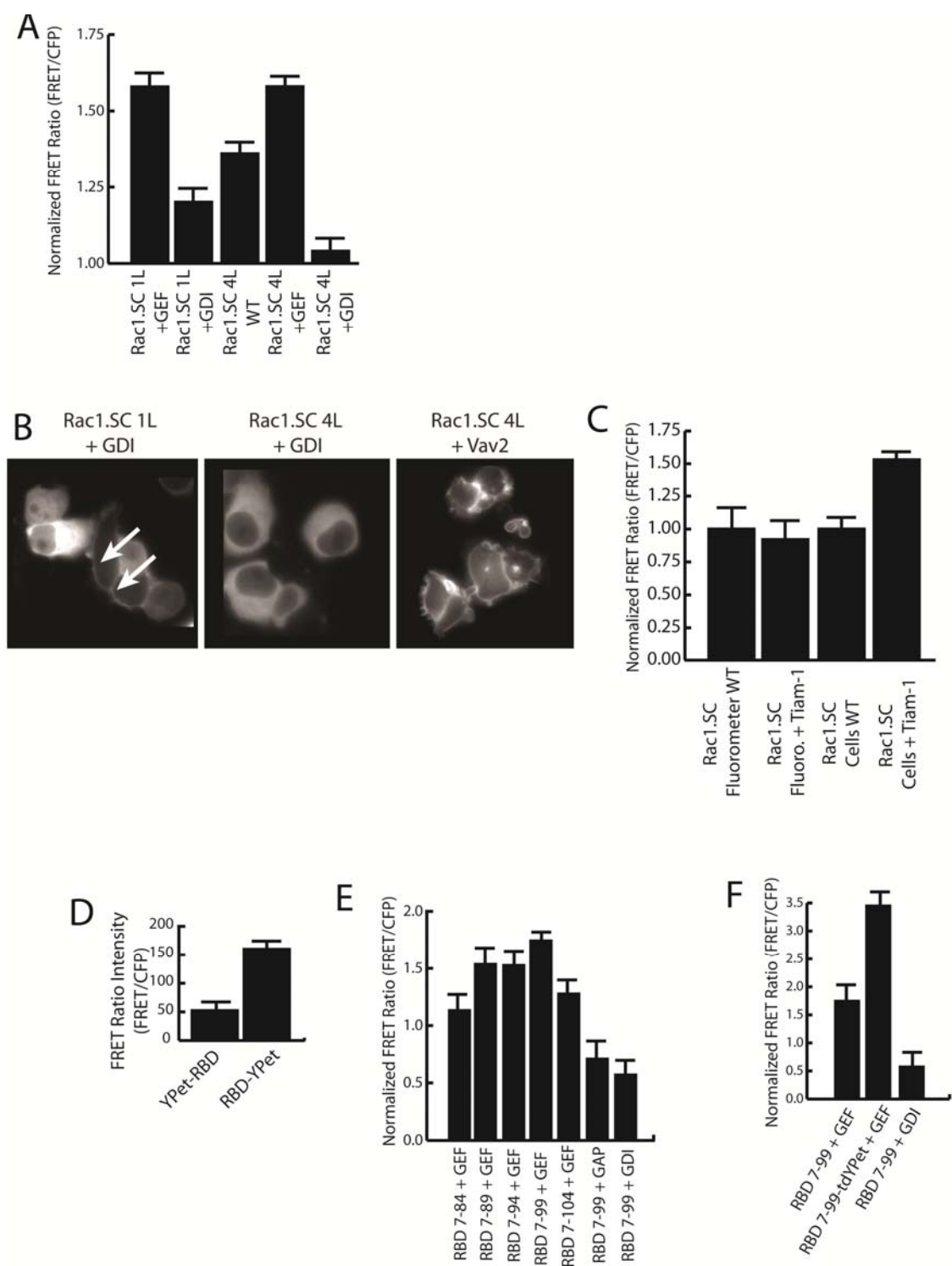
Figure 2.5: Generation of Orthogonal Red-Shifted FRET Probes for use with CFP/YFP FRET Probes.

(A) Dual-chain probe design: a schematic representation of the intermolecular FRET activity biosensor. GTP: guanosine triphosphate, GDP: guanosine diphosphate, mKO: monomeric Kusabira orange fluorescent protein, mCherry: red fluorescent protein.

(B) Emission intensity scans from 293 cell suspension assays with cells expressing a CFP/YFP RhoA single-chain sensor or a red-shifted single-chain RhoA sensor in the presence of either the catalytic DH/PH domain of the GEF Tim (active) or RhoGDI-1 (inactive). Emission intensities are normalized to the CFP or mKO peak at a value of 1.0 for comparison. FRET quantity is indicated by the second, right-most peak in each scan (~525 nm for CFP/YFP and ~ 610 nm for mKO/mCherry). Data are represented as an average of three experiments.

(C) Emission intensity scans from 293 cell suspension assays with cells expressing either a CFP/YFP dual-chain Rac1 sensor or a red-shifted tandem-mCherry acceptor dual-chain Rac1 sensor in the presence of either the catalytic DH/PH domain of the GEF Vav2 (active) or RhoGDI-1 (inactive). Emission intensities are normalized to the CFP or mKO peaks at a value of 1.0 for comparison. FRET quantity is indicated by the second, right-most peak in each scan at ~ 525 for CFP/YFP and ~610 nm for mKO/mCherry). Data are represented as an average of three separate experiments.

Figure 2.5
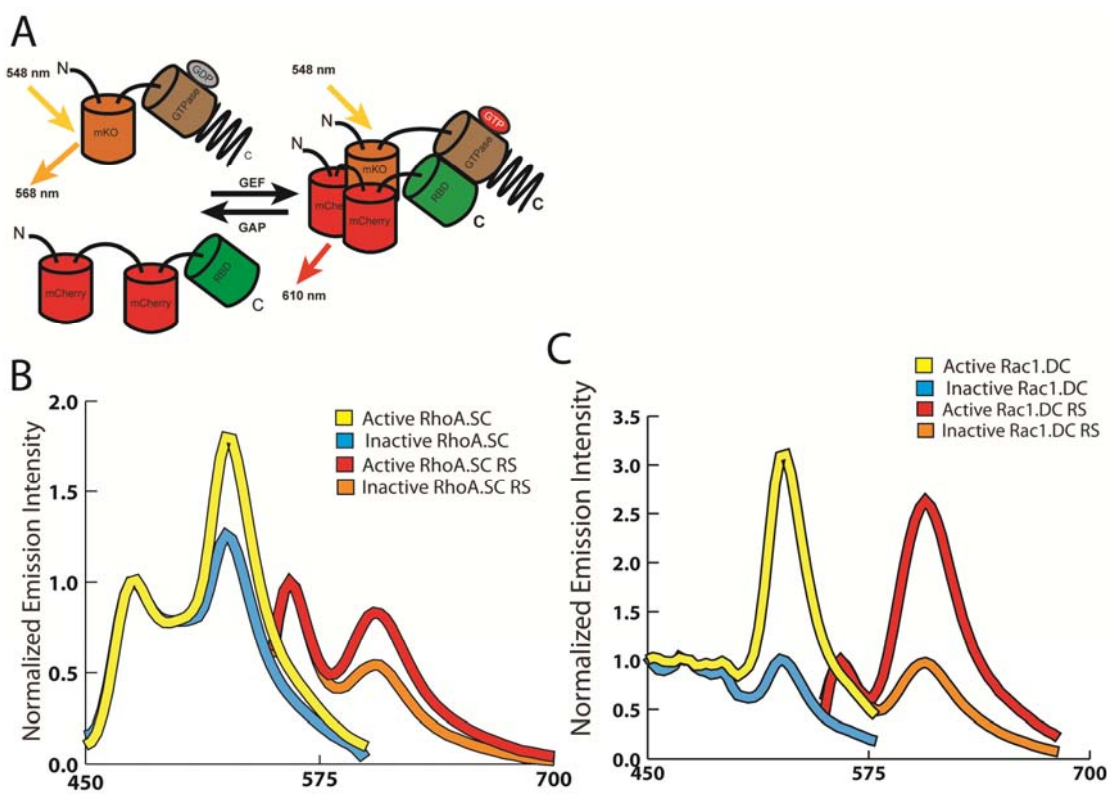
Figure 2.6: Generation of a Novel Expression Cassette for Dual-Chain FRET Sensors.

(A) Dual-chain probe design: a schematic representation of the intermolecular FRET Rac1 activity biosensor. GTP: guanosine triphosphate, GDP: guanosine diphosphate, CyPet: cyan fluorescent protein, YPet: yellow fluorescent protein.

(B) Dual-chain autocleavable probe design: a schematic representation of the intermolecular FRET Rac1 autocleavable activity biosensor. GTP: guanosine triphosphate, GDP: guanosine diphosphate, CyPet: cyan fluorescent protein, YPet: yellow fluorescent protein, A2 sequence: autocleavable motif.

(C) Representative western blot illustrating appropriate cleavage and expression of dual-chain autocleavable Rac1 activity biosensor. Wild-type or mutated versions of the A2 sequence lacking autocleavable function are shown demonstrating that lack of a functional A2 sequence leads to expression of a single higher molecular weight band corresponding to uncleaved product.

(D) Quantitation of CFP:YFP expression level ratio in adherent Cos-7 cells expressing the autocleavable Rac1 dual-chain sensor or selected manually for imaging from a population of Cos-7 cells transfected with both components of the dual-chain sensor. Solid black lines represent means, and dashed black lines indicate 95% confidence intervals at $\alpha = 0.05$.

(E) Representative pseudocolored images of differential localization of the CFP and YFP components (CyPet-Rac1, YPet-PBD) of the Rac1 dual-chain autocleavable sensor (mutant, left panel and wild-type, right panel) demonstrating differential localization.

(F) Representative linescans across the cell body demonstrating the localization of the CFP and YFP components (CyPet-Rac1, Ypet-PBD) of the Rac1 dual-chain

114

autocleavable sensor taken from the images in panel (E) with either the wild-type P2A sequence, or the AA mutant.

(G) Representative images of FRET/CFP emission ratio from wild-type and autocleavable dual-chain Rac1 activity sensors. Images are scaled so that regions of intense GTPase activity are shown in white. Heat map indicating dynamic range scaling is shown for each cell.

Figure 2.6
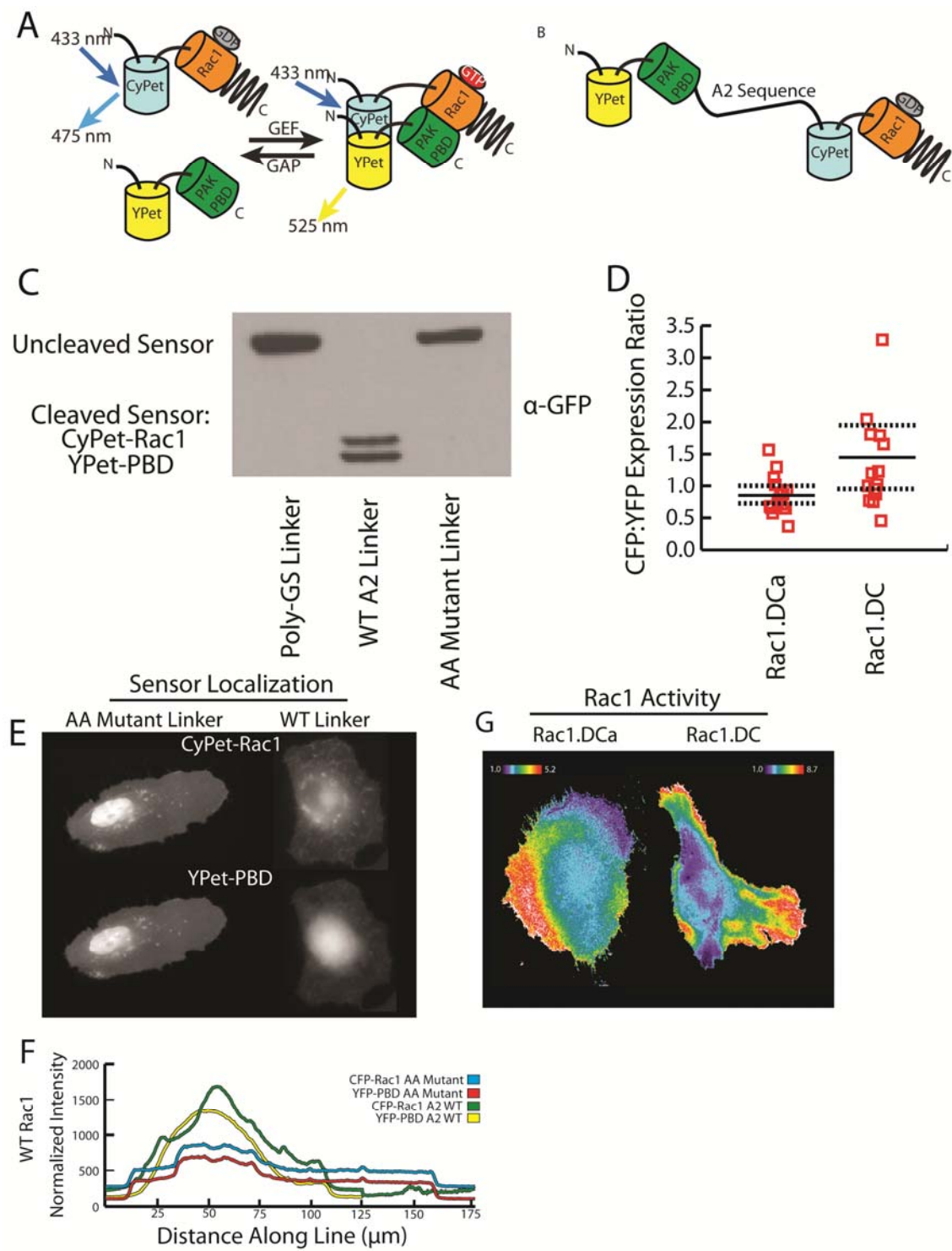
Supplemental Figure 2.1, Related to Figure 2.1: Comparison of FRET Signal and Measurement in Intramolecular and Intermolecular Rho GTPase Activity Sensors.

(A) Response of RhoA.SC RBD truncation mutant sensor to regulation by GEFs, GAPs, and GDI-1 as assessed by changes in normalized FRET/CFP emission ratios representing RhoA activity. Biosensor responses were assessed with an RBD-truncated and wild-type single-chain RhoA biosensor in 293 cell suspension assays in the presence or absence of regulators of RhoA. Data are represented as means $\pm$ 95% confidence intervals at $\alpha =$ 0.05. Asterisks indicate $p < 0.05$ compared to wild-type (RhoA.SC RBD truncation) or GEF (Wild-type RhoA.SC).

(B) Representative images of RhoA activity in mouse embryonic fibroblasts and HeLa cells acquired using RhoA.SC and RhoA.DC sensors illustrating differences in resultant FRET signal from both probes in different cell lines.

(C) Representative images of Cdc42 activity (left panel) and Cdc42 protein localization (right panel) using a constitutively active Cdc42 (Q61L) illustrating areas of non-uniform FRET activity (black arrows) in the cytoplasm.

Supplemental Figure 2.1
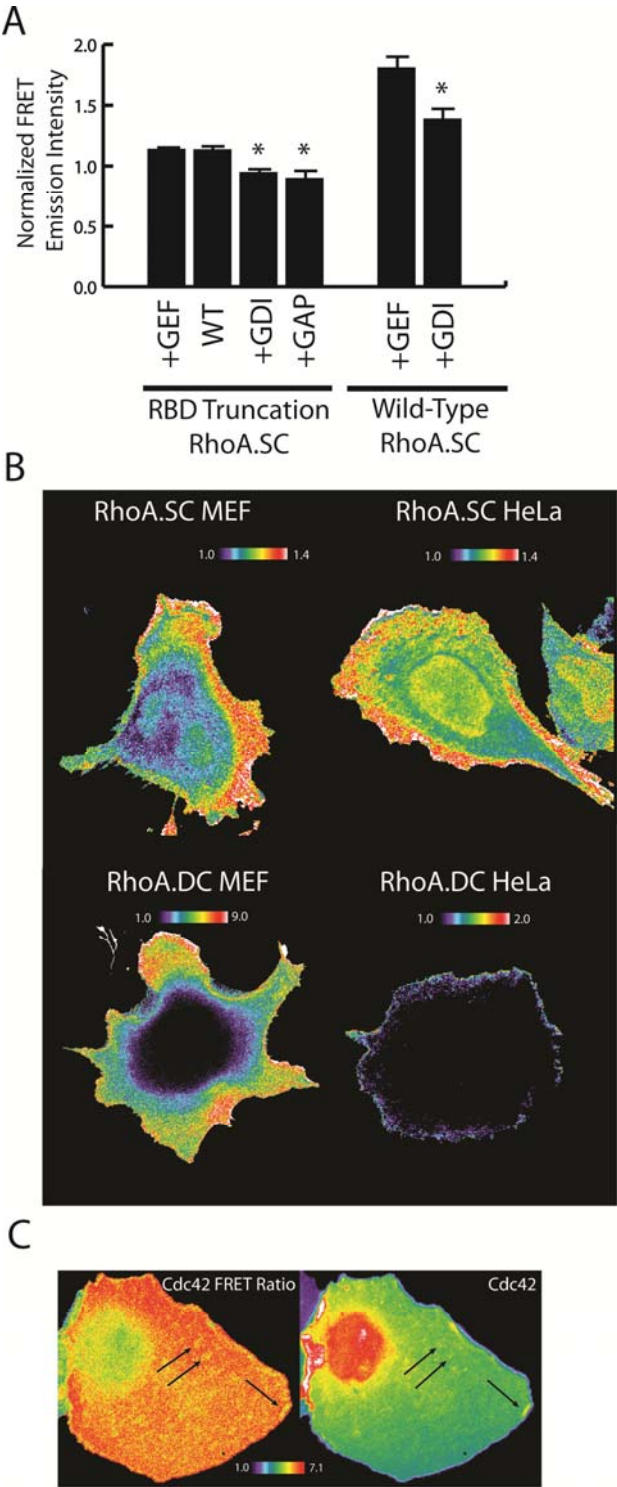
Supplemental Figure 2.2, Related to Figure 2.2: Analysis of Perturbation of Downstream Signaling by Overexpression of Intramolecular and Intermolecular Rho GTPase FRET Biosensors.

Representative western blot illustrating the effects of overexpression of Rac1 and RhoA dual-chain and single-chain sensors on cofilin phosphorylation in the presence or absence of serum stimulation after 20 minutes. Top-most cofilin and phospho-cofilin bands correspond to experiments performed with the Rac1 dual-chain and single-chain sensors. Lower cofilin and phospho-cofilin bands correspond to experiments performed with the RhoA dual-chain and single-chain sensors. Phospho-MAPK and total MAPK levels are given to show that serum stimulation was effective. Short and long exposures for GFP indicate the expression of RhoA dual-chain and single-chain sensors at low and high levels. Actin expression levels are given as a loading control.

Supplemental Figure 2.2

Phospho-Cofilin (S3)

Cofilin

Phospho-Cofilin (S3)

Cofilin

Phospho-p42/44 MAPK

p42MAPK

GFP (Short Exposure)

GFP (Long Exposure)

Actin

RhoA.DC Low
RhoA.DC Low + 20% Serum
RhoA.DC High
RhoA.DC High + 20% Serum
RhoA.SC Low
RhoA.SC Low + 20% Serum
RhoA.SC High
RhoA.SC High + 20% Serum
Mock
Mock + 20% Serum

120
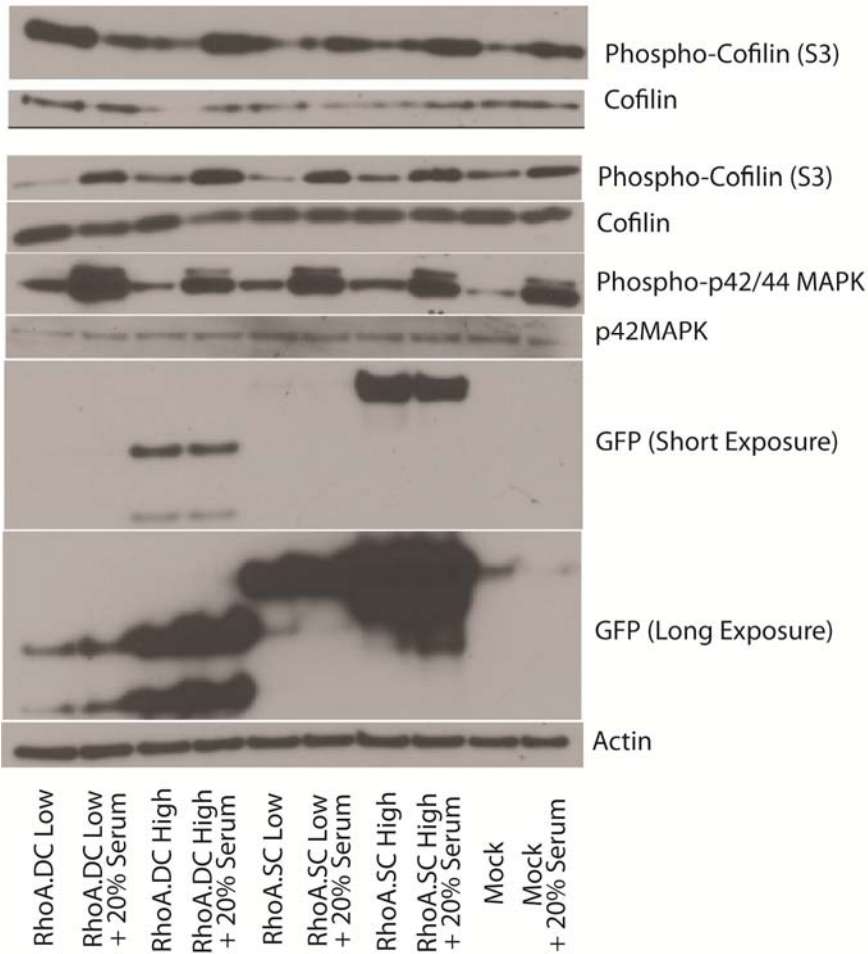
Supplemental Figure 2.3, Related to Figure 2.4: Validation of Updated or Newly Generated GTPase FRET Probes.

Validation of various dual-chain and single-chain GTPase sensors, as indicated, by assessing normalized FRET/CFP emission ratios representing activity in the presence or absence of regulatory molecules, as indicated. Biosensor responses were assessed in 293 cell suspension assays in the presence of GEFs, GAPs, and GDIs, as indicated. Data are represented as means.

Supplemental Figure 2.3
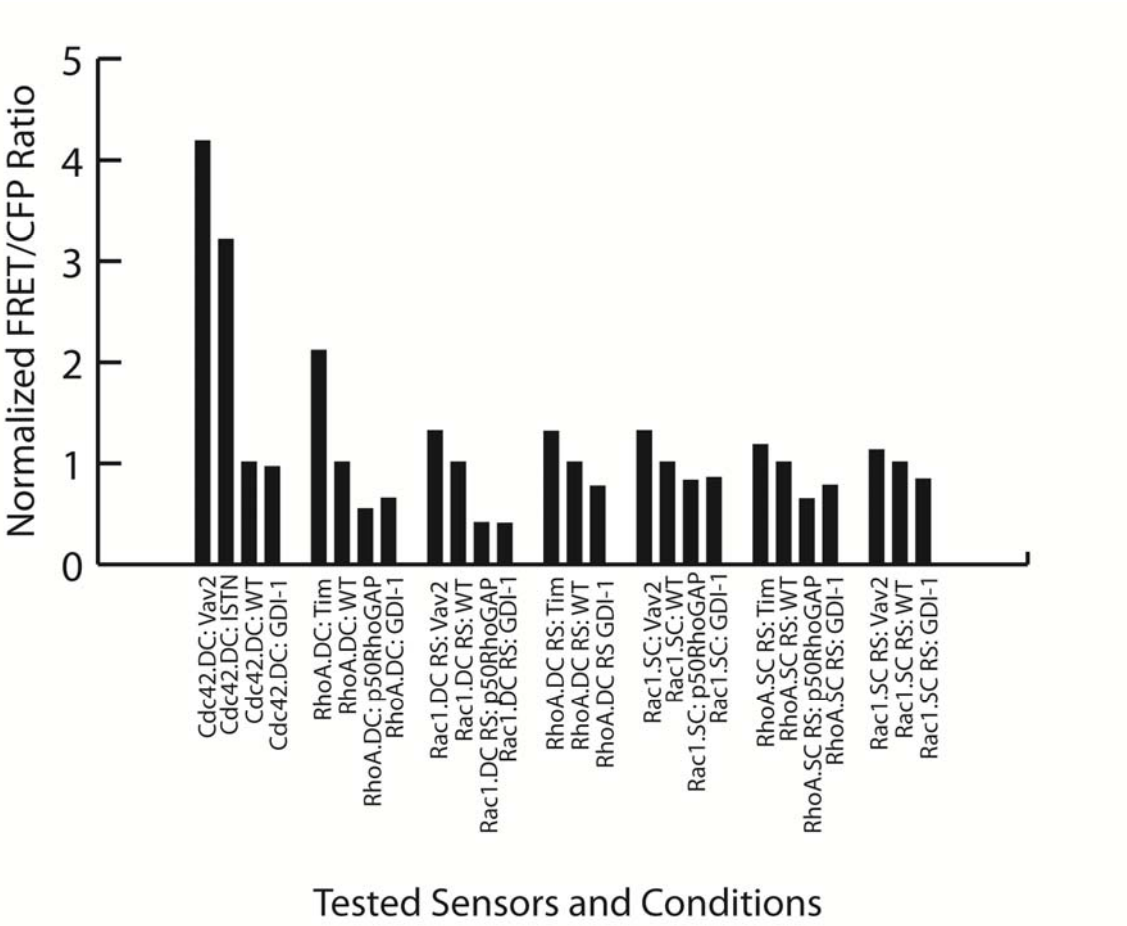
CHAPTER THREE: RHOA, RAC1, AND CDC42 GTPASE DYNAMICS AT THE CELLULAR LEADING EDGE

3.1 Abstract

Rho family GTPases work together to regulate cytoskeleton dynamics during cell migration (Ridley et al. 2003; Burridge and Wennerberg 2004; Jaffe and Hall 2005). Although much has been learned from biochemical and imaging studies regarding the morphogenic pathways they control, the rapidity and tight localization required for motility signaling has precluded a clear understanding of their interactions. Recent biosensor analyses have reported that all three proteins are activated in cell protrusions (Kraynov et al. 2000; Nalbant et al. 2004; Kurokawa and Matsuda 2005; Pertz et al. 2006). Biochemical data suggests that Cdc42 can activate Rac1 (Nobes and Hall 1995), and that Rac1 and RhoA are mutually inhibitory (Rottner et al. 1999; Arthur and Burridge 2001; Nimnual et al. 2003; Ohta et al. 2006). In addition, a variety of signaling inputs regulate these individual GTPases. These synergistic and antagonistic relations may play important roles in the regulation of cell protrusion events. Testing this hypothesis requires measurement of the activation and deactivation kinetics of the three Rho GTPases at single microns and seconds resolution, the typical dimensions of protrusion events in motile cells.

Our analyses show that RhoA is activated at the cell edge synchronous with edge advancement, whereas Cdc42 and Rac1 are activated 2μm behind the cell edge with a delay of 40 s relative to initiation of protrusion. Thus, Rac1 and RhoA operate at the

leading edge antagonistically through spatial separation and precise relative timing. RhoA plays a role in the initial events of protrusion, while Rac1 and Cdc42 signals activate pathways implicated in reinforcement and stabilization of newly expanded protrusions.

To further advance our understanding of the GTPases and their functions at the cell edge, we have studied two regulators of the GTPases, a GEF for RhoA, TEM4, and a GAP for Cdc42, MILO, and their effects on GTPase behaviors at the cell edge.

First, I and my collaborator examined focal adhesion disassembly which is required for optimal cell migration. From imaging studies a model has emerged where microtubules target focal adhesion (FAs) and undergo depolymerization to deliver a factor that promotes FA disassembly. The molecular mechanism of FA disassembly is unknown but entails the suppression of RhoA and actomyosin contractility. Here, it is shown that the Rho-specific exchange factor TEM4 restricts activation of RhoA at the leading edge and thus potentially suppress actomyosin contractility.

Second, another collaborator has identified a GTPase activating protein (GAP) for Cdc42 that binds specifically to mDia2 at the leading edge of cells and is involved in the induction of filopodia. Here, it is demonstrated that a tip complex that contains active Cdc42 exists during the initiation, but not retraction, of filopodia. Further, the GAP regulates Cdc42 activity at a whole-cell level and in these tip complexes during the formation of filopodia, The mechanism by which this GAP controls Cdc42 activity and thus filopodia formation is via its phosphorylation by a kinase, specifically Src kinase. This regulatory mechanism inactivates the GAP to permit increased Cdc42 activation and filopodia formation.

3.2 Introduction

During cell migration, cells respond to environmental cues with a variety of morphological changes, including leading edge, or lamellipodial, extension, and retraction of the rear of the cell. To coordinate these behaviors in time and space, many signaling pathways are engaged, principal among them the Rho GTPases, which regulate the actin cytoskeleton, vesicular trafficking, and cellular polarity, among other functions (Burridge and Wennerberg 2004; Jaffe and Hall 2005; Ridley 2006). Biochemical assays, loss-of-function assays, and gain-of-function assays have all contributed to our understanding of the functions of these Rho GTPases, particularly the major family members RhoA, Rac1, and Cdc42. Each of these GTPases interacts with unique downstream effectors to alter cellular behaviors (Jaffe and Hall 2005), but how they are coordinated in both space and time to yield productive cellular movement has remained difficult to assess, except at a gross biochemical level. This difficulty arises in part because these GTPases must become active to initiate downstream signaling, and perhaps only 5% of any GTPase is active at any time within the cell. Further, the subcellular location of the GTPase alone does not reflect the location of the activity (Kraynov et al. 2000; Pertz et al. 2006). Since it is known that the location of the active form of these GTPases is critical for the resultant cellular behavior, it is important to correlate GTPase activation levels with cellular behaviors.

However, high-resolution measurements of multiple signaling activities simultaneously have been impaired by the spectral constraints of currently available biosensors, limiting imaging to one sensor per experiment. Through collaboration with the Danuser laboratory at Harvard, we developed two new approaches that allowed us to

resolve the coordination of the three Rho GTPases, RhoA, Rac1, and Cdc42, with submicron and seconds resolution. First, our collaborators developed a "computational multiplexing" technique, where the activities of individual Rho GTPases, determined in separate experiments, are related locally to cell morphological activities as a common reference. Using this methodology, we were able to show that despite the complexity and heterogeneity of protrusion behavior from cell to cell, the relationships between the GTPases were remarkably consistent and could be inferred indirectly by correlation analysis of multiple separate imaging experiments.

Our analyses show that RhoA is activated at the cell edge synchronous with edge advancement, whereas Cdc42 and Rac1 are activated 2μm behind the cell edge with a delay of 40 s relative to initiation of protrusion. Thus, Rac1 and RhoA operate at the leading edge antagonistically through spatial separation and precise relative timing. RhoA plays a role in the initial events of protrusion, while Rac1 and Cdc42 signals activate pathways implicated in reinforcement and stabilization of newly expanded protrusions.

N.B.: For the journal article describing this part of the work, there were three co-first-authors, including myself. Thus, the data represented herein are a collaboration of our efforts which are not easily dissected. Dr. Louis Hodgson and I generated the imaging data, while all the computational work was performed on that data by Dr. Matthias Machacek. Where possible, I have used my own examples and data, but many of the graphics are compilations of data from our joint efforts. I have attempted to indicate specifically my contributions to this work rather than claim ownership of all data and data analysis in the following sections. Additionally, I generated an

intermolecular Cdc42 sensor for this paper, though the data I generated was not incorporated for technical reasons. As a consequence, none of the Cdc42 data herein is my work.

We also focus on a little known but widely expressed protein called TEM4. TEM4 (tumor endothelial marker 4) was identified as a gene whose expression was upregulated in endothelial cells during tumor-induced angiogenesis (St Croix et al. 2000) and is a member of the Dbl family of Rho guanine nucleotide exchange factors (RhoGEFs) (Rossman et al. 2005). Our collaborators have shown that TEM4 associates with microtubules and promotes microtubule-dependent FA disassembly by engaging the RhoC/mDia1 signaling pathway. TEM4 also regulates protrusion dynamics of the leading edge and directionality of cellular migration upstream of RhoC/mDia1. Here, we focus on a particular aspect of TEM4 regulation of RhoA activity. Curiously, even though TEM4 has catalytic activity toward all three Rho isoforms *in vitro*, knockdown of TEM4 expression results in an elevation of RhoA activity. To determine the nature of this RhoA activation, we visualized RhoA activity in live cells with or without TEM4, demonstrating that upon TEM4 knockdown, RhoA becomes active all along the cell periphery, rather than solely in protrusions, suggesting that TEM4, through its regulation of RhoC, suppresses RhoA activation at non-protruding regions of the cellular edge and contributes to microtubule mediated focal adhesion disassembly. Thus, we expand the role for RhoA at the leading edge by examining one of its regulators, TEM4.

Lastly, we examine the role of Cdc42 in the formation of another type of leading edge protrusional structure: filopodia. As has been stated above, actin-based structures are responsible for the majority of cytoskeletal changes observed in cells, including the

formation of filopodia, which contain tightly bundled parallel actin filaments (Davenport et al. 1993). These structures perform many functions, including a sensing function in neurons (Lendvai et al. 2000; Sabatini and Svoboda 2000), but their formation is not well understood. The bundled nature of the filopodia has given rise to a number of hypotheses about how these structures might form, and which proteins might be involved, such as the VASP family, formins, and N-WASP/Arp2/3, each of which is controversial (Svitkina et al. 2003; Lebrand et al. 2004; Steffen et al. 2006; Korobova and Svitkina 2008). From these data, two models have been proposed: the convergent elongation and de novo nucleation models, but no good methods exist to resolve these models. Recent work by Kirschner et al. (Lee et al. 2010b) used a reconstituted lipid bilayer system to propose a new model, the clustering-outgrowth model, wherein molecules are locally recruited to initiate linear outgrowth of filopodia from those sites. Here, in a cellular system, we attempt to discern how Cdc42 regulates filpodia formation, and whether its functions are consistent with any of these three models. Our results demonstrate that Cdc42 is activated locally at the sites of filopodia formation and is maintained in an active form during the course of filopodia elongation. The activity of Cdc42 is regulated by a novel GAP whose activity is modulated by Src activity at these filopodia.

3.3 Results and Discussion

Computational Multiplexing of Rho GTPase Activities at the Leading Edge:

Our computational multiplexing approach makes the critical assumption that the relationship between GTPase activation and the movements of the cell edge during constitutive protrusion and retraction cycles is preserved within a cell, and among cells. Thus, the initiation of protrusion and retraction can be used as a timing reference to indirectly determine the activation dynamics of multiple Rho GTPases: First, for each GTPase, the timing of activation relative to protrusion/retraction events is determined in separate experiments. Then, the activation timings of different GTPases are aligned, using protrusion/retraction events as a common reference. GTPase activities were imaged in Mouse Embryo Fibroblasts (MEF) using biosensors for Rac1, Cdc42, or RhoA (Figures 3.1A-C). The Rac1 biosensor was improved over the previously published version, using a fluorescent protein rather than a covalently attached dye. Images were captured at 10 s intervals, sufficient to sample the protrusion-retraction cycles below Nyquist frequency.

As reported previously, all GTPases, including RhoA, were maximally activated proximal to the leading edge. Visual inspection of time lapse sequences indicated substantial fluctuations in GTPase activity as the cell edges protruded and retracted. To quantify the magnitude and location of the fluctuations we extracted time courses of GTPase activity at multiple distances from the cell edge and quantified the extent of signal modulation (Figure 3.1D). For all three GTPases the modulation was highest at the cell edge, decreased monotonically within $\sim 2 - 4$ μm, and then reached a plateau of baseline activity (Figures 3.1E-G). Rac1 displayed the least significant decay, mainly

because of cell-to-cell variations in the extent of the region with high activation. RhoA, on the other hand, decayed tightly over 2 μm. Thus, GTPase activities are regulated most prominently within a few micrometers from the leading edge, supporting our hypothesis that these fluctuations are linked to cell edge movements.

To investigate how GTPase activation relates to edge movement spatially and temporally, we tracked the position of the cell edge and compared edge velocities with the biosensor signal in forty to eighty sampling windows moving with the leading edge (Figure 3.1H). The window width was set to 1.8 - 3 μm, the distance over which edge movements were correlated along the cell boundary, and 0.9 μm in depth, the distance over which signaling molecules bound to the plasma membrane would be expected to diffuse between consecutive movie frames. Edge velocities were sampled every 400 nm, so that 5 - 7 velocity measurements would fall within a window (Figure 3.1I). Thus each window yielded time courses of both edge velocity and GTPase activation level (Figure 3.1J), with independent measurements in each adjacent window. Changes in edge velocity appeared to parallel changes in GTPase activity (shown for the example of a Cdc42 data set), but with a time lag.

We were concerned that the observed Cdc42, Rho and Rac1 activation dynamics might be attributed to the different biosensor designs used for each protein. Since the measurements of Rho, Rac1 and Cdc42 activity were carried out using biosensors of different designs (Figure 3.2A-D). It was conceivable that these design differences contributed to the differences in Rho, Rac and Cdc42 activation kinetics that we observed. Most importantly, the portion of the biosensor that bound to the activated GTPase in each biosensor was in one case attached to the GTPase (RhoA biosensor) and

130

in the other two cases underwent intermolecular interaction with the GTPase (Rac1 and Cdc42 biosensors) (Figure 3.2: CBD for Cdc42, RBD for RhoA, and PBD for Rac1). It was conceivable that endogenous GTPase ligands could compete more effectively for the affinity reagent binding site on the GTPase in the case of the intermolecular sensors, or that response to activation would be faster in the case of the intramolecular RhoA biosensor. Two types of controls were carried out to address these concerns. First, for the intermolecular Cdc42 and Rac1 biosensors, we titrated the intracellular concentrations of the affinity reagent and the fluorescently labeled target to examine how this affected the activation-protrusion correlations that we were measuring. The cell's average intensity/exposure time at fixed illumination intensity was used as a measure of intracellular concentration, a reasonable approximation given the linearity of CCD camera response. For the Rac1 biosensor, both the affinity reagent and the fluorescently tagged Rac were titrated. For Cdc42, only the affinity reagent was titrated, as this biosensor responds to endogenous Cdc42. For the Rac1 biosensor, no systematic effects on the activation-protrusion correlation were observed when either the affinity reagent or the fluorescently labeled Rac1 were varied (Figure 3.3A-D). The affinity reagent:Rac1 ratio was varied over a > 3-fold range, encompassing a > 4 fold variation in affinity reagent concentration and > 3-fold variation in Rac1 concentration. For the Cdc42 biosensor, variation over a > 14-fold range also produced no systematic effect on the correlation. Most importantly, when this data, spanning a broad range of biosensor and target concentrations, was used to recalculate protrusion-activation correlations, results were in excellent agreement with those found using the optimal biosensor concentrations as shown in Figure 3.5.

131

Second, a new intermolecular biosensor of RhoA activation was produced for comparison with the intramolecular biosensor. The existing single chain RhoA biosensor was modified by eliminating the chain connecting the affinity reagent to RhoA, producing a new intermolecular biosensor (Figure 3.2D). Use of this biosensor produced the same correlation between protrusion and RhoA activation (Figures 3.4B-D) as did the single chain biosensor (Figure 3.5). With this new biosensor in hand, all three GTPases had now been measured using intermolecular biosensors. The new intermolecular biosensor showed superior dynamic range (Figure 3.4A), likely because FRET was completely eliminated when the biosensor was in the 'off' state. These data clearly demonstrated that differences in biosensor design did not affect the relative timing of activation determined in our studies, and statistically defined the extent of potential variation produced by design changes.

To investigate how GTPase activation relates to edge movement spatially and temporally, we tracked the position of the cell edge (Machacek and Danuser 2006), comparing local protrusion and retraction velocities with the biosensor signal in the vicinity. Forty to sixty sampling windows were set to track leading edge velocity and the corresponding Rho GTPase activation within each window. The windows were set at 2-3 μm in width, the maximum distances over which edge movements were correlated along the cell boundary, and 0.9 μm in depth, the maximum distance over which signaling molecules bound to the plasma membrane would be expected to diffuse between consecutive movie frames (Marguet et al. 2006). Edge velocities were sampled along the cell edge at an interval of 400 nm so that 5 to 7 velocity measurements would fall within each window. Thus each window yielded a time series of both edge velocity and GTPase

activity level, with measurements in each window independent of those measured in adjacent windows. Visual inspection of GTPase activation and edge velocity time series indicated potential similarity between local signaling and edge dynamics. Salient features of the edge velocity time series resembled similar features in the Cdc42 activity series, but with a time lag. This suggested that Cdc42 activation was delayed relative to the dynamics of edge movement.

To study the potential relationships between edge morphological dynamics and GTPase activation dynamics more systematically the data from the individual sampling windows along the entire cell boundary was assembled, and pasted these into activity maps (Machacek and Danuser 2006). This data analysis revealed tight control and correlation of morphological dynamics and GTPase activation. Protrusion and retraction occurred in a quasi-cyclic fashion with a periodicity of ~100 s. Transitions between active and quiescent portions of the cell edge occurred over distances as short as the width of one sampling window (2 – 3 μm) and were accompanied by an equally sharp gradient in GTPase activity. Thus, this data supports the notion of an immediate coupling of GTPase activation and cell morphological dynamics, in both time and space.

To quantify the relationship between GTPase activation and morphological dynamics we computed Pearson's correlation coefficient between edge velocity and the GTPase activity for every sampling window. We examined how the correlation coefficient depended on the time lag between the edge velocity and GTPase activity. This allowed us to assess firstly the degree of correlation between GTPase fluctuations and constitutive edge movements. High correlation coefficients would indicate a tight coupling of GTPase activation and cell protrusion/retraction events, whereas low

correlation coefficients would suggest a more remote relationship between the two processes. Secondly, if the maximum correlation coefficient was obtained with a time shift between dynamics and GTPase activation, we could identify the relative timing of the two processes. For actively protruding regions, we observed significant correlation coefficient maxima for all three GTPases. For either Cdc42 or Rac1, the correlation maxima occurred with a negative time-shift, i.e. the maximal activation of these two GTPases was delayed relative to the forward movement of the cell edge. In contrast, for RhoA the correlation maxima had no apparent time lag. RhoA activation was synchronous with protrusion. These results showed that GTPase activation occurs at a fixed time interval relative to the dynamics of the proximal leading edge segment. By analyzing the relationships between the biosensor signal and protrusion activities at a local scale it is possible to accumulate statistical evidence for the precise coupling of the two activities, even for random edge movements along the cell boundary. To obtain a robust estimate of the relationship between GTPase activation and protrusion and retraction events, we averaged the correlation coefficient functions over all sampling windows.

We speculated that the GTPases at the leading edge might not only be organized by a tight temporal coordination but also spatially, within the narrow band of highly modulated signaling activity. A visual inspection of the biosensor images did not allow us to infer in what way the GTPases are spatially modulated. Therefore, we repeated the correlation analysis between morphodynamic activity at the cell edge and activation of Rac1, Cdc42, and RhoA in sampling windows of 0.9 μm depth at distances $D = 0, 0.6, 1.3, 2.5, 4.4$ and 6.3 μm from the cell edge. Maxima of the correlation coefficients and

the corresponding time lags Δt were determined for each distance D. The data was fitted with a smoothing spline and 95%-confidence bands were estimated by bootstrap sampling of the residual distributions for at least n = 4 cells (Efron and Tibshirani 1994), dashed lines on both sides of the splines). For RhoA the correlation coefficient was highest at the leading edge and monotonically decreased at larger distances from the edge. At $D > 2$ μm the correlation coefficient was smaller than 0.2, which is the 95% confidence level for correlation coefficients. Thus, beyond 2 μm RhoA activity is no longer related to protrusion and retraction events. In contrast, Rac1 and Cdc42 activities were correlated with edge movements over a wider region (4.5 μm and 3.2 μm, respectively). Interestingly, the highest correlation coefficients were found at a distance $D = 1.8 \pm 0.7$ μm for Rac1 and at $D = 1.3 \pm 0.7$ μm for Cdc42. The spatial location and time lags of the maxima, and the shapes of the correlation functions suggested that both Rac1 and Cdc42 are activated at $D = 1.8$ μm and that the signals then propagate at equal rates in anterior and posterior directions. Together this data directly confirmed that only the GTPase activity within a narrow band at the leading edge is functionally related to edge protrusion. Whereas RhoA is activated at the leading edge, Rac1 and Cdc42 are activated in a region 1-2 μm behind the edge.

We estimated the variability of the cross-correlation time-lag between different cells (Figure 3.5A). The time-lags were consistently negative for all three-GTPases, i.e. the peak in their activation was delayed relative to the protrusion of the cell edge (time lag to protrusion for Rac1: -41 [-61 -13]; Cdc42: -46 [-51 -39]; RhoA -6 [-8 -4] s; mean, ± 95% confidence interval, as determined by bootstrapping 2000 samples from the

135

residual distribution of the spline fit). Together these results show that Rac1, Cdc42 and RhoA each have a different timing of activation, which is well conserved between cells.

Additional work by a previous postdoctoral fellow in the lab confirmed the validity of this computational system by using two biosensors, with orthogonal wavelengths, to visualize the activities of two GTPases in the same cell. The simultaneous measurements of Cdc42 and RhoA confirmed the computational analyses of the timing relationships between these signaling molecules performed in separate experiments (Figure 3.5B).

Together, these data indicate the following dynamics of Rho family GTPase activation during one random protrusion–retraction cycle (Figure 3.5C): RhoA activation increases and decreases in synchrony with protrusion and retraction. RhoA activation that is correlated with leading edge dynamics is confined to a narrow band 2 μm from the leading edge. In contrast, Cdc42 and Rac1 are activated with a 40 s delay relative to protrusion, and their activation is initiated 1.8 μm from the leading edge. Rac1 and Cdc42 are temporally as well as spatially less closely coupled to protrusion. Rac1 and Cdc42 maintain significant levels of activity during the retraction phase, such that low level Rac1 activation overlaps the onset of the next protrusion cycle. Rac1 and Cdc42 signals propagate both in anterograde and retrograde directions via as yet unidentified mechanisms.

The delayed activation of Rac1 and Cdc42 suggests that their primary role may not be in initiating protrusion, as is currently supposed. While the early, low activation of Rac1 we observe may still be sufficient for this role, the peak activities for Rac1 and Cdc42 are localized closer to the sites of maturing adhesions (located ~1.8 μm behind the

protruding leading edge (Zaidel-Bar et al. 2003). Rac1 and Cdc42 appear to be affecting the actin network at least in part through adhesion dynamics, potentially reinforcing the extended lamellipodial network at sites required to balance the increasing protrusive forces at the leading edge. Indeed, Rac1 and Cdc42 have been associated with newly formed focal adhesion sites (Del Pozo et al. 2002; Nayal et al. 2006; ten Klooster et al. 2006) after initial protrusion. In addition, our data supports the notion that Rac1 operates as an antagonist to RhoA (Ohta et al. 2006). RhoA activity is rapidly suppressed after protrusion, as Rac1 reaches its maximum activation. Since our measurements have shown that RhoA was activated during protrusion, and that activity was declining during retraction, RhoA activation at the leading edge may not be linked to contraction, the most commonly proposed role for RhoA in migration. Rather, the synchronized activation of RhoA with protrusion likely relates to a function of RhoA as an initiator of actin polymerization at the onset of the protrusion-retraction cycle, possibly via its ability to activate members of the formin family such as mDia (Narumiya et al. 1997; Yamana et al. 2006). In addition, the RhoA − mDia pathway is known to stabilize microtubules specifically in leading edge adhesions (Palazzo et al. 2001). This may contribute to the delayed activation of Rac1 we measured in adhesion sites; for example, via the localized initiation of a positive feedback between microtubule growth and Rac1 activation (Rodriguez et al. 2003) and/or via the engagement of integrins that regulate the coupling of Rac1 to its effector Pak1 (Del Pozo et al. 2000), which are also known to operate in a mutually positive feedback (Nayal et al. 2006).

These results present a broadly applicable approach to in situ analysis of cellular pathways. "Computational multiplexing" makes use of the spontaneous activation of

pathways by random local changes in signaling molecules due to low level stochastic stimulation of receptors, variations in concentration, and other factors. Thus it is potentially less perturbing than methods that rely on acute cell stimulation to initiate a signaling cascade. Further, while the activity levels of pathway components and hence the pathway outputs may vary between cellular locations and between cells, the hierarchy and timing between pathway components are conserved. The robustness of this computational technique permits pathways to be reconstructed despite significant cell-to-cell heterogeneity. The statistical approaches described here will be useful to integrate the heterogeneous and complex responses made visible by simultaneous imaging of cellular signaling via different biosensor combinations into a consistent pathway model.

The ultimate goal here is to harness the constitutive random fluctuations of cell morphological and signaling activities to establish spatial and temporal relationships between signals. Such constitutive fluctuations are induced via random activation of cell surface receptors by relatively low concentrations of growth factors and chemokines in the medium. The fluctuations are propagated through mechanochemical pathways to induce constitutive morphodynamic responses. In contrast, many studies of GTPase signaling in migration have relied on acute stimulation with growth factors such as EGF. There are two major limitations to an acute stimulation approach, even though it might yield more robust signal: first, acute stimulation may drive the pathways outside the normal range of operation and thus potentially distort the fine balance between the three Rho GTPases characteristic of homeostasis and cell signaling in more physiological settings. For example, PDGF stimulation of MEFs is known to enhance Rac1 and suppress RhoA activity. However, under normal serum conditions RhoA has been shown

to be a key factor in modulating protrusion/retraction events (Arthur et al. 2000; Del Pozo et al. 2002; Pertz et al. 2006). Second, acute stimulation generates a single broad activation signal. Its propagation through signaling intermediates to produce cell morphodynamic behaviors could be followed using correlation analyses similar to those presented in this paper. However, studying constitutive fluctuations is preferable because these contain multiple cycles of activation and deactivation. Despite the lower dynamic range of constitutive fluctuation signals, capturing multiple cycles results in a more accurate definition of timing.

Role of RhoA Regulation by TEM4 at the Leading Edge:

TEM4 depletion elevated levels of active RhoA in cells with intact microtubules (Figures 3.6A and 3.6B). To further investigate the nature of this increase, we employed FRET analysis to visualize spatial activation of RhoA in migrating HUVECs (Figure 3.6C). As reported previously for other cell types, RhoA activity was high in protrusive areas of the leading edge, and low in the areas of local retraction (Figure 3.6D) (Pertz et al. 2006). However, active RhoA in cells depleted of TEM4 revealed a different spatial profile. While activation of RhoA remained high during protrusion, active RhoA was found along the entire leading edge, including the retracting areas, in a ribbon-like pattern (Figure 3.6E). These data suggest that TEM4 extinguishes active RhoA in retracting areas of the leading edge thus promoting the discontinuous pattern of RhoA activation seen in the lamellipodium of control cells. The inability of TEM4-depleted cells to down-regulate RhoA activity and the RhoA-induced contractility along the leading edge likely explains the dampened protrusion dynamics in these cells observed by our collaborators.

139

Expanding our understanding of RhoA at the leading edge, we focused on a GEF for RhoA, TEM4, that appears to be involved in the microtubule-dependent trafficking of vesicles to the leading edge and can activate RhoA. Despite the fact that TEM4 has catalytic activity towards all three Rho isoforms in vitro, our collaborator's data suggest that it engages RhoC specifically to promote FA disassembly and to regulate cell migration. However, the link between TEM4 and RhoA is most puzzling. Whereas the finding that TEM4 does not mediate microtubule polymerization-dependent activation of RhoA was not surprising as it is a well-described function of another Rho GEF GEF-H1 (Chang et al. 2008), the finding that depletion of TEM4 leads to an increase in RhoA-GTP levels in cells with intact microtubules was completely unexpected. Furthermore, analysis of RhoA activation by FRET demonstrates that depletion of TEM4 does not cause a localized hyperactivation of RhoA at discrete protrusive areas as seen in control cells but rather a continuous activation of RhoA across the entire leading edge. These data suggest that TEM signaling is antagonistic to RhoA activity. This observation is of significance as antagonistic roles for RhoA and RhoC in cancer cell migration and invasion have been described (Simpson et al. 2004; Bellovin et al. 2006). How does TEM4 suppress activation of RhoA? The most likely mechanism involves Src kinase and a phosphorylation-mediated activation of a RhoGAP. This mechanism is used by integrin $\beta 1$ to restrict RhoA activity at the leading edge during cell spreading (Arthur et al. 2000; Arthur and Burridge 2001). The RhoC effector mDia1 has been shown to recruit active Src to FAs (Yamana et al. 2006) and Src can phosphorylate and activate p190RhoGAP (Moran et al. 1991; Settleman et al. 1992; Dumenil et al. 2000), thus decreasing RhoA activity. We would like to note that the lack of protrusive activity seen

140

upon TEM4 depletion may be due to the lack of activation of mDia and actin polymerization, but a competing hypothesis is that it could also be due to the local hyperactivation of RhoA and inability to decrease contractility in the protrusive region.

Role of Cdc42 Regulation by the GAP MILO at the Leading Edge:

Lastly, we sought to better understand the role of Cdc42 at the leading edge given its unique ability to both enable lamellipodial protrusion, and filopodium formation. The discovery of a GTPase activating protein for Cdc42 that binds mDia2 by our collaborator prompted us to investigate whether Cdc42 is present and active within filopodia. Although several studies have implicated Cdc42 as essential for the initial formation of filopodia (Nobes and Hall 1995; Rohatgi et al. 1999; Anton et al. 2003; Peng et al. 2003; Ho et al. 2004; Lee et al. 2010b), the localization and activity of Cdc42 in the filopodia ments   PAGEREF   _Toc299910291   \h challenge of signal detection in fine cellular structures. Previously, activation of Cdc42 in filopodia was not observed using the MeroCBD probe (Nalbant et al. 2004). We could not rule out the possibility that active endogenous Cdc42 in the filopodia was below the threshold of detection or inaccessible to the probe. To address this question we used a newly-designed Cdc42 biosensor. This probe is genetically-encoded and utilizes intermolecular FRET between ECFP and YPet fused to Cdc42 and the GTPase-binding domain of N-WASP, respectively (Figure 3.7A). The resulting FRET-based biosensor exhibits up to an 8-fold difference between the "on" and "off" states compared with a 2.8 fold maximum for the MeroCBD. Although the critical activation of mDia2 by an active GTPase through relief of autoinhibition is widely accepted (Wallar et al. 2006), the exact role of the GTPase in

maintaining the mDia2 active state is unknown. For filopodia, Cdc42 could detach from mDia2 after relief of inhibition at the base, leading to subsequent formation of an mDia2 complex with profilin and IRSp53. Alternatively, Cdc42 could remain bound to mDia2 where it would be transported into the newly formed filopodium.

To distinguish between these possibilities, we imaged live cells treated with TNF-α to induce filopodia formation (Gadea et al. 2004). HeLa cells were transfected with the Cdc42 intermolecular FRET sensor and subsequently plated on fibronectin-coated glass coverslips. The cells were then starved in serum-free DMEM for 6 hrs and transferred to the microscope for imaging. Cells were typically imaged for 5 minutes prior to stimulation with TNFα at 10 ng/mL with subsequent imaging for 15 minutes post-stimulation. Filopodium induction was rapid and immediate after TNFα treatment (~ 30 s). Consistent with previous reports, we observed activation of Cdc42 at the leading edge of migrating cells (Machacek et al. 2009), with an increase in signal at the base of filopodia (Fig 3.7B) (Nalbant et al. 2004). In addition, however, we were also able to detect active Cdc42 within the filopodia shaft (Figure 3.7B).

If active Cdc42 is associated with activated mDia2, then we should expect to see an increase in Cdc42 activity at the filopodia tips where mDia2 is enriched (Mellor 2009). To determine this, we performed 2 μm wide linescans along the long axis of filopodia on the FRET ratio image and determined the location of local FRET maxima along the line. We consistently observed a higher signal within 3 pixels of the distal tip of each filopodium compared to controls where local maxima were more randomly distributed along the length of the filopodium (Figure 3.7C). For controls, we performed a ratio of the acceptor divided by the donor images for the same filopodia above, which

accounts for non-meaningful increases in the probe signal at the tip which could be due to differential filopodium thicknesses, bleedthrough artefacts, possible edge artefacts, and non-specific binding to membranes at the filopodia tips which can be club-like in appearance when mDia2 is active. By performing the same linescan analysis on this YFP/CFP ratio as described above for the FRET ratio image, we found that the local maxima were fairly evenly distributed along the length of the filopodium in these images (Figure 3.7D).

If Cdc42 must remain bound to mDia2 for it to remain active, it follows that Cdc42 detachment from mDia2 would inactivate the complex. Since mDia2 controls filopodia growth, the activation of Cdc42 should be comparatively higher in extending filopodia and lower when filopodia are retracting or collapsing. To test this we analyzed filopodia where we could observe the entire extension/retraction cycle of the filopodia. To accomplish this, cells expressing the Cdc42 sensor were imaged at 10 s intervals and treated with TNFα to induce filopodium formation. After image processing to yield the FRET ratio, filopodial extension/retraction cycles were simple to discern based on either elongation or shortening of the filopodium. Filopodia in each state were isolated using the region drawing tool in Metamorph in the accompanying DIC image, and the regions were transferred to the ratio image to quantify filopodial activity within that region. Consistent with our model, Cdc42 showed an average of 25.3% higher FRET signal when filopodia were in the extension phase versus retraction phase (n = 18 filopodia in each state) (Figures 3.7E and 3.7F).

In regions of the cell where the formation of a single filopodium was discernable, the activation of Cdc42 was spatially restricted on the plasma membrane to an area that

marked the formation of the filopodium shaft (Figure 3.7G). To determine this, at membrane regions where single filopodia formed, FRET ratio intensity in a region incorporating the base of the filopodium was measured and compared, pair-wise, with FRET ratio intensity in a nearby region of plasma membrane of similar size (n = 67 filopodia). This observation is consistent with a model where initiation of a filopodium occurs at a discrete focus containing toca-1 and activated N-WASP prior to mDia2 recruitment and de novo polymerization (Ho et al. 2004).

<u>*Role of MILO in Regulating Cdc42 Activation Status:*</u>

Since MILO is a GTPase-activating protein for Cdc42, we next sought to investigate the role of MILO on activation of Cdc42 in live cells using the biosensor combined with an RNAi-based loss of function approach. HeLa cells were treated with control or MILO siRNA, and then transfected with the Cdc42 biosensor and imaged as described above. Consistent with our collaborator's observation that loss of MILO results in an increase in whole-cell activation of Cdc42 in whole-cell extracts, we see a 15% increase in Cdc42 activation in MILO siRNA-treated cells (Figures 3.8A and 3.8B). Because MILO can localize to filopodia by binding to active mDia2, we next sought to determine the effect of MILO depletion on Cdc42 activation at the leading edge in migrating cells where filopodia emerge. To determine this, at membrane regions where single filopodia formed in control cells, FRET ratio intensity in a region incorporating the base of the filopodium was measured and compared to similar regions in MILO siRNA-treated cells (n = 30 control filopodia, n = 82 MILO KD filopodia). The average level of Cdc42 signal at the base of filopodia increased by 18.6% in MILO-depleted cells (Figure

3.8C). Since we detect active Cdc42 within the filopodia shaft we compared wild-type levels to levels in cells treated with MILO siRNA. Filopodia in each state were isolated using the region drawing tool in Metamorph in the accompanying DIC image, and the regions were transferred to the FRET ratio image to quantify filopodial activity within that region. We see an increase of Cdc42 activation of 22.3% in MILO-deficient cells (Figures 3.8E and 3.8F).

As discussed in the introduction, there are three models for filopodial assembly: convergent elongation (Svitkina et al. 2003), de novo nucleation (Faix et al. 2009), and clustering-outgrowth (Lee et al. 2010b). Each model proposes a role for Arp2/3 polyermization of actin filaments, and for bundling proteins, in addition to a tip complex in the case of the latter two models. Our results fit well with the model proposed by (Lee et al. 2010b) , as we demonstrate that Cdc42 is activated early in the process of filopodium formation, and is maintained in an active form at the tip in a tip complex where the recruitment of actin polymerizers (Arp2/3, formins, VASP) and bundling proteins (fascin) occurs to allow for further elongation of the filopodium shaft. Additionally, we demonstrate that a novel mDia-associated GAP, MILO, regulates the the activity of Cdc42 at these filopodium initiation sites. This GAP is regulated by its phosphorylation by Src, leading to its inactivation, an increase in Cdc42 activity, and subsequent formation of filopodia in response to TNFα treatment.

3.4 Materials and Methods

Expression Constructs and Reagents:

A full length TEM4/ARHGEF17 (Genbank accession NM_014786) clone was obtained by subcloning the first exon (PCR amplified from human genomic DNA) encoding the first 456 aa into the KIAA1337 clone (Kazusa DNA Research Institute, Japan) using the internal SalI restriction site. cDNAs encoding full length TEM4/ARHGEF17 were subsequently cloned into pEGFP (Clontech) and pcDNA3-HA vectors. Point mutations (R1215A, N1252A) in the DH domain of TEM4 were introduced by site-directed mutagenesis. Constructs containing wild-type MILO, in addition to the Y→A and Y→E mutant MILO constructs, were fluorescently tagged at the N-terminus with mCherry to allow for monitoring of MILO expression in single cells in parallel to the biosensor imaging. To generate these constructs, genomic clone KIAA1688 was amplified by PCR and ligated into the original source vector. The full-length cDNA encoding MILO was subsequently amplified by PCR and then ligated into a pTriEx-4 vector via the HindIII restriction site within the multiple cloning site. Proper orientation was verified first by PCR screening with subsequent sequencing. The mCherry fluorescent protein was amplified by PCR from template and ligated into these vectors via the BamHI site upstream of HindIII within the multiple cloning site. Again, proper orientation was verified first by PCR screening with subsequent sequencing. The Vav2 DH/PH domain plus C-terminal regulatory domain (amino acids 184-878) was a gift from Keith Burridge, as was full-length RhoGDI-1.

Human recombinant TNFα was obtained from R&D Systems. All growth factors were used at a final concentration of 20 ng/ml unless otherwise indicated.

Human umbilical vein endothelial cells (HUVECs; Clonetics) were maintained in EGM-2 medium supplemented with 10% fetal bovine serum (FBS; HyClone) on gelatin-coated dishes. HUVECs were electroporated with expression constructs or siRNAs using Amaxa Nucleofection technology according to manufacturer's instructions. All experiments were carried out in cells between passages 4 and 5.

HeLa cells and 293T cells were obtained from the Lineberger Comprehensive Cancer Center tissue culture facility (UNC Chapel Hill), and tet-off mouse embryonic fibroblasts (MEFs) were acquired from Clontech, Inc. (Takara Biosciences), and were cultured in DMEM (high glucose, with glutamine, Mediatech) supplemented with 10% fetal bovine serum (HyClone) and antibiotics (Mediatech).

DNA plasmids were transfected into HeLa cells using Fugene6 according to the manufacturer's instructions. For transfection of siRNAs into HeLa cells Oligofectamine reagent (Invitrogen) was used according to the manufacturer's instructions. Briefly, HeLa cells were seeded on coverslips at 175,000-250,000 cells per 35mm dish. The next day, the cells were transfected with siRNA as follows: 11 μl Opti-MEM was combined with 4 μl Oligofectamine. In another tube, 175 μl Optimem was combined with 10 μL of siRNA stock to yield a final concentration of 20 nM. After 5 minutes, the two samples were combined and allowed to complex for 30 minutes, whereupon the solution was added dropwise to the cells, growing in 1 mL Opti-MEM. The cells were incubated with the siRNA for 5 hours at 37 °C, and then supplemented with 1 mL of Opti-MEM with 20% FBS. Cells were used for experiments between 48 and 72 hours post-transfection.

Lentivirus Production and Cellular Transduction:

293T cells (ATCC) were maintained in high glucose Dulbecco's modified Eagle's medium (DMEM) supplemented with 10% FBS and antibiotics. For virus production, 293T cells (plated at 5 x 10^6 cells per T75 flask) were transfected using a standard calcium phosphate DNA precipitation method with a target vector and the ViraPower lentiviral packaging system (Invitrogen). Supernatant containing the virus was collected 48 h post transfection and the titer was determined by infecting fresh 293T cells. HUVECs were transduced for 4-5 h in EGM-2 medium in the absence of serum. The transduction efficiency was close to 100% as determined by observing GFP or mCherry fluorescence marker expression. HUVECs were split 24 h after transduction and used for experiments 24-48 h later.

TEM4 RNA Interference:

Short hairpin (shRNA) oligos were cloned into pLL 5.0 GFP (Cai et al. 2007) or pLL 5.0 mCherry vector. Target sequences were as following: TEM4 #3 5'-GCACCACTCTGAAGCGAA-3', TEM4 #5 5'-GGAAATGACATGAGGAAA-3', The control shRNA (NS; GATCGACTTACGACGTTAT) has no exact match in the human, mouse or rat genomes (Cai et al. 2007). TEM4 shRNA #5 consistently showed a higher degree of knockdown of TEM4 protein expression (about 50%) but caused cell death (same was observed for shRNA #4 and 6). TEM4 shRNA #3 decreased TEM4 expression by about 30% and did not cause cell death and therefore was used predominantly in this study.

Our analyses of the relationships between Rho GTPase activation and protrusion/retraction relied on three previously published and extensively evaluated biosensors, for Rac1, Cdc42, and RhoA. The designs of these sensors are summarized in Figure 3.2A-D. To facilitate the experimental procedures, the original FLAIR biosensor reporting Rac1 activity, which requires microinjection of cells, was modified as follows: The EGFP was replaced by CyPet and the Alexa-546 on the p21-binding domain of p21-Activated Kinase 1 (PBD) was replaced by YPet. Hence, biosensor constructs could be retrovirally co-transduced into MEF/3T3. A stable cell line was produced following selection with puromycin (10 μg/ml). We were concerned that restricting experiments to a fixed, optimized donor/acceptor ratio could result in a particular localization pattern of Rac1 activation and/or a particular timing behavior with respect to the protrusion cycle. Therefore, unlike the single-chain RhoA biosensor discussed below, we did not FAC sort the cell population for specific expression profiles of acceptor and donor components, but maximized the concentration variability of the two components. We then performed control experiments, described above, to examine how the reported Rac1 activation depended on the concentration and ratio of donor and acceptor constructs. For detection of Cdc42 activity, cells were microinjected with the meroCBD biosensor. Before imaging, cells were allowed to recover for 30 minutes. As with the Rac1 sensor, we were concerned that variable amounts of microinjected meroCBD could affect the observed spatiotemporal relationships between Cdc42 activation and protrusion/retraction. To test the potential influence of biosensor concentration we examined the Cdc42 activities at meroCBD concentrations deliberately varied 15-fold. For detection of RhoA activity,

MEF/3T3 cells were stably transduced using a retroviral system with the RhoA FRET

biosensor under the control of a tet-inducible promoter and FAC sorted for

lowexpressors, as described in(Pertz et al. 2006). Cells were kept under 1 µg/ml

Doxycycline in the culture medium to repress biosensor expression. Forty-eight hours

before experiments doxycycline was removed from the medium. These cells did not

exhibit migration behaviors different from non-transfected MEF/3T3 cells.

Production of the Intermolecular FRET RhoA and Cdc42 Biosensors:

For controls a new intermolecular FRET RhoA biosensor was produced. mCyPet

(Nguyen and Daugherty 2005) was subcloned upstream of full length RhoA, followed by

a SGLRSELGS linker which contained a restriction site for BamHI. Full length RhoA

was subcloned at the BamHI site within this linker sequence and the EcoRI site within

the multiple cloning site (MCS) of pEGFP-C1 (Clontech, Inc.) using primer pairs 5'-

GGATCCTCTATGGCTGCCATCCGGAAGAAAC-3' and 5'-

GCGAATTCAGTTTCACAAGACAAGGCACCCAG-3'. The upstream restriction site

for mCyPet was NcoI within the pEGFP MCS. For the binding domain portion and hence

the FRET acceptor, the Rho binding domain (RBD; amino acids 7 to 89) from Rhotekin

was used (Nalbant et al. 2004; Pertz et al. 2006). The binding domains were subcloned

into the pTriEx backbone at the NcoI / BamHI sites within the MCS using the primer

pairs 5'-GGATCCTGTCTTCTCCAGCACCTG-3'. mYPet (Nguyen and Daugherty

2005) was subcloned following the binding domain at BamHI and XhoI sites within the

pTriEX MCS using the primer pair 5'-

ATATGGATCCGGAATGGTGAGCAAGGGCGAAGAGC-3' and 5'-

TTCTCGAGTCATTACTTGTACAGCTCGTCCATGC-3'.

For production of mouse embryonic fibroblasts (MEF) stably incorporating the

biosensor DNA, we used the tet-OFF MEF/3T3 cells (Clontech). The biosensor

components were cut out as cassettes from the pEGFP or pTriEx cloning constructs at

NcoI/EcoRI sites for mCyPet-RhoA, and NcoI/XhoI sites for RBD-mYPet. Digested

fragments were treated with Klenow fragment of the DNA polymerase I in the presence

of 33μM dNTP for 15 minutes at room temperature to perform the end filling reaction of

the 5'-overhangs to produce blunt ends. The pBabe-sin-Puro-tet-CMV was cut at an HpaI

site to produce blunt ends and ligated with the blunt-ended inserts. Bacterial colonies

were screened using polymerase chain reaction (PCR) for the proper directional

incorporation of the biosensor DNA. Retroviral transduction was used to stably

incorporate the biosensor DNA in MEF/3T3 under a tetracycline-repressible promoter

and expression was inhibited via doxycycline at 1 μg/ml until induction for imaging

experiments.

The new dual-chain Cdc42 biosensor uses an intermolecular design as reported by

several groups (Itoh et al. 2002; Seth et al. 2003; Tzima et al. 2003; Hoppe and Swanson

2004), but here is further optimized by the use of different fluorescent proteins and of a

Cdc42-binding domain from Neuronal Wiskott Aldrich Syndrome Protein (N-WASP), a

fragment shown to provide good selectivity for activated Cdc42 in previously developed

biosensors with a different design (Nalbant et al. 2004; Frantz et al. 2007; Koivusalo et

al. 2010). The biosensor was generated by first constructing plasmids encoding either

Cdc42 fused to the C terminus of CyPet, a CFP variant optimized for FRET (Nguyen and

Daugherty 2005), or the Cdc42-binding CRIB domain from WASP (CBD), amino acids

230–314, fused to the C terminus of YPet, a YFP variant optimized for FRET (Nguyen

and Daugherty 2005). The EGFP coding region from the EGFP-C1 vector (Clontech,

Inc.) was replaced with a PCR product containing the CyPet or YPet coding regions

flanked by an NcoI restriction site and a SGLRSELGS linker containing a BamHI

restriction site. The PCR products of the Cdc42 and CBD coding sequences were inserted

between the BamHI restriction site in the SGLRSELGS linker and an EcoRI restriction

site in the downstream multiple cloning site of the vector.

Fluorometry Assays of GAP Activity on Cdc42 Activation:

To determine the ability of wild-type MILO and either phosphomimetic (Y→E)

or non-phosphorylatable (Y→A) MILO mutants to affect Cdc42 activity, we performed

FRET measurements in a spectrophotometer in a bulk cellular suspension assay in which

293 cells were expressing the Cdc42 activity FRET biosensor. In brief, 293 cells were

plated on poly-L-lysine coated wells of a 6-well dish 36 hours before the assay was run.

The following morning, 24 hours before the assay was run, the 293 cells were transfected

with Lipofectamine according to the manufacturer's instructions. A total of 650 ng of

DNA was transfected per well, consisting of 100 ng of CyPet-Cdc42, 100 ng of YPet-

CBD, and the balance consisted of mCherry-tagged MILO, MILO mutants, known

regulators of Cdc42, or blank vector DNA. Each experimental condition was set up in

triplicate. The following morning, the cells were checked for appropriate brightness,

washed once with DPBS, gently trypsinized using 400 μL trypsin which was removed

after 15 seconds, and then resuspended in 500 μL cold DPBS. 400 μL of cell suspension

was then loaded into a spectrophotometer cuvette. Using a SPEX Fluorolog sensitive spectrophotometer, the cell suspension was excited at 433 nm, the excitation of CyPet, and the emission was monitored from 450 nm to 600 nm at 3 nm intervals to monitor the emission spectrum of YPet. For each test, a sample transfected with YPet-CBD only and monitored for FRET as above was monitored to account for differences in brightness and thus bleedthrough into the FRET channel by direct excitation of the acceptor fluorophore. This reading was subtracted from each measurement. For the calculation of FRET ratio, after bleedthrough correction, each sample was normalized such that the peak of CFP emission (475 nm) was set as an intensity value of 1.0. The FRET emission peak (525 nm) was then divided by the CFP peak for each sample, and the samples were averaged for each condition. FRET ratios could then be compared between each condition. Positive and negative controls consisted of the Cdc42 sensor transfected with the catalytic DH/PH domain from Vav2, or GDI-1, respectively, to determine the maximum possible range of Cdc42 activation in the assay. Statistical significance between conditions was assessed by two-tailed students' t-test assuming unequal variance.

Induction of Filopodia During Imaging:

To study filopodia growth, retraction, and dynamics, cells were transfected with control or MILO siRNA 48 hours prior to imaging, and then subsequently transfected with the Cdc42 biosensor with or without mutant GAP constructs 36 hours prior to imaging (Gadea et al. 2004). Cells were then plated on fibronectin-coated coverslips 24 hours prior to imaging. Six hours before imaging, cells were starved in Ham's F12K medium containing 0.5% delipidated BSA plus glutamine. Cells were transferred to a

heated open chamber apparatus to allow for addition of TNFα and allowed to return to 37° C for 30 minutes before imaging. Cells were imaged for 5 minutes at 20 second intervals prior to the addition of 20 ng/mL TNFα and imaged for a subsequent 15 minutes post-stimulation to observe filopodia formation and retraction.

Imaging a Single Rho GTPase Activity in Cells:

Mouse embryonic fibroblasts (MEF/3T3, BD Biosciences, Clontech, # C3018-1) were maintained in Dulbecco's modified Eagle's medium (Gibco, Carlsbad, CA) with 10% FBS. Rac1 activity was imaged using a modified version of the FLAIR biosensor (Kraynov et al. 2000), described above. Forty-eight hours post-induction of expression, cells were plated on fibronectin-coated glass coverslips for 3-4 hours prior to imaging. Imaging was performed in imaging medium (see below) with 2% fetal bovine serum. For emission ratio imaging, the following filter sets were used (Chroma): ECFP: D436/20, D470/40; FRET: D436/20, HQ535/30; EYFP: HQ500/20, HQ535/30. A dichroic mirror ("Quad-Custom" Lot# 511112038) was custom manufactured by Chroma Technology Corp. for compatibility with all of these filter sets. Cells were illuminated with a 200 W Hg arc lamp through a 10% transmittance neutral density filter. At each time point, three images were recorded with the following exposure times: CyPet (1.2 s), FRET (excitation of donor, observation of acceptor emission) (1.2 s), YPet (0.4 s) at binning 2x2. The image sets were taken at 10 s intervals. Ratio calculations to generate activity images were performed following bleed-through correction methods described previously (Kraynov et al. 2000). Briefly, Metamorph software (Universal Imaging) was used for image alignment and ratiometric calculation of activation signals. All images were

154

shading-corrected and background-subtracted. Binary masks with values equal to 1 inside the cell and 0 elsewhere were extracted by applying a threshold to the CyPet image, because it had the largest signal-to-noise ratio. Control cells expressing either CyPet alone or YPet alone were used to obtain bleed-through coefficients α and β in the following equation:

$$R = \frac{FRET_t - \alpha \cdot CyPet - \beta \cdot YPet}{CyPet} \qquad \text{(Eq. 1)}$$

where R is the Ratio, $FRET_t$ is the total FRET intensity as measured, α is the bleed-through of CyPet into FRET channel, β is the bleed-through of YPet into the FRET channel and CyPet is the total CyPet intensity as measured. By calculating the linear slope of the relationship between FRET and CyPet intensities upon CyPet excitation of cells expressing only the CyPet, the bleed-through parameter α can be determined. Similarly, by determining bleed-through into the FRET channel upon CyPet excitation of cells expressing only the YPet, the bleed-through contribution of YPet excitation by CyPet into the FRET channel β can be determined. The α parameter was found to be within 0.4-0.5 and the β parameter was typically ~0.2 Both were dependent on the particular optical configuration of the microscope used. With these parameters, the ratio of corrected FRET over CyPet was calculated and used as a measure of Rac1 activation. In time-lapse experiments, CyPet and YPet typically bleach at different rates. Therefore, the ratio was corrected for photobleaching as described elsewhere (Hodgson et al. 2005). Briefly, by algebraic manipulation, (Eq.1) can be rearranged to:

$$R = \frac{FRET_t}{CyPet} - \beta \frac{YPet}{CyPet} - \alpha = \Gamma - \beta \Psi - \alpha \qquad \text{(Eq.2)}$$

where Γ is the fraction of FRET intensity over CyPet intensity, and Ψ is the fraction of YPet intensity over CyPet intensity, and α and β are the bleed-through constants described above. By taking double exponential fits of the decays of both Γ and Ψ, the correction function, $\overline{R}^{-1}$, can be calculated following the methods outlined in (Hodgson et al. 2005).

For detection of Cdc42 activity, cells were seeded on fibronectin-coated glass coverslips (10 μg/ml fibronectin) for two to four hours. Endogenous Cdc42 activity was visualized using either the fluorescent biosensor MeroCBD (Nalbant et al. 2004; Hodgson et al. 2006) or the genetically encoded probe described above. After microinjection with MeroCBD biosensor, cells were allowed to recover for 30 minutes before imaging, otherwise for the genetically encoded probe, cells were treated just as for the Rac1 probe above. Cells were imaged in imaging medium (Ham's F-12K without phenol red (Biosource), 10 mM HEPEs and 10 μg/ml Oxyfluor reagent (Oxyrase Inc.) with 2 % fetal bovine serum in a heated closed chamber. Images were obtained using a Zeiss Axiovert 100TV microscope, a Zeiss 40× 1.3 N/A EC-Plan NeoFluar DIC lens, a CoolSnapES CCD camera (Roper Scientific), and Metamorph software (Universal Imaging). The exposure times were ~900 ms for the ISO-dye and ~300 ms for EGFP at binning 2x2, with a 10% transmittance neutral density filter for MeroCBD, and for the genetically encoded probe, three images were recorded with the following exposure times: CyPet (1.2 s), FRET (excitation of donor, observation of acceptor emission) (1.2 s), YPet (0.4 s) at binning 2x2. The image sets were taken at 10 – 20 s intervals. For ratio imaging of MeroCBD, the following filter sets were used (Chroma): EGFP: HQ470/40, HQ525/50; ISO: HQ580/30, HQ630/40 for MeroCBD, or. The dichroic mirror ("Scripps

156

Custom" Lot#511111886) was custom manufactured by Chroma Technology Corp. for compatibility with EGFP and ISO fluorescence wavelengths. For emission ratio imaging of the genetically encoded Cdc42 probe, the following filter sets were used (Chroma): ECFP: D436/20, D470/40; FRET: D436/20, HQ535/30; EYFP: HQ500/20, HQ535/30. A dichroic mirror ("Quad-Custom" Lot# 511112038) was custom manufactured by Chroma Technology Corp. for compatibility with all of these filter sets. Image alignment, ratio calculations and correction for photobleaching were performed as described in (Nalbant et al. 2004).

RhoA activation imaging in MEF/3T3 cells was performed by expressing the previously described RhoA FRET biosensor (Pertz et al. 2006) under the control of a tet-inducible promoter. Cells were plated on fibronectin-coated glass coverslips for 3-4 hours prior to imaging. Imaging was performed in imaging medium with 2% fetal bovine serum. The filter sets and the dichroic mirror used for ratiometric imaging were identical to the sets used to image Rac1 above. Cells were illuminated with a 200 W Hg arc lamp through a 10% neutral density filter. At each time point, three images were recorded with the following exposure times: ECFP (1.2 s), FRET (0.6 s) at binning 2x2. The image sets were taken at 10 s intervals. Metamorph software (Universal Imaging) was used for image alignment, ratiometric calculation of activation signals, and photobleaching corrections, as described above for Rac1 imaging. In contrast to Rac1 above, RhoA ratios did not require bleed-through corrections (Pertz et al. 2006) because the ECFP and EYFP are equimolar in any given pixel for this single-chain biosensor (Pertz et al. 2006). For RhoA imaging in HUVECs, cells were infected with a lentivirus-based TEM4 shRNA construct co-expressing an mCherry fluorescent protein marker. Next day, cells were

157

split onto gelatin-coated 25-mm glass slides at 25,000 cells/slide in EGM-2 medium with 10% FBS (HyClone). Five hours after plating, cells were infected overnight with an adenoviral vector-based single chain RhoA FRET construct (Pertz et al. 2006; Machacek et al. 2009). The next morning, the virus was removed and cells were transitioned to imaging medium (phenol red free M199 medium (Gibco) supplemented with 2% FBS, 2 mM glutamine (Glutamax, Invitrogen), 15 mM HEPES buffer, and endothelial cell growth media supplements (Lonza). Cells were then imaged as described above for RhoA MEFs, except image sets were taken at 60 s intervals to avoid cellular photodamage and toxicity.   The mCherry channel was monitored initially to determine whether the cells had been infected with the TEM4 shRNA lentivirus.

RhoA intermolecular FRET activity was imaged using the protocols described for the Rac1 GTPase above (Kraynov et al. 2000). 48 hours post-induction of the stable biosensor MEF cells, cells were plated on fibronectin-coated glass coverslips for 3~4 hours prior to imaging. Imaging was performed in imaging medium with 2% fetal bovine serum. For emission ratio imaging, the following filter sets were used (Chroma): ECFP: D436/20, D470/40; FRET: D436/20, HQ535/30; EYFP: HQ500/20, HQ535/30. The dichroic mirror ("Quad-Custom" Lot# 511112038) was custom manufactured by Chroma Technology Corp. for compatibility with all of the filter sets. Cells were illuminated with a 200 W Hg lamp through a 10% transmittance neutral density filter. At each time point, three images were recorded with the following exposure times: mCyPet (1.2 s), FRET (excitation of donor, observation of acceptor emission) (1.2 s), mYPet (0.4 s) at binning 2x2. The image sets were taken at 10s intervals. Ratio calculations to generate activity

images were performed following the bleed-through correction methods outlined above for the Rac1 biosensor.

For visual representations of ratiometric images, a linear pseudocolor lookup table was applied to all ratio images and the ratio values were normalized to the lower scale value, which was chosen to exclude the bottom 5% of the total histogram distribution, avoiding spurious low intensity pixels. In each experiment, CFP, YFP, and FRET images were carefully inspected to verify that all portions used to create the ratio image had a sufficiently high signal/noise ratio. We routinely target at least 300 gray level values (12 bit dynamic range) above background in the lowest intensity regions within the cell. This was especially important in thin parts of the cell where fluorescence was low.

Cell Edge Tracking:

Rates of protrusion and retraction where obtained from biosensor images by computational edge tracking using a custom-built software package written in Matlab (Mathworks). Cell edges were segmented via an intensity-based criterion and cell edge displacements were tracked by applying the mechanical model described in (Machacek and Danuser 2006) for morphing the edge between consecutive time points.

Tracking of Sampling Windows at Constant Distance to the Cell Edge:

To construct the sampling windows at a constant distance from the cell edge we computed a distance map (Matlab function: *bwdist*) to the segmented cell edge (Machacek and Danuser 2006). The distance map readily yielded lines of constant

distance which were offset by the window depth and equally subdivided to obtain the sampling windows.

Cross-Correlation Analysis:

Pearson's correlation coefficient between two time series of a sampling window at different time lags was computed using the Matlab function *xcorr*. To obtain the correlation for the entire leading edge of a migrating cell we averaged the correlation coefficient over all sampling windows for each time lag regardless of the protrusive state of an edge section. Significance levels of cross-correlation functions at the 95% confidence level were estimated by $N^{(-0.5)} * 1.96$, where N is the time series length.

To investigate the cell-to-cell heterogeneity of the time-lag we pooled the average correlation data from different cells and estimated the common cross-correlation by computing a smoothing spline. Importantly, morphological variations among cells do not affect this analysis because averaging is performed at the level of the cross-correlation coefficient. The central assumption underlying these calculations is that the states of Rho GTPase activity and cell edge movement are locally coupled and that the pathways from regulatory signals to downstream morphology are equal for all cells observed under equal conditions. Therefore, variations in global cell morphology have no influence on the cross-correlation coefficients which are acquired strictly locally.

To estimate the variance of the smoothing spline approximation and hence of the time lag we employed a non-parametric bootstrapping method (Efron and Tibshirani 1994). From the residuals of the spline approximation 2000 bootstrap samples were taken to calculate local variation of the spline about the mean. The 95% confidence interval,

bands between dashed parallels to splines, was then obtained in each location as the

interval containing 95% of the spline samples.

3.5 Acknowledgements

3.6 Figures and Legends

Figure 3.1: Activation of Rho GTPases in Migrating Mouse Embryonic Fibroblasts.

(A) Rac1, (B) Cdc42, and (C) RhoA activation reported by biosensors. White rectangle: Region of interest selected for analysis. Scale bar: 20 μm.

(D) Time course (blue line) of Rac1 activation within 0.6 μm from the cell edge, averaged over a 5 μm long portion of the cell edge. Red line: filtered time-course (Gaussian filter, σ = 5 frames). Green triangles: local maxima and minima of filtered time-course.

(E-G) Modulation of GTPase activation (mean absolute difference between consecutive local extrema of the time-course) as a function of the distance D from the leading edge. Values are normalized to the modulation at the cell edge. Error bars: s.e.m. of n = 6 (Rac1); n = 4 (Cdc42); n = 4 (RhoA) cells.

(H) Sampling windows of 0.9 μm depth placed at the cell edge and at $D = 1.8$ μm from the cell edge.

(I) Parameters to define the position and size of a sampling window. In each window, the time course of GTPase activation was recorded (average of ~10 pixels). For a sampling window at D = 0, a time course of edge velocity was recorded (mean of 6 − 8 measurements).

(J) Time courses of edge velocity (green) and GTPase activation (Cdc42, red) recorded in one sampling window.

163
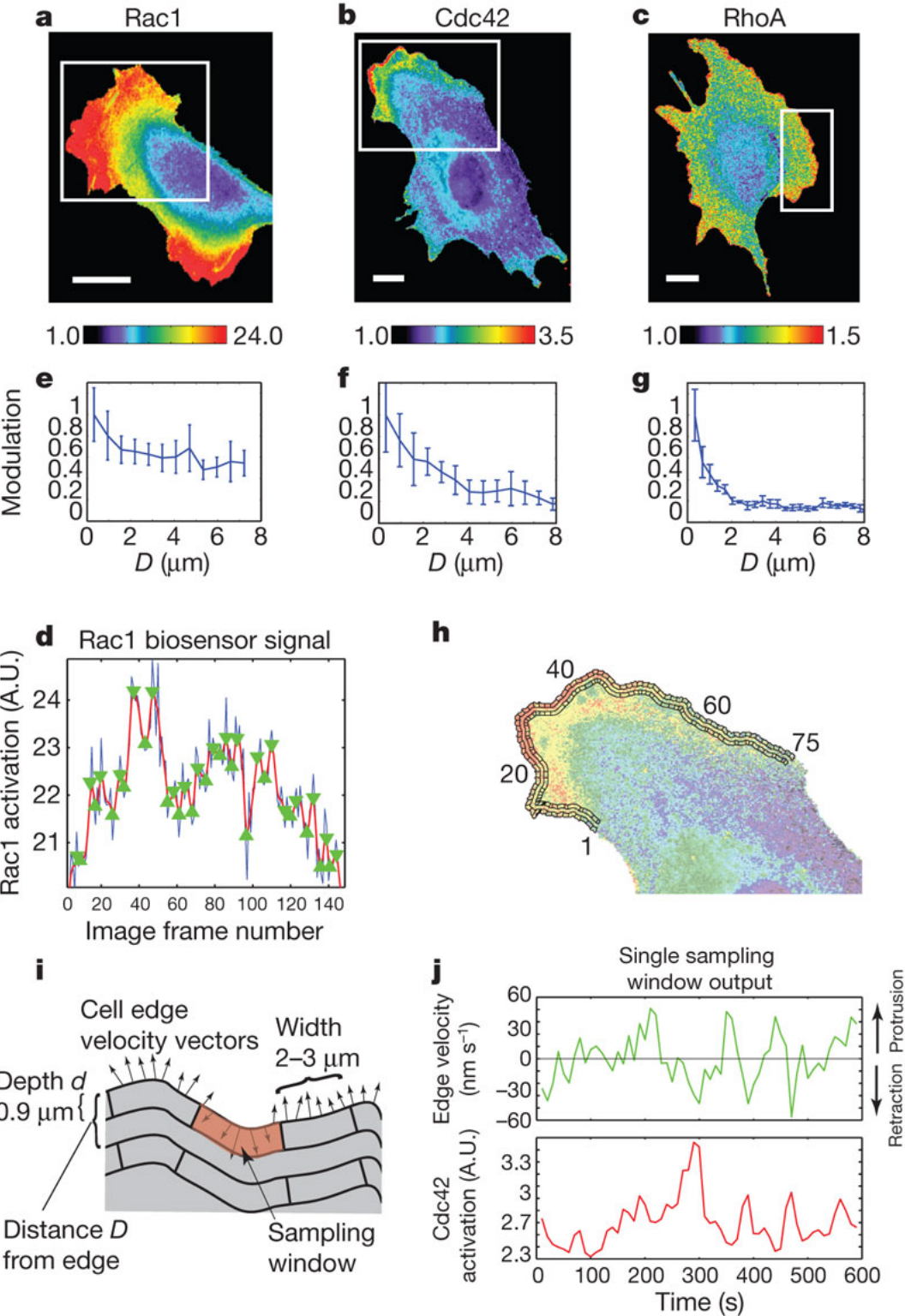
Figure 3.1

Figure 3.2: Designs of the Biosensors Used.

In each biosensor an "affinity reagent", derived from a downstream effector, is used in the biosensor to bind specifically to the active form of the GTPase. The affinity reagents are a fragment of WASP (CBD in panel A, for Cdc42), a fragment of Pak (PBD in panel B, for Rac1) and a fragment of Rhotekin (RBD in panels C and D, for RhoA. The published sensors used in the paper are shown in the left hand column, in panels A, B, and C. Biosensor C differs from the others in that the affinity reagent is covalently linked to the target GTPase. For controls examining the effects of biosensor design, an additional biosensor was produced, the biosensor of panel D. With this biosensor in hand, each GTPase could be examined using an intermolecular design. Biosensors B, C and D use FRET as a proxy for GTPase binding. In design A, an environmentally sensitive dye reports binding to endogenous Cdc42. Titration of affinity reagent concentration, titration of fluorescent GTPase concentration, and comparison of the intermolecular and intramolecular RhoA biosensors C and D all demonstrated that our conclusions were not attributable to differences in biosensor design.

Figure 3.2
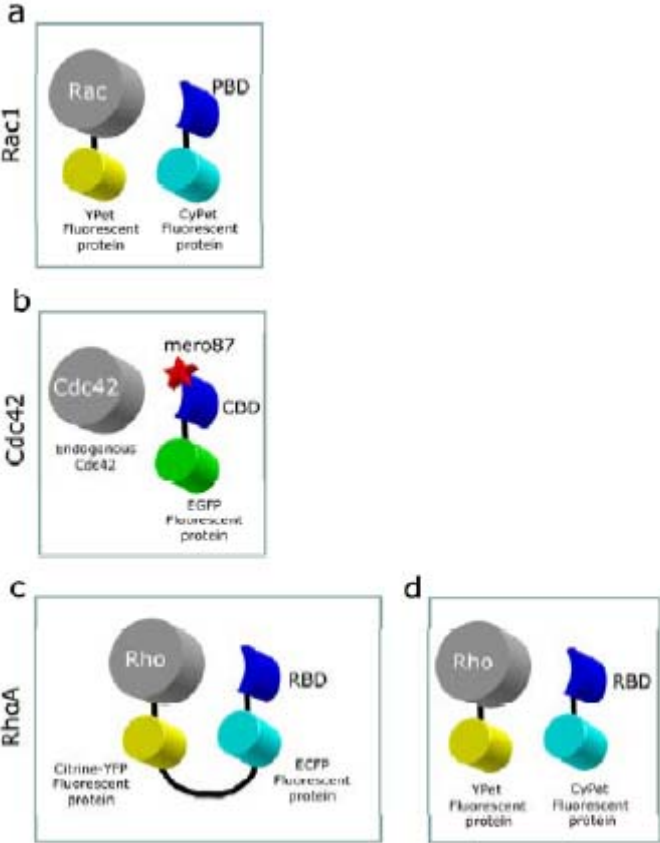
Figure 3.3: Effect of Biosensor Component Concentrations on the Measured Rac1-Protrusion Correlation.

(A) The ratio of acceptor (YFP) to donor (CFP) concentrations and corresponding correlation maxima time lags for each of the cells assessed. A dynamic range of 3:1 was achieved.

(B) Cross-correlation functions for individual cells (color-coded to match A). No trend in the timing as a function of probe concentration was observed.

(C and D) Donor and acceptor concentrations of individual cells, indicating that higher and lower concentration ratios in (A) were associated with high and low acceptor and low and high donor, respectively. Cells were background subtracted and intensities were corrected for channel cross talk. Concentrations were computed as intensity/exposure time, at fixed illumination intensity.

Figure 3.3
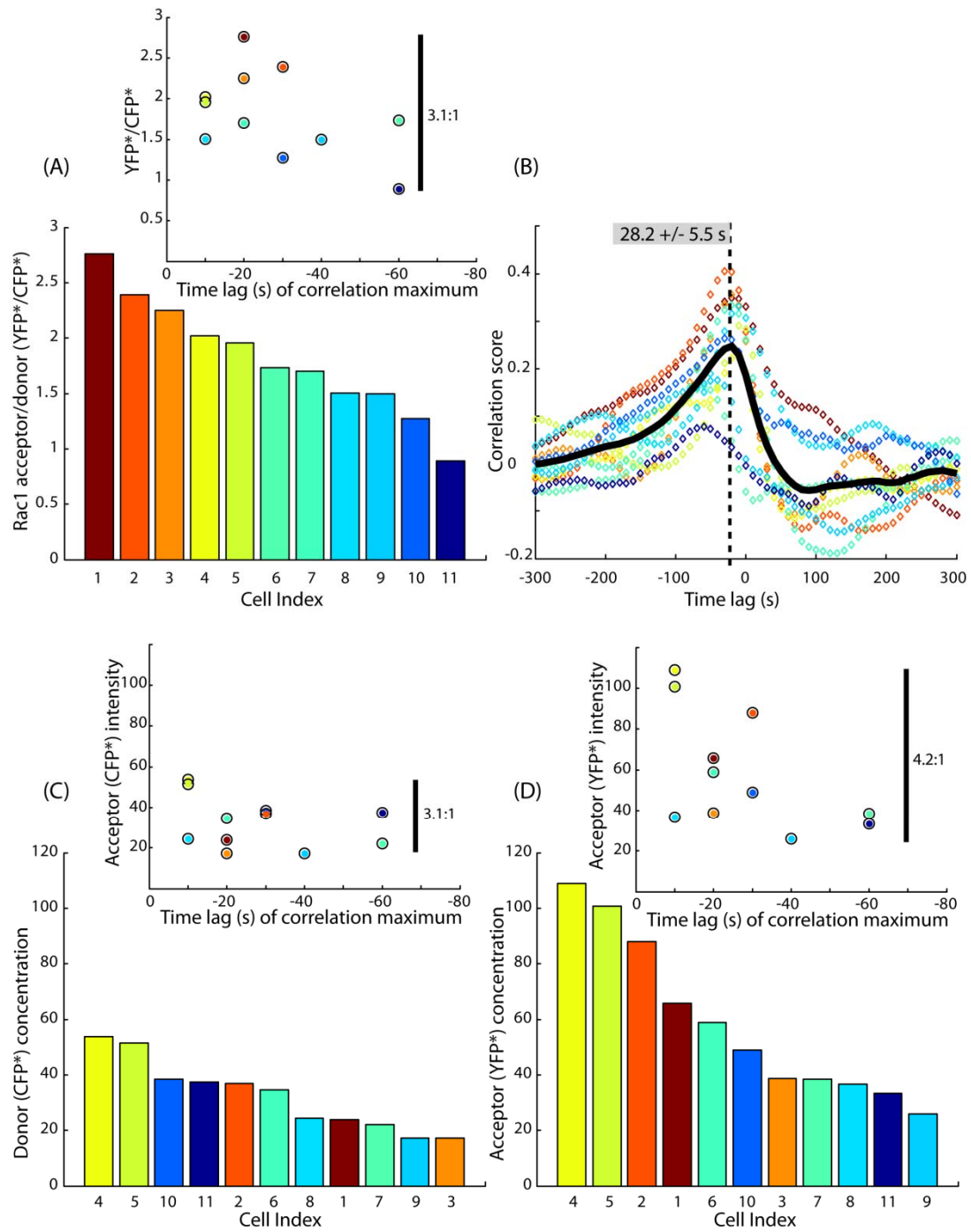
Figure 3.4: Relationship Between RhoA and Protrusion/Retraction Determined by an Intermolecular Biosensor.

(A) Activation of RhoA. Notice the increased dynamic range of the intermolecular sensor as compared to the intramolecular sensor in Figure 3.5. Areas of dynamic activity correspond to regions of rapid protrusion and retraction (shown with white arrows). Scale bar in the 14'00" time point: 20 microns.

(B) Comparing the correlation functions of the intramolecular RhoA biosensor (black) and the intermolecular RhoA biosensor (red). 95%-confidence bands (dashed lines) were calculated by bootstrap analysis of n = 14 cells (intramolecular) and n = 5 cells (intermolecular). The timings of the two probe activations relative to protrusion were statistically indistinguishable: -6 [-8 -4] s (intramolecular) and -10 [-15 -5] s (intermolecular); mean +/- 95% confidence interval.

(C) Correlation of the intermolecular RhoA probe as a function of the distance from the cell edge. Consistent with the results obtained with the intramolecular probe (see Figure 3.5), RhoA activation reported by the intermolecular probe decreases in correlation as the probing windows are placed at increasing distances from the cell edge. In addition, the correlation peaks indicate increasing delay in maximal activation at increasing distance from the cell edge.

(D) Summary of spatial and temporal relationships reported by the intermolecular probe. Blue line: magnitude of the cross-correlation maximum as a function of the distance. Red line: time lag of cross-correlation maxima as a function of the distance. Dashed lines: 95% confidence interval computed by bootstrap analysis. Dots: Values for individual cell shown in B.

Figure 3.4
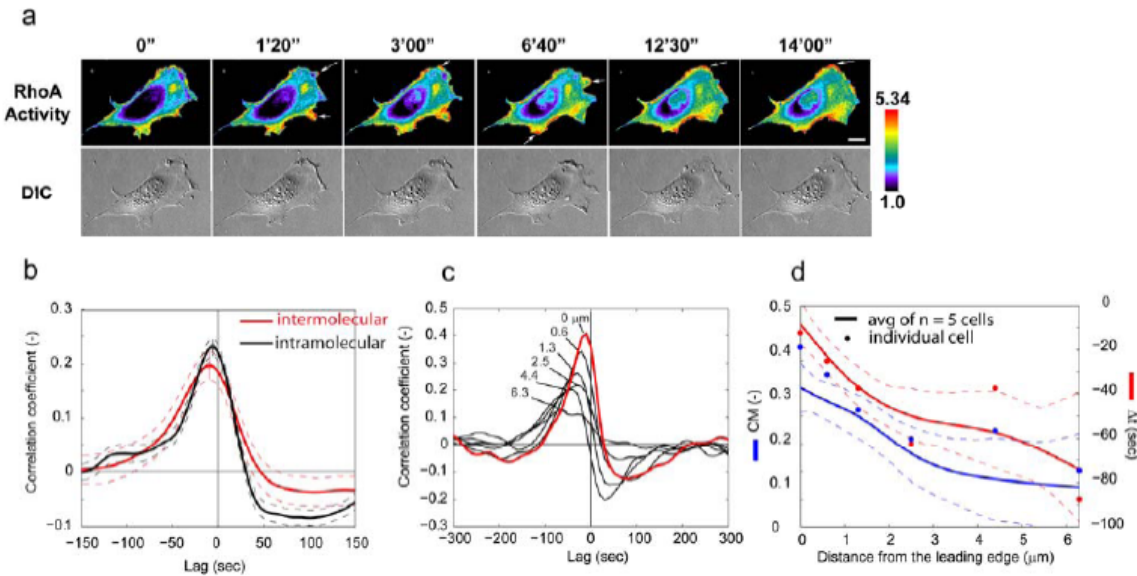
Figure 3.5: Spatiotemporal Coordination of Rac1, Cdc42, and RhoA Activation.

(A) Timing of Rho GTPase activation relative to edge velocity, as determined by temporal cross-correlation functions. The variable 'edge movement' is being used as the reference signal. Thus, correlation maxima in the sector labeled "After" indicate that the GTPase reaches the activation maximum after the protrusion event (time point of fastest edge advancement). Dashed lines: 95% confidence intervals. Data originate from n = 11 cells (Rac1), n = 12 cells (Cdc42), and n=12 cells (RhoA). Confidence intervals were computed by bootstrap sampling of 2000 residuals to the spline fits.

(B) Timing of RhoA activity relative to Cdc42 activity, both monitored in the same cell, as determined by the temporal crosscorrelation function. The variable Cdc42 is being used as the reference signal. Thus, the correlation maximum in the sector labeled "Before" indicates that RhoA reaches the activation maximum before Cdc42 (n = 7 cells).

(C) Model of GTPase activation during protrusion and retraction. Green: Rac1 activation. Black: RhoA activation. Blue: Cdc42 activation.

Figure 3.5
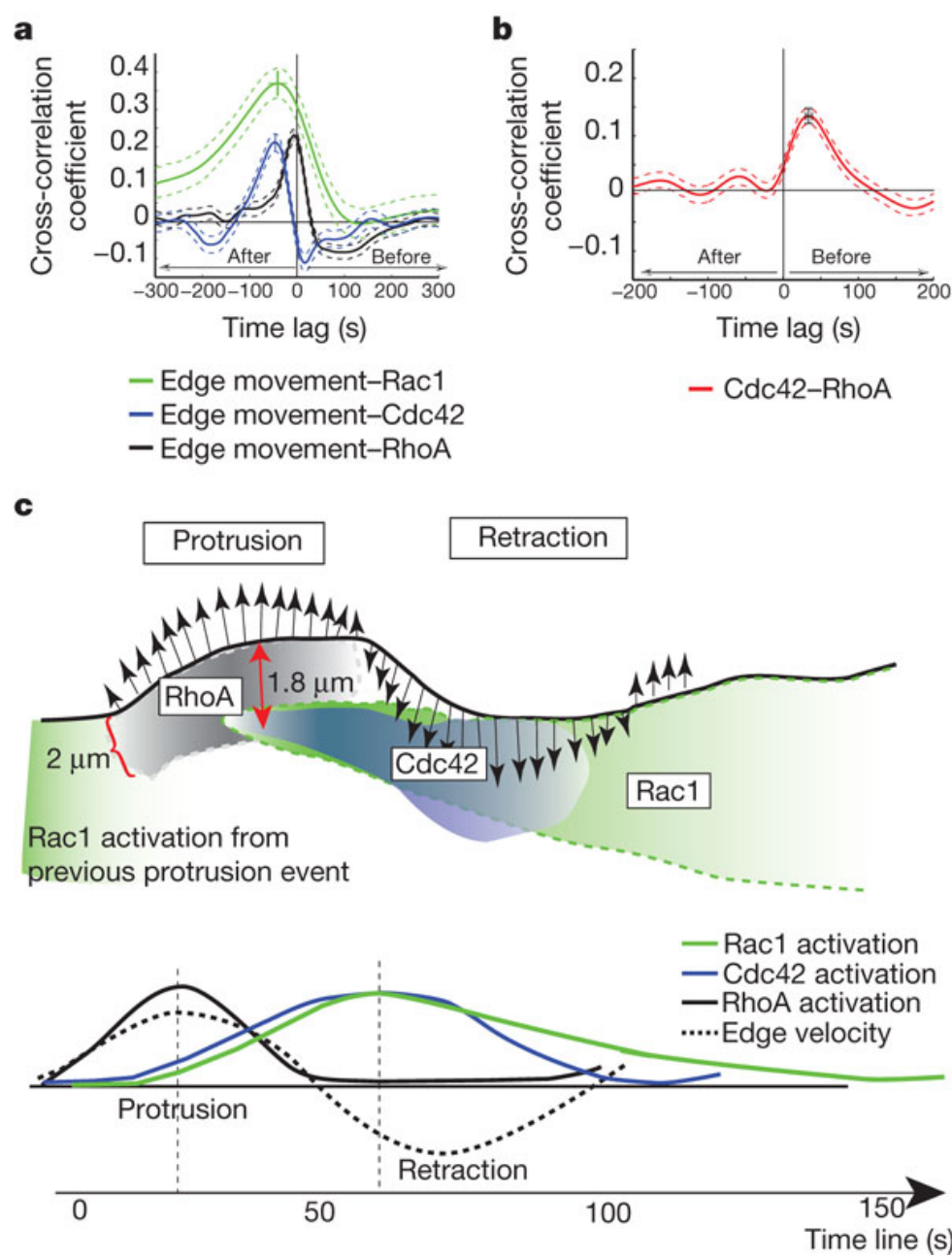
Figure 3.6: TEM4 Activates RhoC during Microtubular Depolymerization.

(A) Levels of activated (GTP-loaded) RhoA and RhoC were measured by affinity

precipitation assay in control or TEM4-depleted HUVECs that were left untreated,

treated with nocodazole, or treated with nocodazole and then incubated with serum for 5

min. The activation levels of RhoA and RhoC and expression levels of RhoA, RhoC and

TEM4 in whole cell lysates were determined by immunoblotting. Numbers below the

gels indicate band intensities relative to the untreated NS control group as determined by

densitometry. Similar results were obtained in four independent experiments.

(B) Quantitation of active RhoA (open bars) or RhoC (grey bars). Ratio between Rho

activation levels in TEM4 sh vs NS group was determined for each experimental

condition for each experiment and then averaged. A horizontal line indicates a baseline

where TEM4 depletion has no effect on Rho activation levels.

(C) Spatial RhoA activation patterns assessed by FRET analysis. RhoA activity was

monitored via FRET analysis of a genetically-encoded biosensor in HUVECs as detailed

in Methods, with and without TEM4 knockdown. Images are representative of NS

shRNA (n = 9) and TEM4 shRNA treatment conditions (n = 11).

Dynamic courses of RhoA activity during protrusive behaviors assessed by FRET

imaging of a genetically-encoded biosensor in HUVECs treated with NS shRNA (D) or

TEM4 shRNA (E). Arrowheads indicate high RhoA activity associated with areas of

active protrusion. Arrows highlight membrane patches with minimal RhoA activity that

correlated with areas of local retraction or protrusion arrest within the leading edge. A

longer time course is presented for TEM4-depleted cells as they showed slower rate of

protrusion. Time course is representative of protrusions in NS shRNA treated cells (n =

9) and TEM4 shRNA treated cells (n = 11). Scale bar = 10 μm. Elapsed time is
indicated in minutes, and warmer colors correspond to higher ratio values per the
representative heat maps, indicating greater RhoA activity.

Figure 3.6
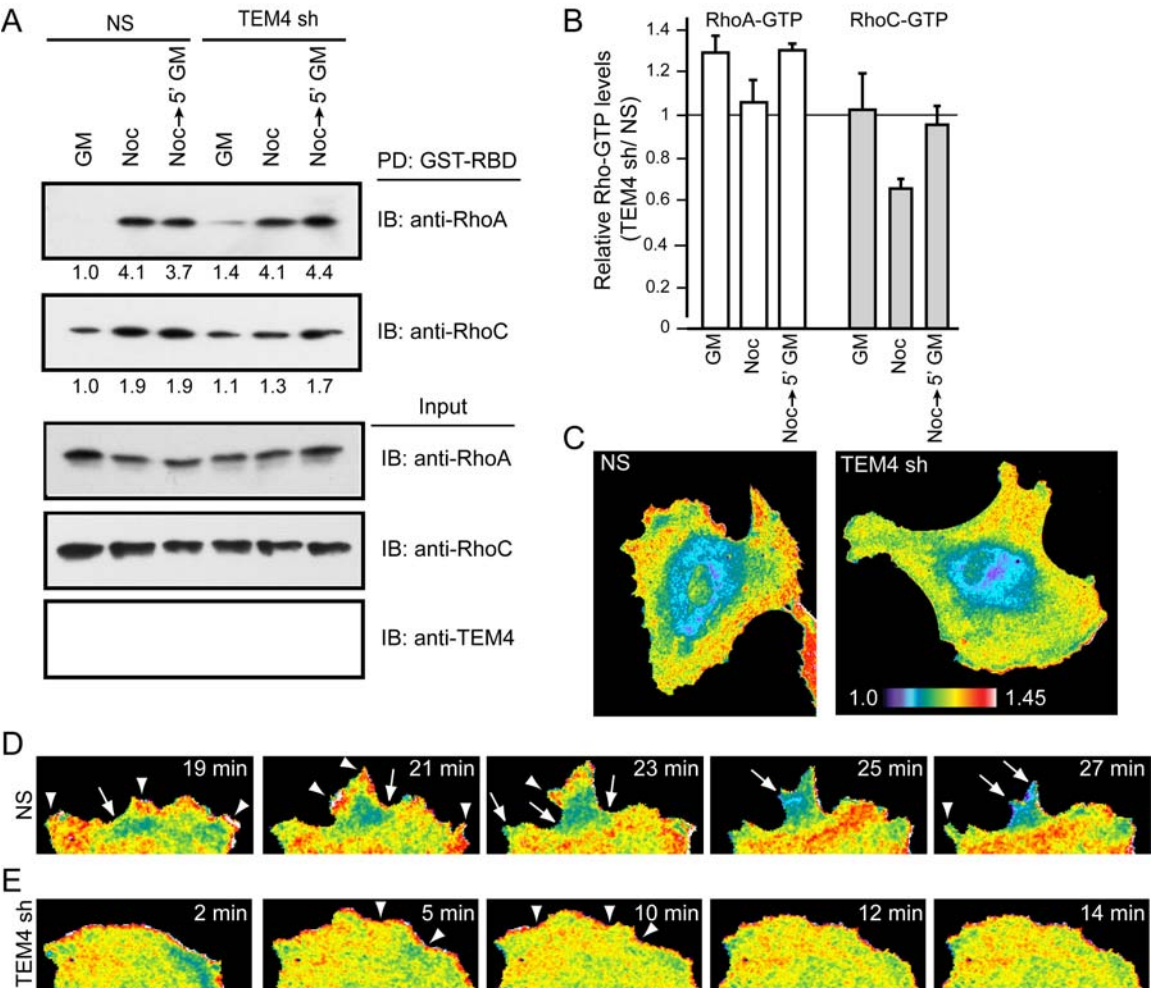
Figure 3.7: Cdc42 Dynamics in TNFα-Stimulated Filopodium Formation.

(A) Schematic of the dual-chain Cdc42 biosensor design and regulation.

(B) Cdc42 activation in TNFα-induced filopodia, demonstrating the ability to detect

Cdc42 activity within these structures using this sensor.

(C) Sample images demonstrating Cdc42 activation at the tips of protruding filopodia,

schematized in (D) with quantitation of the frequency of these local maxima along the

length of the filopodium, comparing the FRET signal versus a simple ratio of YFP/CFP

in the same filopodia as an internal control.

(E and F) Sample images and quantitation of Cdc42 activation levels within the

filopodium shaft during protrusion or retraction. Values are mean Cdc42 FRET ratio

intensities averaged along the filopodium length. Error bars indicate S.E.M. Asterisks

indicate $p < 0.05$.

(G and H) Sample images and quantitation of Cdc42 activation levels at the site of

filopodium formation compared to the whole-cell Cdc42 activity average, and to the

Cdc42 activity in a nearby region of interest that did not form filopodia. Values are mean

Cdc42 FRET ratio intensities averaged along the filopodium length. Error bars indicate

S.E.M. Asterisks indicate $p < 0.05$.

176

Figure 3.7

Figure 3.8: Effects of MILO GAP Activity on Cdc42 Activation Globally and within Filopodia.

(A) Cdc42 activity in control vs. MILO knock-down cells. Activity is represented by the heat map in the upper right corner, and scaling is roughly equivalent.

(B) Quantitation of whole-cell Cdc42 activity in control vs. MILO knock-down cells. Values are mean Cdc42 FRET ratio intensities averaged along the filopodium length. Error bars indicate S.E.M. Asterisks indicate $p < 0.05$.

(C) Cdc42 activity in control vs. MILO knock-down cells at the base of filopodia. Activity is represented by the heat map in the upper right corner, and scaling is roughly equivalent.

(D) Quantitation of Cdc42 activity in control vs. MILO knock-down cells at the base of filopodia. Values are mean Cdc42 FRET ratio intensities averaged along the filopodium length. Error bars indicate S.E.M. Asterisks indicate $p < 0.05$.

(E) Cdc42 activity in control vs. MILO knock-down cells within the filopodium shaft. Activity is represented by the heat map in the upper right corner, and scaling is roughly equivalent.

(F) Quantitation of Cdc42 activity in control vs. MILO knock-down cells within the filopodium shaft. Values are mean Cdc42 FRET ratio intensities averaged along the filopodium length. Error bars indicate S.E.M. Asterisks indicate $p < 0.05$.

Figure 3.8
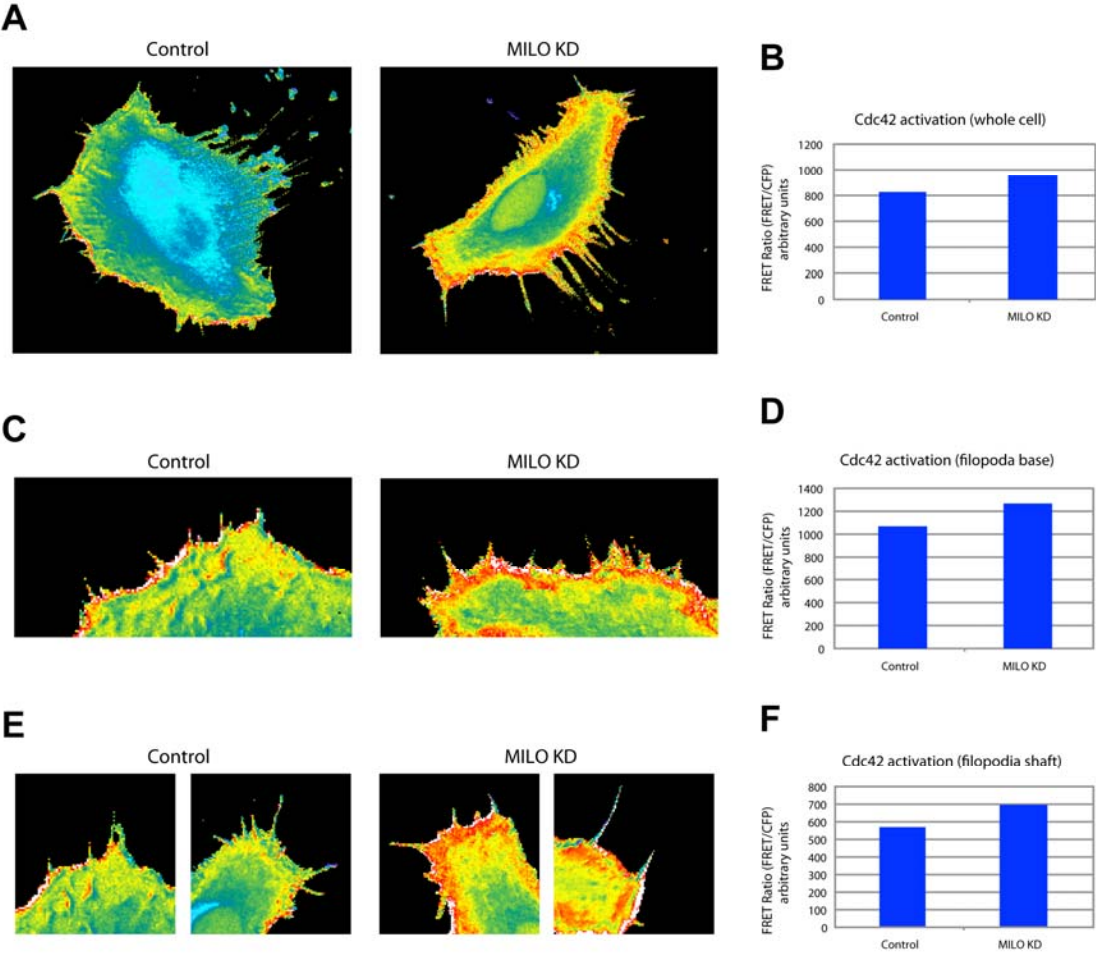
CHAPTER FOUR: ROLE OF RHOG IN CELL MIGRATION

4.1 Abstract

Spatiotemporal control of Rho GTPase activity is required for optimal cell migration through the proper coordination of a variety of cellular behaviors. RhoG, a GTPase, has been shown to act upstream of Rac1, but its role in cell migration is poorly understood. Here we develop a novel FRET activity biosensor for RhoG and show that RhoG is activated coincident with the leading edge of lamellipodial protrusion. Further, RhoG activates a subpopulation of Rac1 at the leading edge of migrating cells via the ELMO/DOCK180 complex, and activation of Rac1 by RhoG is dependent on the endocytic recycling of RhoG to the leading edge as regulated by RhoGDI-3. Dysregulation of RhoG and its endocytic recycling leads to alteration in the recruitment and activation of Rac1 at the leading edge, changes in focal adhesion and actin dynamics, and ultimately the dysregulation of cell migration in both 2D and 3D matrices.

4.2 Introduction

Cell migration is important in a variety of physiological and pathological processes such as embryogenesis, angiogenesis, leukocyte transendothelial migration, wound healing, and tumor invasion and metastasis. The Rho family GTPases are key regulators of cell migration, with RhoA promoting actomyosin contractility, and Rac1 and Cdc42 regulating actin polymerization and membrane protrusion (Burridge and Wennerberg 2004). These roles have been clarified further in cellular protrusion, demonstrating that all three GTPases are activated at the leading edge of cells to enable protrusion and cell migration with precise spatial and temporal activation patterns for each of these GTPases (Machacek et al. 2009).

The functions of these GTPases depend critically on their proper activation and coordination in response to extracellular cues. Cells have developed a large number of regulatory mechanisms that accomplish the spatial and temporal coordination of their activation, often through tight regulation of upstream regulators, and through localized activation of downstream signaling molecules in response to extracellular cues. Cell motility in particular relies on these spatially restricted regulatory processes that coordinate localized Rho GTPase signaling, particularly near the plasma membrane where interaction with extracellular signals occurs. In response to extracellular stimuli, these processes promote polarization and the remodeling of actin at the leading edge of cells for the formation of lamellipodia, one of the first steps in cell migration (Ridley et al. 2003). The mechanisms of how these GTPase signals are locally coordinated and constrained remain an area of active study.

Studies have revealed a number of mechanisms used to achieve this signal restriction and polarization. Among these mechanisms, upstream regulatory molecules may be selectively positioned to engage cell migration machinery, particularly the GTPases, in response to extracellular cues. As an example, integrins are a major class of signaling proteins that are positioned at the leading edge to respond to extracellular cues, often by endocytic recycling, and thus to coordinate GTPase activation. In 3-dimensional matrices, Rab25-coated vesicles associate with β1 integrins and recycle predominantly to the tips of leading edge protrusions, helping to activate GTPases, and regulate directed cell migration (Caswell et al. 2007). Further, the activity of the GTPases may be spatially restricted to generate localized downstream responses. Rac1 is one of the GTPases that is tightly controlled by both of these mechanisms. Rac1 activity has been shown to be high at the leading edge during cell migration (Kraynov et al. 2000; Machacek et al. 2009) at odds with what the broadly uniform localization of Rac1 alone would suggest. Further, the positioning of Rac1 determines its activity. The control of Rac1 activity is thought to depend in part on endosomal recycling (Palamidessi et al. 2008) to the leading edge, and by its recruitment and activation by GEFs at the leading edge of cells. Ultimately the levels and location of Rac1 activity determine cellular behaviors: high and low levels of Rac1 activity, which often correlate with delocalized Rac1 activity, both lead to minimal cell migration, but at intermediate levels of Rac1 activity, productive cell migration occurs (Pankov et al. 2005; Petrie et al. 2009). Much remains to be learned about how Rac1 is spatiotemporally restricted in its activation and how the positioning and regulation of activators and inactivators is controlled.

Among the Rac subfamily of GTPases, three Rac isoforms exist, along with the closely related RhoG, which is 72% identical to Rac1 by sequence identity. Of these, Rac1 and RhoG are ubiquitously expressed and have a unique relationship where RhoG is capable of activating Rac1 through an ELMO/DOCK180 GEF complex (Katoh et al. 2000; Katoh and Negishi 2003; Katoh et al. 2006). This relationship between RhoG and Rac1 is critical in a number of cell behaviors, including phagocytosis and the engulfment of apoptotic cells, where RhoG is required for Rac1-dependent actin reorganization (deBakker et al. 2004; Park et al. 2007). RhoG is unique in that it has been implicated both in lamellipodia formation (Katoh et al. 2006) required for 2-dimensional migration, and in dorsal ruffle (or "wave") formation also implicated in 2-dimensional and 3-dimensional cell migration (Wennerberg et al. 2002; Buccione et al. 2004; van Buul et al. 2007a; Gu et al. 2011). However, the mechanism and precise role of RhoG in regulating Rac1 in these cell migratory processes remains unclear. Since RhoG is upstream of Rac1, this raises a number of questions with regard to the role of RhoG in cell migration. How is RhoG itself regulated? When and where is RhoG active in migrating cells? Is RhoG-dependent activation of Rac1 important during cell migration, or do RhoG and Rac1 have separable functions? Previous work indicates both scenarios are at work, namely that RhoG and Rac1 can signal in parallel and in tandem (Wennerberg et al. 2002; Ellerbroek et al. 2004). Since Rac1 activity is known to be spatiotemporally restricted to the leading edge, does RhoG play a role in this process? Thus, understanding the spatial and temporal dynamics of RhoG activity in relationship to Rac1 will be critical in revealing the roles of these proteins in cell migration.

Here, through the development and use of a novel FRET activity sensor for RhoG, we show first that RhoG is activated coincident with lamellipodial protrusion and tightly associated with the leading edge. Further, RhoG activates a subpopulation of Rac1 at the leading edge of migrating cells via the ELMO/DOCK180 complex, and activation of Rac1 by RhoG is dependent on the endocytic recycling of RhoG to the leading edge as regulated by RhoGDI-3. Dysregulation of RhoG activity and/or trafficking leads to alterations in the recruitment and activation of Rac1 at the leading edge and at focal adhesions and changes in focal adhesion and actin dynamics. Ultimately, we define a role for RhoG in enabling cells to change the direction of their migration during random cell migration due to the ability of RhoG to initiate sites of Rac1 activation at the cell periphery.

4.3 Results

Spatio-temporal Dynamics of RhoG and Rac1 Activity at the Leading Edge of Motile Cells:

In order to study the dynamics of RhoG "activation" (GTP loading) we produced a RhoG biosensor based on intermolecular FRET between RhoG fused to the fluorescent protein CyPet (Nguyen and Daugherty 2005), and an ELMO1 fragment fused to the fluorescent protein YPet (Nguyen and Daugherty 2005) (Figure 4.1A). In this biosensor, when RhoG adopted the activated conformation, the ELMO fragment bound to RhoG, leading to FRET between the two fluorescent proteins. To optimize the brightness and dynamic range of the biosensor, we examined ELMO fragments of different size (85 amino acids to full length ELMO1), in all cases with CyPet on the N terminus of RhoG and YPet at either the C or N terminus of the ELMO fragment. This configuration preserved normal regulation of RhoG by guanosine dissociation inhibitors. We also tested biosensors in which the ELMO fragment and RhoG were linked in a single chain, but the dual chain design provided enhanced sensitivity because it effectively eliminated any FRET in the biosensor 'off' state (optimization of the single chain biosensor led to an approximately 25% FRET increase upon activation - data not shown). The two biosensor chains were co-expressed in adherent Cos-7 cells, and cell populations were examined for the ratio of FRET/CFP fluorescence. We first compared a dominant negative CyPet-RhoG (T17N) and a constitutively active CyPet-RhoG (Q61L) (Figure 4.1B). The expression levels of the two chains were maintained at roughly equal levels by monitoring the intensities in the CFP and YFP channels. Optimum response was obtained using a fragment containing ELMO1 residues 1-95, with YPet at its C terminus.

We examined whether the biosensor responded to upstream stimuli as did unmodified RhoG. Cos-7 cells were co-transfected with wild-type biosensor and different known regulators of RhoG (Figure 4.1B). Cellular concentrations (roughly estimated as fluorescence per unit area) were maintained below levels generating obvious cellular phenotypes, such as dorsal ruffling or effects on activation kinetics relative to protrusion velocity. The limits on maximal concentration defined here were used during the biological studies described below. Biosensor co-transfected with the activating guanosine exchange factors (GEFs) Vav2 and PLEKHG6 displayed FRET similar to that of the constitutively active RhoG. In contrast, minimal FRET was observed with the dominant negative form of RhoG (T17N) or for wild-type RhoG co-transfected with p50RhoGAP or RhoGDI-1. Notably, p50RhoGAP has not been previously identified as a GAP for RhoG; pull-down assays of GTPase activity identified this GAP as a negative regulator (Figure S4.1A). The negative regulators reduced FRET to levels below those seen for wild-type biosensor alone, indicating that the wild-type biosensor reflected constitutive activity and that negative regulators could in fact active reduce RhoG activity=. To test the specificity of the biosensor for RhoG activation, we co-transfected GTPase regulators specific for GTPases other than RhoG. The catalytic domains from the GEFs Tiam-1 (Rac1-specific), Tim (Rho-specific) and Rap1GAP (Rap-specific) produced no effect on FRET. Finally, we modulated endogenous RhoG regulators. Stimulation of cells with EGF, which is known to activate RhoG (Samson et al. 2010), increased FRET (Figure S4.1B). A recent report showed that the scaffold protein synectin prevents RhoG activation by serving as a scaffold for RhoGDI-1, which sequesters RhoG (Elfenbein et al. 2009). As expected, synectin knockdown led to a

significant increase (2.52-fold) in the biosensor FRET/CFP ratio (Figure S4.1C-E). In summary, these data demonstrate that we constructed a RhoG biosensor capable of correctly reporting RhoG activation in living cells, at expression levels that did not perturb normal cell motility or morphology.

The biosensor was first used to examine the kinetics and localization of RhoG activation at the leading edge of motile cells, and to compare these dynamics to those of Rac1 and RhoA, in both mouse embryonic fibroblasts (MEFs) and HeLa cells (Figure 4.1C). Despite the fact that RhoG is much closer in sequence to Rac1 than to RhoA, RhoG dynamics strongly resembled those of RhoA, and not Rac1, in both cell types. RhoG activation was observed in a narrow band proximal to the leading edge of migratory cells, as previously reported for RhoA (Itoh et al. 2005; Pertz et al. 2006). In contrast, Rac1 was activated in a broader band more distal to the leading edge, also consistent with previous reports (Kraynov et al. 2000; Itoh et al. 2002; Machacek et al. 2009) (Figure 4.1C). Automated line scan analysis of > 388,000 lines drawn parallel to the leading edge of motile cells indicated that RhoG was active during protrusion but not retraction, and that activity peaked within the first 2 microns from the edge (Figures 4.1D, 4.1E, and 4.1G). To determine whether RhoG activity was correlated with protrusion or retraction speed, edge movements from migrating cells were binned into groups based on their peak velocities, and these protrusional velocities were correlated with the respective RhoG activity levels. RhoG activity increased proportionately with protrusion speed (Figure 4.1D), but showed no correlation with retraction, regardless of the velocity. These line scans confirmed that RhoA and RhoG peak within 1 micron of the cell edge, while Rac1 activation peaks at approximately 2 microns. (Figure 4.1G).

Using previously described methods we also examined the relative timing of changes in edge velocity and RhoG activation. RhoG activity correlated maximally with edge velocity 6 ± 1.4 seconds after a velocity change (Figure 4.1F and S4.1F), similar to the correlation previously reported for RhoA (-6 seconds) and unlike that reported for Rac1 (-40 seconds) (Machacek et al. 2009). Together, these data indicate that RhoG is activated during cell protrusion, prior to Rac 1 and at a region closer to the cell edge, more closely resembling the dynamics of RhoA than of Rac1.

RhoG is Targeted to the Leading Edge by Endosomal Recycling and Regulated by RhoGDI-3:

Previous studies have shown that RhoG is recruited to both microtubules (Vignal et al. 2001) and to caveolin-positive vesicles (Prieto-Sanchez et al. 2006), so we hypothesized that trafficking of RhoG might contribute to its tight regulation at the leading edge. CFP-RhoG fusion protein was visualized in living HeLa, MEF, and Cos-7 cells. In addition to the membrane and perinuclear localizations commonly seen for GTPases, we observed RhoG in rapidly moving vesicular structures (Figure 4.2A). Co-expression of CFP-RhoG together with mCherry-tubulin showed the RhoG vesicles to be associated with microtubules (Figure 4.2B), as previously described in fixed specimens (Zalcman et al. 1996; Brunet et al. 2002; Dransart et al. 2005; Prieto-Sanchez et al. 2006). By tracking both microtubules and vesicles in living cells, we observed that most of the RhoG-positive vesicles (94.7% of 75 vesicles tracked) moved along microtubules (Figure 4.2B), and moved in both retrograde and anterograde directions (Figure 4.2C). To determine the identity of the vesicles, we imaged CFP-RhoG together with different mCherry-labeled Rab GTPase constructs used to mark specific components of the

endosomal network, particularly Rab4, Rab5, and Rab11 of the rapid endosomal recycling compartments, and Rab7 of the lysosomal degradation pathway. RhoG-positive vesicles were associated with Rab4, Rab5, and Rab11 fluorescence (n = 10-15 cells per condition, > 60% colocalization), but rarely co-localized with Rab7 (n= 10 cells, colocalization 3.5% ± 2.2%) (Figures 4.2C and S4.2A-D).

Time-lapse movies of RhoG biosensor activity showed that RhoG was inactive (70%) or unchanged in activity (24%) at the vesicles (Figure 4.2D) in 178 vesicles examined.We sought to determine how RhoG was maintained there in its inactive form.. Previous studies showed that both RhoGDI-1 and RhoGDI-3 (also known as RhoGDI-γ) bind and sequester RhoG in its inactive form; we pursued RhoGDI-3 because it is known to localize to vesicles and the Golgi apparatus (Figure 4.2E) (Brunet et al. 2002). CFP-RhoG and mCherry-RhoGDI-3 co-localized at vesicles and at a perinuclear accumulation morphologically consistent with the Golgi apparatus (n= 20 cells) (Figure 4.2E). Overexpression of RhoGDI-3 greatly reduced the egress of RhoG vesicles from the perinuclear region to vesicles, and reduced the amout of RhoG at the cell edge (Figures 4.2F and 4.2G). Importantly, although RhoGDI-3 overexpression reduced the number of RhoG vesicles, endosomal trafficking remained intact, as assessed by time-lapse imaging of fluorescent Rab proteins. This data indicated that RhoGDI-3 controls the egress specifically of RhoG from a perinuclear compartment, and maintains RhoG in an inactive state on vesicles. This not only shed light on RhoGDI-3 regulation of RhoG, but provided a powerful tool for further studies: in RhoGDI-3 knockdown cells, the RhoG biosensor showed RhoG to be more activated both globally and diffusely (Figures 4.2H, 4.2I, and S4.2E). Overexpression of RhoGDI-3 led to a decrease in RhoG activity (Figure 4.2I),

189

with more uniform activation not localized to the leading edge (Figure 4.2I compared to controls in Figure 4.1C).

To examine our hypothesis that RhoG trafficking contributes to the tight localization of RhoG activity at the leading edge, and to examine a potential role for RhoG in cell polarization, we tested whether the RhoG vesicles are targeted to actively protruding regions of polarized, moving HeLa cells. Examining the locations traversed by all RhoG vesicles over a 120 minute time interval clearly showed that RhoG vesicles were largely restricted to the region between the nucleus and the leading edge of moving cells (Figure 4.2J). The vesicles appeared to target areas of the cell that were actively protruding, with numerous vesicles tracking both towards and away from the leading edge. Again here, overexpression of RhoGDI-3 blocked transit of vesicles from the perinuclear region to the edge (Figure 4.2J). Together, these data indicate that inactive RhoG is dynamically trafficked to and from the membrane through the endosomal recycling pathway, targeting regions of active protrusion, and that this process is regulated by RhoGDI-3.   In the following sections, RhoGDI-3 is used as a tool to modulate the positioning and level of RhoG activity in living cells.

RhoG Regulates the Spatio-temporal Dynamics of Rac1 Activity in Protrusions:

We sought next to examine whether RhoG regulates Rac activity at the leading edge. Biochemical studies have indicated that RhoG can affect Rac1 by activating the bipartite ELMO/DOCK180 GEF complex that activates Rac1 (Katoh and Negishi 2003; Hiramoto et al. 2006; Katoh et al. 2006). We found that knockdown of RhoG using previously characterized RhoG siRNA (Figure S4.3A) (Samson et al. 2010) did indeed

reduce Rac1 activation in HeLa cells by 50%, as measured by GST-CRIB pull-down assays (Figure 4.3A) . Using our published biosensor of Rac1 activity (Kraynov et al. 2000; Machacek et al. 2009), we examined whether RhoG affects the dynamics of Rac1 activity in cell protrusions, potentially to control cell motility. RhoG knockdown affected both the level and localization of Rac1 activity. Rac1 activity at the cell edge was substantially reduced and peak Rac1 activity was shifted towards the center of the cell (Figures 4.3B-D). In control cells, peak activity was 1.8 μm from the edge, as opposed to 6.4 μm after RhoG knockdown.

We tested whether the ELMO/DOCK180 complex was involved in these effects of RhoG on Rac1. Expression of an ELMO truncation mutant (ELMOΔT625), previously shown to block this pathway (Brugnera et al. 2002; deBakker et al. 2004), reduced Rac1 activation and caused the peak activation to shift inwards. Co-transfection of wild type DOCK180 had no impact on Rac1 activity, but a catalytically inactive dominant negative form (denoted as DOCK180 DN carrying mutations in the residues 1487–1489, Ile-Ser-Pro→Ala-Ala-Ala) (Brugnera et al. 2002) also reduced Rac1 activity and shifted its peak away from the edge. This was quantitatively substantiated with linescan analysis and measurements of peak activation (Figures 4.3D, 4.3E, S4.3B and S4.3C). We also asked whether the RhoGDI-3 regulation of RhoG elucidated in the previous section could impact Rac1 at the cell edge. Consistent with the above results, knockdown of RhoGDI-3 increased Rac1 activation, shifting it closer to the cell edge (Figures 4.3D, 4.3E, and S4.3D). Overexpression of RhoGDI-3 reduced Rac1 activity (Figure 4.3F). Together these results demonstrate that RhoG regulates both the position and level of Rac1 activity in cell protrusions, that these effects are mediated by the

bipartite DOCK180/ELMO GEF complex, and that this pathway is subject to RhoGDI-3 regulation of RhoG.

RhoG Regulates Adhesion and Actin Dynamics at the Leading Edge:

We could now both activate and inactivate RhoG via RhoGDI-3 or RhoG knockdown, enabling us to more precisely define the role of RhoG in regulating Rac and various components of the motile machinery. Because Rac1 activation in cell protrusions is known to be controlled by numerous interactions at adhesion complexes (Ridley et al. 1992; del Pozo et al. 2004; ten Klooster et al. 2006; Chang et al. 2007) we first examined whether RhoG was affecting Rac1 localization at adhesions, or adhesion dynamics. Time lapse imaging of CyPet-Rac1 together with mCherry-Paxillin showed accumulation of Rac1 at leading edge adhesion complexes. This accumulation was strongly reduced by RhoG knockdown, expression of RhoGDI-3, or expression of the ELMOΔT625 construct (Figures 4.4A and 4.4B), indicating that the signaling pathway elucidated above controls Rac1-adhesion interactions. These effects correlated with changes in Rac1 activity seen by TIRF FRET that match those illustrated in Figure 4.3 (Figure S4.4A and S4.4B). We observed that DOCK180 was also localized at adhesions, while RhoG and ELMO were diffusely localized. These localization patterns were not affected by the molecular manipulations that disrupted Rac adhesion localization.
(Figures S4.4C-E).

RhoG signaling affected not only accumulation of Rac1 at adhesions, but also the adhesions themselves. Analysis of GFP-Paxillin within 6 μm of the edge of extending protrusions showed that RhoG knockdown, and overexpression of the ELMOΔT625

192

truncation mutant and RhoGDI-3 overexpression all affected adhesion size and number (Figures 4.4F-H). The number of adhesions was decreased by RhoG knockdown, dominant negative RhoG (T17N), RhoGDI-3 or ELMOΔT625, while a constitutively active RhoG (Q61L) increased adhesion number. The average adhesion area was also sensitive to RhoG, increased by RhoG knockdown and decreased by RhoGDI-3 knockdown, as revealed by automated image analysis. It is clear that RhoG affects the dynamics of adhesions, and this data supports involvement of the RhoG to ELMO/DOCK180 pathway discussed above. Interestingly, the increased adhesion size produced by RhoG knockdown resembles effects of increased RhoA or Rho kinase activity on adhesion size. We hypothesized that RhoG knockdown might affect RhoA activation in these cells, but GST-RBD pull-down assay showed no effect on RhoA activation (Figure S4.4F).

We also tested for effects of RhoG on protrusion/retraction dynamics. Kymograph analysis showed that control HeLa cells showed regular constitutive cycles of protrusion and retraction. Activation of RhoG through knockdown of RhoGDI-3 increased the rate of these cycles, while RhoG knockdown decreased the rate and led to more erratic timing (Figures 4.5A and 4.5B). Consistent with the data presented in Figure 1D, RhoG knockdown decreased protrusion velocity and overactivation of RhoG via RhoGDI-3 knockdown increased protrusion velocity (Figure 4.5C). Surprisingly, perturbation of RhoG activity also led to alterations in retraction velocity, possibly due to de-coupling of Rac1-RhoA feedback signaling at the leading edge (Figure S4.5). Despite changes in velocity, the average protrusion length was relatively unaffected (control = 3.44 microns per protrusion, RhoG knockdown = 2.98, RhoGDI-3 knockdown = 2.98, none

significant) (Figure 4.5D). To more directly assess actin polymerization atlamellipodial protrusions, we performed an actin filament barbed end assay to determine the distribution of polymerization-competent actin. RhoG knockdown significantly shifted the peak barbed end density away from the cell edge (Figures 4.5E and 4.5F).

Collectively, these data show that the differences in Rac1 activity and function observed upon manipulation of RhoG signaling translate to alterations in adhesion and lamellipodial dynamics. Further, we show effects on the initiation of protrusion and the timing of protrusion/retraction cycles, rather than the distance traveled by each protrusion, which may be governed by a different mechanism.

RhoG Plays a Role in Protrusion Formation and Determining the Frequency and Direction of Cell Turning:

Our finding that RhoG is selectively targeted to the leading edge via vesicle trafficking suggested that it may play an important role in determining the direction of cell movement. We set out to test this hypothesis by studying the movement tracks of HeLa cells traveling on fibronectin. To quantify the movement of these cells we computed the average cell speed and persistence of movement. We defined cell speed as the magnitude of distance, |d|, traveled by the cell centroid between successive time frames divided by the time interval, Δt, and persistence as the cosine of the difference, $\Delta\theta$, between the direction of movement of centroid between successive time frames. We found extraordinarily strong effects of both RhoG knockdown and of RhoGDI-3 knockdown on both velocity and persistence (Figures 4.6A and 4.6B). The effects on velocity were consistent with the effects of RhoG on Rac1, as multiple lines of evidence have previously shown that velocity is reduced when Rac1 is either inhibited or

194

overstimulated (Pankov et al. 2005; Petrie et al. 2009). The effects on persistence were, however, unexpected and showed that persistence increased when RhoG activity was increased or inhibited.

To further characterize the role of RhoG on cell movement we developed a mathematical model that describes the motion of the cells as a random walk with persistence. The simplest version of the model treats the distance moved by the centroid, d, and direction of movement, θ, as normally distributed random variables (Figure 4.6C). The distribution for d is characterized by its mean μ_d and variance σ_d. The distribution for θ is characterized by its variance σ_θ and is assumed to have a mean value given by the previous direction of movement. Note that as σ_θ becomes large this model becomes equivalent to two-dimensional diffusive motion and that small values of σ_θ signify highly persistent motion. We used a Monte Carlo method to estimate the three model parameters (μ_d, σ_d and σ_θ) directly from the experimentally measured cell tracks. Interestingly, our analysis revealed that a good fit between the model behavior and experimental data could not be achieved. Therefore we expanded the model to include the possibility that each cell could exist in two states. In each state the motion of the cell is again characterized by the three parameters (μ_d^i, σ_d^i and σ_θ^i), where the subscript i denotes state 1 or 2, and the final parameter α denotes the fraction of time spent in state 1. Therefore, this version of the model contains 7 free parameters. The Monte Carlo method was again used to fit the expanded model to experimental data. In this case, excellent agreement between the model behavior and experimental data for all conditions tested was observed. For the case of control cells, the model predicts the existence of a state in which the cell moves with high speed and persistent motion ('fast' state) and a

second state in which the speed and persistence of the cells are significantly reduced ('slow' state) (Figure 4.6D).

We next used the model to asses the effects of RhoG and RhoGDI-3 knockdown (Figures 4.6E and 4.6F). Despite the overall reduction in velocity, there were still two states with clearly different velocities. In contrast, the difference in persistence between the two states was abolished or greatly reduced, and all states became much more persistent. This indicated that RhoG was not necessary to generate the two states, but played an important role in generating the differences in persistence between them. Because differences in velocity remained throughout our treatments, the two states were denoted the 'fast state' and the 'slow state'.

The model enabled us to predict which specific portions of cell tracks corresponded to the fast or slow states. Using the Rac1 and RhoG biosensors we examined the distribution of Rac1 and RhoG activity in the two states, and determined the effects of RhoG and RhoGDI-3 knockdown on the distributions (Figures 4.6H and 4.6I). In the fast state of control cells, Rac1 activation localized to a single, defined leading edge, as would be expected for persistently moving cells. In contrast, control cells in the slow state showed multiple spots of Rac1 activation distributed around the cell periphery. Movies showed these states to be associated with protrusive activity extending from all sides of the cells. RhoG distributions (Figure 4.6I) paralleled those of Rac1, but RhoG activation was seen along the edge of the cell.

We asked whether RhoG was playing a role in generating the multiple foci of Rac1 by counting the foci in individual cells and examining effects of RhoG and RhoGDI-3 knockdown. Foci were defined as spots where activity at the cell edge was at

least 1.5x greater than that in the perinuclear region. Control cells in the fast state averaged one spot of Rac1 activity per cell, while in the fast state they averaged 2-3 spots. RhoG knockdown cells showed a significant reduction in Rac1 activity at the edge (consistent with Figure 4.3) and reduced polarity (Figure 4.6J) but retained a single focus of Rac1 activity in the fast state. In the slow state, these cells showed reduced Rac1 activity distributed all around their perimeters, without clear foci of activity. In contrast, when RhoGDI-3 was knocked down, Rac1 activity was increased in both states (consistent with Figure 4.3), decreased in polarity (Figure 4.6J) and the number of foci in both states increased. All this data is consistent with RhoG playing an important role in generating multiple foci of Rac1-mediated protrusion.

It was surprising that the increased number of foci in the fast state of RhoGDI-3 knockdown cells was associated with increased persistence. We hypothesize that the cell's ability to turn depends on responding to the changes at the cell edge revealed in our studies of foci of Rac activation, perhaps by picking a new leading edge there. In the RhoGDI-3 knockdown case, foci are generated over a much higher background of activated RhoG and Rac1, as demonstrated by quantitative analysis of activity distributions (Figure 4.6K). This could inhibit the cell's ability to discriminate new regions of polarization.

Finally, we examined whether the ability of RhoG to produce multiple foci of Rac1 activity played a role in three dimensional migration. HeLa cells were embedded within a matrigel plug and allowed to migrate for 18-24 hours before imaging on a two photon laser scanning confocal microscope. As described in previous studies, wild type cells moved by extending several rounded pseudopods in multiple directions (Sahai and

Marshall 2003; Sanz-Moreno et al. 2008).   Consistent with the results above, depletion

of RhoG activity through RhoG knockdown redued the number of these pseudopods, and

overactivation of RhoG through RhoGDI-3 knockdown substantially increased the

number of pseudopods (Figures 4.6L and 4.6M).

4.4 Discussion and Ongoing Studies

RhoG is Activated at the Leading Edge during Protrusion:

In this paper we demonstrate the construction and validation of a novel FRET-based biosensor for RhoG activity that sensitively detects RhoG activation in living cells. A previous sensor for RhoG exists (Mohammadi and Isberg 2009), but was only used to assess host-pathogen signaling at the dorsal surface of cells. Our new sensitive sensor reveals that RhoG is activated coincident with cellular protrusion, as had been previously reported for RhoA, but contrasting with the measures previously reported for Rac1 (Machacek et al. 2009). This was unexpected, given that the similarity of RhoG to Rac1 has led many to propose that RhoG and Rac1 have redundant and overlapping functions in the cell. Thus it appears that RhoG activation is temporally separable from Rac1 activation. There is evidence that RhoG can signal both independently of Rac1, and in parallel (Wennerberg et al. 2002; Katoh and Negishi 2003; Ellerbroek et al. 2004). Thus, it is conceivable that the activation of RhoG prior to Rac1 accomplishes two goals: 1) to prime the locations of Rac1 activity, perhaps by initiating actin polymerization, and then 2) to activate Rac1 through the ELMO/DOCK180 complex, whereby Rac1 continues to polymerize actin during lamellipodial protrusion, and where Rac1 can also contribute to the turnover of focal adhesions at the leading edge.

While the role of RhoG has clearly been delineated in engulfment behaviors where it activates Rac1 through ELMO/DOCK180, its role has been difficult to discern in cell migratory behaviors. Early studies of RhoG indicated that it could signal both in tandem and in parallel with both Rac1 and Cdc42. Most subsequent studies have focused predominantly on its activation of Rac1, and no mechanism has yet been elucidated for

199

its ability to activate Cdc42. How RhoG is regulated has also remained unclear. For example, the molecule(s) that activate RhoG are largely unknown. As was reported recently, RhoG can also be held in its inactive form on the scaffolding protein synectin at the leading edge (Elfenbein et al. 2009), but the GEF(s) responsible for activating RhoG in this system was not identified. We do know that upon EGF stimulation the GEFs Vav2/3 are capable of activating RhoG (Samson et al. 2010). With the recent discovery of a protein complex found in vesicles consisting of the sorting nexins (SNX 1 and 2), Trio, and RhoG (Prosser et al. 2010), it is tempting to speculate that Trio may be the GEF that is responsible for activating RhoG upon release from vesicles. Indeed, we have evidence that Trio regulates a large percentage of RhoG activation in the cell systems described in this study (unpublished data). Further, given the results in this paper identifying RhoG activity as being closely correlated with protrusional velocity, its similarity to RhoA in these same measurements (Machacek et al. 2009), and the presence of GEF domains in Trio that activate both RhoG/Rac1 and RhoA (Debant et al. 1996), Trio could conceivably coordinate the activation of both GTPases in response to environmental cues.

RhoG Activity is Regulated by Trafficking and RhoGDI-3:

We also demonstrate that RhoG localization and activity are dependent on endocytic recycling as regulated by RhoGDI-3, as shown in the model in Figure 7. RhoG has been shown to associate with protein components involved in cellular trafficking, including microtubules via kinectin, caveolin-1 and clathrin (Prieto-Sanchez et al. 2006; Samson et al. 2010), and with GDI-3 (Brunet et al. 2002) which has a vesicular

localization pattern. However, the importance of these subcellular localization patterns had not been elucidated. Here, we present evidence that RhoG is actively trafficked to and from the leading edge in vesicular structures, and that this pathway regulates its membrane targeting and presence at the leading edge of migrating cells. However, several questions remain about this RhoG/Rac1 signaling axis. First, how does the cell regulate the recycling of RhoG: does this occur through regulation of RhoGDI-3 itself, or through some other mechanism that targets RhoG to the plasma membrane, and RhoGDI-3 only serves to prevent the activation of RhoG? Much still remains to be discerned about the regulation of RhoGDI-3 and its precise cellular function.

RhoG Activity Coordinates the Local Activation of Lamellipodial Rac1:

We also define that RhoG regulates the recruitment and activation of lamellipodial Rac1, leading to changes in focal adhesion dynamics, actin rearrangement, and productive polarized cell migration in the system tested herein. This is largely due to the ability of active RhoG at the leading edge to recruit Rac1 through ELMO/DOCK180 and orchestrate its local activation. Dysregulation of RhoG and its trafficking results in either indiscriminate activation of Rac1, or loss of activation of Rac1 in the lamellipodium. Thus, RhoG represents an upstream signaling molecule that serves as a local coordinator of Rac1 activation, both preventing indiscriminate activation of Rac1, and priming Rac1 for appropriate localized activation. Given the rapid recycling of RhoG, this provides a mechanism by which the cell can rapidly shuttle an activating factor to the appropriate site along the leading edge to activate a downstream molecule, in this case Rac1, and thus initiate cellular behaviors.

201

Many questions remain, however, about how these molecules are regulated in the lamellipodium. For example, what are the cues that terminate both RhoG and Rac1 signaling? Traditionally, GAPs and GDIs have been identified as major inactivators of the GTPases, so these are certainly possibilities in this signaling pathway. Also, since RhoG and Rac1 have both been shown to be endocytosed (Prieto-Sanchez et al. 2006; Palamidessi et al. 2008; Samson et al. 2010), and since endocytosis is a commonly used strategy to terminate or alter intracellular signaling, perhaps endocytosis of the GTPases themselves from the membrane leads to association with proteins that terminate their signaling, or sequestration away from GEFs preventing their activation.

Such signaling pathways are highly conserved throughout evolution: RhoG signal transduction, and endocytic recycling for the coordination of cell signaling. Rac1 appears to be at the confluence of these mechanisms which precisely position and regulate its localized activation, and thus Rac1's ability to orchestrate the actin dynamics required for lamellipodial protrusion and productive cell migration.

RhoG Regulates the Ability of Cells to Turn during Random Migration:

The role of RhoG in cell migration has been difficult to discern, in large part due to its ability to directly activate Rac1, its closest homolog. Divergent results have been obtained, with some work suggesting RhoG is dispensable for cell spreading (Meller et al. 2008), others suggesting it is important for cell migration in a wound-healing assay (Katoh et al. 2006), and other studies demonstrating that downstream targets of RhoG are present at the leading edge of cells (Ho et al. 2009). A RhoG knockout mouse was even generated (Vigorito et al. 2004), which was viable and showed few, if any, defects.

However, it is clear that RhoG does indeed respond to growth factors such as EGF and FGF2 (Elfenbein et al. 2009; Samson et al. 2010), but these growth factors are often applied at concentrations that also activate Rac1 independently of RhoG, hindering an analysis of RhoG function in such a chemotactic system.

We demonstrate that RhoG signaling is important for cell migration, since dysregulation of RhoG alters migratory behaviors in a random migration assay due to the altered activation patterns of Rac1. By using random, non-stimulated motility in this study, we believe that we have overcome prior difficulties in assessing the independent role of RhoG in migration. In such an assay, the cell responds to cues in a shallow gradient, and thus is continually changing directions as new "dominant" cues or cell-intrinsic mechanisms drive the motility of the cell in a new direction. The precise defects we observe with perturbation of RhoG activity are a decrease in velocity, consistent with previous studies (Monypenny et al. 2009), and an increase in persistence. The decrease in velocity is not unexpected, as most of the GTPases, when perturbed, lead to reductions in cellular velocity, but are still capable of motility. Indeed, even in cells where Rac1 has been genetically ablated, the cells are still motile and respond to growth factors such as PDGF (Vidali et al. 2006). However, the alterations in persistence are quite striking and are present in both the low and high activity states of RhoG, indicating that proper regulation of RhoG signaling is required for the ability of cells to turn in a random migration assay. We find that this ability to turn is dependent on the cell's ability to generate a distinguishable high activity "focus" of Rac1 activity. With loss of RhoG, cells have difficulty in initiating new sites of Rac1 activation and thus there are fewer foci with which to turn. Curiously, even though Rac1 is increasingly activated in the

high RhoG activity condition, the cell is prevented from distinguishing these high activity foci due to the high baseline activity. Thus, in both cases, cells remain persistent, albeit slower.

Small GTPase Signaling in the Regulation of Directed Cell Migration:

We have described a signaling pathway that uses a number of mechanisms to properly orchestrate the amount, timing, and positioning of Rac1 activation to guide cell migration. This study also clarifies the role of RhoG in cell migration, which has previously been difficult to elucidate (Katoh et al. 2006; Meller et al. 2008), using complementary biochemical and live-cell imaging techniques. It also elucidates the role of RhoGDI-3 in regulating RhoG, and its importance for the regulation of Rac1 activity, demonstrating the complex mechanisms by which cells define the spatial and temporal parameters of GTPase activities to permit coordination of productive cell migration. The mechanisms reported here resemble in some ways previous work (Palamidessi et al. 2008) examining the endocytic recycling of Rac1 and its activation on endosomes by Tiam-1 in that the activity of Rac1 is controlled by endocytic recycling. However, there are significant differences in that the subpopulation of lamellipodial Rac1 here does not appear to be "pre-activated" before delivery to the edge, but rather is recruited and activated by RhoG-dependent signaling for the regulation of cell migration. Similarly, RhoG remains inactive in vesicles as well until delivered to the edge for activation, and simply happens to use the endocytic machinery to target specific regions of the cell to regulate Rac1. In this study, and in previous studies (Hasegawa et al. 1996; Kiyokawa and Matsuda 2009; Tachibana et al. 2009), it has been shown that DOCK180 localizes to

focal adhesions independent of RhoG, and is known to activate Rac1 there via a number

of signaling pathways (Cote and Vuori 2007). Since we show that RhoG regulates the

recruitment of Rac1 to focal adhesions, the question emerges whether RhoG signaling

and integrin function converge on these high-affinity Rac1 binding sites to localize and

anchor Rac1 to the leading edge for the promotion of lamellipodial protrusion (del Pozo

et al. 2004; Del Pozo and Schwartz 2007). Integrins have been shown to be critical for

lamellipodial protrusion, and indeed redistribution of these integrins to the leading edge

can even promote protrusion. Curiously, these integrins often prevent the internalization

of caveolin-rich lipid rafts, which are sites of high affinity for Rac1 (Del Pozo and

Schwartz 2007), and these are also sites where focal adhesions form (ten Klooster et al.

2006; Nethe et al. 2010). Since RhoG is also known to associate with caveolin-positive

vesicles and traffic along microtubules, focal adhesions and the nearby membrane at the

leading edge may be the target for endosomally recycled RhoG. The common thread is

that these strategies are used by the cell to define the spatial and temporal constraints on

Rac1 activity required for appropriate function.

Spatiotemporal Coordination of Signaling in Physiological Migration:

Lastly, since we show that RhoG has significant impacts on the migratory

behaviors of cells in both 2- and 3-dimensional matrices, this has implications for cellular

behaviors *in vivo*. Given that RhoG is known to promote both lamellipodium and dorsal

wave formation (Ellerbroek et al. 2004; van Buul et al. 2007a), and that both actin-rich

structures have been proposed to be important for 3-dimensional motility (Buccione et al.

2004; Gu et al. 2011), it would be reasonable to expect RhoG to have more profound

effects in 3-dimensional matrices as we have shown. Thus one might expect RhoG to influence physiological migration behaviors, such as cell migration during development, or cancer cell metastasis. Indeed, in parallel to studies that show that RhoA levels decrease and RhoC levels increase in highly aggressive metastatic breast cancers and that this was associated with decreased patient survival (Clark et al. 2000), a study showed that RhoG and RhoGDI-3 protein levels were increased and decreased, respectively, in tandem, also associated with decreased patient survival (Jiang et al. 2003). As we have shown in this study, such a molecular change would serve to alter the spatial and temporal constraints on signaling by increasing and broadening the activation of RhoG, and consequently increasing and broadening Rac1 activity. *In vivo*, this would likely translate to increased protrusion formation and potentially increased cell migration. Further, one of the scaffolds known to regulate RhoG signaling, synectin, is highly expressed in a number of malignancies and promotes tumor growth (Lee et al. 2009; Muders et al. 2009; Choi et al. 2010; Wang et al. 2010). Thus, our findings suggest that RhoG may be a key regulatory node for the precise regulation of Rac1 localization and activity. Further, since RhoG only regulates a subpopulation of Rac1 and manipulation of RhoG does not appear to directly interfere with the behavior or expression levels of any of the other major GTPases, RhoG and its regulators could be potential targets of pharmacological intervention to control migration-related disease processes, such as in cancer or inflammation. Such a strategy could have potentially fewer side effects than inhibiting the major GTPases themselves. Understanding these signaling processes, particularly those upstream of this RhoG/Rac1 signaling axis, will be important in further

understanding how cells properly orchestrate cellular signaling to permit normal function
and behavior.

4.5 Materials and Methods

Expression Constructs and Antibodies:

Expression constructs: To generate CyPet-RhoG, the full-length cDNA for RhoG was amplified by PCR using the primers: and subcloned into the pCyPet vector previously described via BamHI and EcoRI restriction sites. The Q61L and T17N point mutants in RhoG were generated by site-directed mutagenesis. To generate mCherry-RhoG, the full-length cDNA for mCherry was amplified by PCR and subcloned into the pTriEx-4-6x-His vector via BamHI and EcoRI restriction sites (creating pTriEx-mCherry-C1), followed by subcloning of full-length RhoG cDNA into EcoRI and XhoI restriction sites with a GSGS linker between mCherry and RhoG. An identical strategy was used to generate mCherry-Rac1. The GST-ELMO1, GST-PBD, CyPet-Rac1, Rac1 biosensor, RhoA.SC biosensor, Vav2, Tim, Tiam-1, p50RhoGAP, Rap1GAP, GDI-1 (Pertz et al. 2006) and mCherry-PLEKHG6 constructs (Samson et al. 2010) have all been described previously. Full-length cDNA for RhoGDI-3 was acquired from Open Biosystems. To generate RhoGDI-3-mCherry, the full-length cDNA for mCherry was amplified by PCR and subcloned into the pTriEx-4-6x-His vector via NotI and XhoI restriction sites (creating pTriEx-mCherry-N1), with subsequent amplification and subcloning of full-length RhoGDI-3 into NcoI and HindIII restriction sites, Full-length cDNAs for DOCK180 and DOCK180 dominant negative (ISP to AAA mutant) were generous gifts from the Ravichandran laboratory (University of Virginia), and were amplified by PCR, with subcloning into the pTriEx-mCherry-C1 vector described above via NotI and XhoI restriction sites. To generate mCherry-ELMO1, full-length ELMO1 was amplified by PCR and subcloned into the pTriEx-mCherry-C1 vector described

above via NotI and XhoI restriction sites. To generate mCherry-ELMO1ΔT625, a stop

codon was generated after amino acid 625 in the mCherry-ELMO1 construct by site-

directed mutagenesis. EGFP-Paxillin, mCherry-Paxillin, EGFP-Vinculin, and mCherry-

Vinculin were gifts from the Burridge laboratory. The constructs for EGFP-Rab4, EGFP-

Rab5, EGFP-Rab7, EGFP-Rab11 were generous gifts from the Ehlers laboratory (Duke

University). To generate the mCherry-Rab4, mCherry-Rab5, mCherry-Rab7, and

mCherry-Rab11 constructs, the full-length cDNA from each Rab was amplified by PCR

and cloned into the pTriEx-mCherry-C1 vector above via NotI and XhoI restriction sites.

For western blotting, the anti-RhoG antibody was acquired from Millipore (mouse

monoclonal antibody, clone 1F3B3E5), the anti-Rac1 antibody was acquired from BD

Transduction Laboratories (mouse monoclonal antibody, #610651), the anti-ELMO1 was

acquired from abcam (goat polyclonal antibody, #ab2239), and the anti-synectin antibody

was acquired from Santa Cruz Biotechnology (goat polyclonal antibody, #sc-9648).

Cell Culture and Transient Transfections:

Cos-7, HeLa, and Mouse Embryonic Fibroblast (MEF) cells were maintained in

Dulbecco's modified Eagle's Medium (DMEM) (Cellgro) supplemented with 10% fetal

bovine serum (FBS) (HyClone), 100 U/mL penicillin and 100 μg/mL streptomycin

(Cellgro) and 2 mM L-glutamine (Invitrogen) at 37 °C and 5% CO_2. All cDNA

constructs were transfected into cells using FuGene6 (Roche) according to the

manufacturer's instructions. siRNA was transfected into HeLa cells using the TransIt

siRNA transfection reagent (Mirus) according to the manufacturer's instructions. Briefly,

1.5 ml serum-free media was mixed with 18 μl siQuest reagent and 11.25 μl of a 20 μM

siRNA stock solution. After 20 min incubation at room temperature the complexes were added to a 10 cm tissue culture dish (cell confluency ~ 50%) with 7.5 ml fresh media containing serum. After 24 hours, the cells were re-transfected by the same method. 48 h after the first transfection the cells were split 1:3 and used for experiments between 72 to 96 h post transfection where knock-down efficiency was found to be maximal.

siRNA Sequences:

Target sequences were as follows: RhoG anti-sense: GCAACAGGAUGGUGUCAAGUU, sense: CUUGACACCAUCCUGUUGCUU; RhoGDI-3 anti-sense: UCUGUAAUCAACACCUUCCdTdT,, sense: GGAAGGUGUUGAUUACAGAdTdT. The control siRNA (anti-sense: UCACUCGUGCCGCAUUUCCdTdT, sense: GAAAUGCGGCACGAGUGAdTdT) has been used previously (Cai et al. 2007).

RT-PCR:

To test effective knock-down of GDI-3 we performed RT-PCR. Total RNA was isolated from transfected HeLa cells using Trizol reagent (Invitrogen). For reverse transcription 'iScript cDNA Synthesis Kit' (Biorad) was used according to the manufacture's protocol. For semi-quantitative RT-PCR, an aliquot of the RT-reaction was amplified using Taq polymerase. Primers: GDI-3: fwd: 5'-ATGCTGGGCCTGGACGCGTGCGAGCTG-3'; rev: 5'-TCAGGGGAGACACGGACTGGG-3', β2-microgobulin: fwd: 5'-CTCGCGCTACTCTCTCTTTCTGG-3'; rev : 5'-

GCTTACATCTCTCAATCCCACTTAA-3'. PCR conditions: 28 cycles: 15 sec 94 °C, 30 sec 55° C, 60 sec 72° C.

Biochemical Measurement of RhoG and Rac1 Activity:

To measure endogenous levels of GTP-loaded RhoG and Rac1, we used pull-down assays as previously described. Briefly, cells were washed twice with ice cold TBS (50 mM Tris, pH 7.4, 5 mM MgCl2, 150 mM NaCl) and then lysed in lysis buffer (50 mM Tris, pH 7.4, 10 mM MgCl2, 150 mM NaCl, 1% Triton X-100, 1 mM PMSF, and 10 μg/ml each of aprotinin and leupeptin). After clearing the lysates by centrifugation at 14,000 g for 5 min, protein concentrations of the supernatants were determined and equal amounts of total protein were used to measure RhoG.GTP and Rac1.GTP. The supernatants were rotated for 30 min with glutathione-sepharose beads (GE Healthcare) which were loaded with 60–90 μg of either GST-ELMO (GST fusion protein containing the full-length RhoG effector ELMO) or GST-PBD (GST fusion protein containing the Pak1-binding domain). Subsequently the beads were washed four times in lysis buffer. Pull-downs and lysates were then immunoblotted for RhoG or Rac1, respectively.

Actin Barbed End Assay:

The density of free F-actin barbed ends was measured as previously described (Bryce et al. 2005), but with slight modifications: HeLa cells were plated at subconfluent density on fibronection (10 ug/ml) coated cover slips in DMEM / 2% FBS. After 4 hours, the cells were briefly washed with prewarmed PBS. Barbed end labeling was done for 180 seconds in Permeabilization Buffer: 20 mM HEPES, 138 mM KCl, 4 mM $MgCl_2$, 3

mM EGTA, 0.2 mg/ml saponin, 1 % BSA, 1 mM ATP, 3 µM phalloidin, 0.4 µM Rhodamine-Actin (Cytoskeleton). Subsequently the cells were quickly washed with PBS and then fixed for 10 min in 4% paraformaldehyde in Krebs Buffer (20 mM HEPES pH 7.4, 145 mM NaCl, 5 mM KCl, 1.2 mM $CaCl_2$, 1.3 mM $MgCl_2$, 1.2 mM NaH_2PO_4, 10 mM glucose, 0.4 M sucrose). Epifluorescence images of randomly chosen isolated cells were taken. Binary image masks were generated from median filtered images (20x20 matrix) and applied on the original image. Line scans (line width 20 pixels, perpendicular to the cell edge) were placed at randomly selected positions which appeared to be actively protruding cell areas at the moment of cell fixation. Counted from the cell edge, the distance of the point with maximum fluorescence value on this line scan was determined within a distance range of 8 µm from the cell edge.

Rho GTPase Activity Biosensors:

The RhoA and Rac1 biosensors were used as originally described and validated (Pertz et al. 2006; Machacek et al. 2009). The RhoG biosensor consists of two plasmids: for the first plasmid, the fluorescent protein YPet (Nguyen and Daugherty 2005) was fused to the C-terminus of amino acids 1-95 of full-length ELMO1 with an intervening linker coding for the amino acid sequence: SGLRSELGS, while for the second plasmid, CyPet (Nguyen and Daugherty 2005) was fused with the N-terminus of full-length RhoG with an intervening linker coding for the amino acid sequence: SGLRSELGS, leaving the C-terminus free for appropriate lipid modification and interaction with guanine dissociation inhibitors (GDIs).

For TIRF imaging, cells were plated on fibronectin-coated coverslips (10 mg/l fibronectin) 4 h before imaging, then transferred to Ham's F12-K imaging medium (described above) supplemented with 2% FBS and 15 mM HEPES. Live cell imaging was performed in a closed heated chamber (20/20 Bionomic Controller) using an Olympus IX-81 microscope equipped with an objective-based total internal reflection fluorescence (TIRF) system and a PlanApo N 60× TIRFM objective (NA 1.45). All images were collected using a Photometrics CoolSnap ES^2 CCD camera controlled by Metamorph software. The 440 nm line from a Kimmon IK Series HeCd laser, the 468 nm and 568 nm lines from an omnichrome series 43 Ar/Kr laser, and the 594 nm line from a Cobolt Mambo laser were used for TIRF imaging. Epifluorescence images were taken using a 100 W Hg arc lamp light source. Cells expressing the various fluorescent constructs used throughout the paper were selected using epifluorescence imaging. Time-lapse movies were taken at anywhere from 20 second to 1 minute time intervals as noted elsewhere. TIRF image analysis was performed using Metamorph software. TIRF FRET image analysis was performed as described below for FRET acquisition and FRET Ratiometric image analysis.

Live Cell Imaging for FRET Acquisition and FRET Ratiometric Corrections:

For live cell imaging, cells were plated on fibronectin-coated coverslips (10 mg/l fibronectin) 4 h before imaging, then transferred to Ham's F12-K imaging medium (described above) supplemented with 2% FBS and 15 mM HEPES. Live cell imaging was performed in a closed heated chamber (20/20 Bionomic Controller). Biosensors

were imaged as previously described (Pertz et al. 2006; Machacek et al. 2009). Briefly,

cells observed by widefield microscopy for cross-correlation analysis and the analysis of

Rac1 activity were filmed at 10-20 second intervals using a 40X/1.3 NA objective and

2X2 binning, a CCD camera (CoolsnapES^2; Photometrics), and MetaMorph software

(Universal Imaging). Cells observed by TIRF microscopy for FRET were filmed at 30

second intervals using a 60X/1.45 NA objective and 2X2 binning, a CCD camera

(CoolsnapES^2; Photometrics), and MetaMorph software (Universal Imaging). For

emission ratio imaging by widefield microscopy, the following filter sets were used

(Chroma Technology Corp.): CFP: D436/20, D470/40; FRET: D436/20, ET535/30; YFP:

D500/20, ET535/30. mCherry was imaged using an D580/30, HQ630/40 filter where

indicated, and EGFP was imaged using D470/40, HQ525/50 where indicated. Cells were

illuminated with a 100 W Hg arc lamp through an ND 1.0 neutral density filter. For

emission ratio imaging by TIRF, the same filtersets were used as above, but instead of

illumination with a Hg lamp, the 440 nm line from a Kimmon IK Series HeCd laser, the

468 nm and 568 nm lines from an omnichrome series 43 Ar/Kr laser, and the 594 nm line

from a Cobolt Mambo solid-state laser were used.   Dichroic mirrors were custom-

manufactured by Chroma for compatibility with all of these filters. At each time point,

three images were typically recorded with the following exposure times for ratio imaging:

CFP (1.2 s), FRET (1.2 s), and YFP (0.4 s). These exposure times were more variable for

TIRF but typically reflected the same ratio of times. Raw images were sub-pixel aligned

and background subtracted to allow ratiometric correction of volume effects and variation

in sensor concentration. Ratio calculations to generate activity images were performed

following bleedthrough and photobleaching correction methods described previously

(Hodgson 2009), since each component of the dual-chain biosensor is not distributed equally throughout the cell. For bleedthrough correction, cells expressing the CFP fluorophore or YFP fluorophore alone were imaged using the same imaging medium, exposure times, and intensities as those for the actual experiment. These measurements were used to determine the amount of bleedthrough of each fluorescent protein's direct emission into the FRET channel. Images from each channel were shade corrected and background subtracted. Plotting FRET intensity as the dependent variable versus CFP or YFP intensity as the independent variable yielded a linear relationship where the slope of the line defined the bleedthrough coefficient for that fluorescent protein and condition. Using these parameters, the ratio was derived using equation (1):

$$FRET\ Ratio = \frac{FRET - \alpha \cdot CyPet - \beta \cdot YPet}{CyPet} \qquad (1)$$

This equation corrects the raw FRET signal for bleedthrough from both CFP and YFP into the FRET channel, with subsequent calculation of the ratio. For visual representations, a linear pseudocolor look-up table was applied to all ratio images and the ratio values were normalized to the lower scale value, which was chosen to exclude the bottom 5% of the total histogram distribution, thereby avoiding spurious low intensity pixels. In each experiment, all images were carefully inspected to verify that all portions used to create the ratio image had a sufficiently high signal to noise ratio. We targeted at least 400 gray level values (12-bit dynamic range) above background in the lowest intensity regions within the cell (S/N > 4). This was especially important in thin parts of the cell where fluorescence was low.

Dual-Camera FRET Imaging:

Dual-camera FRET imaging of vesicles was performed to minimize between-acquisition movement of vesicles and improperly aligned resultant images. Experimental design followed the protocols above for live-cell imaging, except for the filtersets used and order of image acquisition. For these experiments, an Olympus IX-81 body was outfitted with a side-port dual-camera splitter (Photometrics DC$_2$) with an HQ470/24 emission filter placed before one CoolSnap ES^2 camera and a long-pass 505 nm emission filter placed before the second CoolSnap ES^2 camera. With excitation from a 100 W Hg arc lamp through an HQ436/20 excitation filter, CFP and FRET emission can be acquired simultaneously. Subsequent YFP emission is acquired using excitation through a D500/20 excitation filter and emission through the long-pass 505 nm emission filter. A custom dichroic (Chroma) was manufactured for compatibility with each fluorophore. Image acquisition considerations and processing was performed as described above.

Whole-Cell FRET Analysis:

To calculate whole-cell average FRET ratio, photobleach-corrected FRET ratio (FRET/CFP) time-lapse image stacks acquired and processed as described above were loaded into Metamorph, thresholded to generate masks for each cell, and regions were drawn around each cell using the mask. From these regions, a number of parameters, including average pixel intensity, could be measured and recorded. Average FRET ratio was calculated for three separate time points, averaged, and recorded for each cell.

HeLa cells treated as described were sparsely plated on fibronectin-coated coverslips in growth medium (DMEM (Mediatech) supplemented with 10% FBS (HyClone)) and allowed to attach for 6 hours. 10× phase time-lapse movies were recorded for 18 h with frames taken every 5 minutes on an Olympus IX-81 inverted microscope. In each experiment 20-25 fields (containing 10-15 cells per field) were simultaneously recorded using an automated stage. For the analysis, every cell in each movie that met the tracking criteria (was completely within the field of view for the entire experiment, did not divide, and did not touch another cell for more than three frames) was tracked using the Track Objects plug-in for Metamorph. Data were exported into Microsoft Excel for analysis. The velocity was calculated as an average of distance traveled between each time point (μm)/time between each time point (h) for each time segment. The persistence of migration was calculated as an average net angular displacement from origin (radians) relative to an assumption of no net angular displacement from origin for each time segment.

For kymography, 60X DIC time-lapse movies that contained 120 images were captured at 30 s or 1 minute intervals on an Olympus IX-81 inverted microscope and processed using Metamorph for each individual cell. Kymographs were generated from 3-5 protrusive areas of at least 12 cells per experimental group and lamellipodial parameters were calculated as follows: a line was traced along the cell border for each kymograph and the x-y coordinates along the line over time were extracted and recorded. From these x-y coordinates, positive net x displacement with increasing y values was defined as a protrusion, and negative net x displacement with increasing y values was

defined as a retraction. A protrusion/retraction cycle was defined as the first positive net

x displacement to the last negative net x displacement before positive net x displacement

began again.   The number of these cycles per time length of the movie (hours)

determined the retraction/protrusion cycles per hour. Average protrusion or retraction

distance was calculated by determining the net positive or negative x displacement.

Average protrusion or retraction velocity was calculated by taking the average protrusion

or retraction distance and dividing by the time frame encompassing the protrusion or

retraction (displacement/time).

Imaging and Quantitation of Focal Adhesion Dynamics:

For time-lapse microscopy, HeLa cells were transiently transfected with EGFP- or

mCherry-Paxillin-β, or mCherry-Vinculin, and plated on fibronectin-coated glass

coverslips (Warner Instruments) in growth medium (DMEM with supplemented with

10% FBS, Pen/Strep, and L-glutamine as above) the next day. Cells were transferred to

imaging medium (Ham's F12K supplemented with 2% FBS, Pen/Strep, and L-glutamine)

and imaged using an inverted Olympus IX-81 with a 60x 1.45 NA TIRFM objective.

Cells were recorded for at least 60 minutes with frames taken every 1 min. In 12-15 cells

over three experiments, at least 15 focal adhesions that localized within 8 μm of the

leading edge per cell were analyzed with Metamorph software. Only cells with a single

nucleus were used for the analysis to avoid variations in relative area comprising the

lamellipodium, and the total number of focal adhesions, due to cell size. Number of focal

adhesions per area was measured from thresholded images of at least 15 cells using

Metamorph. To calculate adhesion size, Matlab code for automated image processing and

calculation of adhesion parameters was used (manuscript in submission). In brief, the code was designed to accept time-lapse image sequences of cells expressing a focal adhesion marker such as Paxillin-β or Vinculin. The program first creates a mask around each cell to exclude any background noise. Next, the images are high-pass filtered and thresholded to isolate individual adhesions from the background. Further, "connected" or adhesions in close proximity to one another are identified and isolated as individual adhesions. Last, each individual adhesion is sequentially numbered and outlined by a region trace. These regions are then analyzed for their properties, and in this case, particularly for the size in pixels. Pixel number is then converted to size in square microns based on the size of a single pixel for a given lens and camera as measured by a micrometer standard.

Linescan Analysis of Protrusional Rac1 Activity:

To calculate protrusional Rac1 activity, photobleach-corrected Rac1 FRET ratio time-lapse (FRET/CFP) image stacks acquired and processed as described above were loaded into Metamorph. Cells were visually inspected for cell health (defined as non-retracting, non-blebbing cells) and regions of active protrusion to identify cells for analysis. Once a protrusion was identified, the mid-protrusion frame was determined and analyzed for Rac1 activity. Briefly, a line was drawn perpendicular to the direction of protrusion at mid-protrusion. The line was then expanded to a width of 10-25 pixels (3.2 μm to 8 μm) depending on the width of the protrusion, at least sufficient to encompass the entire protrusion, and a depth of at least 15 μm to prevent bias by user placement of the linescan. The average Rac1 activity along the entire width and length of the line was

219

then recorded. By inspecting the values measured along the line, the position of peak

Rac1 activity could be determined and recorded for each cell measured. In cases where

co-transfection of an additional plasmid was needed, expression of that construct was

monitored by fluorescence in the red channel for mCherry (D580/30, HQ630/40 emission

filter as above).

Rac1 Activity "Spot" Analysis:

To calculate the number of high Rac1 activity "spots" or regions, long (~18 hours,

5 minute intervals) photobleach-corrected Rac1 FRET ratio time-lapse (FRET/CFP)

image stacks acquired and processed as described above were loaded into Metamorph.

Cells were visually inspected for cell health (defined as non-retracting, non-blebbing

cells) and regions of high activity were observed (~20% over cell center) and quantified

for cells treated with control, RhoG, and RhoGDI-3 siRNAs throughout the duration of

the movie. If two regions protruded in divergent directions, but were not separable by a

20% difference in activity between the regions, they were still separated into two regions

of high activity, but such occasions were infrequent.

RhoGTPase Activity Correlation Analysis:

Correlation analysis was performed as previously reported (Machacek et al.

2009). Briefly, corrected biosensor images were segmented and cell edge displacements

tracked as in (Machacek and Danuser 2006). Sampling windows of 0.9 mm depth and

1.8–3 mm width were constructed to follow morphological changes at a fixed distance

from the cell edge. For each window, biosensor activation time courses were recorded.

For windows placed at the cell edge, additionally, a time course of protrusion/retraction velocity was recorded. Coupling of two activity time courses was analyzed per window by Pearson's cross-correlation function. Subsequently, for a cell the per-window correlation functions between edge velocity and biosensor activation were averaged over all windows following the edge at a specific distance. Per-cell correlation functions were averaged over multiple cells and statistically analyzed by bootstrap sampling to determine the significance and time lag of the coupling between two activities. These procedures have been described previously in (Machacek and Danuser 2006; Machacek et al. 2009).

3-D Migration Assay:

To create 3-dimensional matrices, 3D gels were assembled in ¼" diameter polypropylene gas tubing cut and firmly secured to glass-bottom 35-mm dishes using epoxy resin. The tubing was punctured in several sites to allow diffusion with medium in the rest of the dish. HeLa cells transfected with mCherry, were resuspended and then mixed with 2X 3D gel master mix and added to the tubing. The gel master mix, at final concentration (1x), consisted of 0.6 mg/mL LDEV-free, growth-factor reduced, phenol-red free Matrigel (BD Biosciences), 0.6 mg/mL type I collagen (BD Biosciences), and 10 ug/mL fibronectin (Sigma) in DMEM supplemented with 10% FBS containing 300,000 cells. The 3D gel-cell mixture was allowed to solidify for 20 min at room temperature, and DMEM supplemented with 10% FBS was subsequently added to the tubing and the remainder of the dish surrounding the tube. Live cell imaging was then performed on an Olympus Fluoview FV1000MPE Multiphoton laser scanning microscope outfitted with a

zero-drift compensation (ZDC) device for active focal plane maintenance. The matrix

was kept in Ham's F12K medium supplemented with 10% FBS and 15 mM HEPEs

buffer (to create CO_2-independent medium at 37° C by means of a Prior on-stage

incubation chamber. Automated image acquisition was performed using Olympus

Fluoview software. Z-stacks were acquired for single cells at sufficient intervals to

satisfy Nyquist sampling requirements.

Cell-Tracking and Cell-Track Modeling:

Cell tracks were generated by 20x phase contrast imaging of HeLa cells plated on

fibronectin-coated coverslips, imaged in Ham's F12K medium supplemented with 2%

FBS for 18-24 hours at 5 minute intervals in a closed heated chamber. Movies were

captured of ~200 frames, 5 minutes apart. Our approach here is to extract parameters

that describe migration by fitting of a mathematical model to experimental data.

Specifically, by fitting our model to data from the experimental cell tracks we derive

parameters describing speed and persistence of migration. Furthermore, we fit standard

deviations for these values for a given time interval.

We model migration as a stochastic sequence of steps, Figure 4.6C. Since the

speed $\dot{r}$ is generated independently from the angle θ, the probability density function for

the position at t_i is

$$f(r, \theta) = g_R(r)g_\theta(\theta)$$ Equation (2)

where $g_R(r)$ is the pdf for the normal distribution $\mathcal{N}(\mu_r, \sigma_r^2 \Delta t)$ and $g_\theta(\theta)$ is the pdf for

the normal distribution $\mathcal{N}(\theta_{i-1}, \sigma_\theta^2 \Delta t)$, where θ_{i-1} is the orientation from the previous

step and $t_i = t_{i-1} + \Delta t$. Note that inherent in the model (due to the linearity of the

normal distribution) the standard deviations (of speed and persistence) scale proportional to the square root of time – so our findings are independent of the frequency of time points in the cell tracks. Although, the higher the frequency of time points the less degeneracy there will be in our model fitting. In this paper we have normalized so that $\Delta t = 1$.

To fit the model we compare the pdf to a histogram representing the cell data. In principle, we could generate histograms for θ and r by measuring these directly from the data. However, consider $r = r'$ and $\theta = \theta'$. Since it is likely that in some cases cells take a backward step while maintaining their orientation (as part of the protrusion, retraction cycle), we note this case is degenerate (in the sense of leading to the same Cartesian co-ordinates) with $r = -r'$ and $\theta = \theta' + \pi$. To take account of this degeneracy we analyze our model in Cartesian co-ordinates.

This histogram is generated from the cell tracks as follows. For all pairs of steps in a cell track, defined by $\{(x_{i-1}, y_{i-1}), (x_i, y_i), (x_{i+1}, y_{i+1})\}$, we rotate the pair as a rigid body about (x_{i-1}, y_{i-1}) by $\tan^{-1}\dfrac{y_i - y_{i-1}}{x_i - x_{i-1}}$ then analyze the step $(x'_{i+1} - x'_i, y'_{i+1} - y'_i)$. The result of this is that all steps are pre-orientated in an easterly direction and initiated at $(0,0)$, and can be plotted as a histogram of step distance in the x or y direction. By a change of variables, into Cartesian coordinates, equation (3) **Error! Reference source not found.** is fitted to a histogram of step distance in the x direction. In Cartesian coordinates the pdf is

$$f_x(x) = \int_{-1}^{1} \frac{f_u\left(x/h, h\right)}{h}\, dh$$

Equation (3)

where $h = \cos(\theta)$, and,

Equation (4)

$$f_h\left(\frac{x}{h}, h\right) = g_r\left(\frac{x}{h}\right)\sum_k \frac{1}{(1-h^2)^{\frac{1}{2}}\{g_\phi(\arccos[(h)+2\pi k) + g_\phi(-\arccos[(h)+2\pi k)]\}}$$

The final histograms for both the control and KD case were amalgamated from multiple cells (n = 17 in the RhoG KD case, n = 74 in the RhoGDI3 KD and n = 40 in the control case).

We fitted model parameters by simulated annealing. However, initially we found that the model could not satisfactorily fit the data (not shown). To improve this we introduced the possibility for multiple states of behavior, so that our model is now a mixture model. So in the case of two states, the fitted pdf is

$$f_x(x) = \alpha\, f_x^1(x) + (1-\alpha)f_x^2(x)$$

where α is the weight between pdfs $f_x^1(x)$ and $f_x^2(x)$ which are parmeterized by $(\mu_r^1, \sigma_r^1, \sigma_\theta^1)$ and $(\mu_r^2, \sigma_r^2, \sigma_\theta^2)$ respectively.

Note that the one state solution was still permitted by the simulated annealing (initially parameters are set such that $f_x^1(x) = f_x^2(x)$, with $\alpha = 0.5$). However, we found consistent convergence towards multiple states, and indeed the multiple state solutions were ~20% better (as quantified by sum of square deviations from the experimental data).

Given that we have identified that in the data sets as a whole there exists two states of migration, we next asked how these states partitioned the data-sets. For example, *a priori* there was no reason to suspect that the case where some of the cells were entirely in one state versus, the more interesting observation, where over the course of the experiment, cells switch between states. To identify what state a cell is in at a given time-point we used Bayes' theorem to invert the problem. That is we calculate the probability that a cell is in s_i given the experimental data. Note that in calculating this probability we

also get the false positive rate, or p-value. In order to make a reliable prediction of s_t we

found that we had to consider a 5-step window, $X = \{x_{t-2}, x_{t-1}, x_t, x_{t+1}, x_{t+2}\}$. Then:

$$P(s_t \mid X) = (P(X \mid s_t)P(s_t))/(P(X \mid s_t)P(s_t) + P(X \mid s_t^{\top c})P(s_t^{\top c}))$$

where $P(X \mid s_t)$ is calculated from the model, and we take $P(s_t) = \alpha_t$.

Rac1 and RhoG Activity Polarity Analysis:

We assessed polarity using a measure (polarity index – I_p)   previously

developed:

$$I_p = \frac{C_G - C_A}{r_e}$$
    Equation (5)

where C_G is the geometric center, C_A the activity center (a weighted average of position,

with pixels in the cell having the weight of the intensity ratio, and zero otherwise), and

r_e is the effective radius of the cell ($r_e = \sqrt{\dfrac{A}{2\pi}}$, where the area of the cell is A). The

partition of the data into multiple subsets (for each state) allowed us to calculate the mean

polarity index for each state. To test if the difference between the mean polarity index,

$\overline{I_p^i}$, for each state was significant we used a boot-strapping method: by sorting the data in

to subsets at random, and repeating this multiple times, we built a distribution of the test

statistic $z = \overline{I_p^B} - \overline{I_p^A}$.

Statistical Analysis:

Microsoft Excel was used for statistical analysis. In each case, p-values were calculated using a two-tailed unpaired t-test assuming unequal variance. Significance for all tests was assumed at $p<0.05$ (α 0.05).

4.6 Acknowledgments

4.7 Figures and Legends

Figure 4.1: Localization and Timing of RhoG Activation at the Leading Edge of Motile Cells.

(A) Probe design: a schematic representation of the intermolecular FRET RhoG activity biosensor. GTP: guanosine triphosphate, GDP: guanosine diphosphate, CyPet: cyan fluorescent protein, YPet: yellow fluorescent protein.

(B) Normalized FRET/CFP emission ratios representing RhoG activity. Biosensor responses were assessed with mutant and wild type RhoG biosensors in adherent Cos-7 cells. Biosensor response to GEFs was assessed in the presence of the catalytic DH-PH domains of Vav2 and Tim, C-terminally truncated Tiam-1 (C1199), or full-length PLEKHG6. Response to GAPs and GDI was assessed in the presence of full-length p50RhoGAP, Rap1GAP, and RhoGDI-1. Asterisks indicate $p < 0.001$ for signal from all conditions compared to WT (*t*-test), and data are represented as means ± 95% confidence intervals at $\alpha = 0.05$.

(C) Representative images of RhoG, Rac1, and RhoA activity in randomly migrating mouse embryonic fibroblasts (left panels) and HeLa cells (right panels). Scale bar, 20 μm. Images are scaled so that regions of intense GTPase activity are shown in white. Heat map indicating dynamic range scaling is shown for each cell.

(D) Correlation of RhoG activity level in migrating mouse embryonic fibroblasts migrating on fibronectin with protrusion or retraction velocity and distance from the edge as assessed by automated linescan analysis. Correlation is derived from 388,000 measurements from 9 cells.

(E) Timelapse images of RhoG activity in a mouse embryonic fibroblast migrating on fibronectin. First panel illustrates the whole cell and subsequent panels are magnified images of the region outlined in white at noted time steps. Scale bar, 20 μm.

(F) Cross-correlation analysis of RhoG activity with protrusional velocity as assessed by Pearson's correlation coefficient. Cross-correlation is significant above 0.42, represented by the dashed black horizontal line and indicating strong correlation. Peak time lag between peak RhoG activity and protrusional velocity is indicated by the dashed red vertical line at $t = -6$ seconds $\pm$ 1.4 seconds. Each line represents correlation of RhoG activity with protrusional velocity in regions 1 (red line), 2 (yellow line), 3 (blue line), 4 (green line), 5 (orange line), or 6 μm (black line) from the leading edge of the cell. Data is derived from 320 measurements from 9 cells across 3 separate experiments.

(G) Ten pixel-wide linescans of RhoG, Rac1, and RhoA activity in protrusive regions of migrating cells were normalized and averaged for 12 cells for each GTPase activity. Average normalized activity along the length of protrusions is given for RhoG (blue trace), Rac1 (red trace), and RhoA (green trace). Dashed lines indicate 95% confidence intervals for each trace. See also Supplemental Figure S4.1.

Figure 4.1
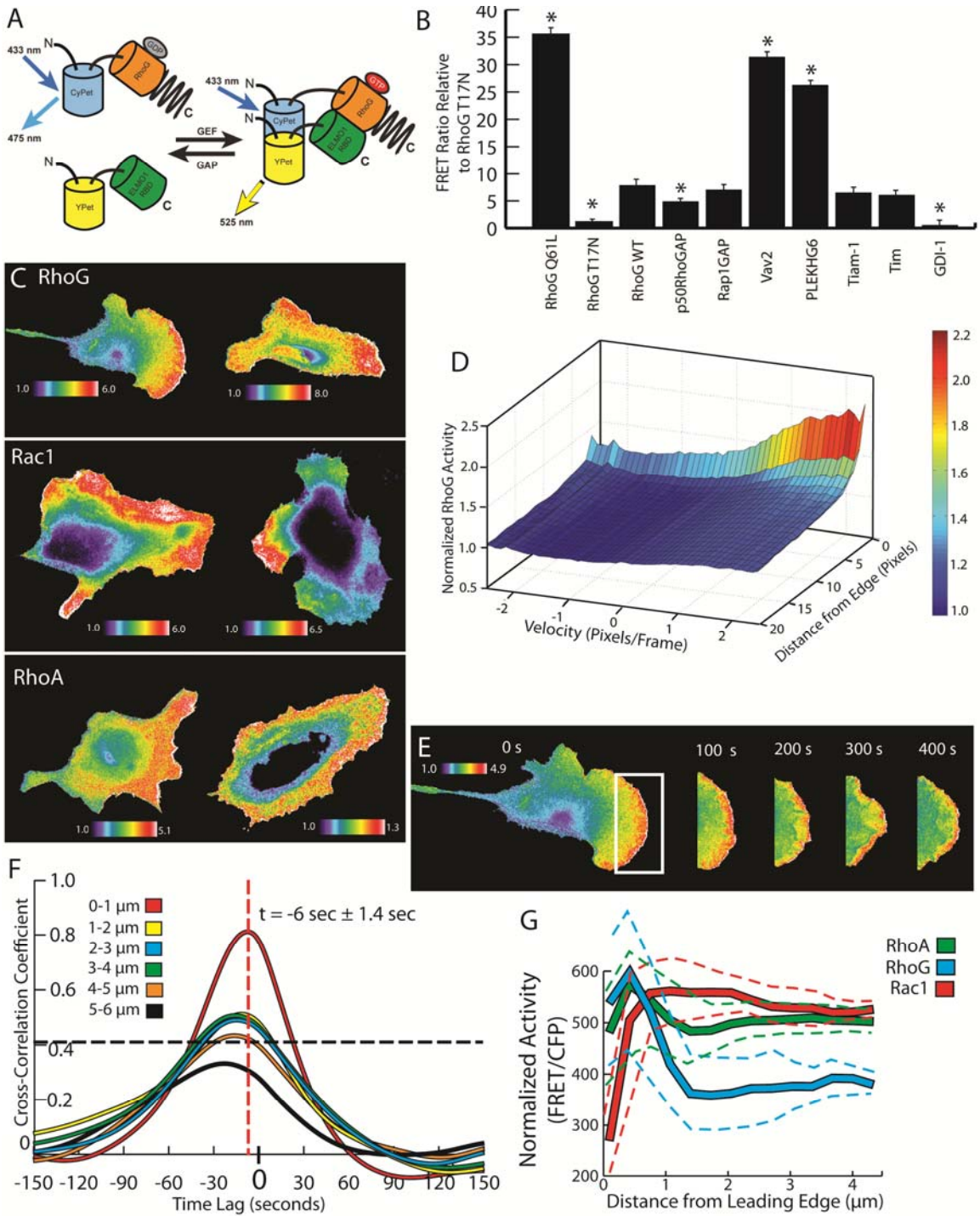
Figure 4.2: RhoG is Targeted to the Leading Edge by Endosomal Recycling and is Regulated by RhoGDI-3.

(A) Cos-7 cell expressing mCherry-RhoG showing localization to vesicles.

(B) Disk-spinning confocal images of a HeLa cell co-expressing CyPet-RhoG and mCherry-tubulin showing colocalization of motile vesicles (arrows) on microtubules (yellow trace).

(C) Quantitation of colocalization of RhoG-positive vesicles with Rab-GTPase positive vesicles. Colocalization is represented as a percent of RhoG-positive vesicles co-stained with Rab-positive vesicles. Data are represented as means ± 95% confidence intervals at α = 0.05. N > 270 vesicles for each condition for at least 10 cells per condition.

(D) Quantitation of RhoG activity in vesicles as assessed by live-cell dual-camera epifluorescence imaging. CyPet-RhoG image shows RhoG-positive vesicle (red arrow), and corresponds with the middle RhoG activity image. Right panel shows a trace of activity corresponds to white line in RhoG activity image showing peak activity at the edge and minimum activity within the vesicle (black arrows).

(E) Epifluorescence images (inverted) of live cells expressing mCherry-tagged RhoGDI-3 (left panel) showing predominantly perinuclear localization but also presence in vesicles that colocalize with CyPet-RhoG.

(F) Epifluorescence images of live cells expressing mCherry-tagged RhoGDI-3 (right panel) in one of two cells (second cell outlined in red) and CyPet-RhoG (left panel) in both cells illustrating effects of RhoGDI-3 on RhoG localization. RhoG remains predominantly perinuclear in the presence of RhoGDI-3, but is lamellipodial and membrane-bound in the absence of ectopic RhoGDI-3 expression.

(G) Quantitation of RhoG fluorescence intensity ratio of the lamellipodium to the perinuclear region in cells expressing CyPet-RhoG and transfected with mCherry-RhoGDI-3, a control siRNA, or RhoGDI-3 siRNA.

(H) Quantitation of RhoG activity in the presence or absence of RhoGDI-3 as assessed by FRET in adherent HeLa cells. Data are represented as means ± 95% confidence intervals at α = 0.05. Asterisks indicate p < 0.05 by t-test.

(I) Representative images of RhoG activity in HeLa cells expressing a RhoG activity sensor and transfected with either mCherry-RhoGDI-3 or RhoGDI-3 siRNA. Images are scaled so that regions of intense GTPase activity are shown in white, and both cells are scaled identically to allow visual comparison. Heat map indicating dynamic range scaling is shown for each cell.

(J) Timelapse image integrated over 120 minutes of a HeLa cell expressing either CyPet-RhoG, or CyPet-RhoG and mCherry-RhoGDI-3 illustrating the preference of RhoG-positive vesicles for the perinuclear region and the leading edge in the direction of cellular movement in the wild-type condition (left panel).   With RhoGDI-3 overexpression, transit of vesicles to the leading edge is blocked (right panel). Cells were thresholded to isolate vesicles, and integrated time spent by vesicles in a given pixel is indicated by white coloration on a blue background. Cell outline is indicated in red, and direction of movement is indicated by large white arrow. See also Supplemental Figure S4.2.

Figure 4.2
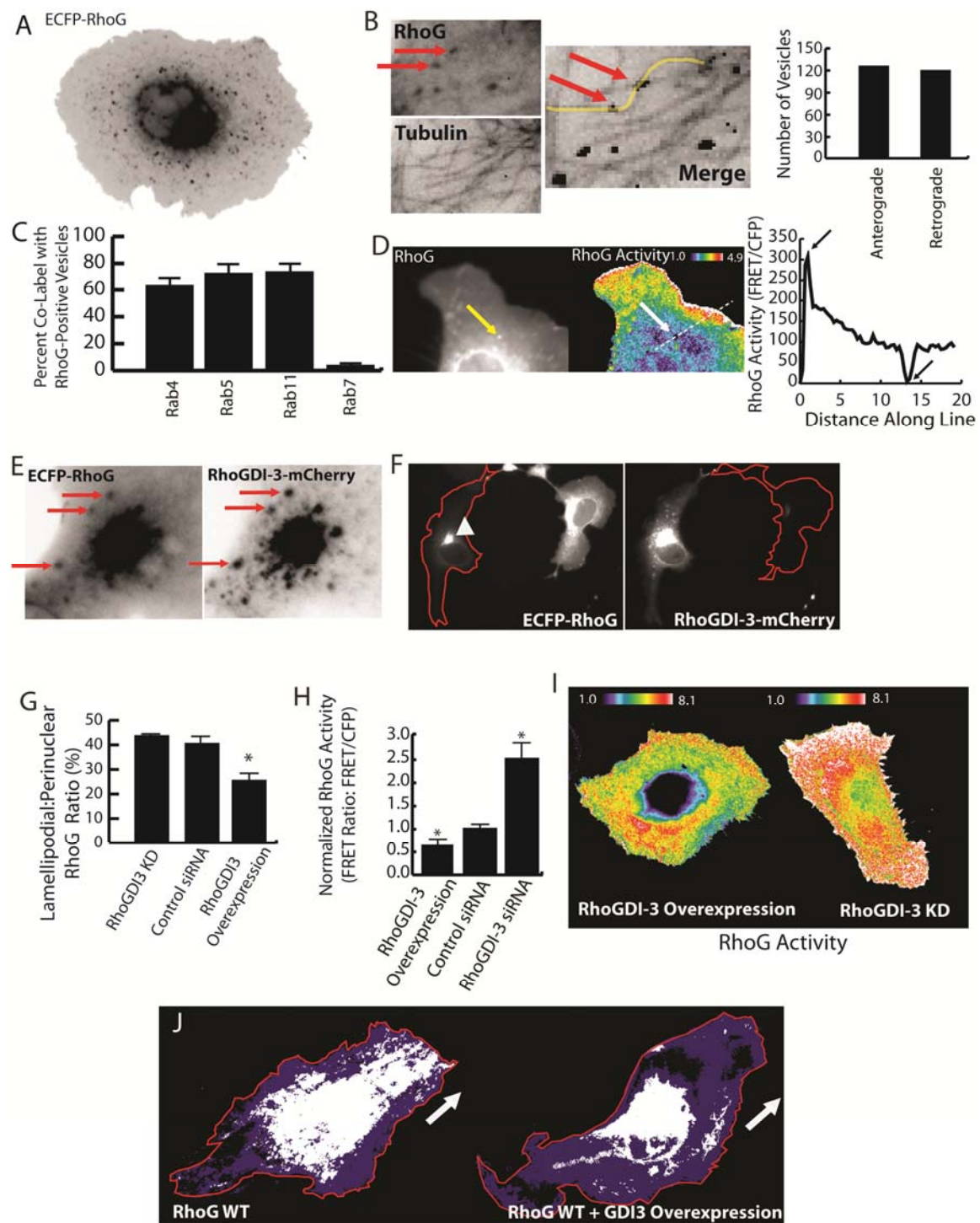
Figure 4.3: RhoG Regulates the Spatio-temporal Dynamics of Rac1 Activity in Protrusions.

(A) Representative western blot of endogenous Rac1 activity in HeLa cells migrating on fibronectin with or without RhoG knockdown as assessed by GST-CRIB pulldown. Bands were quantified and normalized with intensities expressed in arbitrary units relative to control (assumed as 1). Values are means ± SEM (n = 6). Asterisk indicates p < 0.05 by *t*-test.

(B and C) Representative Rac1 activity spatial patterns in control siRNA-treated (B) and RhoG siRNA-treated HeLa cells migrating on fibronectin. Right-most panels correspond to regions outlined with red boxes. Scale bar, 20 μm. Activity scale is indicated by heat map in upper left corner of each figure.

(D) Representative linescans from panels (B) and (C) and Figure S3.B-D indicated by the dashed white lines quantifying Rac1 activation along the protrusion. Control siRNA (red line), RhoG siRNA (black line), ELMOT625 (blue line), DOCK180 DN (yellow line), and RhoGDI-3 siRNA (green line) are represented.

(E) Quantitation of distance from leading edge of maximal Rac1 activity during protrusion and migration of HeLa cells on fibronectin for individual cells treated with control siRNA (*n =25*), RhoG siRNA (*n=24*), ELMO1/2 siRNA (*n=15*), ELMOT625 (*n=12*), DOCK180 WT (*n=15*), DOCK180 DN (*n=15*), RhoGDI-3 siRNA (*n = 12*) as assessed by linescan analysis. Solid black lines indicate average peak of Rac1 activity; dashed red lines represent SEM. Asterisks indicate p < 0.05 by student's *t*-test compared to control siRNA.

(F) Quantitation of RhoGDI-3 effects on Rac1 activity by FRET as measured by whole-cell average of FRET ratio with n > 10 cells per condition. Data are represented as means

± 95% confidence intervals at α = 0.05. Asterisks indicate $p < 0.05$ by t-test. See also

Supplemental Figure S4.3.

Figure 4.3
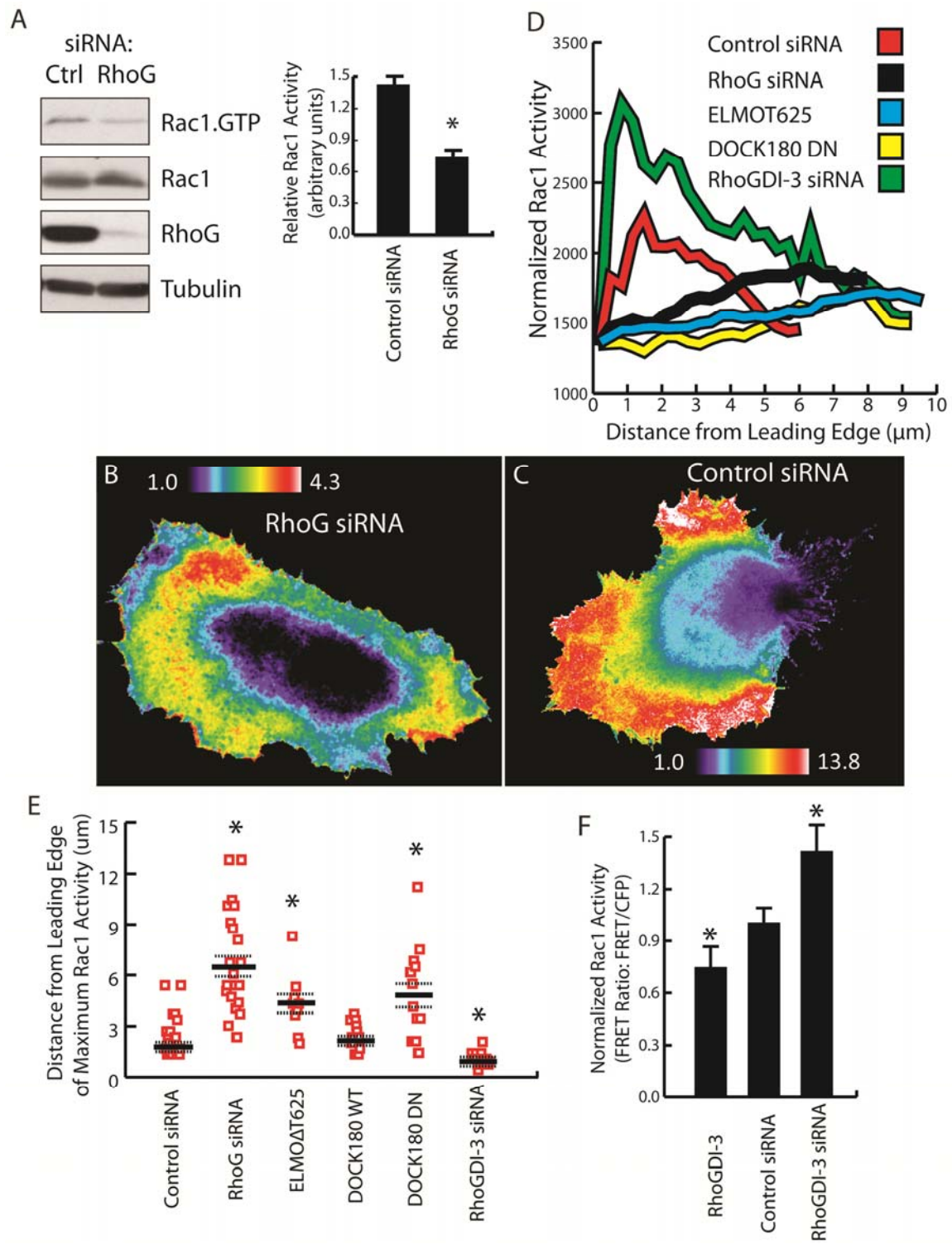
Figure 4.4: RhoG Regulates Adhesion Dynamics at the Leading Edge.

(A) Migrating cells expressing mCherry-Paxillin-β and CyPet- Rac1 as assessed by total internal reflectance microscopy (TIRFM). Lower panel inset from regions outlined in black. Arrows indicate areas of Paxillin-β and Rac1 colocalization. Images inverted. Scale bar, 20 μm.

(B) Rac1 activity as assessed by TIRFM in control siRNA-treated migrating cells expressing mCherry- Paxillin-β and a Rac1 FRET biosensor. Yellow arrows indicate regions of adhesion formation. Red arrows indicate regions of adhesion stabilization. Scale bar, 20 μm. Heat map for Rac1 activity is shown at lower right.

(C) Rac1 activity and Rac1 localization to adhesions as assessed by TIRFM in RhoG siRNA-treated migrating cells expressing mCherry-Paxillin-β and a Rac1 FRET biosensor. Lower panels magnified from inset of regions in black or white in top panels. Arrows indicate location of adhesion identified in mCherry-Paxillin-β inset in subsequent images. Scale bar, 20 μm. Heat map for Rac1 activity is shown at lower right.

(D) Quantitation of Rac1 recruitment to adhesions as percentage intensity increase over background as assessed by TIRFM in cells expressing mCherry-Paxillin-β and CyPet-Rac1 and treated with control or RhoG siRNA, or expressing Rac1 Q61L, Rac1 T17N, ELMOΔT625, or RhoGDI-3. Data are represented as means ± 95% confidence intervals at α = 0.05. Asterisks indicate p < 0.05 as assessed by t-test.

(E) Assessment of DOCK180 recruitment to adhesions by TIRFM in migrating cells expressing EGFP- Paxillin-β and mCherry-DOCK180. Arrows indicate the same adhesions in each inset for DOCK180. Scale bar, 20 μm.

(F) Migrating cells expressing mCherry-tagged Paxillin-β as assessed by total internal reflectance microscopy (TIRFM) and treated with control siRNA, RhoG siRNA, or expressing CFP-RhoG Q61L. Images inverted. Direction of protrusion indicated by black arrow. Scale bar, 20 μm.

(G) Quantitation of leading edge adhesion number per 100μm^2 in cells treated with control siRNA, RhoG siRNA, or expressing RhoG Q61L, RhoG T17N, ELMOΔT625, or RhoGDI-3 as assessed by TIRFM. Data are represented as means ± 95% confidence intervals at α = 0.05. Asterisks indicate $p < 0.05$.

(H) Quantitation of leading edge adhesion size in cells treated with control, RhoG, or RhoGDI-3 siRNA as assessed by TIRFM. Data are represented as means ± 95% confidence intervals at α = 0.05. Asterisks indicate $p < 0.05$ by t-test. See also Supplemental Figure S4.4.

Figure 4.4
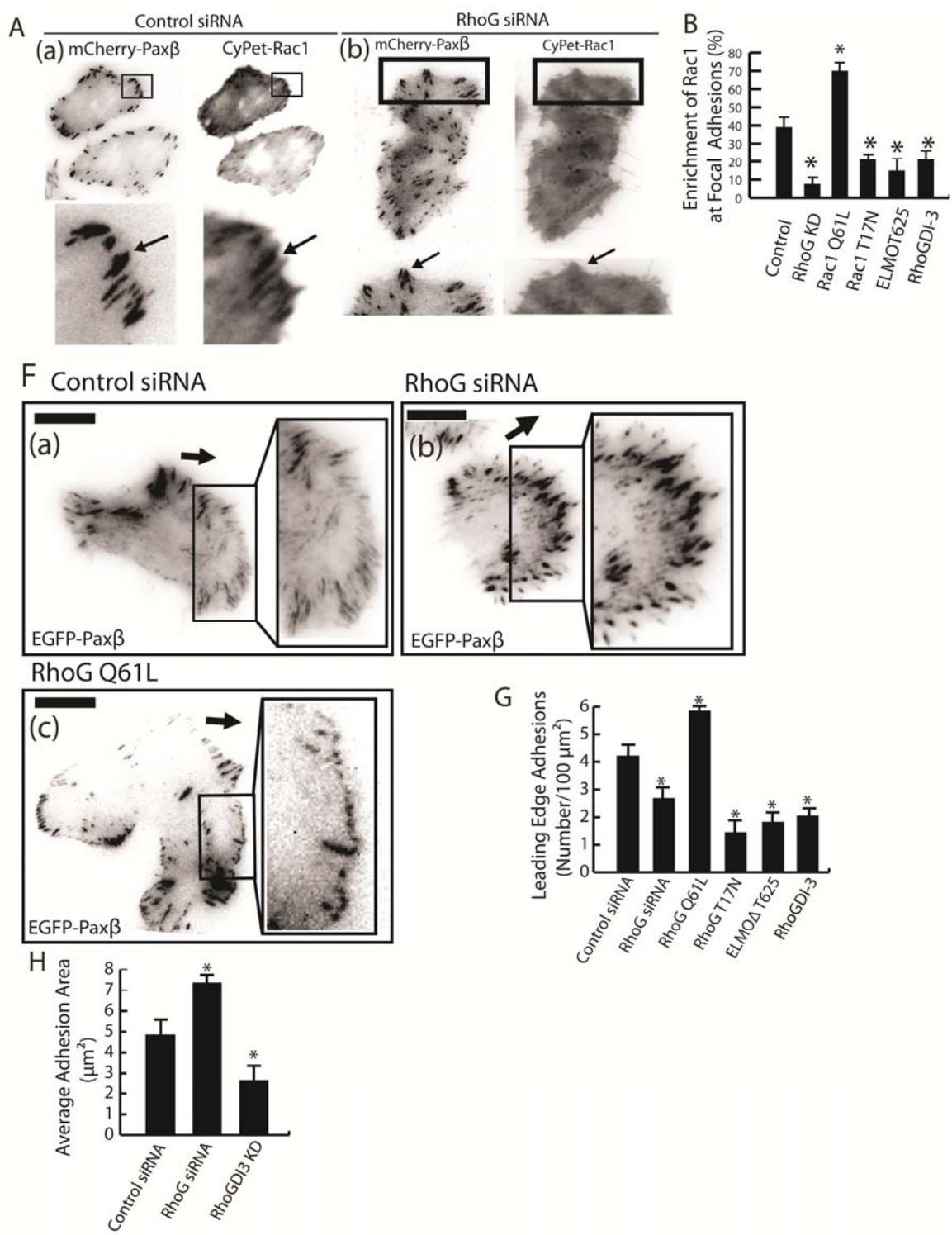
Figure 4.5: RhoG Regulates Actin and Protrusion Dynamics at the Leading Edge.

(A) Representative kymographs of protrusions from migrating cells treated with control or RhoG siRNA as assessed by DIC. Direction of protrusion, distance traveled, and time are all indicated for each image. The cell edge is traced in black outline.

(B) Quantitation of protrusion/retraction cycle frequency from kymographs of migrating cells treated with control, RhoG, or RhoGDI-3 siRNA as assessed by DIC. Data are represented as means $\pm$ 95% confidence intervals at $\alpha = 0.05$. Asterisks indicate $p < 0.05$ by t-test.

(C) Quantitation of average distance traveled by a protrusion from kymographs of migrating cells treated with control, RhoG, or RhoGDI-3 siRNA as assessed by DIC. Data are represented as means $\pm$ 95% confidence intervals at $\alpha = 0.05$. Asterisks indicate $p < 0.05$ by t-test.

(D) Representative pseudocolored actin barbed end density images as assessed by epifluorescence in fixed control and RhoG siRNA-treated cells. Lower panel is magnified inset in region highlighted in white in top panel. Arrows indicate potential regions of protrusion. Barbed end density corresponds to the heat map in upper right corner. Scale bar, 20µm. Heat map at upper right indicates density scaling.

(E) Quantitation of actin barbed end density as assessed by linescans from the entire cell edge in epifluorescence images of fixed control, RhoG, and RhoGDI-3 siRNA-treated cells. Data are represented as means $\pm$ 95% confidence intervals at $\alpha = 0.05$. Asterisks indicate $p < 0.05$ by t-test. See also Supplemental Figure S4.5.

Figure 4.5
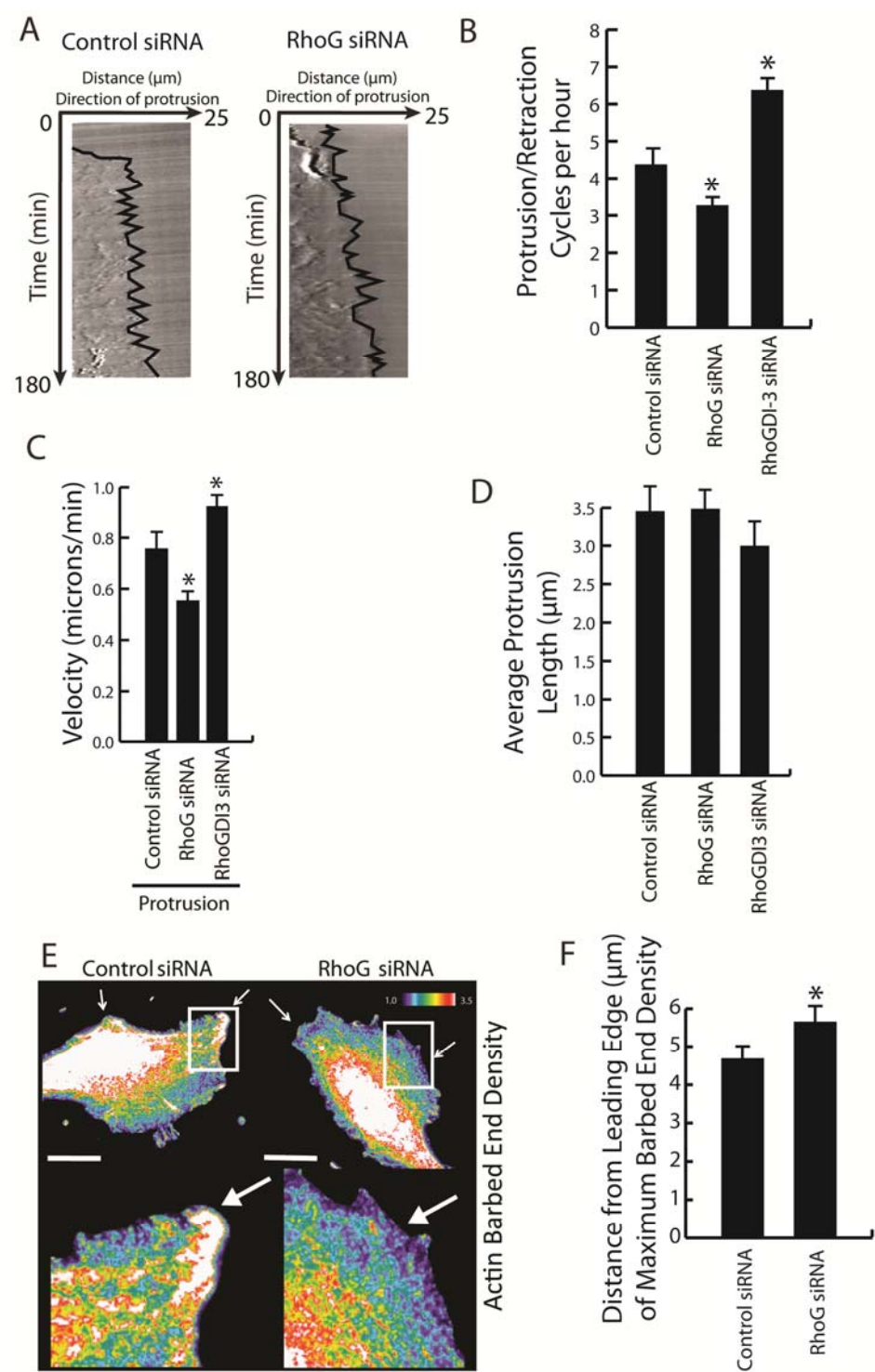
Figure 4.6: RhoG Regulates Cell Migration Behaviors on 2-D and 3-D Substrates.

(A) Quantitation of cell migration velocity from tracks in control, RhoG, or RhoGDI-3 siRNA-treated cells. Data are represented as means $\pm$ 95% confidence intervals at α = 0.05. Asterisks indicate $p < 0.05$ by t-test.

(B) Quantitation of cell migration persistence from tracks in control, RhoG, or RhoGDI-3 siRNA-treated cells. Data are represented as means $\pm$ 95% confidence intervals at α = 0.05. Asterisks indicate $p < 0.05$ by t-test.

(C) Illustration of the parameter space and methods of measurement of cellular behaviors during cell migration tracks that give rise to State 1 and State 2. Parameters measured include velocity (μ_r), change in directional angle (σ_θ), and deviation in velocity (σ_r).

(D) Representative traces of cell migration tracks for control and RhoG siRNA-treated cells with color shading indicating the behavior state of the cell. Scale bar, 10 μm. Time frames indicated for each cell.

(E) Quantitation of cell migration velocity from tracks in control, RhoG, or RhoGDI-3 siRNA-treated cells and separated by behavior state. Data are represented as means $\pm$ 95% confidence intervals at α = 0.05. Asterisks indicate $p < 0.05$ by t-test.

(F) Quantitation of cell migration persistence from tracks in control, RhoG, or RhoGDI-3 siRNA-treated cells and separated by behavior state. Data are represented as means $\pm$ 95% confidence intervals at α = 0.05. Asterisks indicate $p < 0.05$ by t-test.

(G) Quantitation of foci of Rac1 activation (> 1.5x increase in Rac1 activation compared to cell center) for control, RhoG, and RhoGDI-3 siRNA-treated cells separated by behavior state. Data are represented as means $\pm$ 95% confidence intervals at α = 0.05. Asterisks indicate $p < 0.05$ by t-test.

(H and I) Representative examples of RhoG and Rac1 activity in cell migration as assessed by FRET in State 1 or State 2 for control, RhoG, or RhoGDI-3 siRNA-treated cells, and used for the analysis in Figure 5G.

(J) Quantitation of polarity of Rac1 and RhoG activation in migration tracks from cells expressing a RhoG or Rac1 activity sensor and separated by behavior state. Data are represented as means ± S.E.M. at $\alpha = 0.05$. Asterisks indicate $p < 0.05$ by t-test.

(K) Quantitation of average maximum peak Rac1 and RhoG activity as a proportional increase relative to average baseline Rac1 and RhoG activity for states 1 and 2. Black bars represent normalized baseline Rac1 and RhoG activity for each state, with the white bars representating the additional amount of Rac1 and RhoG activity found at peak in protrusions, or "spots." Data are represented as means ± S.E.M. at $\alpha = 0.05$. Asterisks indicate $p < 0.05$ by t-test.

(L) Representative images of cell morphology of control, RhoG, and RhoGDI-3 siRNA-treated cells embedded in 3-D matrices expressing mCherry alone.

(M) Quantitation of protrusional number in control, RhoG, and RhoGDI-3 siRNA-treated cells embedded in 3-D matrices as assessed by laser scanning microscopy. Data are represented as means ± 95% confidence intervals at $\alpha = 0.05$. Asterisks indicate $p < 0.05$ by t-test. See also Supplemental Figure S4.6.

Figure 4.6
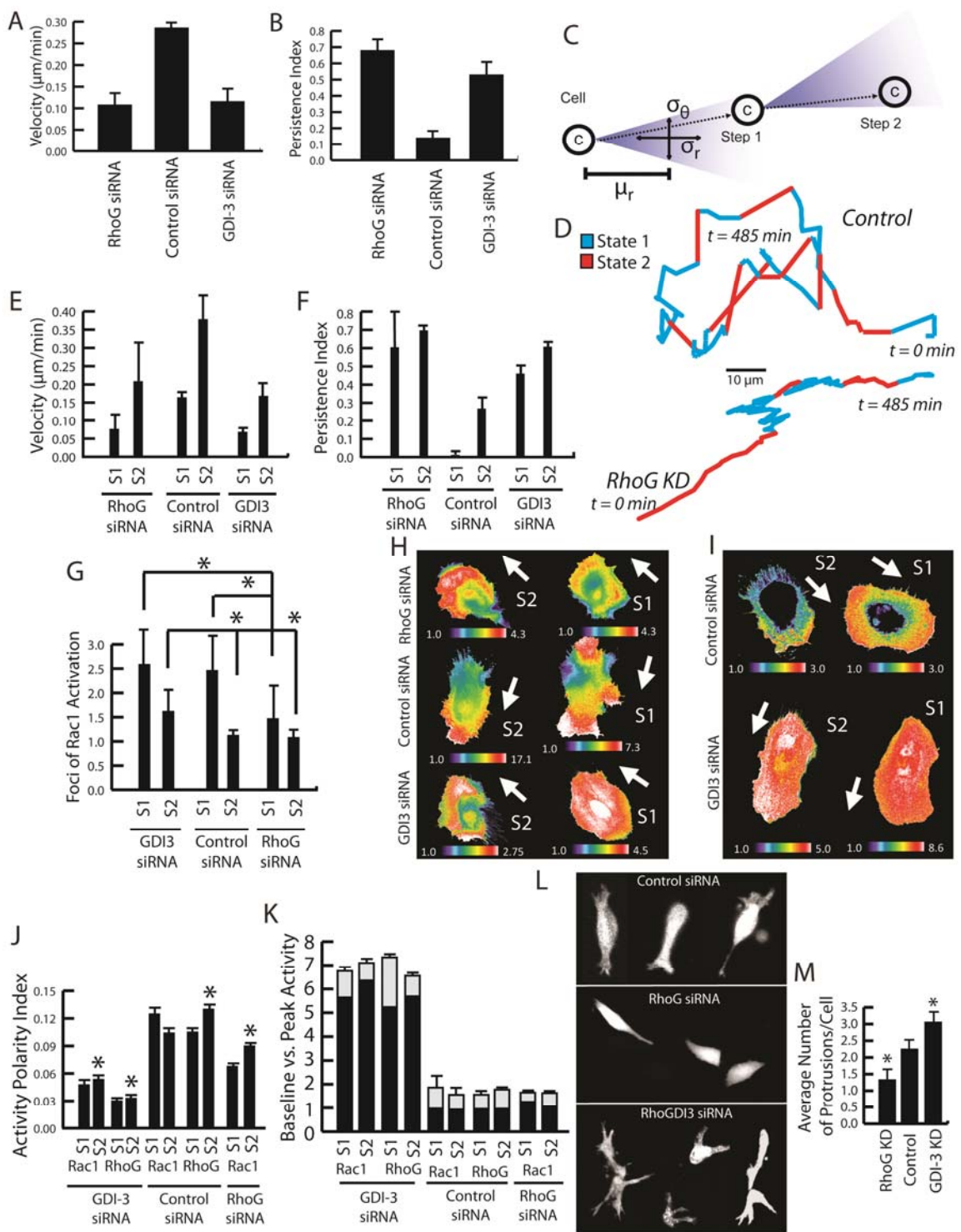
Figure 4.7: Model for the Regulation of Lamellipodial Rac1 Activity by RhoG.

Model of cellular signaling depicting the regulation of RhoG and its trafficking by

RhoGDI-3, and RhoG regulation of Rac1 in the lamellipodium and proposed model of

RhoG mediation of cellular turning during random migration.

Figure 4.7
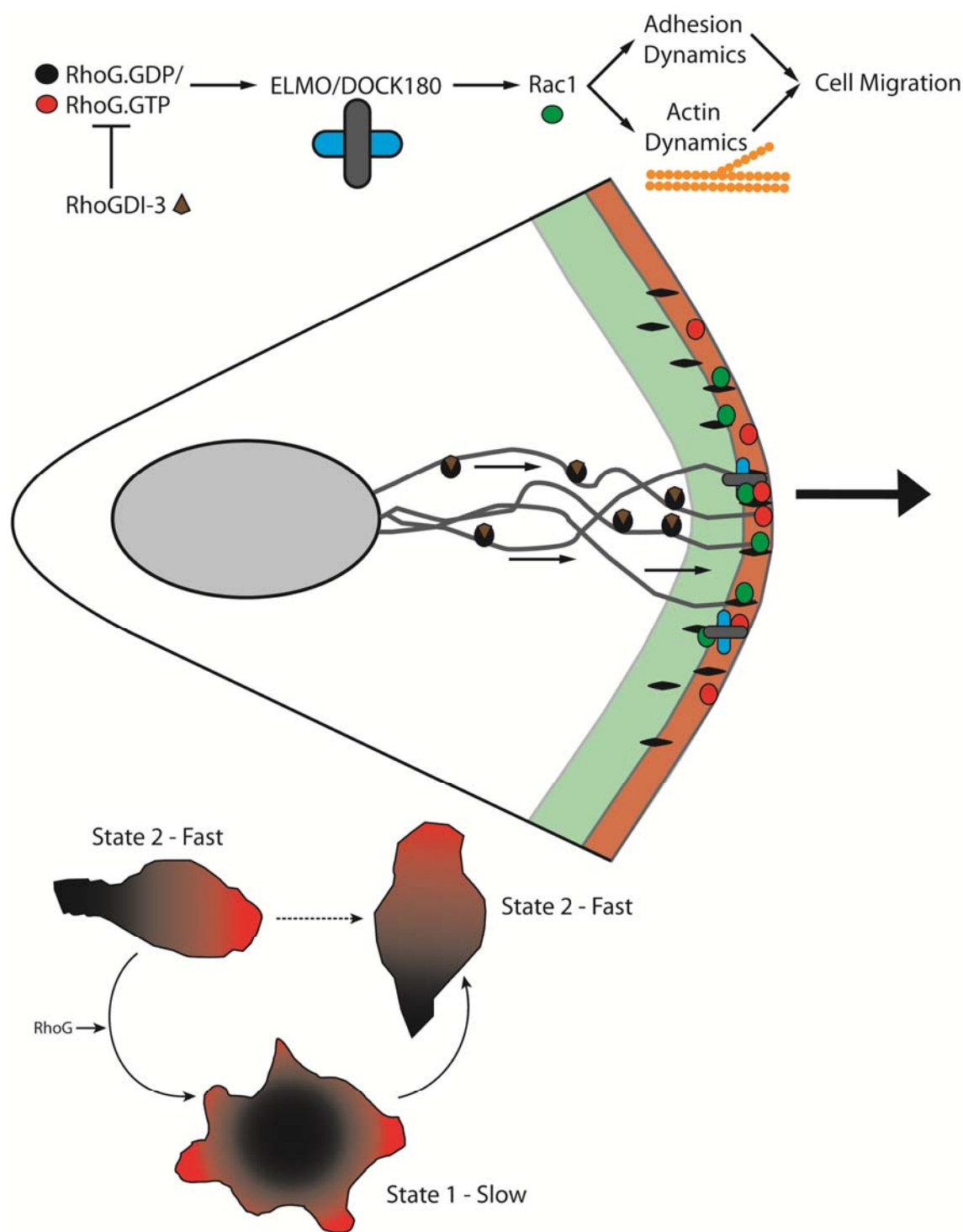
Supplemental Figure S4.1, Related to Figure 4.1: Validation of a RhoG Activity Biosensor and Observed Activity at the Leading Edge.

(A) Analysis of RhoG-GTP and Rac1-GTP levels by GST-ELMO or GST-CRIB pulldown assay in cells treated with empty vector or p50RhoGAP. Total RhoG and Rac1 levels are shown as loading controls.

(B) Normalized FRET/CFP emission ratios representing RhoG activity in response to EGF stimulation, Synectin siRNA-treatment, and RhoGDI-3 overexpression versus controls as assessed in imaging of adherent HeLa cells. EGF was used at a concentration of 20 ng/mL and activation of RhoG peaked within 30 seconds of stimulation as previously described (Samson et al. 2010). Asterisks indicate $p < 0.001$ for signal from all conditions compared to WT (*t*-test), and data are represented as means ± 95% confidence intervals at $\alpha = 0.05$. *N* of at least 15 cells per condition.

(C) HeLa cells were transfected with control siRNA or synectin siRNA and assessed for endogenous synectin protein levels by Western blot. Tubulin levels are given as a loading control.

(D) Representative images of RhoG and Rac1 activities in HeLa cells transfected with either control or synectin siRNA and expressing either a RhoG or Rac1 activity sensor. Images are scaled so that regions of intense GTPase activity are shown in white. Heat map indicating dynamic range scaling is shown for each cell.

(E) Quantitation of RhoG and Rac1 activity (FRET intensity) in cells transfected with either control or synectin siRNA and expressing either a RhoG or Rac1 activity sensor. Asterisks indicate $p < 0.05$ for signal for each synectin knockdown condition compared to control (*t-test*), and data are represented as means ± 95% confidence intervals at $\alpha = 0.05$. *N of at least* 10 cells per condition.

(F) Cross-correlation analysis of timing of peak RhoG activity with change in velocity versus distance from leading edge where RhoG activity is assessed (red line) or the cross-correlation coefficient as assessed with increasing distance from the leading edge (blue line). A cross-correlation coefficient above 0.42 is considered statistically significant at p < 0.05.

Supplemental Figure S4.1
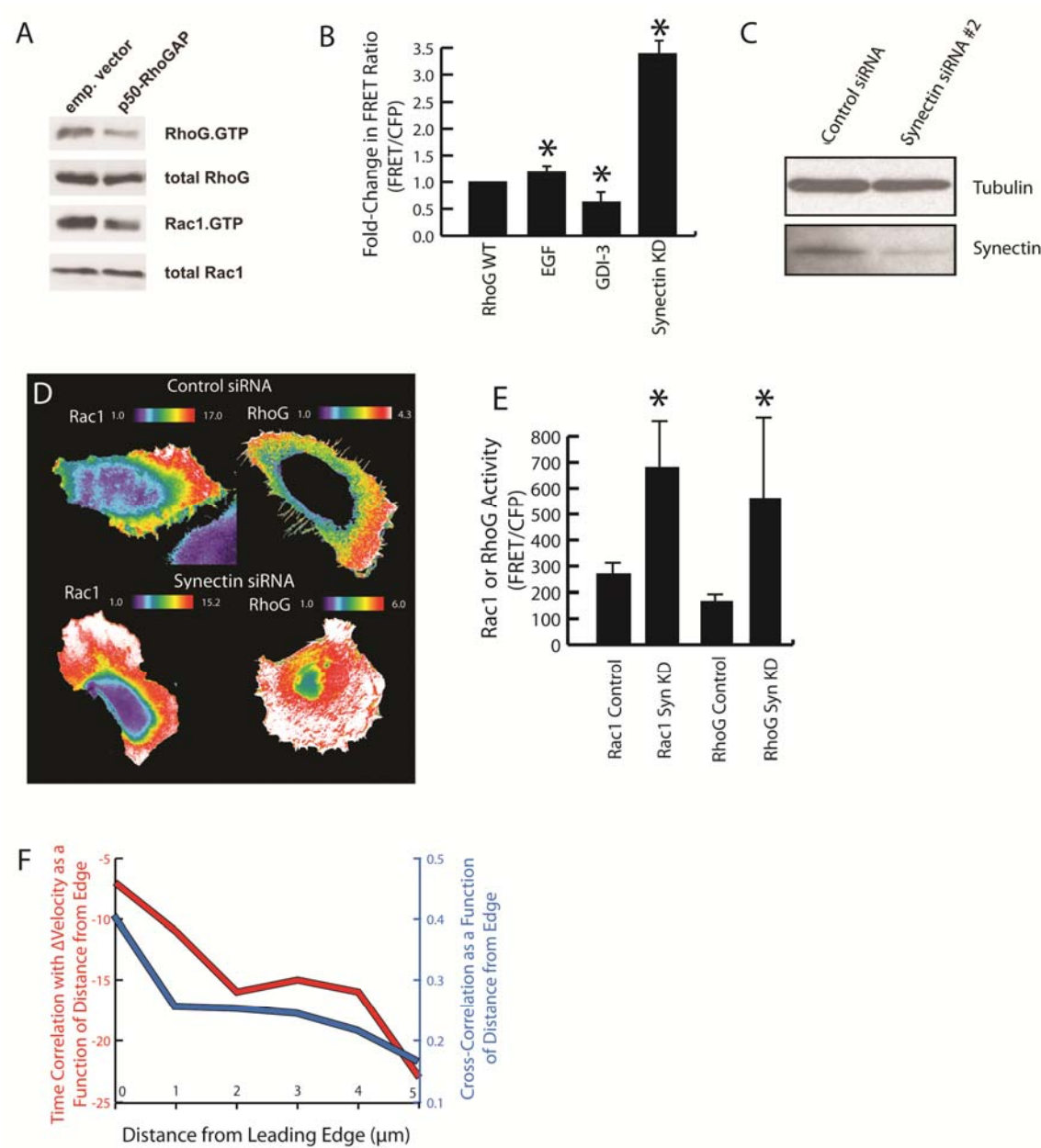
Supplemental Figure S4.2, Related to Figure 4.2: Vesicular RhoG Localization and Trafficking and its Regulation by RhoGDI-3.

(A, B, C, and D) As indicated, coexpression of CyPet-RhoG with mCherry-tagged Rab4, Rab5, Rab7, or Rab11 in vesicles as assessed by epifluorescence in live Cos-7 cells. Arrows indicate the same vesicle in both images, or in the case of Rab7, absence of the associated vesicle. Rightmost panels are magnified insets of the regions outlined in black for each image pair.

(E) Endogenous mRNA levels of RhoGDI-3 in HeLa cells treated with control or RhoGDI-3 siRNA as assessed by RT-PCR. β2-microglobulin levels are given as a control.

Supplemental Figure S4.2
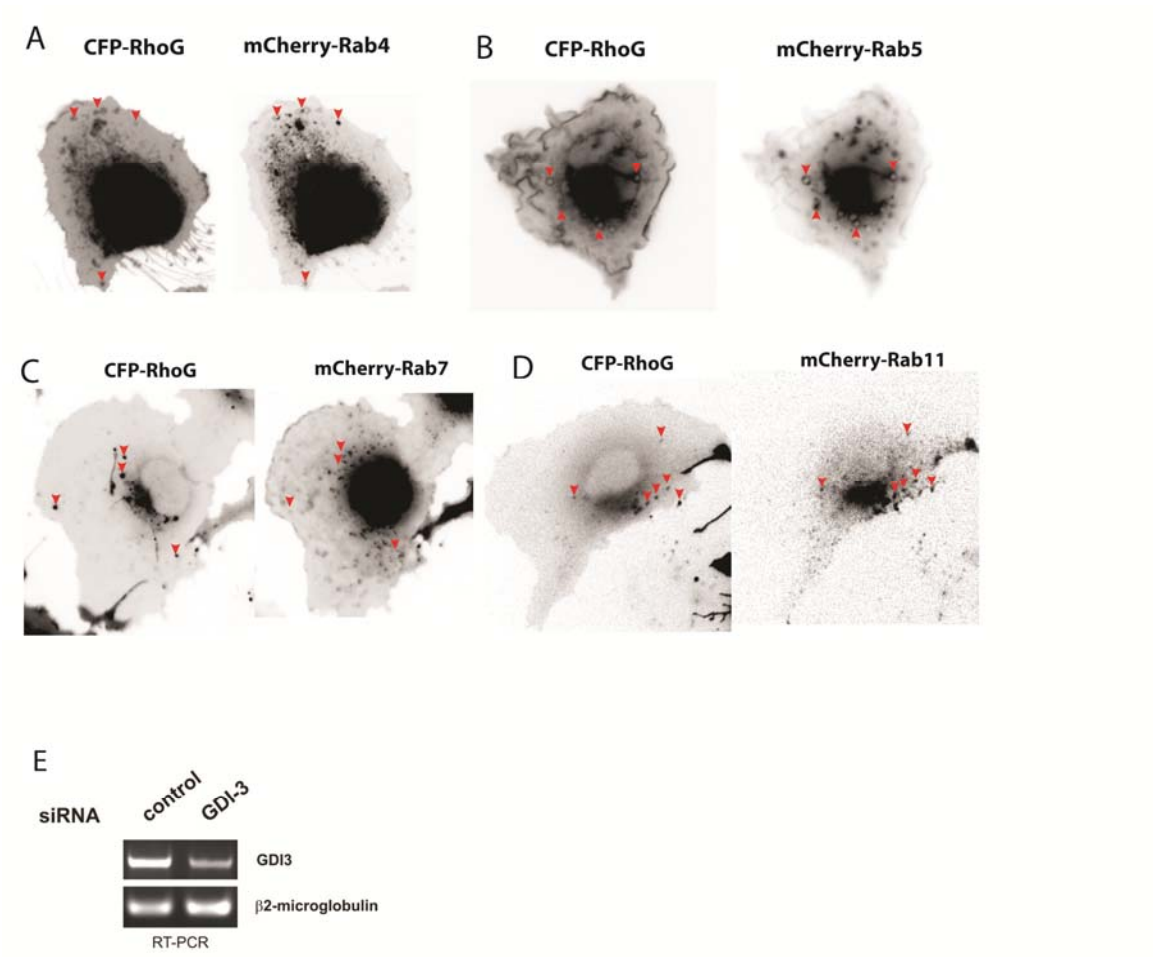
Supplemental Figure S4.3, Related to Figure 4.3: Effects of RhoG Activity on Lamellipodial Rac1 Activity.

(A) Endogenous RhoG and Rac1 expression in cells treated with control or RhoG siRNA as assessed by western blot. Tubulin levels are given as a loading control.

(B) Representative Rac1 activity spatial patterns in HeLa cell migrating on fibronectin expressing mCherry-ELMOΔT625. Bottom panel corresponds to region outlined with red box. Activity is indicated by heat map in upper left corner of each panel.

(C) Representative Rac1 activity spatial patterns in HeLa cell migrating on fibronectin expressing mCherry-DOCK180 DN. Bottom panel corresponds to region outlined with red box. Activity is indicated by heat map in upper left corner of each panel.

(D) Representative Rac1 activity spatial patterns in HeLa cell migrating on fibronectin transfected with RhoGDI-3 siRNA. Bottom panel corresponds to region outlined with red box. Activity is indicated by heat map in upper left corner of each panel.

Supplemental Figure S4.3
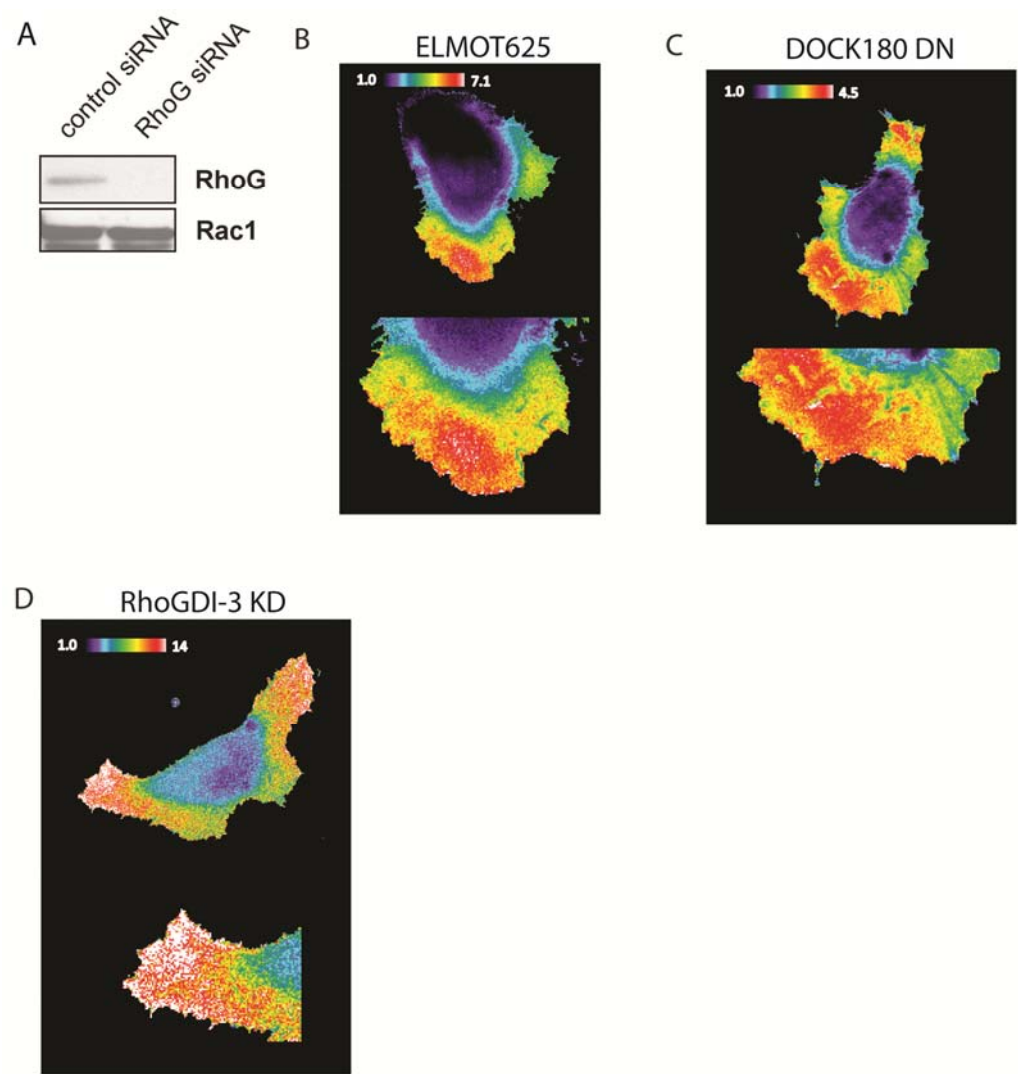
Supplemental Figure S4.4, Related to Figure 4.4: Effects of RhoG Manipulation on Rac1 Activity at the Ventral Cellular Surface and Adhesion Dynamics.

(A) Representative Rac1 activity spatial patterns in control siRNA-treated (B) and RhoG siRNA-treated HeLa cells migrating on fibronectin as observed via TIRF microscopy. Bottom panels are enlarged from the area of the leading edge outlined with white box. White arrows indicate direction of cellular movement. Activity scale is indicated by heat map in each figure.

(B) HeLa cell plated on fibronectin treated with control siRNA expressing mCherry-DOCK180 and EGFP-Paxillin-β as assessed by TIRFM. DOCK180 colocalizes with focal adhesions in both conditions.

(C) HeLa cell plated on fibronectin expressing CyPet-RhoG and mCherry-Paxillin-β as assessed by TIRFM. RhoG is diffusely localized within the membrane in the TIRF plane with no apparent colocalization with adhesions.

(D) HeLa cell plated on fibronectin treated with control or RhoG siRNA expressing mCherry-ELMO1 and EGFP-Paxillin-β as assessed by TIRFM. ELMO1 is diffusely localized within the membrane in the TIRF plane with no apparent changes in localization compared to control siRNA treated cells.

(E) Representative western blot of endogenous RhoA activity in HeLa cells migrating on fibronectin with or without RhoG knockdown as assessed by GST-RBD pulldown in two separate experiments (from four total experiments). Total RhoG levels are shown to indicate the effectiveness of RhoG knockdown. Total RhoA levels are shown to demonstrate that RhoG knockdown did not influence the levels of RhoA protein. Tubulin levels are given as a loading control.

Supplemental Figure 4.4
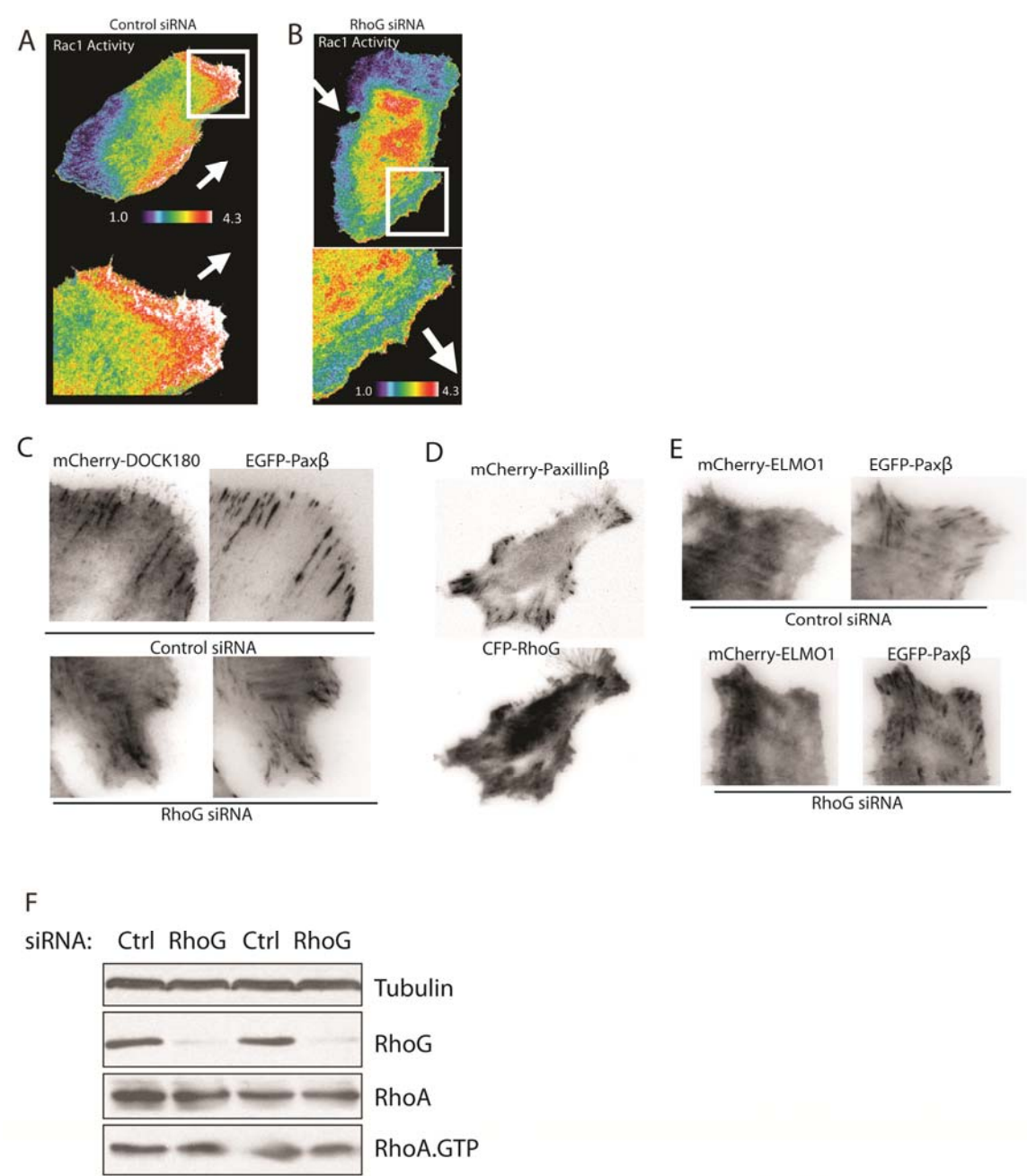
Supplemental Figure S4.5, Related to Figure 4.5: RhoG Regulates Retraction Velocities in Migrating Cells.

Quantitation of retraction velocities from kymographs of migrating cells treated with control, RhoG, or RhoGDI-3 siRNA as assessed by DIC. Asterisks indicate $p < 0.05$ as assessed by t-test. Data are represented as means $\pm$ 95% confidence intervals at $\alpha = 0.05$.

Supplemental Figure 4.5
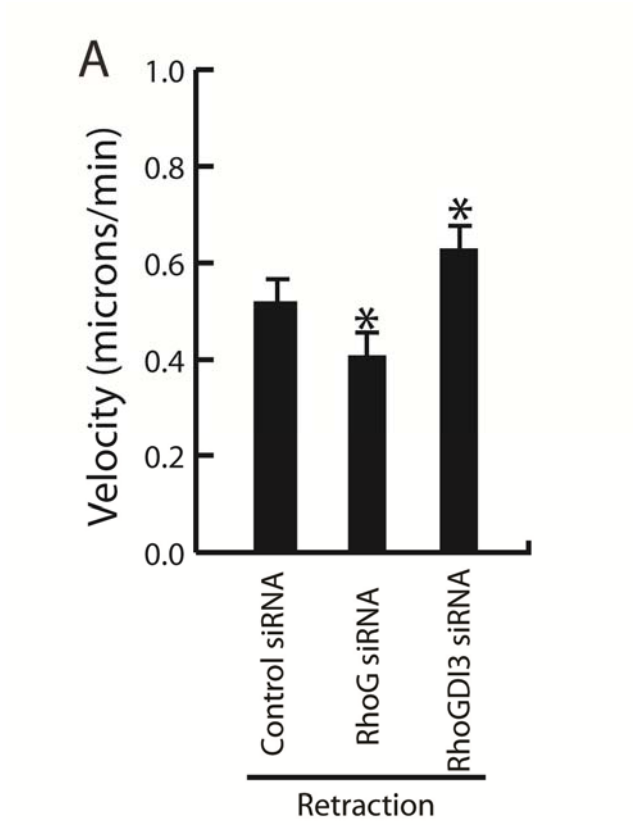
Supplemental Figure S4.6, Related to Figure 4.6: RhoG Modulation of Rac1 Activity Regulates Random Cell Migration Patterns.

(A, B, and C) Representative traces of cell migration tracks acquired over 18 hours for control, RhoG, and RhoGDI-3 siRNA-treated cells. Scale bar, 20 μm.

(D) Quantitation of cell migration velocity variance from tracks in control, RhoG, or RhoGDI-3 siRNA-treated cells and separated by behavior state. Data are represented as means ± 95% confidence intervals at α = 0.05.

(E) Representative image of Rac1 activity with RhoGDI-3 knockdown. Red arrows in lower panel indicate areas of protrusion and high Rac1 activity. Activity level corresponds to heat map in upper right corner of image.

(F) Quantitation of Rac1 activation foci for HeLa cells migrating on fibronectin treated with control, RhoG, or RhoGDI-3 siRNA in short time frames.

(E) Quantitation of migration velocity based on the presumed levels of Rac1 activity and total Rac1 levels for HeLa cells migrating on fibronectin transfected with Rac1 T17N, RhoG siRNA, control siRNA, RhoG Q61L, or Rac1 Q61L, or combinations of RhoG siRNA with wild-type Rac1 or control siRNA with wild-type Rac1.

Supplemental Figure 4.6
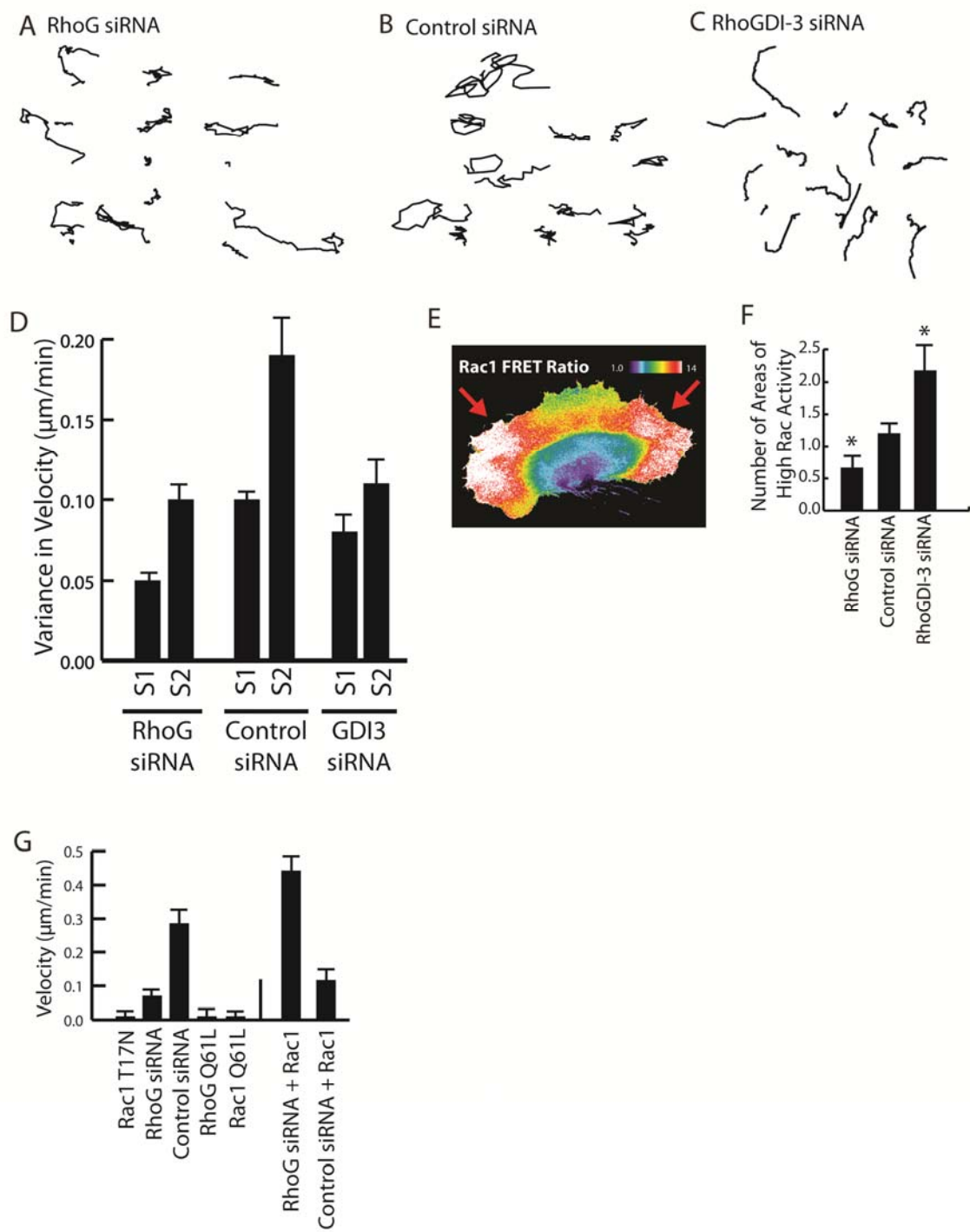
CHAPTER FIVE: ACTIVATION OF RHO GTPASES BY GROWTH FACTORS

5.1 Abstract

RhoG is a member of the Rac-like subgroup of Rho GTPases and has been linked to a variety of different cellular functions. Nevertheless, many aspects of RhoG upstream and downstream signaling remain unclear; in particular extracellular stimuli which modulate RhoG activity. Here we describe that stimulation of epithelial cells with epidermal growth factor leads to the induction of macropinocytosis and strong and rapid activation of RhoG. The kinetics of RhoG activation after EGF stimulation parallels the previously described Rac1 activation. By using nucleotide-free RhoG pull down assays and siRNA mediated knock-down studies we further show that GEFs of the Vav-family mediate EGF-induced rapid activation of RhoG. In addition, we found that in certain cell types the recently described RhoG GEF PLEKHG6 can also contribute to the rapid activation of RhoG after EGF stimulation.

In addition to these findings, we noted that EGF-induced macropinocytosis is differentiated from other types of endocytosis by its unique susceptibility to inhibitors of Na^+/H^+ exchange. Yet, the functional relationship between Na^+/H^+ exchange and macropinosome formation remains obscure. In A431 cells, stimulation by EGF simultaneously activated macropinocytosis and Na^+/H^+ exchange, elevating cytosolic pH and stimulating Na^+ influx. Our collaborators have been able to show that, using novel probes of submembranous pH, metabolically-generated acid at sites of macropinocytosis

accumulates, an effect counteracted by Na^+/H^+ exchange. The acidification observed in the presence of the inhibitors significantly altered the activation of the GTPases that promote actin remodelling and this sensitivity confers to macropinocytosis its unique susceptibility to inhibitors of Na^+/H^+ exchange.

5.2 Introduction

The family of Rho GTPases comprises 20 members which are divided into five

subgroups based on amino acid sequence similarity (Wherlock and Mellor 2002;

Burridge and Wennerberg 2004). The discovery of their role in regulating actin

organization and focal adhesion dynamics was a seminal moment in understanding the

importance of these molecules (Ridley and Hall 1992; Ridley et al. 1992) in cellular

signaling. Rho GTPases are now known to control a diverse set of cellular functions,

including cell migration, gene expression, endocytosis, cell cycle progression and

differentiation (Jaffe and Hall 2005).

Regulation of RhoG Signaling:

RhoG is an evolutionarily conserved member of the Rac-like subgroup of Rho

GTPases, with homologues identified in mammals, *Drosophila,* and *C. elegans* (Hakeda-

Suzuki et al. 2002; Kishore and Sundaram 2002; Vigorito et al. 2004), as described in

Chapter 4. However, RhoG upstream and downstream signaling pathways are to date

poorly characterized. Only a few RhoG downstream effectors have been identified, such

as the ELMO protein family, PI3K, and kinectin (Vignal et al. 2001; Katoh and Negishi

2003; Yamaki et al. 2007). Further, only a few GEFs for RhoG have been described and

no cellular RhoG GAPs are currently known. Until recently, ICAM-1 and syndecan-4

were the only cell surface receptors shown to modulate RhoG activity after their

engagement (van Buul et al. 2007a; Elfenbein et al. 2009) by ligands. However, given the

high degree of conservation of RhoG, its broad expression pattern, and the diversity of

RhoG functions, other receptors are also likely involved in modulating RhoG activation.

Epidermal growth factor (EGF) receptor signaling involves a complex network of pathways (Oda et al. 2005). Upon ligand binding, the dimerized EGF receptor (EGFR) undergoes a conformational shift which stimulates its intrinsic kinase activity (Ferguson 2008; Landau and Ben-Tal 2008), resulting in autophosphorylation of the receptor. This autophosphorylation facilitates binding of numerous proteins to phosphorylated residues on the receptor, thereby initiating downstream signaling pathways. Additionally, direct phosphorylation of target proteins by the EGFR also contributes to signaling. Major signaling targets activated by EGFR signaling are src-family kinases (Osherov and Levitzki 1994), phosphatidylinositol 3-kinase (PI3K) (Rodrigues et al. 2000) and the mitogen-activated protein kinase (MAPK) (Sasaoka et al. 1994; Jones et al. 1999). Additionally, several Rho GTPases are regulated by EGF. For instance, several different mechanisms have been described for the activation of Rac1 and Cdc42 after EGF stimulation (Scita et al. 1999; Marcoux and Vuori 2003; Ray et al. 2007; Itoh et al. 2008).

In the first part of this study we looked for extracellular factors which stimulate RhoG activity and the signaling pathways involved. We identified EGF as a strong and rapid activator of RhoG, whereas other growth factors were not. We focused our studies on the immediate activation of RhoG and its close homologue Rac1 within 30 s after EGF stimulation. This early time point suggested that activation occurs by direct signaling from the activated EGFR to RhoG GEF(s) that could rapidly activate the GTPase. We found different GEFs to be involved in EGF-induced RhoG activation in a cell type-specific manner, including members of the Vav family and PLEKHG6, suggesting that the composition of GEFs in a given cell type dictates the morphological change induced by EGF stimulation (dorsal ruffling versus cell spreading).

Unique Properties of Signaling during Macropinocytosis:

The macropinocytosis induced by EGF stimulation in this study is the most effective way for cells to ingest large amounts of extracellular fluid. In some cell types macropinocytosis is a constitutive process: immature dendritic cells use it to sample soluble antigens (Sallusto et al. 1995) and *Dictyostelium* amoeba for nutrient uptake (Cardelli 2001). Constitutive macropinocytosis is also observed in fibroblasts transformed with oncogenic v-Src or K-Ras (Amyere et al. 2000; Amyere et al. 2002). Alternatively, macropinocytosis can be transiently induced by growth factors, such as epidermal growth factor (EGF) or macrophage colony-stimulating factor (Racoosin and Swanson 1989; West et al. 1989).

The remodelling of the cytoskeleton that leads to macropinocytosis requires phosphatidylinositol-3-kinase (PI3K) activity at the plasma membrane (Araki et al. 1996; Rupper et al. 2001; Lindmo and Stenmark 2006). While the entire signaling sequence is incompletely understood, the GTPases Rac1 (West et al. 2000) and Cdc42 (Garrett et al. 2000) as well as p21-activated kinase-1 (PAK1) (Dharmawardhane et al. 1997; Dharmawardhane et al. 2000) are involved in actin polymerization, and CtBP1/BARS is required for macropinosome closure (Liberali et al. 2008). The activation of PI3K and the engagement of Rho-family GTPases are common to a variety of actin-dependent processes such as phagocytosis and chemotaxis. Thus, treatment with inhibitors like wortmannin and *Clostridium difficile* toxin B effectively block most actin-based processes, as well as macropinocytosis. In contrast, macropinosome formation appears to be uniquely susceptible to inhibition by amiloride and its analogues, and this property has been extensively used as an identifying feature of macropinocytosis (West et al. 1989;

264

Veithen et al. 1996; Meier et al. 2002). Amiloride, a guanidinium-containing pyrazine derivative, has been used extensively as an inhibitor of Na^+/H^+ exchangers (NHEs) (Grinstein et al. 1989; Orlowski and Grinstein 2004). However, amiloride is not a universal, nor a specific inhibitor of NHE: the affinity of the different NHE isoforms for amiloride varies greatly and, importantly, the drug also inhibits conductive Na^+-channels and Na^+/Ca^{2+} exchangers (Alvarez de la Rosa et al. 2000; Masereel et al. 2003). To increase the potency and selectivity of NHE inhibitors several amiloride analogs have been synthesized, including ethylisopropylamiloride (EIPA) (Masereel et al. 2003) and (3-methylsulphonyl-4-piperidinobenzoyl)guanidine methanesulphonate (HOE-694), which is specific for the NHE1 isoform (Counillon et al. 1993).

How amiloride inhibits macropinocytosis remains unknown. To the extent that EIPA also blocks macropinocytosis, NHEs are likely to play a role in the process (Cosson et al. 1989; West et al. 1989), but the mechanism linking ion exchange and vacuole formation is not apparent. Three possible mechanisms can be contemplated: 1) uptake of Na^+ by the exchangers may increase the intracellular solute concentration, driving osmotically obliged water and causing swelling that would favor the protrusion of macropinocytic pseudopods. Though the stoichiometric exchange of Na^+ for H^+ is osmotically neutral, extruded H^+ are replaced from intracellular buffers, resulting in a net osmotic gain; 2) NHE could be acting indirectly by altering the cytosolic concentration of calcium, which has been suggested to regulate macropinocytosis (Falcone et al. 2006). Na^+ delivered intracellularly in exchange for H^+ can promote the uptake of calcium via Na^+/Ca^{2+} exchange; 3) the effect of NHE on macropinocytosis may be mediated by changes in cytosolic pH. Stimulation of NHE by hormones or growth promoters has

been shown to alkalinize the cytosol (Rothenberg et al. 1983; L'Allemain et al. 1984; Grinstein et al. 1985; Pouyssegur et al. 1985; Van Obberghen-Schilling et al. 1985). Conversely, inhibition of the antiporters impairs the ability of cells to eliminate H^+ generated metabolically and can cause acidification (L'Allemain et al. 1984; Grinstein et al. 1985; L'Allemain et al. 1985; Liaw et al. 1998). The changes in pH resulting from modulation of NHE activity could conceivably alter the signaling and/or cytoskeletal rearrangements required for macropinocytosis.

Functional Relationship between Macropinocytosis and Na^+/H^+ Exchange:

In addition to the studies delineating a novel signaling pathway to RhoG downstream of EGF stimulation, and the GEFs involved, we investigated the functional relationship between macropinocytosis and Na^+/H^+ exchange. Macropinocytosis was induced in A431 cells by EGF, and NHE activity was modulated pharmacologically and by ion substitution. Our results indicate that NHE1 activity is required to attain a critical H^+ concentration in the immediate vicinity of the plasma membrane that promotes actin polymerization during macropinocytosis.

Our collaborators were able to demonstrate that the prototypical NHE inhibitor amiloride effectively inhibited EGF-induced fluid phase uptake and actin polymerization, as did HOE-694, a more selective NHE antagonist that also blocks Na^+/H^+ exchange. Together, their work confirms the burst of metabolic acid generation downstream of EGF stimulation and demonstrates that its effects are more pronounced in the immediate vicinity of the membrane, where macropinocytic lamellipodia extend. These and previous data (Cosson et al. 1989; West et al. 1989), however, cannot define whether entry of Na^+

or extrusion of H^+ is the critical event. By omitting Na^+ from the medium, they were able to effectively neutralize the metabolic acidification triggered by EGF via an K^+/H^+ ion exchange ionophore. Importantly, the ability of EGF to induce TMR-dextran uptake was restored by nigericin, implying that extrusion of H^+, and not the entry of Na^+, per se, is the key requirement for macropinosome formation. Their work also showed that the alkalinization mediated by NHE1 that normally accompanies stimulation by EGF through the extrusion of H^+ ions is not absolutely required for macropinocytosis because the latter persists when pH_c is clamped with nigericin/K^+. Instead, it is more likely that NHE activity is required to prevent the development of a membrane-localized acidification that may be deleterious to macropinocytosis. To evaluate this possibility, they measured the intracellular pH dependence of macropinocytosis. The uptake of TMR-dextran in response to EGF was quantified in cells where pH_c was clamped at the desired level using nigericin/K^+. Maintaining pH at a level comparable to that attained when cells are stimulated in physiological media enabled the cells to respond to EGF with robust macropinocytosis, despite the absence of Na^+. Normal macropinocytosis was also observed when pH_c was clamped near the resting level recorded in unstimulated cells (7.5-7.6). However, even modest reduction in pH produced marked, highly significant decreases in macropinocytic efficiency and virtually complete inhibition was noted at pH 6.8. They further were able to show that in contrast to the exquisite sensitivity of macropinocytosis to acidification, clathrin-mediated endocytosis was virtually unaffected by modest changes in pH_c and was inhibited only after marked cytosolic acidification. Next, they attempted to ascertain the pH sensitivity of the signals leading to macropinocytosis. Dynamic assessment of the behavior of pH_c-clamped cells by DIC

microscopy revealed that the extension of membrane ruffles, rather than their closure to form macropinosomes, was affected by moderate acidification. This suggested that an early step in the signalling cascade was impaired by pH. However, phosphorylation of the EGF receptor was robustly stimulated by EGF and this effect persisted in the presence of HOE-694 or in the absence of Na^+. This implies that downstream signalling events must be responsible for most of the pH dependence of macropinocytosis. Through sequential analysis of the signaling components, neither adaptors that bind the EGF receptor to transduce downstream signals, nor recruitment and activation of PI3K were affected by clamping the pH_c at either pH 7.8 or 6.8. Of interest, however, PIP_3 generated by PI3K serves to target to the membrane and to stimulate guanine nucleotide exchange factors (GEFs) that activate Rho-family GTPases (Lemmon et al. 2002; Lindmo and Stenmark 2006). GEFs like Vav2 and Tiam1 transduce the signals of the PI3K to Rac1 and Cdc42, contributing to membrane ruffling and macropinocytosis (West et al. 2000; Marcoux and Vuori 2003; Ridley 2006; Garrett et al. 2007; Ray et al. 2007). Of note, initial imaging studies suggested that EGF-induced redistribution of Rac1/Cdc42 binding partners to the membrane was eliminated when cells were stimulated in Na^+-free, NMG^+-rich buffer, implying that Rac1/Cdc42 activation is impaired by decreased cytosolic pH.

5.3 Results and Discussion

EGF Induces Rapid Activation of RhoG:

In order to identify physiologic stimuli which regulate RhoG signaling, our collaborator tested a panel of growth factors and measured the activity status of RhoG. Interestingly, when starved HeLa cells were treated with media containing physiologic concentrations of EGF (20 ng/ml) (Sigismund et al. 2005), a strong increase in active RhoG levels compared to cells treated with media lacking EGF was noted. Levels of active Rac1 also increased after EGF treatment, as described previously (Dise et al. 2008).

To understand the kinetics of RhoG activation after EGF stimulation we measured levels of active RhoG in HeLa cells at time points from 30 seconds to 10 minutes after EGF treatment. Interestingly, RhoG peak activation was observed as early as 30 seconds after EGF treatment, whereupon its activity began to decrease between 5 and 10 minutes. Rac1 activity followed the same kinetic as also reported by others in a different cell type (Patel et al. 2007). Equivalent activation kinetics of RhoG and Rac1 occurred in experiments using higher concentrations of EGF (data not shown). We also observed RhoG activation after 30 seconds of EGF treatment in a different cell line (A431), which showed that EGF-induced RhoG activation at 30 seconds is not limited to HeLa cells. Using our previously developed biosensor for RhoG activity (Chapter 4), we showed that in single cells, these kinetics were consistent, with rapid activation of RhoG initiating at 10 seconds, peaking 30-40 seconds after stimulation, and trailing off at 5 to 10 minutes. This activation was diffuse, with stronger activation within the lamellipodium where it has been shown previously that more EGF receptor exists (Assaker et al. 2010). A

striking difference between our results with EGF-induced RhoG activation compared to the recently reported FGF-induced RhoG activation (Elfenbein et al. 2009) is the time course with which this occurs. RhoG activation in response to FGF treatment peaks after 10 minutes, whereas the peak activation of RhoG is already reached 30 seconds after treating cells with EGF and has returned almost to baseline levels by 10 minutes. EGF-induced RhoG activation also differs mechanistically from FGF-induced RhoG activation. Syndecan-4 engagement by FGF induces the release of RhoG from GDI-1 by PKCα-mediated phosphorylation of GDI-1 (Elfenbein et al. 2009). In contrast, EGF stimulation leads to rapid RhoG activation by activating GEFs and does not require PKC activity.

Because of the fast activation of RhoG and Rac1 by EGF treatment (30 seconds) and in order to separate these events from later (potentially secondary or autocrine loop) activation events of these GTPases, we refer from here on to their activation at 30 seconds as the 'rapid activation'.

Identification of GEFs Mediating the Rapid Activation of RhoG:

Next we aimed to identify GEFs involved in the rapid activation of RhoG after EGF stimulation. Only a limited number of GEFs have been described which stimulate nucleotide exchange of RhoG. We first sought to test the involvement of the RhoG GEF SGEF (Ellerbroek et al. 2004) and our collaborators' results suggested that SGEF does not play a role in the rapid activation of RhoG after EGF treatment.

Given their strong link with EGF signaling, GEFs of the Vav family appeared to be other likely candidates for the rapid activation, (Pandey et al. 2000; Zeng et al. 2000),

270

since Vav2 and Vav3 are expressed in many different cell types (Turner 2002) and they are known GEFs implicated in Rac1 activation after EGF stimulation. Interestingly, our collaborator found that Vav2 and Vav3 activation increased after 30 seconds of EGF stimulation. This result strongly suggested that Vav2 and Vav3 are mediating the rapid activation of RhoG. Thus, he tested whether Vav2 and Vav3 were essential for RhoG activation by EGF. When Vav2 or Vav3 were knocked down simultaneously the rapid activation of RhoG after EGF treatment was completely abolished.

Therefore, we conclude that Vav2 and Vav3 jointly mediate the rapid activation of both RhoG and Rac1 by their direct phosphorylation by the EGFR kinase. A possible explanation for the EGF-specific activation of RhoG is the involvement of a receptor-specific scaffold which promotes coupling of Vav GEFs to RhoG. It was previously shown that after EGF and PDGF stimulation 90% of the activated signaling proteins are identical, but 10% are unique (Kratchmarova et al. 2005). It will be interesting to look for the critical component(s) mediating EGF signaling to RhoG activation. Our results do not exclude that other tyrosine kinase receptors exist which activate RhoG. The TrkA receptor is a potential candidate for this, as NGF was shown to stimulate neurite outgrowth through RhoG (Katoh et al. 2000).

Involvement of PLEKHG6 in Rapid Activation of RhoG in A431 Cells:

Recently, another GEF, PLEKHG6, was implicated in RhoG activation in the epidermoid carcinoma cell line A431 (D'Angelo et al. 2007). It has also been shown that EGF-induced macropinocytosis in A431 cells depends on PLEKHG6. As macropinocytosis is a known RhoG-mediated function, we wondered if PLEKHG6 also

contributes to RhoG activation in A431 cells in a cell type specific manner. First we wanted to confirm that PLEKHG6 has *in vivo* GEF specificity for RhoG. In agreement with results from D'Angelo and coworkers, endogenous RhoG activity was increased when myc-PLEKHG6 was expressed in Cos-7 cells. PLEKHG6 does not appear to be ubiquitously expressed in all tissues and cell lines (D'Angelo et al. 2007). We therefore considered that PLEKHG6 might be an additional GEF mediating the rapid activation of RhoG after EGF stimulation in those cells in which it is expressed. siRNAs targeting PLEKHG6 were transfected into HeLa and A431 cells. Strikingly, our collaborator observed decreased RhoG activity after EGF stimulation in A431 cells, but not in HeLa cells. Our collaborator also tested the influence of knock-down of Vav-GEFs in A431 cells and found that Vav2 knock-down led to the same decrease of rapid activation of RhoG and Rac1 as did the double knock-down of Vav2/Vav3. In summary, the composition of GEFs in A431 cells is different from HeLa cells (PLEKHG6 and Vav2 versus Vav2/Vav3) in terms of GEFs that regulate the rapid activation of RhoG and Rac1.

A431 cells are well known for the rapid formation of dorsal ruffles after EGF application (Araki et al. 2007). Furthermore, PLEKHG6 was previously shown to induce dorsal ruffle formation when over-expressed in different mammalian cells (D'Angelo et al. 2007). We therefore tested if RhoG and PLEKHG6 regulate EGF-induced dorsal ruffle formation of A431 cells. siRNA-transfected A431 cells were plated at sub-confluent densities and serum-starved before being stimulated with 20 ng/ml EGF. Differential interference contrast (DIC) microscopy movies of isolated cells were taken and later categorized for cells that form dorsal ruffles (dorsal-ruffle phenotype; Figure

5.1A, upper row) versus cells that spread a large lamellipodium in multiple directions (Rac1-like phenotype; Figure 5.1A, bottom row). We found that the majority of control siRNA-transfected cells (78%; ±3.5% SEM) responded to EGF treatment with the formation of dorsal ruffles (Figure 5.1B). Interestingly, when we knocked down RhoG or PLEKHG6, the fraction of dorsal ruffling cells significantly decreased and increased numbers of cells showed the Rac1-like phenotype (RhoG siRNA: 39% dorsal ruffling and 61% Rac1-like phenotype (each ±10.2% SEM); PLEKHG6 siRNA: 52% dorsal ruffling, 48% Rac1-like phenotype (each ±4.7% SEM)). These results show that RhoG and PLEKHG6 are necessary for dorsal ruffle formation in A431 cells after EGF stimulation. Furthermore, when we analyzed A431 cells transfected with siRNA targeting Vav2 / Vav3, we observed significantly fewer cells with a Rac1-induced phenotype, with more cells forming dorsal ruffles (95% dorsal ruffling, 5% Rac1-like phenotype (each ±2.7% SEM). Of note, the dorsal ruffles formed by cells transfected with Vav2 / Vav3 siRNA had an overall different morphology compared to control cells, in that the dorsal protrusions appeared to be extended further out of the dorsal surface of the cell (data not shown). Overall, these results indicate that PLEKHG6 is the critical component which dictates the different EGF-induced morphological response of HeLa cells compared to A431 cells. PLEKHG6 was previously shown to induce spontaneous dorsal ruffle formation when overexpressed in HeLa cells. To test, if PLEKHG6 is indeed the component which leads to EGF induced ruffle formation in A431 cells, we expressed very low levels of PLEKHG6 in HeLa cells. At this expression level the cells did not form spontaneous ruffles (Figure 5.1C), but after stimulating the cells with EGF, we observed formation of dorsal ruffles, which could not be observed in cells transfected

with mCherry empty vector (Figure 5.1D). In conclusion, multiple GEFs (Vav-GEFs and PLEKHG6) are involved in EGF induced RhoG activation in a cell type specific manner and dictates the resulting cellular response.   Our results with HeLa cells and A431 cells demonstrate that the composition of GEFs involved in EGF-induced signaling varies between different epithelial cell types. Furthermore, the timing of activation of a Rho GTPase downstream from EGF is likely another critical parameter that determines which kinases, GEFs, and GAPs are involved.

At the outset of this work, we did not anticipate finding a role for the GEF PLEKHG6 in the rapid activation of RhoG in response to EGF stimulation. PLEKHG6 was previously described as a GEF for RhoG, and to a lesser extent also for Rac1 (D'Angelo et al. 2007). Furthermore, PLEKHG6 appears to be a critical factor which controls cellular morphological responses after EGF treatment, since we could convert non-ruffling HeLa cells expressing very low levels of PLEKHG6 to ruffling HeLa cells after stimulating with EGF. Interestingly, D'Angelo and coworkers found that PLEKHG6 can act as a scaffold and forms a ternary complex consisting of Ezrin, PLEKHG6, and RhoG (D'Angelo et al. 2007). Thus, it is possible that in addition to its function as a RhoG GEF, PLEKHG6 might also serve to localize RhoG to the plasma membrane, placing it into close proximity with the EGFR. Experiments with PLEKHG6 mutants which do not bind to Ezrin, but retain GEF activity could further clarify the role of PLEKHG6 in rapid activation of RhoG.

Thus, we demonstrate here that RhoG is rapidly activated by EGF through GEFs of the Vav-family and, depending on the cell type, through the GEF PLEKHG6. We found that this rapid activation regulates dorsal membrane dynamics, including ruffling

274

and EGFR internalization. Our future work will focus on RhoG activation after longer periods of EGF stimulation and the functional consequences of this activation.

Role of pH in the Regulation of Rho GTPases during Macropinocytosis:

It has been known for some time that cellular pH strongly regulates both cell migration (Heuser 1989; Heuser and Anderson 1989) and macropinocytosis. Based on our collaborator's work, we ruled out pH sensitivity of most signaling proteins upstream of the Rho GTPases. To assess whether decreased pH_c affects preferentially Rac1 or Cdc42, we used two different methods. We initially performed a biochemical assay, sedimenting the active form of the GTPases using immobilized PBD-GST, followed by immunoblotting with Rac1 or Cdc42-specific antibodies. In cells clamped at pH 7.8, both Rac1 and Cdc42 were stimulated by EGF, as found earlier (Kurokawa et al. 2004). At pH_c 6.8, however, the activation of both GTPases was depressed. The effect was more apparent for Rac1, which is stimulated more robustly at pH 7.8 (Figures 5.2A and 5.2B).

We analyzed the spatio-temporal dynamics of Rac1 and Cdc42 activation using FRET biosensors (Figures 5.2C and 5.2D). A clone of A431 cells that is more amenable to transfection was used for these experiments, which require simultaneous expression of two constructs. This clone responded to EGF with ruffling and macropinocytosis and the response was largely suppressed at pH 6.6. As shown in Figure 5.2C, treatment with EGF induced localized activation of Rac1 at the ruffles and similar, though less robust responses were recorded for Cdc42. When the cytosol was acidified, however, the responses of both GTPases were largely obliterated (Figures 5.2C and 5.2D). Thus, the FRET analysis is consistent with the biochemical data, indicating that Rac1 and to a

lesser extent Cdc42 are activated by EGF and that both GTPases are sensitive to moderate cytosolic acidification. These data are consistent with our previous results showing that EGF-induced dorsal ruffling leading to macropinocytosis is greatly impaired by the loss of the GEFs Vav2/Vav3 in HeLa cells and Vav2/PLEKHG6 in A431 cells, suggesting that the GTPases are the critical mediators of macropinosome formation.

The preceding results indicate that Rac1 and Cdc42 are stimulated by EGF, but do not directly link their activity to ruffling and macropinocytosis. A causal relationship was established taking advantage of the ability of the PBD domain of PAK and the CRIB domain of WASP to bind to active Rac1 and Cdc42, respectively. When expressed at low levels, these domains serve as reliable probes of GTPase activation, but when overexpressed they can scavenge away a major fraction of Rac1 or Cdc42 and thereby induce functional inhibition (Figures 5.2E and 5.2F). Thus, involvement of both Rac1 and Cdc42 is required for optimal macropinocytosis.

EGF is a potent activator of macropinocytosis. Concomitantly, EGF also stimulates Na^+/H^+ exchange via NHE1. Stimulation of NHE1 by growth promoters, including EGF, has been repeatedly found to induce cytosolic alkalinization, particularly when bicarbonate is omitted (Rothenberg et al. 1983; L'Allemain et al. 1984; Ganz et al. 1989; Sardet et al. 1991; Yanaka et al. 2002). These observations prompted the widely held view that the stimulatory effects of the growth factors were mediated by, or at least required, an increase of pH_c above its resting value. In support of this notion, amiloride and its analogues were reported to preclude the alkalinization and in parallel inhibit cellular proliferation (L'Allemain et al. 1984; L'Allemain et al. 1985; Van Obberghen-Schilling et al. 1985).

Amiloride and HOE-694 also effectively inhibit macropinocytosis (West et al. 1989; Sallusto et al. 1995; Veithen et al. 1996; Meier et al. 2002). Extending the rationale applied to cellular proliferation, it can be postulated that cytosolic alkalosis signals, or is permissive to macropinosome formation. An alternative possibility is that the net osmotic gain associated with Na^+/H^+ exchange drives water influx and swelling of the advancing lamellipodia. While appealing, these possibilities are not consistent with our data: EGF activated macropinocytosis under conditions where pH_c was maintained at or even slightly below the resting (unstimulated) level. Moreover, macropinocytosis persisted in the absence of Na^+, e.g. when nigericin/K^+ were used to clamp pH_c.

These observations can be reconciled when considering the changes in pH_c induced by EGF. The growth factor stimulates metabolic generation of H^+ equivalents, but these are effectively extruded by NHE1, which is activated concomitantly. Indeed, in the presence of physiological $[Na^+]$ the stimulation of the antiporter outstrips the rate of H^+ generation, resulting in a net alkalinization. The occurrence of a metabolic burst is only unmasked when Na^+/H^+ exchange is prevented. We therefore propose that macropinocytosis is not directly sensitive to amiloride or even to inhibition of NHE1, but is instead impaired by the acidification that results when excess H^+ production is uncompensated by the regulatory action of the Na^+/H^+ antiporter.

If macropinocytosis is merely responding to the cytosolic acidification, what makes it uniquely sensitive to amiloride and its analogues? Other endocytic processes, including uptake of transferrin through clathrin-coated pits, are also affected by low pH_c (Davoust et al. 1987; Sandvig et al. 1987; Cosson et al. 1989). However, individual endocytic pathways display differential sensitivity to changes is pH_c: a modest

acidification ($pH_c \approx 6.8$) virtually eliminated macropinosome formation, while inhibition of clathrin-mediated endocytosis requires a more profound acidification ($pH_c \leq 6.0$) (Davoust et al. 1987; Sandvig et al. 1987). Moreover, geometrical considerations may accentuate the drop in pH experienced during macropinocytosis. When Na^+/H^+ exchange is impaired, the H^+ generated metabolically during signalling and actin polymerization is likely to accumulate in the thin lamellipodia, where diffusional exchange with the bulk cytosolic buffers is restricted. Accordingly, our probes of submembranous pH revealed that during macropinocytosis the acidification is more profound in the immediate vicinity of the receptors than in the cytosol overall. Cell motility, another process dependent on extension of lamellipodia, is similarly sensitive to the pH_c and requires NHE1 for optimal function (Lagana et al. 2000; Denker and Barber 2002; Stock et al. 2005; Frantz et al. 2007; Frantz et al. 2008).

The nature of the pH-sensitive step(s) in macropinocytosis was analyzed by measuring individual events in the signaling cascade while clamping pH_c. We found that the activation of Rac1/Cdc42 and their effectors was profoundly inhibited (Figure 5.2). This conclusion is consistent with earlier observations of Frantz et al. (Frantz et al. 2007), who noted the pH dependence of Cdc42 activation at the leading edge of migrating cells. We therefore conclude that the exchange factors that activate Rac1/Cdc42 and/or the GTPases themselves are highly sensitive to pH_c. Tiam1, Vav2, and Dock180 have been implicated in EGF-R mediated activation of Rac1 and Cdc42 (Marcoux and Vuori 2003; Tamas et al. 2003; Makino et al. 2006; Ray et al. 2007). However, initial attempts to discern which GEFs were involved in this process were unsuccessful.

Irrespective of the exact mechanism whereby decreased cytosolic pH affects small GTPase activation and actin assembly, our results indicate that amiloride and related compounds generate their inhibitory effects as a consequence of submembranous acidification caused by metabolic H^+ generation, unopposed by the regulatory extrusion across the membrane. The unique sensitivity of macropinocytosis, compared to other endocytic processes, results from a complex convergence of circumstances: a large and sustained metabolic burst that occurs within a diffusionally constrained compartment, the thin lamellipod.

5.4 Materials and Methods

Materials and Reagents:

Nigericin and EGF were from Molecular Probes (Carlsbad, CA). Lipofectamine LTX was from Invitrogen (Carlsbad, CA), Fugene6 from Roche (Basel, Switzerland), mouse monoclonal anti-Rac1 and anti-Cdc42 were from BD Biosciences (Franklin Lakes, NJ). All other chemicals were from Sigma.

Isotonic Na$^+$-rich buffer contained 140 mM NaCl, 3 mM KCl, 1 mM MgCl$_2$, 1 mM CaCl$_2$, 5 mM glucose and 20 mM HEPES (pH 7.4). In NMG$^+$-rich buffer NaCl and KCl were replaced by 143 mM NMG-chloride, and in K$^+$-rich buffer NaCl was replaced by 100 mM K-glutamate and 43 mM KCl.

Cells, Media, Transfection and Growth Factor Stimulation:

HeLa and A431 cells were obtained from the LCCC tissue culture facility (UNC Chapel Hill). HeLa and A431 cells were cultured in DMEM (high glucose, with glutamine, Gibco) supplemented with 10% fetal bovine serum (Sigma) and antibiotics (Gibco). For transfection of plasmid DNA, FuGene6 (Roche) was used according to the manufacturer's protocol. For transfection of siRNAs into HeLa cells siQuest reagent (Mirus) was used according to the manufacturer's instructions. Briefly, 1.5 ml serum-free media was mixed with 18 µl siQuest reagent and 11.25 µl of a 20 µM siRNA stock solution. After 20 min incubation at room temperature the complexes were added to a 10 cm tissue culture dish (cell confluency ~ 50%) with 7.5 ml fresh media containing serum. 24 h after transfection the media was changed and 48 h after transfection the cells were

split 1:2. The cells were used for subsequent experiments between 72 to 96 h post

transfection.

For growth factor stimulation experiments, cells were initially starved in

DMEM/0.5% delipidated BSA or Ham's F12K without phenol red (Invitrogen, CA,

delipidated BSA, Sigma) for 4 h. Subsequently, the media was replaced by DMEM/0.5%

delipidated BSA or Ham's F12K without phenol red supplemented with the

corresponding growth factor at the indicated concentration. Human recombinant EGF

was obtained from R&D Systems. All growth factors were used at a final concentration

of 20 ng/ml unless otherwise indicated.

Plasmids and Expression Constructs:

The Rac1 FRET biosensor was reported previously (Kraynov et al. 2000; Machacek et al.

2009), and here includes modifications to improve FRET efficiency reported in

(Machacek et al. 2009). The Cdc42 biosensor uses an intermolecular design as reported

by several groups (Itoh et al. 2002; Seth et al. 2003; Tzima et al. 2003; Hoppe and

Swanson 2004), but here is further optimized by the use of different fluorescent proteins

and of a Cdc42-binding domain from WASP, a fragment shown to provide good

selectivity for activated Cdc42 in a previously developed biosensor with a different

design (Nalbant et al. 2004; Frantz et al. 2007; Machacek et al. 2009). Both biosensors

were generated by first constructing plasmids encoding either Rac1 or Cdc42 fused to the

C terminus of CyPet, a CFP variant optimized for FRET (Nguyen and Daugherty 2005),

and either the CRIB domain from p21-activated kinase (PBD) published previously

(Machacek et al. 2009) or the Cdc42-binding CRIB domain from WASP (CBD), amino

acids 230–314, fused to the C terminus of YPet, a YFP variant optimized for FRET (Nguyen and Daugherty 2005). The EGFP coding region from the EGFP-C1 vector (Clontech, Inc.) was replaced with a PCR product containing the CyPet or YPet coding regions flanked by an NcoI restriction site and a SGLASELGS linker containing a BamHI restriction site. The PCR products of the Rac1, Cdc42, PBD, and CBD coding sequences were inserted between the BamHI restriction site in the SGLASELGS linker and an EcoRI restriction site in the downstream multiple cloning site of the vector. The 殘邢瑤裳猪术雙择ぐ　教壮款transfected into A431 cells using Lipofectamine LTX, Amaxa Nucleofection kit according to the manufacturer's instructions.

Rac1 and Cdc42 Activity Assays

FRET biosensor imaging cell culture conditions: A431 cells were maintained in Dulbecco's modified Eagle's medium (Mediatech, Manassas, VA) with 10 % FBS. For all imaging experiments, cells were plated on fibronectin-coated (5 μg/ml) glass coverslips 12 hours prior to imaging. Cells were initially starved in Ham's F-12K without phenol red (Invitrogen, Carlsbad, CA) with 0.01% delipidated BSA (Sigma) and 15 mM HEPES (Mediatech, Manassas, VA) for 4 hours. The cells were then incubated in an open chamber (Warner Instruments, Hamden, CT) in the K^+-rich/nigericin isotonic buffer described above for 10 minutes, then transferred to a heated stage for imaging. After imaging for 3 minutes, 200 ng/mL EGF (Sigma, St. Louis, MO) was added to the open chamber, and imaging was continued for an additional 10 minutes. Cells were chosen for low expression levels so that neither YPet-PBD nor YPet-CBD inhibited macropinocytosis.

Imaging the Activity of One Rho GTPase per Cell:

Activation levels of both Rac1 and Cdc42 were measured in living cells by monitoring the ratio of FRET (CyPet to YPet) to CyPet emission, and corrected for bleed-through from CyPet and YPet as detailed below. Time-lapse sequences were acquired on an Olympus IX81 inverted epifluorescence microscope, using an Olympus 40x UPlan FLN1.3 N/A DIC lens, CoolsnapES^2 CCD camera (Roper Scientific) and Metamorph software (Universal Imaging). For emission ratio imaging, the following filter sets were used (Chroma): CyPet: D436/20, D470/40; FRET: D436/20, HQ535/30; YPet: HQ500/20, HQ535/30. A dichroic mirror ("Quad-Custom" Lot# 511112038) was custom manufactured by Chroma Technology Corporation for compatibility with all of these filter sets. Cells were illuminated with a 100 W Hg arc lamp through an ND 1.0 neutral density filter. At each time point, three images were recorded with the following exposure times: CyPet (1.2 s), FRET (excitation of donor, observation of acceptor emission) (1.2 s), YPet (0.4 s) at binning 2x2. We routinely changed the order of acquisition for all experiments, varying between the order CyPet, FRET, YPet, or FRET, CyPet, YPet. The image sets were taken at 10s intervals. Ratio calculations to generate activity images were performed following bleed-through correction methods described previously. Briefly, Metamorph software was used for image alignment and ratiometric calculation of activation signals. All images were shading-corrected and background-subtracted. Binary masks with values equal to 1 inside the cell and 0 elsewhere were extracted by applying a threshold to the CyPet image, because it had the largest signal-to-noise ratio. Control cells expressing either CyPet alone or YPet alone were used to obtain bleed-through coefficients, α and βin the following equation:

$$FRET\ Ratio = \frac{FRET - \alpha \cdot CyPet - \beta \cdot YPet}{CyPet}$$ (Equation 1)

where R is the Ratio, $FRET_t$ is the total FRET intensity as measured, α is the bleed-through of CyPet into the $FRET_t$ signal, β is the bleed-through of YPet into the $FRET_t$ signal and CyPet and YPet are the total CyPet and YPet intensities as measured through the CyPet and YPet filter sets, respectively. The bleed-through parameter α is given by the slope of the linear relationship between FRET and CyPet intensities upon CyPet excitation of cells expressing only CyPet. Similarly, the bleed-through parameter β is given by the slope of the linear relationship between FRET and mYPet intensities of cells expressing only the mYPet. The α parameter was found to be 0.4~0.5 and the β parameter was ~0.2. Both were dependent on the particular optical configuration of the microscope used. With these parameters, the ratio of corrected FRET over CyPet was calculated and used as a measure of Rac1 and Cdc42 activation. In time-lapse experiments, CyPet and YPet typically bleach at different rates. Therefore, the ratio was corrected for photobleaching as described in {Hodgson, 2006 #648; Nalbant, 2004 #190}.

For visual representations of ratio images, a linear pseudocolor lookup table was applied to all ratio images and the ratio values were normalized to the lower scale value, which was chosen to exclude the bottom 5% of the total histogram distribution, avoiding spurious low intensity pixels. In each experiment, all images were carefully inspected to verify that all portions used to create the ratio image had a sufficiently high signal/noise ratio. We targeted at least 300 gray level values (12 bit dynamic range) above background in the lowest intensity regions within the cell (S/N > 3). This was especially important in thin parts of the cell where fluorescence was low. Furthermore, we routinely reversed the order of image acquisition to confirm that the effects of motion artefacts

associated with sequential image acquisition were not significant. We have used this

approach previously to show that the order of data acquisition did not affect the measured

ratio (Nalbant et al. 2004; Pertz et al. 2006).

5.5 Acknowledgments

5.6 Figures and Legends

Table 5.1: siRNA Sequences Used in this Study

A list of siRNA sequences used and their targets.

Protein	Anti-sense	Sense
PLEKHG6 (#1)	UAGCAGAUCAGUCAUGAUCdTdT	GAUCAUGACUGAUCUGCUAdTdT
PLEKHG6 (#2)	UUAGUUUCUUGCUGUUCUCdTdT	GAGAACAGCAAGAAACUAAdTdT
RhoG	GCAACAGGAUGGUGUCAAGUU	CUUGACACCAUCCUGUUGCUU
Vav2	UCACAGAGGCCAAGAAAUUdTdT	AAUUUCUUGGCCUCUGUGAdTdT
Vav3	UUUCAGAACUUAAUGCUCCTGdTdT	GGAGCAUUAAGUUCUGAAAdTdT
Control	UCACUCGUGCCGCAUUUCCdTdT	GGAAAUGCGGCACGAGUGAdTdT

287

Figure 5.1: RhoG and PLEKHG6 are Required for Dorsal Ruffle Formation in A431 cells after EGF Stimulation.

(A) A431 cells were transfected with the control, RhoG or PLEKHG6-specific siRNAs. After 72 hours the cells were plated on fibronectin-coated coverslips (20 μg/ml). After 4 hour serum starvation, the cells were treated with 20 ng/ml EGF and DIC microscopy movies of individual cells were taken (10 seconds per frame, 480 seconds total). Cellular ruffling response showed either a 'dorsal ruffling phenotype' (upper row, arrowheads indicate dorsal ruffles, also shown enlarged in the inset) or a 'Rac-like ruffling phenotype' (bottom row). Bar: 20 μm.

(B) Quantification of the occurrence of dorsal-ruffle phenotype versus Rac1-like phenotype after transfecting the different siRNAs. Shown are averaged results from three independently performed experiments. Asterisk indicate significant difference compared to control siRNA transfected cells (according to ttest, $p < 0.05$ and $p < 0.01$, respectively).

(C) HeLa cells were transfected with low amounts of expression constructs for mCherry or mCherry-PLEKHG6 and analyzed for dorsal ruffle formation after EGF treatment.

(D) Quantification of the frequency of EGF induced dorsal ruffle formation of HeLa cells transfected with the indicated expression constructs.

Figure 5.1

A

Dorsal ruffle phenotype (A431 cells)

0 sec | 60 sec | 120 sec | 240 sec | 480 sec

Rac1-like phenotype (A431 cells)

B
EGF induced ruffles (A431 cells)

ctr siRNA | RhoG siRNA | PLEKHG6 #2 siRNA | Vav2/3 siRNA

■ dorsal
□ Rac-like

C **mCherry transfected HeLa cells**

-EGF
+EGF

mCherry-PLEKHG6 transfected HeLa cells

-EGF
+EGF

D
EGF induced dorsal ruffles (HeLa cells)

cells forming dorsal ruffles after EGF stimulation (%)

EGF − + − +

mCherry | mCherry-PLEKHG6

Figure 5.2: Effect of pH on Activation of Rac1 and Cdc42.

(A) Analysis of activated Rac1 and Cdc42 before and after treatment for 5 min with EGF, while clamping pHc at the indicated values. Active Rac1 and Cdc42 were pulled down using GST-PBD–coated beads.

(B) Quantification of the effect of pHc-clamping on EGF-induced Rac1 and Cdc42 activation analyzed by GST-PBD pull-down. Data are means ± SE of three experiments. Data were compared between pHc 7.8 and pHc 6.8; *, $P < 0.05$.

(C) Assessment of Rac1 activation by FRET imaging of genetically encoded biosensors. Activation of Rac1 was measured by FRET as detailed in Materials and methods before and after treatment with EGF, while clamping pH at pHc 6.6 or pHc 7.8. Dashed lines in whole-cell images (middle) align with the direction of protrusion and indicate the area selected for kymography and line-scan analysis (right). Bar, 10 μm.

(D) Quantification of Rac1 and Cdc42 activation analyzed by FRET using line-scan analysis of the regions studied by kymography as in A. Data are means ± SE of three experiments analyzing 6–8 cells in each; ***, $P < 0.001$.

(E) Effect of overexpression or PBD-YPet or CBD-YPet on macropinocytosis. Confocal images of cells transfected with PBD-YPet or CBD-YPet (left) incubated with EGF and TMR-Dextran (right) for 10 min in Na^+-rich medium to assess macropinocytosis. Dashed lines indicate outlines of cells. Bar, 10 μm.

(F) Quantification of macropinocytosis in untransfected or in highly transfected cells by measuring TMR-Dextran fluorescence intensity (right). Data are means ± SE of three experiments. Data were compared between untransfected and transfected cells; ***, $P < 0.001$.

Figure 5.2
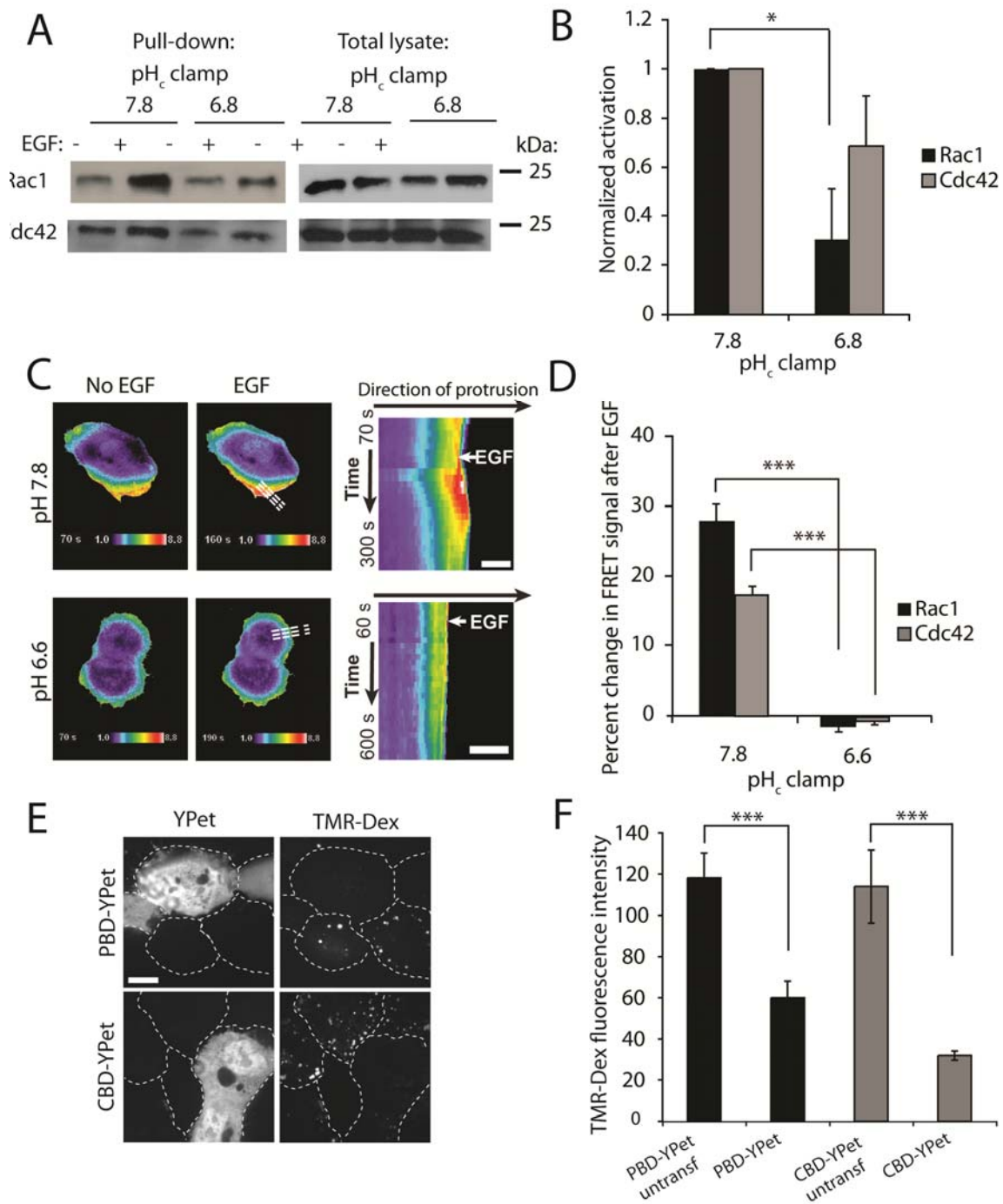
CHAPTER SIX: ROLE OF RHO GTPASES IN TRANSENDOTHELIAL MIGRATION

6.1 Abstract

Blood leukocytes play a critical role in immune surveillance and the host response to foreign antigens. In inflammation, an inflammatory stimulus or antigen causes the extravasation of leukocytes to the site of the stimulus or antigen. Extravasation of these leukocytes into tissues is the critical process of transendothelial migration (TEM), and excessive TEM is seen in a variety of inflammatory disorders, including ischemia-reperfusion injury after heart attack, atherosclerosis, and asthma (Jones et al. 2000; Worthylake and Burridge 2001; Hordijk 2006; Galkina and Ley 2007; van Buul et al. 2007b), among others. Interestingly, mouse models predisposed to atherosclerosis demonstrate that disruption of endothelial cell adhesion molecule interactions reduces the development of atherosclerotic plaques (Lichtman et al. 1996; Lutters et al. 2004; Galkina and Ley 2007). One of these adhesion molecules, intracellular adhesion molecule 1 (ICAM-1), is critical for leukocyte adhesion in TEM, and is upregulated by inflammatory stimuli (Ross 1999; Cybulsky et al. 2001). It is unclear how engagement and clustering of ICAM-1 by leukocyte integrins induces cytoskeletal changes necessary to produce TCs and the directional TEM of leukocytes. However, given their prominence in signaling leading to cytoskeletal rearrangement and previous studies in this field, the Rho GTPases are known to be key coordinators of this process. In this study, we attempt to better understand the roles of the Rho GTPases in TEM, with the

goal of identifying novel signaling targets for reducing the pathological inflammation

seen in the development and consequences of CVD and other inflammatory diseases.

6.2 Introduction

Blood leukocytes play a critical role in immune surveillance and the host response to foreign antigens. In inflammation, an inflammatory stimulus or antigen causes the extravasation of leukocytes to the site of the stimulus or antigen via the critical process of transendothelial migration (TEM). Excessive TEM is seen in a variety of inflammatory disorders. In an effort to modulate inflammatory signals and leukocyte recruitment, TEM has been studied intensively. The paradigm of leukocyte TEM signaling divides the process into three steps: rolling adhesion, firm adhesion, and TEM. In rolling adhesion, selectins on the leukocyte bind weakly to carbohydrate ligands on the endothelial surface. Next, leukocytes encounter endothelial-bound chemokines which in turn activate leukocyte integrins, facilitating firm adhesion through binding and clustering of the leukocyte integrins $\alpha_4\beta_1$ and $\alpha_{L/M}\beta_2$ to the endothelial ligands VCAM-1 and ICAM-1, respectively (Springer 1994). At this point, it is thought that engagement and clustering of VCAM-1 and ICAM-1 stimulates endothelial cell signaling which permits leukocytes to pass through or between cells to reach the inflammatory stimulus. How the endothelium responds still remains a subject of controversy.

Transmigratory Cup Composition:

Current knowledge of transcellular TEM signaling suggests that leukocyte adhesion to the endothelium clusters endothelial ICAM-1 via the integrins $\alpha_{L/M}\beta_2$, inducing the formation of microvillous cup-like structures that embrace the migrating leukocytes within minutes. The leukocytes also probe the endothelial cells via podosomes during TC formation (Carman et al. 2007). ICAM-1 signaling is clearly

294

important in TEM since the cytoplasmic tail is required for TC formation and leukocyte TEM across the endothelium (Greenwood et al. 2003). The signals downstream of ICAM-1 are poorly defined in TC formation, but recent studies have delineated a number of molecules that co-localize to TCs. TCs are thought to be caveolar compartments containing clustered ICAM-1 (Millan et al. 2006), closely linked to the actin cytoskeleton by filamin (Gauthier-Rouviere et al. 1998; Bellanger et al. 2000), to the cortical cytoskeleton by the modulators ezrin and moesin (Barreiro et al. 2002), to the intermediate filament cytoskeleton by vimentin (Nieminen et al. 2006), and to the microtubule cytoskeleton (Carman and Springer 2004). Morphological alteration of the cytoskeleton to form TCs also depends critically on Ca^{2+}, intact microtubules, and actin, since Ca^{2+}-chelators, microtubule polymerization inhibitors, and actin polymerization inhibitors all impair TC formation and leukocyte TEM (Carman et al. 2003). Once formed, TCs also present chemokines apically to adhered leukocytes (Middleton et al. 1997), guiding leukocytes through the endothelium.

Transmigratory Cup and TEM Signaling Pathways:

It is unclear how engagement and clustering of ICAM-1 by leukocyte integrins induces cytoskeletal changes necessary to produce TCs and the directional TEM of leukocytes. TCs are thought to be similar to phagocytic cups found in other cell types (Millan et al. 2006), and it is possible that similar molecules are involved in their formation. One signaling molecule involved is RhoG, a Rho GTPase 72% identical to Rac1 and 62% identical to Cdc42 in sequence, which has been shown to be activated in the phagocytosis of apoptotic cells (deBakker et al. 2004; Henson 2005). Upon

stimulation, RhoG activates effector proteins while also activating Rac1 via the ELMO/DOCK180 complex in parallel (Wennerberg et al. 2002; Prieto-Sanchez and Bustelo 2003), but the *in vivo* significance of this RhoG-mediated Rac1 activation remains unknown. RhoG has also been localized to the plasma membrane with microtubules and filamin (Gauthier-Rouviere et al. 1998), as well as with ICAM-1 in TCs (van Buul et al. 2007a), and can modulate the actin cytoskeleton similar to Rac1 (Wennerberg et al. 2002). RhoA has also been proposed to play a role in TC formation but its role is controversial as different labs have obtained different results regarding its importance (Etienne et al. 1998; Barreiro et al. 2002; Thompson et al. 2002; Carman et al. 2003; Carman and Springer 2004; Millan et al. 2006; van Buul et al. 2007a). Since TC formation is rapid and highly dynamic, the signaling activity producing TCs must be spatio-temporally orchestrated, making traditional biochemical and fixed cell approaches ineffective in resolving the signaling kinetics of the Rho GTPases (Pertz et al. 2006), but the approach in this study overcomes many of these problems.

To study the Rho GTPases involved in this process, we have used our previously developed sensors for RhoA, Rac1, and RhoG to study their activation downstream of ICAM-1 ligation by anti-ICAM-1-antibody-coated beads. By analysis of RhoA, Rac1, and RhoG activity, we have been able to establish a sequence of timing events for the activation of these GTPases downstream of ICAM-1 ligation.

6.3 Results

Establishment of a Model System for Studying ICAM-1 Ligation and Downstream Signaling:

Previous work has established the use of anti-ICAM-1-antibody coated beads as a method for ligating ICAM-1 and activating endothelial Rho GTPases (Thompson et al. 2002; Millan et al. 2006; van Buul et al. 2007a). Using this information as a starting point, we attempted to establish a model cell system in which to study ICAM-1 ligation and activation of downstream pathways. First, 3 μm latex beads were conjugated with anti-ICAM-1 antibody or a control anti-IgG antibody to ascertain whether the beads would bind to Cos-7 cells, the choice model cell system, given their lack of endogenous ICAM-1 expression. When both the anti-ICAM-1 and control beads were added to Cos-7 cells, or to mouse embryonic fibroblasts, a parallel control, neither bead type bound the cells. However, if ICAM-1-mCherry was overexpressed in either cell line, only the anti-ICAM-1 beads were demonstrated to bind tightly (Figure 6.1A) and only to the cells expressing ICAM-1, and generally tracked along with retrograde actin flow toward the center of the cell (Figure 6.1B). Further, bead binding led to clustering of ICAM-1 around the beads, as expected (Figure 6.1C). Interestingly, 8μm and 10 μm beads, while closer to the size of leukocytes, had some significant disadvantages. One, they were much more autofluorescent, and compared to the 3μm beads which demonstrated a directional flow over the cells due to convective heating within the imaging chamber, they simply fell onto cells and adhered non-selectively preventing a specific analysis of ICAM-1 ligation.

Examining Rac1 Activity Downstream of ICAM-1 Ligation:

Once established that ICAM-1 could be selectively bound and ligated by 3μm anti-ICAM-1 beads, we attempted to study the activation of Rac1 in this system. Cos-7 cells expressing both a dual-chain Rac1 activity FRET sensor and ICAM-1-mCherry were treated with the anti-ICAM-1 beads and examined for changes in Rac1 activation under or surrounding the beads (Figure 6.2A). Addition of beads and binding to the ICAM-1-mCherry expressing cells led to an initial decrease in Rac1 activation directly beneath the bead, which was persistent over time. However, these bead binding events ultimately led to transient, robust activation of Rac1 downstream of the ligation of ICAM-1 (Figure 6.2B). This was in contrast to initial observations that showed immediate recruitment of Rac1 protein to these bead-binding sites. Thus, protein recruitment did not correlate with the observed activity. These bursts of Rac1 activation were short in duration (~10 minutes maximal duration) but of high intensity, reaching between 5 and 10-fold higher than baseline Rac1 activity. To confirm that this activation was not an artefact of the sensor itself, or of optical alterations due to the refraction of light by beads on the surface of the cell, a Rac1 dominant negative sensor (T17N) was tested, in addition to replacing components of the sensor with fluorophore only. None of these conditions led to the transient, high-level Rac1 activation events seen in the wild-type condition. Quantitation of bead binding events that led to Rac1 activation showed that Rac1 was activated by over 40% of bead binding events, whereas sensor controls (fluorophore only donor or acceptor constructs) and the Rac1 T17N dominant negative sensor showed virtually no transient Rac1 activation events. Further, when the C-terminus of ICAM-1, which is responsible for binding signaling partners, was truncated,

transient Rac1 activation events were reduced dramatically, suggesting that the ligation of ICAM-1 specifically activates Rac1 in a transient manner downstream (Figure 6.2C). We again noted the recruitment of ICAM-1-mCherry to sites of bead adhesion with the wild-type ICAM-1 construct, but not when the C-terminus was truncated (Figure 6.2D).

Further, upon bead recruitment of ICAM-1, we attempted to discern as previously reported whether a transmigratory "cup" or docking structure was formed. By performing imaging on a disk-spinning confocal microscope, we were able to assess the structure of the membrane around the bead. After deconvolution and 3-D reconstruction of the image, it was noted that ICAM-1-mCherry formed finger-like projections that surround the attached bead (Figure 6.2E), consistent with previous reports in the literature. These finger-like projections seemed to form before the initiation of Rac1 activity, as they were present on the majority of attached beads (but not all). These behaviors have also been confirmed in human umbilical vein endothelial cells (HUVECs) and primary microvascular cells (data not shown) pre-treated with TNFα to induce ICAM-1 surface expression.

Examining RhoA Activity Downstream of ICAM-1 Ligation:

Previous biochemical work has shown that both RhoA and Rac1 are activated downstream of ICAM-1 in endothelial cells (Adamson et al. 1999; Thompson et al. 2002; van Buul et al. 2007a; Fernandez-Borja et al. 2010). Since Rac1 activation was visualized as described above, we wanted to establish a spatiotemporal relationship between RhoA and Rac1 signaling downstream of ICAM-1 ligation. Thus, we attempted to perform the same experiments as done above for Rac1. At this point, we shifted most

of our experimentation to primary microvascular endothelial cells as it had been established that bead-binding and Rho GTPase activation were detectable in the model system. Microvascular cells express low levels of ICAM-1 at the cell surface at baseline (Wertheimer et al. 1992), and therefore should not bind anti-ICAM-1 or control beads, and indeed this was found to be the case. After treatment with TNFα to induce ICAM-1 expression at the surface of cells, we found that the anti-ICAM-1 beads did bind selectively to the endothelial cells. A single-chain RhoA activation FRET biosensor was expressed in these cells via adenoviral transduction, and the cells were treated first with TNFα, then with anti-ICAM-1 beads.

Surprisingly, consistent depression of RhoA activity around the site of the bead was observed. This depression was immediate and sustained (Figure 6.3A). This result was at odds with previous biochemical data demonstrating activation of RhoA (Adamson et al. 1999; Thompson et al. 2002). Thus, there were two possibilities: 1) RhoA was being activated focally at another site that was not previously appreciated, or 2) RhoA was being activated globally in response to local ligation of ICAM-1 (with evidence being the formation of stress fibers (Adamson et al. 1999; Thompson et al. 2002)). To address this, we examined cells more closely. First, it was noted that in DIC images, cells did seem to contract almost immediately upon bead adherence, especially at junctional regions between cells. Examination of RhoA activity at these sites demonstrated activation of RhoA at junctional regions, perhaps indicating a contractile response mediated by actomyosin contractility (Figure 6.3B). Further, examining global, rather than local (around the bead) RhoA activity demonstrated a small increase in diffuse RhoA activation of approximately 2.5% compared to controls at 0.5% (data not

shown) in a limited data set. Thus, it is possible that the activation seen biochemically is a diffuse activation of RhoA coupled to the actomyosin network. Further experiments would need to be performed to address this possibility, such as blocking actomyosin contractility downstream of RhoA and observing whether cell junctions were separated upon bead binding as seen previously. Further, if stress fiber formation in these cells was examined, an increase upon bead binding would be likely, and should happen rapidly if RhoA activation is diffuse rapid. Additionally, blockade of actomyosin contractility would abrogate the stress fiber response if this hypothesis were true.

Examining RhoA Activity Downstream of Applied Mechanical Force:

To attempt to answer the previous question about whether RhoA activation is global, focal, or possibly both, we examined RhoA activation in a well-characterized system, namely mechanical force application, to determine whether RhoA activation could be detected. Previous work has repeatedly demonstrated that the application of mechanical force to cells causes cellular stiffening via RhoA activation leading to actomyosin contractile forces (Choquet et al. 1997; Matthews et al. 2006) . Thus, it was anticipated that this would be an excellent system in which to address whether a focal application of force to cells would activate RhoA locally or globally, and whether it could be detected. To address this, bovine aortic endothelial cells (BAECs) were used as a model system, as they have many of the cell surface receptors that the endothelial cells used previously do. To treat these cells, 3 μm magnetic beads were conjugated with anti-PECAM-1 antibody specific for PECAM-1 on the surface of the endothelial cells, since PECAM-1 is known to transduce force in endothelial cells (Tzima et al. 2005). The cells

were plated, allowed to spread, and subsequently treated with the beads. The beads were then subjected to mechanical force application of 2 nN and observed at 0, 2, 5, or 30 minutes post-force, in addition to the same experiments performed with control IgG beads that would not bind the cells. When the endothelial cells were plated on fibronectin, biochemical pull-down assays for GTP-loaded RhoA showed RhoA activation at 2, 5, and 30 minutes post-force application. In contrast, when endothelial cells were plated on collagen, the same experimental setup showed that RhoA activation was seen very prominently at 5 minutes post-force application but less at other time points, suggesting that cellular stiffening responses vary depending on the substrate upon which the cells are plated.

Next, we attempted to discern the nature of these changes in RhoA activation, spatiotemporally. These same cells were transfected with the RhoA activity FRET sensor and the same experiments were performed. Our data (Figure 6.4A) illustrate that the biochemical findings can be recapitulated using the RhoA activity FRET sensor with slightly more variance than is seen biochemically (Matthews et al. 2006). Indeed, in cells plated on fibronectin, we see activation at 2 and 5 minutes, but not at 30 minutes. However, an examination of the individual cellular values at the 30 minute time point suggest that some of the cells are responding with higher than average activity values, and some have returned to baseline by this point, suggesting that the blots were only detecting a portion of the cell population. Similarly, on collagen, we found activation of RhoA to be significant only at the 5 minute time point, consistent with the biochemical data. When we examined these cells for spatial and temporal patterns associated with RhoA, we saw no consistent pattern with the cells plated on fibronectin. In each case,

302

RhoA activation increased globally (Figure 6.4B), as indicated by taking region measurements in different areas of the cell. There was no local increase in RhoA activation surrounding the beads through which force was applied (though this may have been masked by significant autofluorescence from the beads).

With cells plated on collagen, global RhoA activation also increased as with the cells plated on fibronectin (Figure 6.4C), but we also noted a specific increase at the edges of cells, suggesting an increase in cellular ruffling and protrusion, which was not observed in the cells plated on fibronectin. Thus, this provides evidence that RhoA can be activated or inactivated both globally and locally by different stimuli and that these processes may be separable. Thus, this data is consistent with the possibility that RhoA is depressed locally upon ICAM-1 ligation, yet activated globally, as seen in biochemical assays, stress fiber formation assays, and by biosensor studies. Additionally, it is consistent with the hypothesis and data that cells move faster when presented with a stiffer environment, such as a fibronectin-coated glass coverslip (Peyton and Putnam 2005). Thus, if a leukocyte were to move across the surface of cells, it would likely gain greater speed from a stiffer substrate, such as an endothelium exhibiting contractile properties due to RhoA activation, rather than a pliable endothelial surface. Such an idea would be very interesting to test and demonstrate *in vivo*.

Examining RhoG Activity Downstream of ICAM-1 Ligation:

Given that we have established a relationship between RhoA and Rac1 in endothelial cells upon ICAM-1 ligation, we sought to address an additional relationship. It is well known from the literature that the small GTPase RhoG, covered in Chapter 4,

can activate Rac1 directly via the ELMO/DOCK180 complex. This relationship has been

shown to play a role in leukocyte transmigration downstream of ICAM-1 ligation, but the

dynamics of this process have remained poorly understood (van Buul et al. 2007a). Is

RhoG activated first? Are Rac1 and RhoG activated in parallel? To address this

question, we sought to examine RhoG activation downstream of ICAM-1 ligation as

described for Rac1 and RhoA above. Endothelial cells were infected with adenovirus

carrying the RhoG sensor, stimulated with TNFα, and treated with anti-ICAM-1 beads.

Initial observations showed that both RhoG and the ELMO binding domain components

of the biosensor were immediately and rapidly recruited to adhering beads (Figure 6.5A).

In contrast with what we observed for Rac1, RhoG was also immediately activated at the

site of the bead and gradually increased over the first 10 minutes of bead binding (Figure

6.5B). To confirm the specificity of this RhoG activation, and since we were unable to

manipulate the endogenous ICAM-1 as we did in our previous model system, we turned

to endothelial cells derived from mice missing the RhoG-selective GEF, SGEF,

previously shown to be involved in the leukocyte transendothelial migration process (van

Buul et al. 2007a). By performing this same assay in aortic endothelial cells derived

from comparable wild-type (SGEF$^{+/+}$) and knock-out (SGEF$^{-/-}$) mice, stimulated with

TNFα and treated with anti-ICAM-1 beads, the recruitment of RhoG and ELMO binding

domain to beads is abrogated, as is the observed activation of RhoG (Figure 6.5C) in

SGEF$^{-/-}$ cells compared to wild-type cells. This strongly suggests that the ligation of

ICAM-1 leads to activation of SGEF, which in turn activates RhoG selectively

downstream of ICAM-1. The rapidity of this activation further places it upstream of

Rac1 given the results in Figure 6.1 where Rac1 is transiently activated with a delay, but

no causal link between RhoG and Rac1 has yet been demonstrated. We hope to address this by manipulating the ELMO/DOCK180 pathway and showing that the transient activation of Rac1 we see downstream of ICAM-1 ligation is altered or absent when the ELMO/DOCK180 complex is disrupted.

6.4 Discussion and Ongoing Studies

In the present study, we demonstrate differing spatiotemporal dynamics of RhoA, Rac1, and RhoG activation after ligation of ICAM-1 by anti-ICAM-1-antibody conjugated beads. Consistent with the literature (Wennerberg et al. 2002; Katoh and Negishi 2003; van Buul et al. 2007a), RhoG is typically activated before Rac1, and is more constant in nature, suggesting that RhoG is the among the first GTPases activated at these sites of bead binding. Subsequently, Rac1 is transiently activated and the cells attempt to engulf the bead, suggesting that Rac1 may be critical for the closure and internalization of the bead, or *in vivo*, the leukocyte. However, this remains to be elucidated. Further, the temporal delay between RhoG and Rac1 also warrants further investigation. While it is not surprising that Rac1 would be activated after RhoG, given the robust literature indicating that in phagocytic behaviors, and that Rac1 is activated by RhoG via the ELMO/DOCK180 pathway (deBakker et al. 2004), the constant nature of RhoG activity compared to the highly transient Rac1 activation indicates other factors are at play. Is RhoG activation mediated independent of phosphoinositide production and accumulation after ICAM-1 ligation? In contrast, is the delay to Rac1 activation due to the necessary accumulation of phosphoinositides (Chung et al. 2001; Huang et al. 2003; Merlot and Firtel 2003; Welch et al. 2003), or the organization of the ELMO/DOCK180 complex? The literature suggests that indeed, RhoG activation is mediated rapidly, either by the GEFs Trio (deBakker et al. 2004; Park et al. 2007), or SGEF (Ellerbroek et al. 2004; van Buul et al. 2007a), or perhaps both. These questions remain to be investigated, and a variety of tools can be used to address them, such as siRNA against the GEFs, or probes that are available for detecting phosphoinositide accumulation.

We have attempted to address one of these questions, whether RhoG activation is mediated rapidly and immediately downstream of ICAM-1 ligation and clustering. Through the use of SGEF knockout mice, we could quantify RhoG recruitment and activation at sites of anti-ICAM-1-antibody coated bead binding in cells with or without SGEF. These results indicate that SGEF is critical for the immediate, strong activation of RhoG downstream of ICAM-1. However, it remains to be determined how SGEF is activated, and what other signaling partners might be involved in this process.

RhoA, on the other hand, is a stark contrast to RhoG and Rac1. Our findings that RhoA is inactivated locally at the sites of bead binding conflict directly with the literature (Adamson et al. 1999; Wojciak-Stothard et al. 1999; Etienne-Manneville et al. 2000; Thompson et al. 2002; van Buul et al. 2007a). At the moment, I still remain uncertain of the reason for this discrepancy, but believe that the biochemical data do not accurately reflect the possibility that RhoA could be differentially regulated at different locations in the cell at the same time. For example, whole-cell increases in RhoA activation downstream of ICAM-1 ligation are observed, in addition to junctional separation with high RhoA activity. This may be more consistent with the literature, given that ICAM-1 ligation leads to immediate formation of stress fibers (Adamson et al. 1999; Wojciak-Stothard et al. 1999; Etienne-Manneville et al. 2000; Thompson et al. 2002; van Buul et al. 2007a) suggesting global RhoA activation. However, Rac1 is known to antagonize RhoA activation (Arthur et al. 2000; Nimnual et al. 2003; Noren et al. 2003) and thus if activation of Rac1 at bead recruitment sites is observed, this may lead to RhoA inactivation locally. Ongoing studies are attempting to address this issue.

One method used to address this issue indirectly is through the study of RhoA activation by a separate stimulus, magnetic bead-applied mechanical force. Mechanical force, when applied to adherent cells, is well known to activate RhoA (Wang et al. 2005; Matthews et al. 2006). Indeed, these findings were reproduced using a RhoA activity FRET sensor, and it was noted that the activation induced by force application was global, at least on fibronectin, in that activity over the entire cell increased, rather than being due to local increases in activity, which were observed on collagen (Figure 6.4). These findings give credence to the idea that ICAM-1 ligation by beads may lead to global changes in RhoA activation independent of local changes in RhoA activation at the sites of the beads. Certainly more study is warranted in deciphering the mechanisms of RhoA regulation downstream of ICAM-1 ligation.

Once the spatial and temporal relationships between Rac1, RhoA, and RhoG are established, many additional studies can be performed. For example, through genetic manipulation, does loss of any of these GTPases cause blockade of cup formation, and if so, at what stage of formation is the process disrupted? Second, what are the upstream regulators that control this cup formation process? SGEF has been fairly well characterized as one of the GEFs for RhoG in this process, but what are the GEFs for RhoA and Rac1? Does Rac1 become activated due to RhoG and the ELMO/DOCK180 pathway alone? What other signaling partners are required for this process? Are the phases of cup formation, such as ruffle extension versus cup closure distinguishable at a molecular level? Do any new targets for therapeutic intervention in inflammatory disease emerge from these studies? All these answers, and many more experiments await future efforts.

6.5 Materials and Methods

Materials and Reagents:

Lipofectamine was purchased from Invitrogen (Carlsbad, CA), Fugene6 from Roche (Basel, Switzerland).   Mouse monoclonal anti-human ICAM-1 and anti-mouse ICAM-1 antibodies were purchased from BD Biosciences (Franklin Lakes, NJ). All other chemicals were from Sigma. Adenoviral plasmids were generated using the Virapower system from Invitrogen (Carlsbad, CA).

Cell Culture and Constructs:

The Rac1 FRET biosensor was reported previously (Kraynov et al. 2000; Machacek et al. 2009), and here includes modifications to improve FRET efficiency reported in (Machacek et al. 2009), and the RhoG sensor is described in detail in Chapter 4. The Rac1 and RhoG biosensors were generated by first constructing plasmids encoding Rac1 or RhoG fused to the C terminus of CyPet, a CFP variant optimized for FRET (Nguyen and Daugherty 2005), and the CRIB domain from p21-activated kinase (PBD) published previously (Machacek et al. 2009) or the first 95 amino acids of ELMO1 fused to the C terminus or N-terminus, respectively, of YPet, a YFP variant optimized for FRET (Nguyen and Daugherty 2005). The EGFP coding region from the EGFP-C1 vector (Clontech, Inc.) was replaced with a PCR product containing the CyPet or YPet coding regions flanked by an NcoI restriction site and a SGLASELGS linker containing a BamHI restriction site. The PCR products of the Rac1 and PBD coding sequences were inserted between the BamHI restriction site in the SGLASELGS linker and an EcoRI restriction site in the downstream multiple cloning site of the vector.

CyPet-Rac1 T17N was generated by site-directed mutagenesis to generate a point mutation at residue 17 of Rac1. The ELMO-YPet construct was generated by inserting the PCR product for YPet via the EcoRI and XhoI restriction sites in the pTriEx-4 backbone. Then, the PCR product for amino acids 1-95 of ELMO was then cloned in via the restriction sites NcoI and BamHI in the pTriEx-4 backbone. The RhoA FRET biosensor is used as described previously (Pertz et al. 2006). Each of these sensors was then subsequently cloned into the D-Topo pENTR entry vector and then pAd-DEST-CMV-V5 destination vector according to the manufacturer's instructions for the ViraPower adenoviral cloning system (Invitrogen). ICAM-1-mCherry was generated by amplifying ICAM-1 from a template and ligating the PCR product into the EcoRI and BamHI restriction sites within the multiple cloning site of the pEGFP-N1 vector. EGFP was replaced with mCherry in this plasmid by amplifying mCherry from template by PCR and ligating it into the vector via NotI and XhoI restriction sites within the plasmid. To generate the ICAM-1-mCherry C-terminal truncation mutant, a shortened version of ICAM-1 corresponding to amino acids 1-1512 was amplified by PCR and ligated into the EcoRI and BamHI restriction sites within the multiple cloning site of the vector above.

The plasmids were transfected into Cos-7 cells or Bovine Aortic Endothelial cells (BAECs) using Lipofectamine, Fugene6, or the Amaxa Nucleofection kit according to the manufacturer's instructions. For Human Umbilical Vein Endothelial Cells (HUVECs) or primary microvascular endothelial cells, adenovirus containing the coding sequences for the RhoG and RhoA sensors was added to cells to obtain uniform expression at a level appropriate for imaging.

Cos-7 cells were maintained in DMEM supplemented with 10% FBS, penicillin/streptomycin, and 2 mM glutamine. All endothelial cells were maintained in EBM-2 basal growth medium supplemented with endothelial Bullet Kit containing all appropriate growth factors and serum (Lonza Biosciences).

For imaging studies with BAECs, cells were plated on glass coverslips either on fibronectin or collagen, then treated and fixed at the referenced time points in 3.7% paraformaldehyde in Dulbecco's Phosphate Buffered Saline. The coverslips were then mounted on glass microscopy slides for imaging on an inverted Olympus IX81 epifluorescence system set up for FRET imaging as described below.

Antibody Conjugation to Beads:

Three μm amino-functionalized polystyrene beads were acquired from Polysciences, Inc. and coupled with control IgG or anti-ICAM-1 anti-human or anti-mouse antibody according to the manufacturer's instructions. In brief, a 2.5% solution of beads was washed three times with PBS and then reacted with 8% glutaraldehyde at room temperature for 6 hours with agitation. The beads were then washed twice with DPBS, and 200-400 μg of protein per 0.5 mL of 2.5% bead solution was reacted overnight at 4 °C with agitation. The beads were then sequentially blocked with 0.2 M ethanolamine and BSA solution for 30 minutes each at room temperature and resuspended in storage buffer for use. Beads were washed three times in imaging medium before addition to imaging chambers. Magnetic beads were conjugated with control IgG antibody or anti-PECAM-1 antibody and washed in a similar fashion before addition to BAECs.

Magnetic Bead Force Application:

Application of force through control or anti-PECAM-1 antibodies was performed by Caitlin Collins of Dr. Ellie Tzima's lab in collaboration with Dr. Richard Superfine's laboratory using pre-specified protocols.

Rac1, RhoG, and RhoA Activity Assays:

Cos-7 cells were imaged in Ham's F-12K without phenol red (Invitrogen, Carlsbad, CA) with 2% FBS and 15 mM HEPES (Mediatech, Manassas, VA) while endothelial cells were imaged in the same medium they were grown in, EBM-2 supplemented with 2% FBS and endothelial growth factor supplements (Lonza, Inc.). The cells were then incubated in a closed chamber (Warner Instruments, Hamden, CT) with beads added, and immediately transferred to a heated stage for imaging. Cells were chosen for medium expression levels so that in the case of primary endothelial cells junctions remained intact and cellular morphology did not change noticeably. Mouse aortic endothelial cells were isolated by another laboratory and cultured using previously established protocols for the isolation of primary endothelial cells from vasculature.

Imaging the Activity of One Rho GTPase per Cell:

Activation levels of both Rac1 and RhoG were measured in living cells by monitoring the ratio of FRET (CyPet to YPet) to CyPet emission, and corrected for bleed-through from CyPet and YPet as detailed below. Time-lapse sequences were acquired on an Olympus IX81 inverted epifluorescence microscope, using an Olympus 40x UPlan FLN1.3 N/A DIC lens, CoolsnapES^2 CCD camera (Photometrics) and Metamorph software (Universal Imaging). For emission ratio imaging, the following filter sets were

used (Chroma): CyPet: D436/20, D470/40; FRET: D436/20, HQ535/30; YPet: HQ500/20, HQ535/30. A dichroic mirror ("Quad-Custom" Lot# 511112038) was custom manufactured by Chroma Technology Corporation for compatibility with all of these filter sets. Cells were illuminated with a 100 W Hg arc lamp through an ND 1.0 neutral density filter. At each time point, three images were recorded with the following exposure times: CyPet (1.2 s), FRET (excitation of donor, observation of acceptor emission) (1.2 s), YPet (0.4 s) at binning 2x2. We routinely changed the order of acquisition for all experiments, varying between the order CyPet, FRET, YPet, or FRET, CyPet, YPet. The image sets were taken at 10s intervals. Ratio calculations to generate activity images were performed following bleed-through correction methods described previously. Briefly, Metamorph software was used for image alignment and ratiometric calculation of activation signals. All images were shading-corrected and background-subtracted. Binary masks with values equal to 1 inside the cell and 0 elsewhere were extracted by applying a threshold to the CyPet image, because it had the largest signal-to-noise ratio. Control cells expressing either CyPet alone or YPet alone were used to obtain bleed-through coefficients, α and β in the following equation:

$$FRET\ Ratio = \frac{FRET - \alpha \cdot CyPet - \beta \cdot YPet}{CyPet} \quad \text{(Eq. 1)}$$

where R is the Ratio, $FRET$ is the total FRET intensity as measured, α is the bleed-through of CyPet into the $FRET$ signal, β is the bleed-through of YPet into the $FRET$ signal and $CyPet$ and $YPet$ are the total CyPet and YPet intensities as measured through the CyPet and YPet filter sets, respectively. The bleed-through parameter α is given by the slope of the linear relationship between $FRET$ and $CyPet$ intensities upon CyPet excitation of cells expressing only CyPet. Similarly, the bleed-through parameter β is

313

given by the slope of the linear relationship between *FRET* and *mYPet* intensities of cells expressing only the mYPet. The α parameter was found to be 0.4~0.5 and the β parameter was ~0.2. Both were dependent on the particular optical configuration of the microscope used. With these parameters, the ratio of corrected *FRET* over *CyPet* was calculated and used as a measure of Rac1 and RhoG activation. In time-lapse experiments, CyPet and YPet typically bleach at different rates. Therefore, the ratio was corrected for photobleaching as described in (Nalbant et al. 2004; Hodgson et al. 2006) (Nalbant 2004, Hodgson 2006). For RhoA activity, since both donor and acceptor fluorophores are present on the same molecule, no bleedthrough correction was required. At each time point for RhoA, two images were recorded with the following exposure times: CFP (1.2 s) and FRET (0.6 s) using illumination from a 100 W Hg arc lamp through an ND 1.0 neutral density filter. The FRET ratio was calculated as the ratio of FRET/CFP after image processing as described above.

For visual representations of ratio images, a linear pseudocolor lookup table was applied to all ratio images and the ratio values were normalized to the lower scale value, which was chosen to exclude the bottom 5% of the total histogram distribution, avoiding spurious low intensity pixels. In each experiment, all images were carefully inspected to verify that all portions used to create the ratio image had a sufficiently high signal/noise ratio. We targeted at least 300 gray level values (12 bit dynamic range) above background in the lowest intensity regions within the cell (S/N > 3). This was especially important in thin parts of the cell where fluorescence was low and where beads typically adhered. Furthermore, we routinely reversed the order of image acquisition to confirm that the effects of motion artefacts associated with sequential image acquisition were not

significant. We have used this approach previously to show that the order of data acquisition did not affect the measured ratio (Nalbant et al. 2004; Pertz et al. 2006). Further, for the Cos-7 cells where ICAM-1-mCherry and mutants were exogenously expressed, expression was monitored via the red fluorescence channel using the following filter set: D580/30; HQ630/40.

Disk-spinning Confocal Imaging and 3-D Deconvolution:

To obtain three-dimensional images of transmigratory cup formation and ICAM-1 clustering, we utilized an Olympus IX81 inverted epifluorescence microscope, using an Olympus 60x UPlan FLN1.3 N/A DIC lens, CoolsnapES[2] CCD camera (Photometrics) and Metamorph software (Universal Imaging) outfitted with a Nipkow-type disk-spinning confocal unit. Sequential images were acquired for the entire depth of the cell at 50 nm intervals at single time points after the addition of 3μm anti-ICAM-1 beads using 100% illumination from a 100 W Hg arc lamp with a filter set for mCherry: D580/30; HQ630/40 through the custom dichroic described above. Deconvolution and reconstruction of the acquired 3-dimensional image stacks was performed using AutoQuant deconvolution software (Media Cybernetics, Bethesda, MD).

6.6 Acknowledgments

6.7 Figures and Legends

Figure 6.1: Establishment of a Model System for Studying ICAM-1 Ligation and Downstream Signaling.

(A) Cos-7 cells with or without expression of ICAM-1 showing selective adherence of

ICAM-1 beads to mCherry-ICAM-1 expressing cells only (red arrow).

(B) Actin retrograde flow-based movement of beads from the cell edge to cell interior

after bead adherence. Time points shown are at 0 and 200 minutes, and the right-most

panel illustrates the bead track over time.

(C) Cos-7 cell expressing mCherry-ICAM-1 shows that bead adherence leads to

recruitment of ICAM-1 around the beads (red arrows).

Figure 6.1
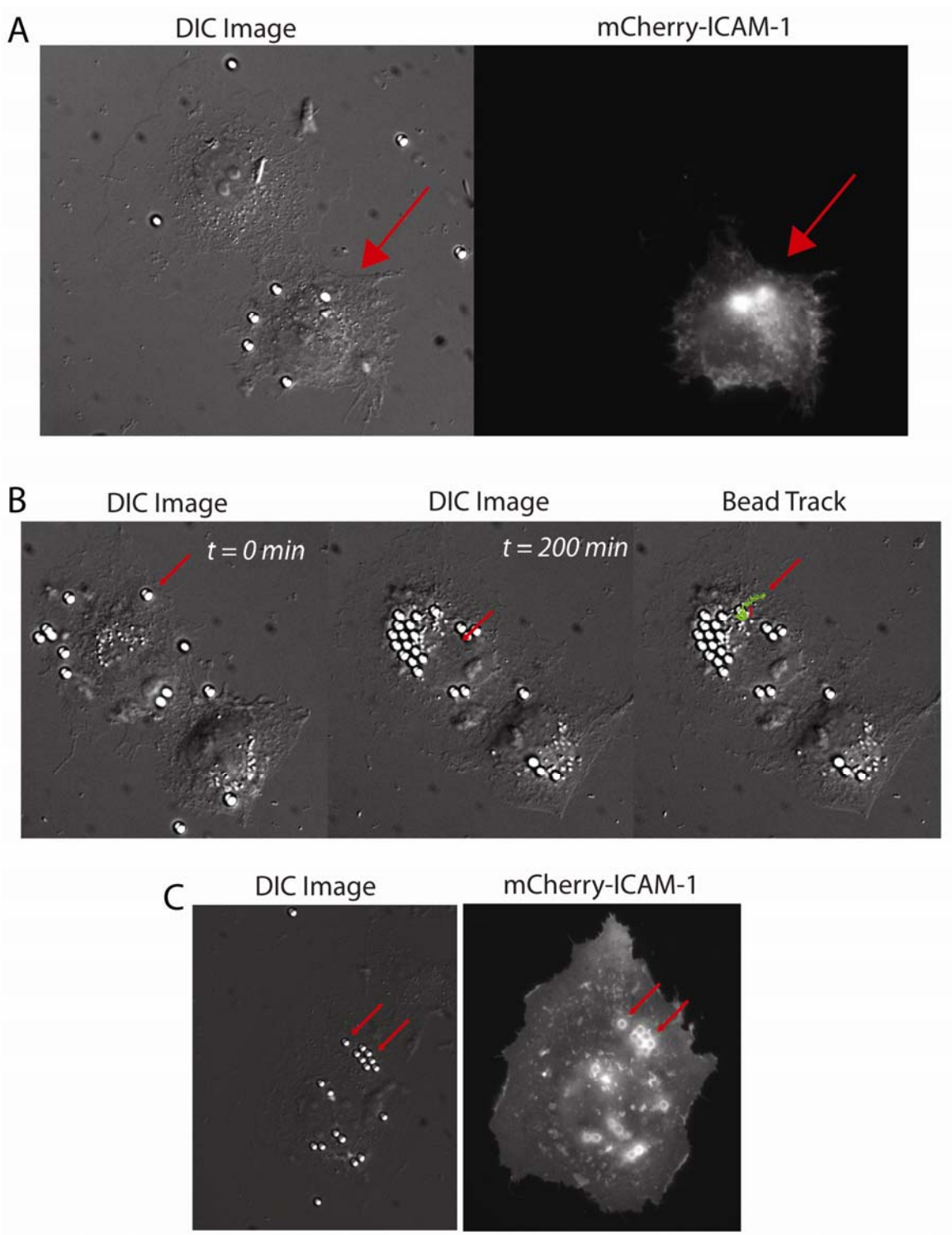
Figure 6.2: Rac1 Activation Downstream of ICAM-1 Ligation.

(A) Cos-7 cell expressing both a Rac1 dual-chain sensor and mCherry-ICAM-1 showing that FRET can be detected in the presence of anti-ICAM-1-antibody coated beads. Activity heat map is indicated in the upper right corner of the lower panel.

(B) Time course of Rac1 activation after bead binding to a Cos-7 cell expressing both a Rac1 dual-chain sensor and mCherry-ICAM-1. Rac1 activity is indicated by the heat map in the upper left corner. DIC image is shown to provide bead location.

(C) Quantitation of transient Rac1 activation events in the context of wild-type ICAM-1, C-terminally truncated ICAM-1, Rac1 T17N, or an optical biosensor control. Rac1 activation events were defined as a 5x increase in Rac1 activation over a nearby region of interest.

(D) Comparison of bead-induced clustering of ICAM-1 in cells expressing wild-type mCherry-ICAM-1 or C-terminally truncated mCherry-ICAM-1.

(E) Deconvoluted disk-spinning confocal image of beads adhered to Cos-7 cell expressing mCherry-ICAM-1. Top panel illustrates recruitment in the x-y plane. Bottom panel illustrates recruitment to cup-like structures in the x-z plane.

Figure 6.2
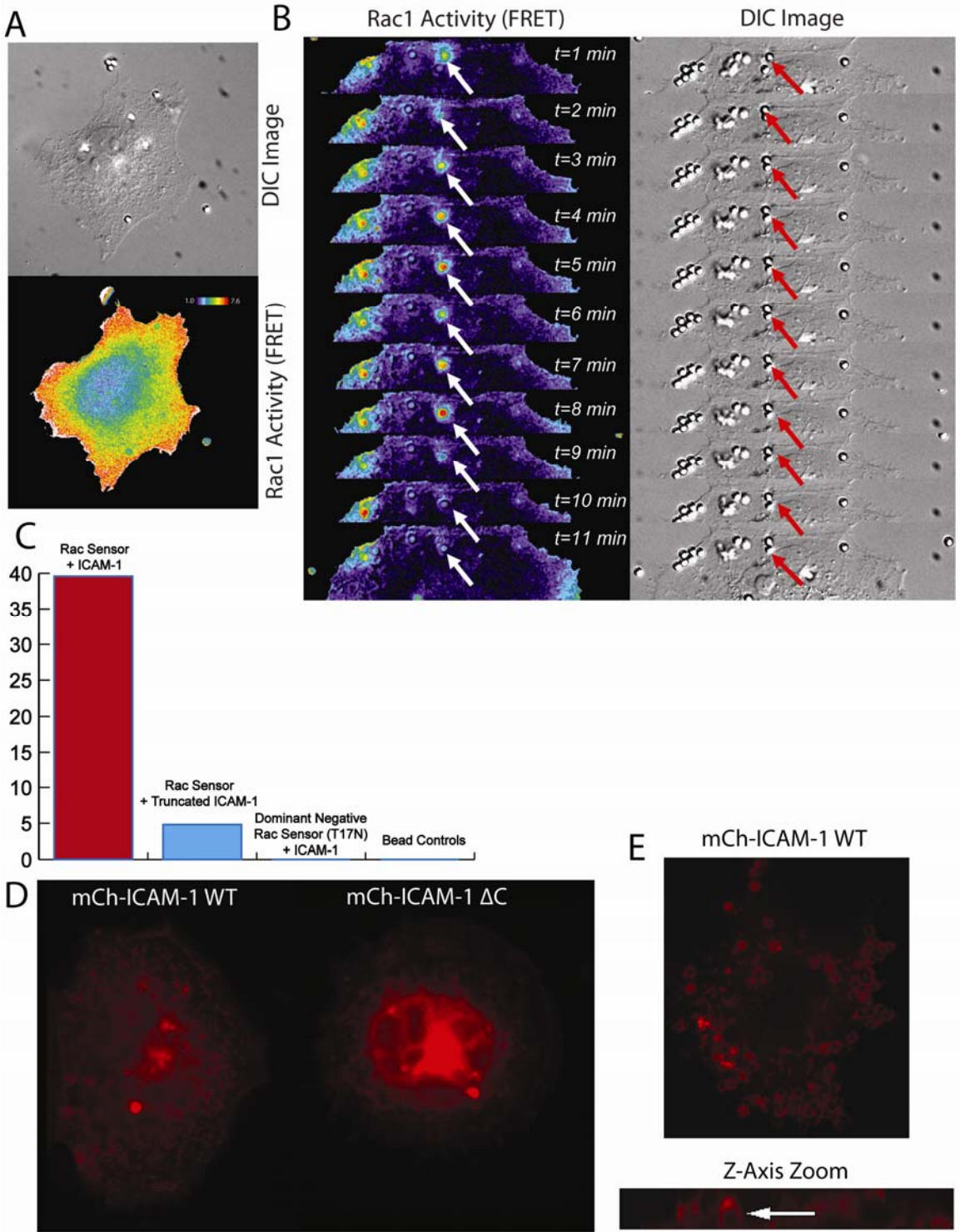
Figure 6.3: RhoA Inactivation Downstream of ICAM-1 Ligation.

(A) Human umbilical vein endothelial cell (HUVEC) expressing a RhoA single-chain sensor after TNFα treatment shows bead binding. RhoA is locally depressed at the site of bead adherence (red arrows). Activity heat map is indicated in the upper left corner. A quantitative illustrative trace of RhoA activity along a linescan through the bead is illustrated at left.

(B) Human umbilical vein endothelial cell (HUVEC) expressing a RhoA single-chain sensor after TNFα treatment shows bead binding. RhoA appears to be activated at regions where cell-cell junctions separate (red arrows). Activity heat map is indicated in the upper right corner.

Figure 6.3
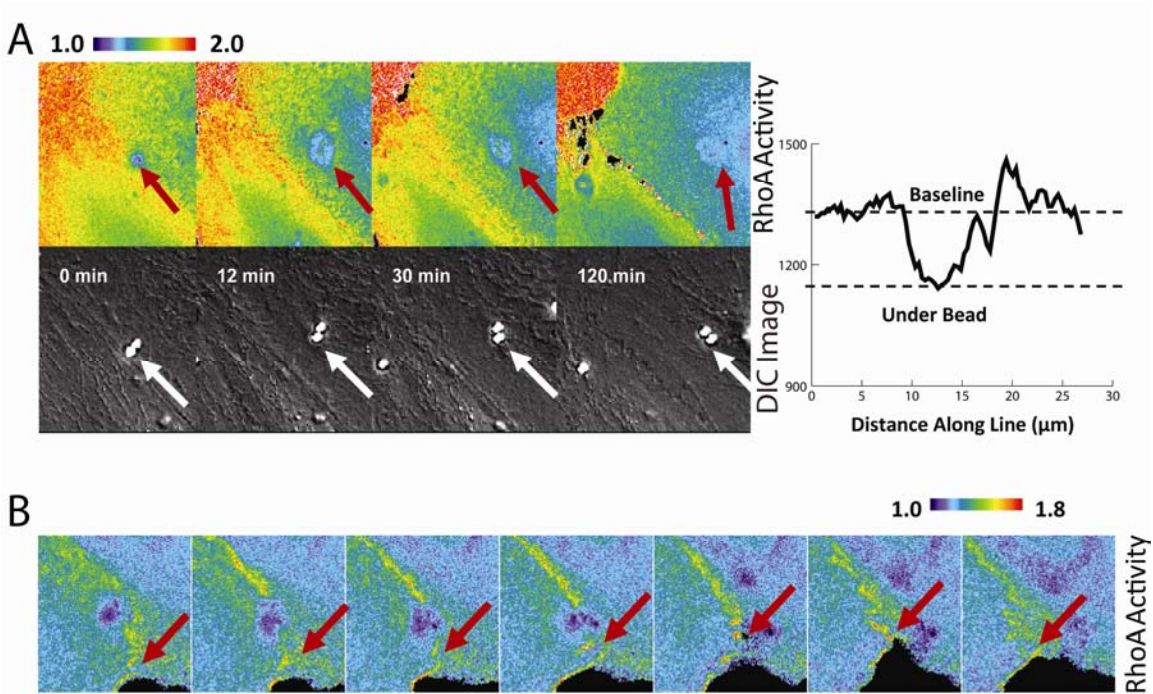
Figure 6.4: RhoA Activation Downstream of Applied Mechanical Force.

(A) Quantitation of whole-cell RhoA activity in fixed Bovine Aortic Endothelial Cells
(BAECs) expressing a RhoA single-chain activity sensor, treated with force and fixed at
the indicated time points.

(B) Example images of whole-cell RhoA activity in fixed Bovine Aortic Endothelial
Cells plated on fibronectin expressing a RhoA single-chain activity sensor, treated with
force, and fixed at the indicated time points. RhoA activity is indicated by the heat map
in the upper panel center.

(C) Example images of whole-cell RhoA activity in fixed Bovine Aortic Endothelial
Cells plated on collagen expressing a RhoA single-chain activity sensor, treated with
force, and fixed at the indicated time points. RhoA activity is indicated by the heat map
in the upper left panel. Red arrows indicate sites of increased peripheral membrane
ruffling after force application.

Figure 6.4

324
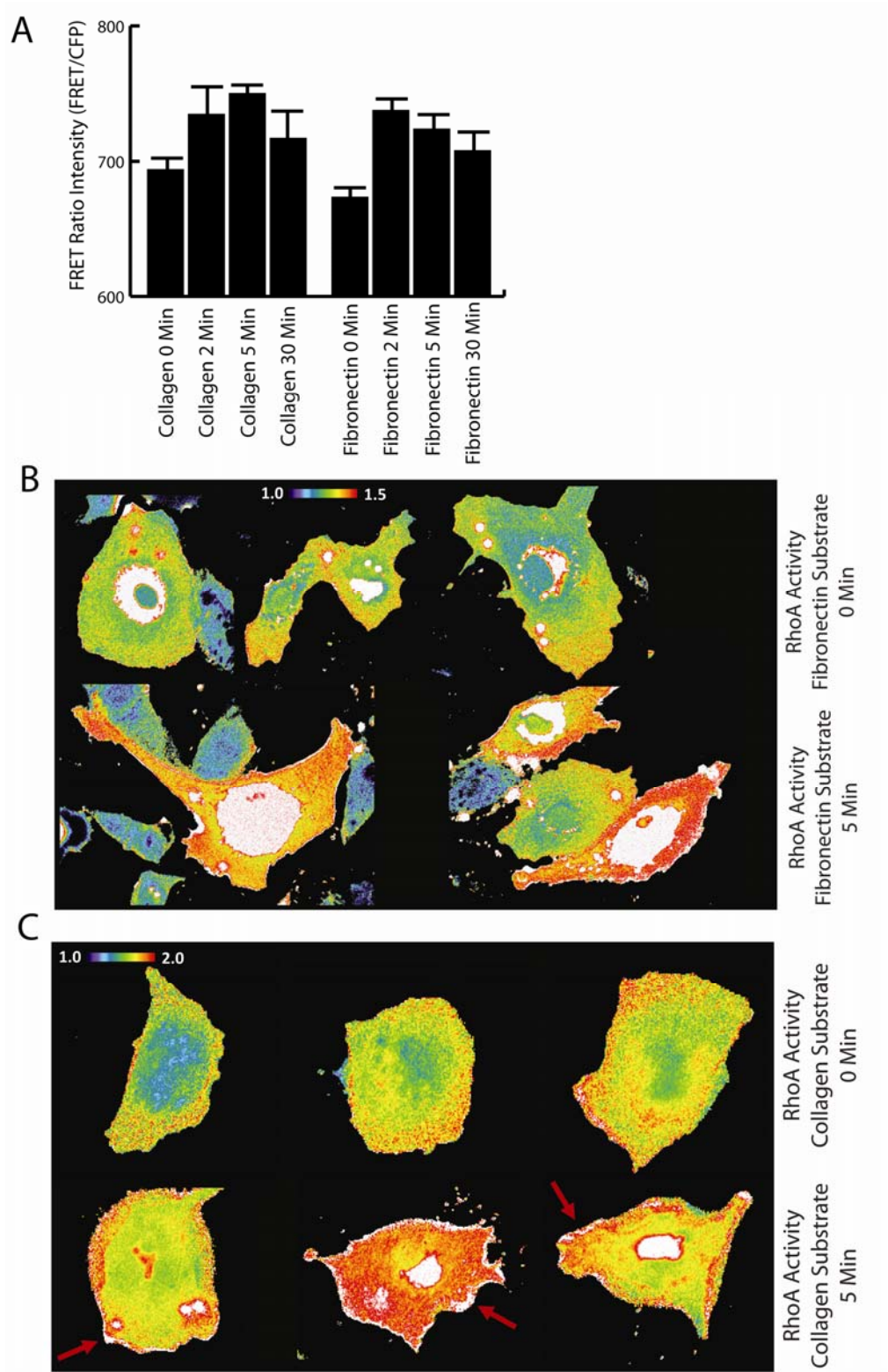
Figure 6.5: RhoG Activation Downstream of ICAM-1 Ligation.

(A) Quantitation of recruitment of CFP-RhoG and YPet-ELMO, components of a RhoG dual-chain biosensor, to adherent beads on mouse aortic endothelial cells isolated from SGEF WT or SGEF$^{-/-}$ mice expressing a RhoG dual-chain biosensor after treatment with TNFα. Right-most panels are examples of increased CFP-RhoG and YPet-ELMO recruitment to an adhered bead on an SGEF WT mouse aortic endothelial cell.

(B) HUVEC expressing a RhoG dual-chain biosensor after treatment with TNFα demonstrating adherence of a bead with subsequent rapid and increasing activation at the site of the bead within 15 minutes of bead adherence. Relative RhoG activity is indicated by the heat map at left.

(C) Mouse aortic endothelial cells isolated from SGEF$^{-/-}$ mice expressing a RhoG dual-chain biosensor after treatment with TNFα demonstrating reduced RhoG activity at the site of bead adherence compared to (B). Right-most panels are examples of the reduced recruitment of CFP-RhoG and YPet-ELMO to adhered beads in SGEF$^{-/-}$ mouse aortic endothelial cells.

Figure 6.5
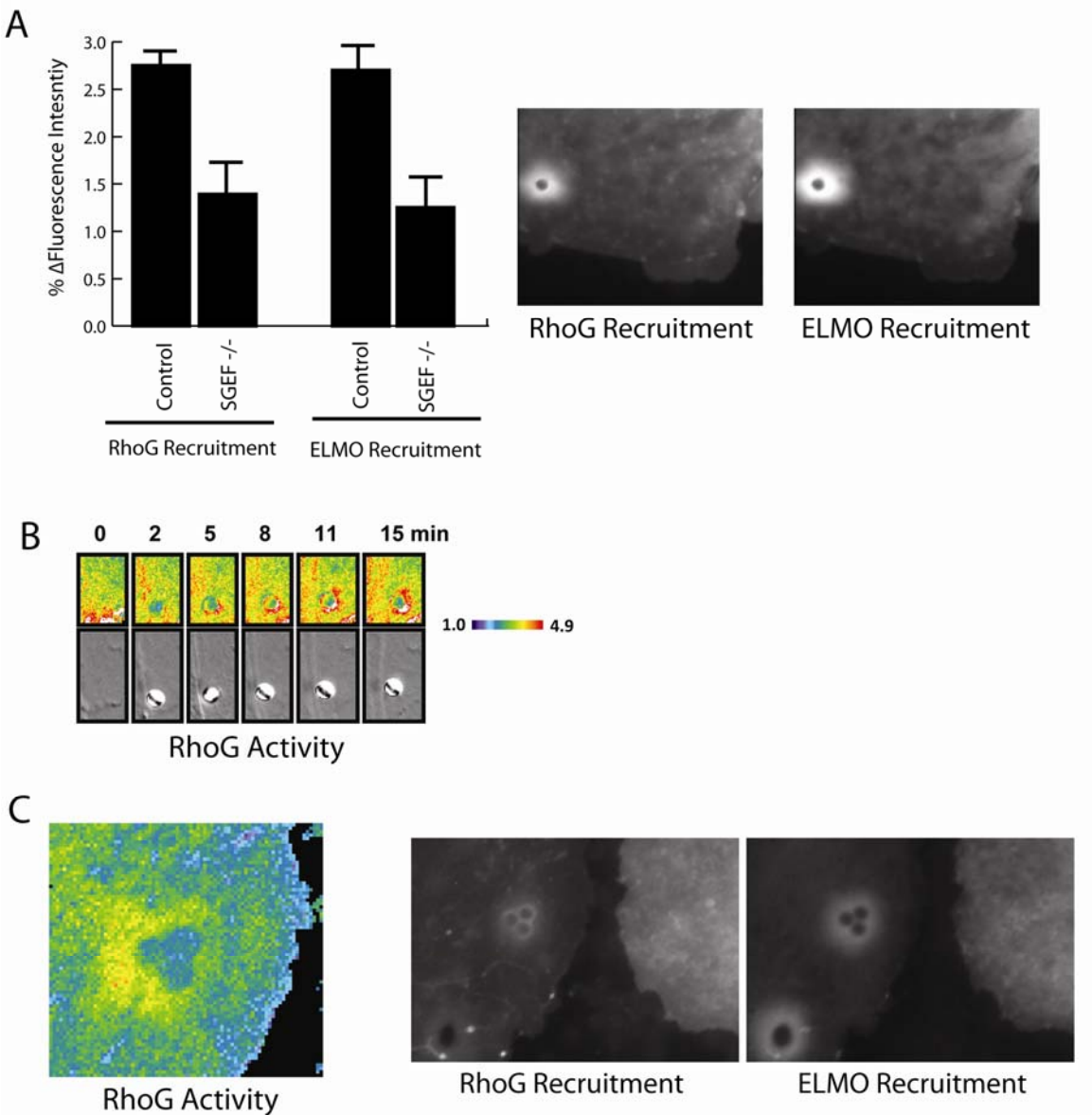
CHAPTER SEVEN: DISCUSSION, CLINICAL RELEVANCE, AND FUTURE DIRECTIONS

7.1 Summary of Findings

Cell migration is a highly complex process that requires the coordination of multiple signaling pathways in both time and space to orchestrate the myriad functional and morphological changes in a cell that lead to polarization, protrusion, and retraction of the rear of the cell. Clearly, the activities of these pathways coordinating migration operate within a fairly tight window of control to properly respond to environmental cues in either an attractive or repulsive fashion. These pathways are also differentially regulated depending on the cells studied: for example, the cues that cause a neuronal cell process to be extended, or that cause dendrites to form on the neuron may be entirely unimportant for the movement and migration of leukocytes to sites of inflammation (Franz et al. 2002; Ridley 2006; Ley et al. 2007). Remarkably, however, the myriad cues that tell cells what to do and how to behave often engage the same core cellular machinery regardless of the cell type, namely the Rho GTPases (Burridge and Wennerberg 2004). The commonality of these molecules to the whole of cell migration makes them excellent targets for study of how cells respond to environmental cues and translate those cues into functional behaviors.

Biochemical studies have provided a great deal of evidence about the roles and functions of the GTPases, identifying 20 Rho GTPases to date and categorizing many of their functions. Many of these GTPases are cell-type specific or function-specific and

play less important roles (Jaffe and Hall 2005). Further, biochemical evidence has often

taken advantage of growth factor stimulation to exaggerate the differences between

conditions of study, often pushing cellular signaling outside the boundaries of normal

cellular controls. Thus, we lose sight of many of the intrinsic regulatory mechanisms

found in cells that operate predominantly in the non-stimulated state (Machacek et al.

2009). Further, it is quite apparent that the location and timing of the signals from these

patterns matters greatly in determining their functions. For example, RhoA is capable of

both polymerizing actin through mDia1 (Lammers et al. 2008), and causing cellular

contractility through myosin activation (Burridge and Chrzanowska-Wodnicka 1996). It

would be unproductive for the cell to perform both functions in the same place at the

same time, so RhoA is likely segregated with different signaling partners or scaffolds

which respond to different cues to orchestrate specific behaviors in specific locations of

the cell, such as with IQGAP (White et al. 2009). Through the use of a combination of

biochemistry, imaging techniques, and FRET-based probes for GTPase activity I have

begun to characterize and elucidate the mechanisms by which cells control the spatial and

temporal dynamics of the Rho GTPases both during constitutive cell migration

movements, and in response to specific cellular cues. In the process of this work, I have

developed significant new tools for the study of Rho GTPase activation in living cells.

The main findings of this work are summarized below:

Rational Design and Development of Rho GTPase Biosensors for Live Cell Imaging:

1. Two major GTPase activity FRET probe designs have been further improved and

   optimized, specifically generating a new single-chain Rac1 sensor, and generating

new, enhanced sensitivity versions of dual-chain sensors for RhoA, Rac1, Cdc42, and RhoG.

2. Single-chain and dual-chain sensor designs, along with their modifications, both present unique advantages and disadvantages in terms of ease of use, simplicity of signal analysis, and resultant false positive and false negative results. Further, dual-chain sensors are amenable to a different format of analysis, permitting a better recognition of total activity within a region of a cell, and permitting study of activity in low signal situations. Choice of sensor will strongly depend on the experimental conditions.

3. Rho GTPase sensors have been generated and optimized with wavelengths orthogonal to the CFP/YFP pairs currently in use by using mKO/mCherry as donor and acceptor fluors.

4. A novel system to control the expression of the two components of the dual-chain sensor has been developed and utilized to express dual-chain sensors at appropriate concentrations.

Coordination of the Spatiotemporal Dynamics of Rho GTPases during Cell Migration:

1. Rac1, RhoA, and Cdc42 activities can be directly correlated to constitutive cell edge movements.

2. Using cell edge movements as a common reference point, we can infer the relationships between Rac1, RhoA, and Cdc42 activities in both time and space.

3. Computational modeling provides a powerful tool with which to correlate multiple signaling protein activities derived from imaging data from single experiments in both time and space.

4. RhoA is activated coincident with cell protrusion and is active at the very cell edge. Rac1 and Cdc42 are both activated with a time delay of 40 seconds relative to cell protrusion, and are found to attain maximal activity approximately 1.3 to 1.8 μm from the cell edge.

5. Leading edge RhoA activity is modulated by the GEF TEM4, likely indirectly through RhoC. Loss of TEM4 leads to increased RhoA activity at the whole-cell level. Spatially, we see uniform activation of RhoA along the entire cellular periphery, rather than activity in protruding regions alone.

6. Cdc42 is activated during filopodium formation, in addition to cellular protrusion.

7. Cdc42 is found to be active at the base of filopodium, in the shaft of the filopodium, and at the filopodium tip during filopodium extension. Cdc42 activity drops sharply upon filopodial retraction.

8. Filopodial Cdc42 activity is regulated by a novel mDia2-associated GAP, MILO. Knockdown of the GAP leads to increased Cdc42 activity at the whole-cell level and in filopodia. Overexpression of the "active" GAP decreases Cdc42 activity.

9. Src kinase increases filopodial Cdc42 activity by phosphorylating and inactivating MILO.

10. Not only can it be discerned how the Rho GTPases are coordinated in space and time through biosensor imaging, but it can also be discerned how they are regulated by upstream regulators.

Role of RhoG in Cell Migration:

1. RhoG is activated coincident with cell protrusion and is active at the very cell edge.

2. The leading edge activation pattern of RhoG is tightly regulated by the vesicular trafficking of RhoG along microtubules, which in turn is regulated by RhoGDI-3, a unique cellular GDI that only interacts with RhoG. RhoG activity can be modulated by overexpression or knockdown of RhoGDI-3.

3. RhoG precisely positions Rac1 activation within the lamellipodium via the ELMO/DOCK180 pathway as described for other RhoG behaviors.

4. RhoG appears to control Rac1 activation within the lamellipodium due to its ability to recruit and activate Rac1 at focal adhesions via DOCK180, which is a focal adhesion anchor point.

5. Due to the control of a small subpopulation of Rac1 activity by RhoG, we find that cell edge dynamics, in particular protrusion/retraction periodicity and velocity, and actin polymerization are all affected.

6. RhoG is critical for long-term random cell migration, controlling the ability of cells to polarize Rac1 activity in response to environmental cues, and to turn in response to generation of new foci of Rac1 activity.

Regulation of Rho GTPase Dynamics in Response to Growth Factors:

1. RhoG, Rac1, and Cdc42 are all activated rapidly by EGF stimulation.

2. Rac1 and Cdc42 activation by EGF is regulated by submembranous pH: low pH (< pH 6.6) prevents activation of Rac1 and Cdc42 in response to EGF stimulation.

331

3. RhoG activation in specifically mediated by Vav2/Vav3 GEFs in HeLa cells and Vav2/PLEKHG6 in A431 cells.

4. PLEKHG6 is a GEF that activates RhoG and defines the morphological response of cells to EGF stimulation. In A431 cells, PLEKHG6 is responsible for dorsal ruffling of cells, while Vav2 controls the peripheral spreading response.

Role of Rho GTPases in Transendothelial Migration:

1. Cos-7 cells, lacking endogenous ICAM-1, make an excellent model system to study ICAM-1 ligation and clustering, and subsequent downstream signaling as a proxy for leukocyte transendothelial migration.

2. Rac1 is activated locally, transiently, and in a delayed fashion in response to ICAM-1 ligation and clustering.

3. RhoG is activated locally and immediately in response to ICAM-1 ligation and clustering. RhoG activation is mediated in large part by the RhoG-selective GEF, SGEF.

4. RhoA is locally and immediately inactivated in response to ICAM-1 ligation and clustering, but is activated globally.

5. Global RhoA activation was confirmed in a model of mechanical force transduction by endothelial cells. This mechanical force transduction is strongly dependent on the substrate on which the cells are growing.

7.2 Clinical Relevance

Role of Rho GTPases in Cancer:

Given that the Rho GTPases are at the core of a variety of normal and pathological processes, such as embryonic development, neuronal development, inflammatory signaling, and cancer development and metastasis, among a whole host of other cellular behaviors (Burridge and Wennerberg 2004; Jaffe and Hall 2005), immense effort has been expended trying to understand their roles in these processes.

To date, many cancer-promoting genes, or oncogenes, have been shown to exert their effects because of specific mutations causing unchecked downstream signaling with dramatic consequences on cellular behaviors. Curiously, there have been very few mutations identified in the Rho GTPases themselves that cause disease, with the exception of RhoH (Hiraga et al. 2007; Sanchez-Aguilera et al. 2009). The Rho GTPases appear to affect cancer progression predominantly through increased expression or increased activation. For example, in a seminal study on Rho GTPases and cancer metastasis, RhoC was consistently identified as a molecule whose overexpression was correlated strongly with increased metastatic potential and poor survival outcomes (Clark et al. 2000). In contrast, a variety of GEFs responsible for activating Rho GTPases and GAPs responsible for inactivating Rho GTPases have been identified as either mutated, amplified, or deleted in a number of cancers. For example, Tiam-1, Vav2, LARG, and Dbl are all GEFs that were identified as oncogenes in the study of cancer mutations (Ridley 2004; Vega and Ridley 2008). Similarly, DLC1 and DLC2 have been identified in liver cancer samples as GAPs that have been lost (Yuan et al. 2003), permitting

increased Rho GTPase activation. What each of these changes in gene expression or these mutations have in common is that they cause hyperactivation of the GTPases.

Hyperactivation of each of the GTPases has even been correlated to the different modes of movement and metastatic migration of cancer cells. These studies have identified three major types of metastatic migration strategies: 1) single-cell amoeboid movement, 2) single-cell mesenchymal movement, and 3) multicellular sheet-like movement, each associated with activation of different Rho GTPases. For single-cell amoeboid movement, cells tend to have much higher Rho activation and actomyosin contractility and move slowly via a propulsive mechanism (leukemia, lymphoma, small-cell lung cancer). For single-cell mesenchymal movement, cells have higher Rac1 activation at the leading edge with Rho contractility at the rear to enable a more protrusive movement (fibrosarcomas, glioblastomas, anaplastic cancers). For collective migration of cellular sheets, Rho and Rac activation are both increased and work in parallel to permit the entire cluster of cells to migrate (epithelial-derived cancers, melanoma, vascular tumors) (Sahai and Marshall 2003; Wolf and Friedl 2006; Gaggioli et al. 2007; Sanz-Moreno et al. 2008; Friedl and Wolf 2009; Ilina and Friedl 2009; Wolf et al. 2009).

Thus, it is interesting to note that groups have attempted to examine the prognostic values of all these Rho GTPases in breast cancer progression and found an interesting pair of proteins that were increased and decreased respectively: RhoG and RhoGDI-3 (Jiang et al. 2003). Coupled with another study identifying overexpression of both DOCK180 and ELMO1 in gliomas (Jarzynka et al. 2007), there is fairly strong evidence that RhoG is overactivated in cancers. Whether these proteins play a causative

role in cancer progression is unknown, but given their role in cell migration, it is highly likely that RhoG is overactivated, resulting in Rac1 overactivation and downstream signaling. Thus, RhoG may help to drive mesenchymal and collective sheet migration during metastasis, which would be an interesting hypothesis to test. Further, these studies would also seem to indicate that the Rho GTPases would be excellent targets for anti-cancer therapy, but due to the myriad functions they regulate, side effects are likely to be a significant issue.

Cell migration has been an extremely difficult target to tackle in cancer metastasis because the cellular signaling components are common to so many non-pathological behaviors, particularly the GTPases, and because cancer cells have an amazing capacity to adapt and avoid what would seemingly be blockade of critical signaling pathways. For example, if matrix metalloproteases necessary for invasion of tissues are inhibited, cancer cells can still invade (Coussens et al. 2002). Similarly, if RhoA pathways are inhibited in cells demonstrating amoeboid migration, they often switch to a mesenchymal mode of migration, and vice-versa when Rac1 pathways are inhibited, confounding therapeutic intervention (Friedl and Wolf 2009). Thus, it is becoming clear that combinatorial therapy may be the most viable treatment strategy in the future, attempting to inhibit multiple critical pathways required for cancer progression and metastasis, such as cell cycle progression, angiogenesis, and migration.

Where RhoG may play a unique role in cancer therapy is by virtue of the uniqueness of RhoG signaling and its upstream regulators. If it is identified that RhoG-specific GEFs such as SGEF play a significant role in cancer cell migration, or if RhoGDI-3 is found to play a significant role in cancer cell migration, these might be

viable targets for therapeutic intervention because they would impact other important signaling pathways to a significantly lesser degree than targeting the other major GTPases. When combined with other therapeutic agents, inhibition of RhoG signaling in cancer types where RhoG signaling has been found to be elevated (Jiang et al. 2003; Jarzynka et al. 2007) may help slow or stop metastatic progression.

Role of Rho GTPases in Inflammatory Signaling:

As delineated above for cancer development and metastasis, Rho GTPases also play a significant role in inflammatory diseases because both the immune cell and the vasculature have to change their cytoskeletal structure to permit leukocyte extravasation into tissues. However, because of the narrow therapeutic window between blocking abnormal inflammatory cell recruitment and blocking normal immune surveillance behaviors which would cause immune suppression, viable therapies have been slow in development. From the development process, it seems that most successful therapeutic agents have targeted leukocyte-endothelial interactions or the endothelium itself. For example, one of the more successful drugs for multiple sclerosis and Crohn's disease, Tysabri (natalizumab), blocks $\alpha_4\beta_1$ integrins on leukocytes that interact with VCAM-1 on the endothelium (Miller et al. 2003; Sandborn and Yednock 2003; Dalton et al. 2004). Another example, Fasudil, a Rho kinase inhibitor, has been used in Japan for a number of years to treat cerebral cavernous malformation which causes vascular leakiness (Olson 2008), and is also being tested in clinical trials for pro-inflammatory diseases since vascular leakiness is also a hallmark of inflammation and leukocyte extravasation (Olson 2008). Thus, a better understanding of the mechanisms behind leukocyte-endothelial

interactions and the resultant leaky endothelium would likely lead to better therapeutic agents. Many of the anti-inflammatory agents currently in the clinical trial pipeline impinge upon cell migration and the Rho GTPases, including chemokine receptor inhibitors, adhesion molecule inhibitors, complement receptor inhibitors, and others (Norman and Kubes 2005; Kelly et al. 2007). In principle, targeting the Rho GTPases would be a desirable approach, but again specificity and side effects are issues. In addition to the role of Rho kinase mentioned above, it has also been reported that cAMP-dependent Rac1 activation is important for the stabilization of the endothelial barrier function and thus could be used to block inflammation (Waschke et al. 2004; Schlegel et al. 2008; Baumer et al. 2009). In support of this hypothesis, cAMP-increasing agents had protective effects on the microvasculature during sepsis (Trager et al. 2003), further validating indirect targeting of the Rho GTPases as a viable method for controlling inflammation and vascular leakiness.

Where RhoG may play a unique role in the study of inflammation and leukocyte recruitment is illustrated in Chapter 6 in bead-binding studies and in the works of others (van Buul et al. 2007a). It is known that a docking structure or "transmigratory cup" forms around adhering leukocytes as they bind to the endothelium. SGEF, one of the key upstream GEFs for RhoG, appears to mediate this process, as loss of RhoG or SGEF abrogates transmigratory cup formation during leukocyte adhesion and reduces transendothelial migration. By identifying the mechanistic pathways leading to RhoG activation downstream of ICAM-1, we may identify unique targets, such as SGEF, that may be amenable to inhibition without disrupting many other signaling pathways in the body and thus successfully reduce transendothelial migration in areas of high

inflammation. It is particularly important to note that ICAM-1, the main focus of our work on transendothelial migration, is a highly inducible inflammatory marker. For example, in atherosclerosis, ICAM-1 is markedly upregulated at sites of plaque formation and inflammation (Nakashima et al. 1998; Rohlena et al. 2009). Further, associated molecules such as the tetraspanins which help regulate ICAM-1 and VCAM-1 signaling, are also upregulated, suggesting that ICAM-1, VCAM-1, and their downstream signaling partners may be excellent targets for the disruption of inflammatory diseases (Fernandez-Borja et al. 2010). Indeed, some of the best successes in targeting transendothelial migration during inflammation have come from inhibitors of ICAM-1 and VCAM-1-mediated signaling, natalizumab and efalizumab, which has been shown to be useful for treating severe multiple sclerosis and Crohn's disease (Miller et al. 2003; Sandborn and Yednock 2003; Dalton et al. 2004; Jullien et al. 2004).

Imaging Probes for in vivo *Detection of Aberrant Signaling:*

Additionally, the development of novel probes for the study of cellular signaling has clinical relevance. Currently, most imaging probes are used in cells plated in 2-dimensional cultures. While this provides us a great deal of information about how signals are propagated in single cells, it does not tell us how signaling pathways behave in more complex models such as 3-dimensional cell cultures or in animals. To this end, the development of novel biosensors that are much more sensitive to endogenous signals will allow the introduction of even smaller amounts of probe into cells and tissues for imaging without perturbing downstream signaling, particularly if new FRET analysis techniques are applied. Second, with the use of orange/red FRET pairs, light can

338

penetrate tissues more deeply (Shaner et al. 2005; Shaner et al. 2008), permitting

visualization of FRET from within deeper structures, perhaps even from live animals.

Lastly, the conversion of our novel sensitive dual-chain probes to autocleavable forms

allows for the introduction of these probes into animals at a single gene locus, rather than

optimizing the expression of two separate loci within an animal which has been

extremely difficult due to heterogeneity in expression levels (Trichas et al. 2008). Thus,

these advances bring us closer to understanding signaling pathways and their

spatiotemporal constraints *in vivo*, where we might be able to see aberrant activation of

Rho GTPases in response to genetic or exogenous insults. Perhaps at some point in the

future, tracer probes will be used in clinical studies to detect aberrant cellular signaling

and pinpoint the sources of those aberrant signals, such as cancer stem cells or actively

proliferating cancer cells.

7.3 Long-term Directions

Large-scale Analysis of GTPase Regulators During Random Cell Migration:

Now that we have developed a spatial and temporal relationship map among the Rho GTPases during constitutive cell movement behaviors, precisely mapping when and where these GTPases are active, myriad hypotheses present themselves for testing. Given that computational analysis discussed in Chapter 3 can account for fairly broad cell-to-cell heterogeneity, it seems it would be of great value to begin by perturbing molecules involved in regulating Rac1, RhoG, RhoA, or Cdc42, or the GTPases themselves, and observing how the timing and positioning patterns change for each of the GTPases. It is also possible, given the consistency of the data, that this methodology could be applied to a high-throughput analysis. For example, the Cell Migration Consortium has sponsored high-throughput siRNA screens intended to identify whether cell migration was perturbed by knockdown of specific cellular proteins (Kamath et al. 2003; Cram et al. 2006; Simpson et al. 2008), generally in simple assays such as wound healing assays or presence/absence of migration. These results, however, do not tell us how migration is perturbed: whether directionality, response to growth factors, turning ability, or a variety of other parameters is perturbed. Through the analysis of single-cells in a high-throughput manner, GTPase activity sensors could be introduced into cells and imaged in a 96-well format to cover a variety of parameters, including but not limited to directionality, persistence, velocity, polarity, GTPase activation level, and edge dynamics. By application of siRNA libraries enriched for siRNAs already known to affect cellular morphology or migration (genome-wide could be done but would likely be very burdensome in terms of imaging data and analysis), the effects of these siRNAs on

the timing and positioning of the GTPases due to knockdown of the target proteins could be determined. Ultimately, through confirmation and validation of the siRNA targets, this could lead to the development of spatiotemporal maps of cellular signaling pathways that more accurately describe the roles of the Rho GTPases and their regulators in cellular behaviors.

I am particularly interested in such an analysis that would target three classes of proteins: 1) GEFs, 2) GDIs, and 3) scaffolding proteins. Clearly, with the very precise positioning and activation of the GTPases found during cell protrusion, there must be molecules that determine their positioning and activation. The three classes of proteins I mention above seem to hold the most promise in determining GTPase positioning and activation. First, it is known that for Rac1, GEFs play a prominent role in recruitment and activation, such as β-Pix and its ability to recruit and activate Rac1 at focal adhesions (Koh et al. 2001; ten Klooster et al. 2006; Chang et al. 2007; Lee et al. 2010a). Loss of this GEF would alter the Rac1 dynamics that we see in our cellular protrusion system and could thus be quantified spatially and temporally. It would be very interesting to test this for a number of GEFs and determine whether very specific subsets of GTPase activity are regulated by each GEF, or whether there is redundancy and overlap in the ability to position and activate the GTPases. Second, GDIs are extremely interesting as well, as they have the ability to hold GTPases in the inactive form until the GDI is released, permitting activation of the GTPase. For example, both PKA and PKC are capable of phosphorylating GDI on specific residues, leading to the release of RhoA or RhoG (Elfenbein et al. 2009; Tkachenko et al. 2011), respectively, from GDI and thus activation of those GTPases. Through modulation of GDI by replacement with

phosphorylation mimics (rather than knockdown of GDI which has been shown to have more broad-scale effects) we could ascertain how each of the GTPases is governed by GDI and how GDI influences the positioning and activation of the GTPases. A recent study has done precisely this, demonstrating that PKA acts as a master regulator of the protrusion-retraction cycle through RhoA (Tkachenko et al. 2011). Lastly, it has long been known for the mitogen-activated protein kinase (MAPK) signaling pathways that scaffolds play an enormous role in bringing together specific signaling components to activate specific downstream signaling pathways in response to extracellular cues (Dhanasekaran et al. 2007). These scaffold proteins provide much of the specificity for these kinases, preventing inappropriate interactions within the cell. The same design also appears to play a part in Rho GTPase signaling as well. For example, the protein synectin was recently identified as a component of a complex that tied fibroblast growth factor (FGF) signaling to RhoG activation by serving as a scaffold for both RhoG and GDI, holding RhoG in its inactive state. This molecular complex prevents RhoG activation until FGF stimulation activates protein kinase C (PKC) which in turn phosphorylates RhoGDI-1, releasing RhoG and permitting its activation (Elfenbein et al. 2009). Thus, inappropriate interactions with other molecules could be prevented and specific downstream signaling cascades through RhoG could be initiated. In independent studies, synectin has been shown to be a critical player in cell migration, due to its role as a scaffold for a variety of signaling proteins (Muders et al. 2009; Wang et al. 2010). By knockdown of various scaffold proteins, their effects on both the timing and positioning of GTPase activation could also be determined. Further work could then elucidate the specific molecules that bound to the scaffold with the GTPase and which extracellular

cues were responsible for activating the pathway. Analysis of how each of these sets of molecules contribute to Rho GTPase regulation would greatly enhance our understanding of how these molecules operate in living cells.

Regulation of RhoG in Cell Migration:

The work in Chapter 4 detailing the role of RhoG in cell migration in some ways raises more questions than it answers. RhoG and its regulation still remains poorly understood. We and others have identified the role of RhoG in cell migration (Wennerberg et al. 2002; Katoh and Negishi 2003; Hiramoto et al. 2006; Katoh et al. 2006; Hiramoto-Yamaki et al. 2010), in particular its regulation via vesicular trafficking by RhoGDI-3 and its ability to regulate the lamellipodial subpopulation of Rac1 activity. We also show that it appears to be critical for the ability of cells to reorient and polarize Rac1 activity during the turning process in random cell migration. However, we do not fully understand the cues that are responsible for activating RhoG at the leading edge. Our preliminary experimentation suggests that Trio may be the critical GEF that activates RhoG at the leading edge of cells, but there may also be others such as Ephexin4, Vav2/3, and PLEKHG6 (Ellerbroek et al. 2004; D'Angelo et al. 2007; Hiramoto-Yamaki et al. 2010; Samson et al. 2010).

The next steps in this study would be to identify the GEFs that regulate RhoG during cell migration, and the specific extracellular cues that activate those GEFs. For example, we have shown that in HeLa cells, the Vav2/Vav3 GEFs are critical for EGF response, and in A431 cells, Vav2 and PLEKHG6 are responsible for EGF response (Samson et al. 2010). Other groups have identified that fibroblast growth factor (FGF)

activates RhoG via the FGF2 receptor coupled with Syndecan-4, but no GEF was identified in that study that might subsequently activate RhoG; the authors simply stated that FGF stimulation prepared RhoG for activation by releasing GDI (Elfenbein et al. 2009). Thus, there appears to be fertile ground for identifying and characterizing the GEFs that activate RhoG.

While many of the growth factors have been tested for their ability to activate RhoG, and their roles vary from cell type to cell type, other signals have been less well characterized. Since Syndecan-4 was previously identified as part of a scaffold that can regulate RhoG activity (Elfenbein et al. 2009), it is interesting to note that Syndecan-4 is also a receptor for fibronectin (Bass et al. 2007), suggesting that multiple signal inputs could use the Syndecan-4 pathway to activate RhoG. It has not yet been tested whether fibronectin can also activate RhoG through the Syndecan-4 co-receptor.

By examining these pathways, I not only wish to identify what activates RhoG, but what the activation of RhoG causes cells to do, i.e. the functional consequences of that pathway. Does RhoG activation guide directionality or environmental cue-finding, and are these behaviors linked to specific extracellular cues? In Chapter 4, I show that RhoG helps cells to change direction, but I do not identify the specific cue that activates RhoG in this process. Through these studies I would hope to identify the cue(s) responsible for these cellular behaviors.

The ultimate goal of such a study would be to identify novel, specific regulators for RhoG in cellular behaviors that could be targeted for therapeutic effect in a number of different diseases where RhoG plays a role. Given that many of the molecules so far identified that activate RhoG are fairly specific to RhoG (Ellerbroek et al. 2004;

D'Angelo et al. 2007; Hiramoto-Yamaki et al. 2010), we could potentially identify unique cellular targets whose inhibition would have little to no effect on other GTPases, which has been a problem to date with many strategies attempting to inhibit the Rho GTPases.

Rho GTPases in Leukocyte Transendothelial Migration:

Lastly, much work remains to be done in understanding endothelial Rho GTPase activation during leukocyte transendothelial migration. Again, from biochemical studies (Barreiro et al. 2002; Thompson et al. 2002; Carman et al. 2003; Carman and Springer 2004; Millan et al. 2006; van Buul et al. 2007a; Carman 2009), we know some of the molecules involved in this process, such as Rac1, RhoG, RhoA, vimentin, and ICAM-1, among others. I have also been able to show that Rac1, RhoG, and RhoA are activated downstream of ICAM-1 with different kinetics, and that for RhoG, SGEF appears to be one of the GEFs involved in this process. However, we still poorly understand the role each of these GTPases has in the morphological changes that occur for cup formation and leukocyte transmigration, either through the cell or between cells (Dejana 2006; Ley et al. 2007; Fernandez-Borja et al. 2010). For the next steps, we would want to knock out each of the GTPases to observe the effects both on cup formation and on the dynamics of the Rho GTPases during ICAM-1 ligation and clustering, and the subsequent cup formation response. For example, which is the first step in cup formation: RhoA, RhoG, or Rac1 activation? By perturbing each of the GTPases individually, I could attempt to determine which GTPase(s) were the most critical for cup formation. If this first step is lost, is cup formation lost entirely? If later steps in cup formation are disrupted, is GTPase activation altered, or is the ability of the cup to close and engulf the bead or white blood cell

altered? These answers are currently unknown and would represent the next steps in our understanding of leukocyte TEM. Ultimately, I will shift away from using beads to using leukocytes for these studies. Neutrophils and lymphocytes would likely be the cells of choice as both readily undergo transendothelial migration, both engage ICAM-1 effectively, and both are capable of undergoing both transcellular and paracellular transendothelial migration (Dejana 2006). I would then determine whether white blood cells cause endothelial Rho GTPases to become activated in the same patterns as we saw with our bead studies, and whether perturbation of those GTPases caused the same changes in cup formation. There is some concern that signaling via VCAM-1, which has also been shown to be important for transendothelial migration, may activate a number of pathways in parallel to ICAM-1 (van Wetering et al. 2003; van Buul et al. 2007b; Fernandez-Borja et al. 2010). By blocking VCAM-1 with specific antibodies or ICAM-1 with specific antibodies, we could then isolate the effects of leukocytes on either signaling pathway and thus elucidate GTPase activation downstream more effectively.

Many attempts have been made to more effectively block inflammatory processes that are mediated by aberrant leukocyte TEM. However, most of the drugs targeting TEM pathways have had the consequence of immune suppression due to affecting normal TEM needed for immune surveillance (Norman and Kubes 2005; Kelly et al. 2007). We hope that through our studies we could identify novel signaling components such as GEFs that are aberrantly activated in these inflammatory disease processes, and thus target those molecules for therapeutic intervention without significantly affecting normal TEM pathways.

7.4 Concluding Remarks

The work described above has made strides toward providing better tools for the imaging of GTPase activity in living cells, while at the same time providing a better understanding of potential analysis methods for these tools. Additionally, this work is among the first to extend the use of Rho GTPase biosensors beyond descriptive analyses of GTPase activation patterns, to being able to quantify causal relationships among the GTPases and their regulators. These analyses have helped us better understand the role of Rho GTPases in cellular protrusion, and in particular the role of RhoG in cell migration and its regulation of Rac1. Additionally, we have gained a better understanding of the regulation of Rho GTPases in response to extracellular cues.

Lastly, these studies have helped to develop a framework for the better understanding of leukocyte TEM by development of a system wherein we can observe GTPase activation in response to ICAM-1 clustering and activation. This system should be translatable to studies of primary leukocytes migrating through an endothelium, a much more complex system closely resembling *in vivo* behaviors. Each of these studies described above provides the framework for much larger-scale analyses of the proteins that regulate the Rho GTPases in each of these processes, and the Rho GTPases themselves.

REFERENCES

Adamson, P., Etienne, S., Couraud, P.O., Calder, V., and Greenwood, J. 1999. Lymphocyte migration through brain endothelial cell monolayers involves signaling through endothelial ICAM-1 via a rho-dependent pathway. *J Immunol* **162**(5): 2964-2973.

Ai, H.W., Hazelwood, K.L., Davidson, M.W., and Campbell, R.E. 2008. Fluorescent protein FRET pairs for ratiometric imaging of dual biosensors. *Nat Methods* **5**(5): 401-403.

Allingham, M.J., van Buul, J.D., and Burridge, K. 2007. ICAM-1-mediated, Src- and Pyk2-dependent vascular endothelial cadherin tyrosine phosphorylation is required for leukocyte transendothelial migration. *J Immunol* **179**(6): 4053-4064.

Alon, R., Kassner, P.D., Carr, M.W., Finger, E.B., Hemler, M.E., and Springer, T.A. 1995. The integrin VLA-4 supports tethering and rolling in flow on VCAM-1. *J Cell Biol* **128**(6): 1243-1253.

Alvarez de la Rosa, D., Canessa, C.M., Fyfe, G.K., and Zhang, P. 2000. Structure and regulation of amiloride-sensitive sodium channels. *Annu Rev Physiol* **62**: 573-594.

Amos, W.B. and White, J.G. 2003. How the confocal laser scanning microscope entered biological research. *Biol Cell* **95**(6): 335-342.

Amyere, M., Mettlen, M., Van Der Smissen, P., Platek, A., Payrastre, B., Veithen, A., and Courtoy, P.J. 2002. Origin, originality, functions, subversions and molecular signalling of macropinocytosis. *Int J Med Microbiol* **291**(6-7): 487-494.

Amyere, M., Payrastre, B., Krause, U., Van Der Smissen, P., Veithen, A., and Courtoy, P.J. 2000. Constitutive macropinocytosis in oncogene-transformed fibroblasts depends on sequential permanent activation of phosphoinositide 3-kinase and phospholipase C. *Mol Biol Cell* **11**(10): 3453-3467.

Ananthanarayanan, B., Ni, Q., and Zhang, J. 2005. Signal propagation from membrane messengers to nuclear effectors revealed by reporters of phosphoinositide dynamics and Akt activity. *Proc Natl Acad Sci U S A* **102**(42): 15081-15086.

Andrew, N. and Insall, R.H. 2007. Chemotaxis in shallow gradients is mediated independently of PtdIns 3-kinase by biased choices between random protrusions. *Nat Cell Biol* **9**(2): 193-200.

Anton, I.M., Saville, S.P., Byrne, M.J., Curcio, C., Ramesh, N., Hartwig, J.H., and Geha, R.S. 2003. WIP participates in actin reorganization and ruffle formation induced by PDGF. *J Cell Sci* **116**(Pt 12): 2443-2451.

Araki, N., Egami, Y., Watanabe, Y., and Hatae, T. 2007. Phosphoinositide metabolism during membrane ruffling and macropinosome formation in EGF-stimulated A431 cells. *Exp Cell Res* **313**(7): 1496-1507.

Araki, N., Johnson, M.T., and Swanson, J.A. 1996. A role for phosphoinositide 3-kinase in the completion of macropinocytosis and phagocytosis by macrophages. *J Cell Biol* **135**(5): 1249-1260.

Arthur, W.T. and Burridge, K. 2001. RhoA inactivation by p190RhoGAP regulates cell spreading and migration by promoting membrane protrusion and polarity. *Mol Biol Cell* **12**(9): 2711-2720.

Arthur, W.T., Petch, L.A., and Burridge, K. 2000. Integrin engagement suppresses RhoA activity via a c-Src-dependent mechanism. *Curr Biol* **10**(12): 719-722.

Assaker, G., Ramel, D., Wculek, S.K., Gonzalez-Gaitan, M., and Emery, G. 2010. Spatial restriction of receptor tyrosine kinase activity through a polarized endocytic cycle controls border cell migration. *Proc Natl Acad Sci U S A* **107**(52): 22558-22563.

Barreiro, O., Yanez-Mo, M., Serrador, J.M., Montoya, M.C., Vicente-Manzanares, M., Tejedor, R., Furthmayr, H., and Sanchez-Madrid, F. 2002. Dynamic interaction of VCAM-1 and ICAM-1 with moesin and ezrin in a novel endothelial docking structure for adherent leukocytes. *J Cell Biol* **157**(7): 1233-1245.

Bass, M.D., Roach, K.A., Morgan, M.R., Mostafavi-Pour, Z., Schoen, T., Muramatsu, T., Mayer, U., Ballestrem, C., Spatz, J.P., and Humphries, M.J. 2007. Syndecan-4-dependent Rac1 regulation determines directional migration in response to the extracellular matrix. *J Cell Biol* **177**(3): 527-538.

Baumer, Y., Spindler, V., Werthmann, R.C., Bunemann, M., and Waschke, J. 2009. Role of Rac 1 and cAMP in endothelial barrier stabilization and thrombin-induced barrier breakdown. *J Cell Physiol* **220**(3): 716-726.

Bellanger, J.M., Astier, C., Sardet, C., Ohta, Y., Stossel, T.P., and Debant, A. 2000. The Rac1- and RhoG-specific GEF domain of Trio targets filamin to remodel cytoskeletal actin. *Nat Cell Biol* **2**(12): 888-892.

Bellovin, D.I., Simpson, K.J., Danilov, T., Maynard, E., Rimm, D.L., Oettgen, P., and Mercurio, A.M. 2006. Reciprocal regulation of RhoA and RhoC characterizes the EMT and identifies RhoC as a prognostic marker of colon carcinoma. *Oncogene* **25**(52): 6959-6967.

Bokoch, G.M., Reilly, A.M., Daniels, R.H., King, C.C., Olivera, A., Spiegel, S., and Knaus, U.G. 1998. A GTPase-independent mechanism of p21-activated kinase activation. Regulation by sphingosine and other biologically active lipids. *J Biol Chem* **273**(14): 8137-8144.

Boulter, E., Garcia-Mata, R., Guilluy, C., Dubash, A., Rossi, G., Brennwald, P.J., and Burridge, K. 2010. Regulation of Rho GTPase crosstalk, degradation and activity by RhoGDI1. *Nat Cell Biol* **12**(5): 477-483.

Bourdillon, M.C., Poston, R.N., Covacho, C., Chignier, E., Bricca, G., and McGregor, J.L. 2000. ICAM-1 deficiency reduces atherosclerotic lesions in double-knockout mice (ApoE(-/-)/ICAM-1(-/-)) fed a fat or a chow diet. *Arterioscler Thromb Vasc Biol* **20**(12): 2630-2635.

Brugnera, E., Haney, L., Grimsley, C., Lu, M., Walk, S.F., Tosello-Trampont, A.C., Macara, I.G., Madhani, H., Fink, G.R., and Ravichandran, K.S. 2002. Unconventional Rac-GEF activity is mediated through the Dock180-ELMO complex. *Nat Cell Biol* **4**(8): 574-582.

Brunet, N., Morin, A., and Olofsson, B. 2002. RhoGDI-3 regulates RhoG and targets this protein to the Golgi complex through its unique N-terminal domain. *Traffic* **3**(5): 342-357.

Bryce, N.S., Clark, E.S., Leysath, J.L., Currie, J.D., Webb, D.J., and Weaver, A.M. 2005. Cortactin promotes cell motility by enhancing lamellipodial persistence. *Curr Biol* **15**(14): 1276-1285.

Buccione, R., Orth, J.D., and McNiven, M.A. 2004. Foot and mouth: podosomes, invadopodia and circular dorsal ruffles. *Nat Rev Mol Cell Biol* **5**(8): 647-657.

Burridge, K. and Chrzanowska-Wodnicka, M. 1996. Focal adhesions, contractility, and signaling. *Annu Rev Cell Dev Biol* **12**: 463-518.

Burridge, K. and Wennerberg, K. 2004. Rho and Rac take center stage. *Cell* **116**(2): 167-179.

Cai, L., Marshall, T.W., Uetrecht, A.C., Schafer, D.A., and Bear, J.E. 2007. Coronin 1B coordinates Arp2/3 complex and cofilin activities at the leading edge. *Cell* **128**(5): 915-929.

Campbell, R.E. 2009. Fluorescent-protein-based biosensors: modulation of energy transfer as a design principle. *Anal Chem* **81**(15): 5972-5979.

Cardelli, J. 2001. Phagocytosis and macropinocytosis in Dictyostelium: phosphoinositide-based processes, biochemically distinct. *Traffic* **2**(5): 311-320.

Carlson, H.J. and Campbell, R.E. 2009. Genetically encoded FRET-based biosensors for multiparameter fluorescence imaging. *Curr Opin Biotechnol* **20**(1): 19-27.

Carman, C.V. 2009. Mechanisms for transcellular diapedesis: probing and pathfinding by 'invadosome-like protrusions'. *J Cell Sci* **122**(Pt 17): 3025-3035.

Carman, C.V., Jun, C.D., Salas, A., and Springer, T.A. 2003. Endothelial cells proactively form microvilli-like membrane projections upon intercellular adhesion molecule 1 engagement of leukocyte LFA-1. *J Immunol* **171**(11): 6135-6144.

Carman, C.V., Sage, P.T., Sciuto, T.E., de la Fuente, M.A., Geha, R.S., Ochs, H.D., Dvorak, H.F., Dvorak, A.M., and Springer, T.A. 2007. Transcellular diapedesis is initiated by invasive podosomes. *Immunity* **26**(6): 784-797.

Carman, C.V. and Springer, T.A. 2004. A transmigratory cup in leukocyte diapedesis both through individual vascular endothelial cells and between them. *J Cell Biol* **167**(2): 377-388.

Caswell, P.T., Spence, H.J., Parsons, M., White, D.P., Clark, K., Cheng, K.W., Mills, G.B., Humphries, M.J., Messent, A.J., Anderson, K.I. et al. 2007. Rab25 associates with alpha5beta1 integrin to promote invasive migration in 3D microenvironments. *Dev Cell* **13**(4): 496-510.

Chalfie, M., Tu, Y., Euskirchen, G., Ward, W.W., and Prasher, D.C. 1994. Green fluorescent protein as a marker for gene expression. *Science* **263**(5148): 802-805.

Chang, F., Lemmon, C.A., Park, D., and Romer, L.H. 2007. FAK potentiates Rac1 activation and localization to matrix adhesion sites: a role for betaPIX. *Mol Biol Cell* **18**(1): 253-264.

Chang, Y.C., Nalbant, P., Birkenfeld, J., Chang, Z.F., and Bokoch, G.M. 2008. GEF-H1 couples nocodazole-induced microtubule disassembly to cell contractility via RhoA. *Mol Biol Cell* **19**(5): 2147-2153.

Choi, J.S., Paek, A.R., Kim, S.Y., and You, H.J. 2010. GIPC mediates the generation of reactive oxygen species and the regulation of cancer cell proliferation by insulin-like growth factor-1/IGF-1R signaling. *Cancer Lett* **294**(2): 254-263.

Choquet, D., Felsenfeld, D.P., and Sheetz, M.P. 1997. Extracellular matrix rigidity causes strengthening of integrin-cytoskeleton linkages. *Cell* **88**(1): 39-48.

Chrzanowska-Wodnicka, M. and Burridge, K. 1996. Rho-stimulated contractility drives the formation of stress fibers and focal adhesions. *J Cell Biol* **133**(6): 1403-1415.

Chung, C.Y., Potikyan, G., and Firtel, R.A. 2001. Control of cell polarity and chemotaxis by Akt/PKB and PI3 kinase through the regulation of PAKa. *Mol Cell* **7**(5): 937-947.

Clark, E.A., Golub, T.R., Lander, E.S., and Hynes, R.O. 2000. Genomic analysis of metastasis reveals an essential role for RhoC. *Nature* **406**(6795): 532-535.

Condeelis, J. and Segall, J.E. 2003. Intravital imaging of cell movement in tumours. *Nat Rev Cancer* **3**(12): 921-930.

Cosson, P., de Curtis, I., Pouyssegur, J., Griffiths, G., and Davoust, J. 1989. Low cytoplasmic pH inhibits endocytosis and transport from the trans-Golgi network to the cell surface. *J Cell Biol* **108**(2): 377-387.

Cote, J.F. and Vuori, K. 2007. GEF what? Dock180 and related proteins help Rac to polarize cells in new ways. *Trends Cell Biol* **17**(8): 383-393.

Counillon, L., Scholz, W., Lang, H.J., and Pouyssegur, J. 1993. Pharmacological characterization of stably transfected Na+/H+ antiporter isoforms using amiloride analogs and a new inhibitor exhibiting anti-ischemic properties. *Mol Pharmacol* **44**(5): 1041-1045.

Coussens, L.M., Fingleton, B., and Matrisian, L.M. 2002. Matrix metalloproteinase inhibitors and cancer: trials and tribulations. *Science* **295**(5564): 2387-2392.

Cram, E.J., Shang, H., and Schwarzbauer, J.E. 2006. A systematic RNA interference screen reveals a cell migration gene network in C. elegans. *J Cell Sci* **119**(Pt 23): 4811-4818.

Cybulsky, M.I., Iiyama, K., Li, H., Zhu, S., Chen, M., Iiyama, M., Davis, V., Gutierrez-Ramos, J.C., Connelly, P.W., and Milstone, D.S. 2001. A major role for VCAM-1, but not ICAM-1, in early atherosclerosis. *J Clin Invest* **107**(10): 1255-1262.

D'Angelo, R., Aresta, S., Blangy, A., Del Maestro, L., Louvard, D., and Arpin, M. 2007. Interaction of ezrin with the novel guanine nucleotide exchange factor PLEKHG6 promotes RhoG-dependent apical cytoskeleton rearrangements in epithelial cells. *Mol Biol Cell* **18**(12): 4780-4793.

Dalton, C.M., Miszkiel, K.A., Barker, G.J., MacManus, D.G., Pepple, T.I., Panzara, M., Yang, M., Hulme, A., O'Connor, P., and Miller, D.H. 2004. Effect of natalizumab on conversion of gadolinium enhancing lesions to T1 hypointense lesions in relapsing multiple sclerosis. *J Neurol* **251**(4): 407-413.

Das, S.R. and Piccirilli, J.A. 2005. General acid catalysis by the hepatitis delta virus ribozyme. *Nat Chem Biol* **1**(1): 45-52.

352

Davenport, R.W., Dou, P., Rehder, V., and Kater, S.B. 1993. A sensory role for neuronal growth cone filopodia. *Nature* **361**(6414): 721-724.

Davoust, J., Gruenberg, J., and Howell, K.E. 1987. Two threshold values of low pH block endocytosis at different stages. *Embo J* **6**(12): 3601-3609.

deBakker, C.D., Haney, L.B., Kinchen, J.M., Grimsley, C., Lu, M., Klingele, D., Hsu, P.K., Chou, B.K., Cheng, L.C., Blangy, A. et al. 2004. Phagocytosis of apoptotic cells is regulated by a UNC-73/TRIO-MIG-2/RhoG signaling module and armadillo repeats of CED-12/ELMO. *Curr Biol* **14**(24): 2208-2216.

Debant, A., Serra-Pages, C., Seipel, K., O'Brien, S., Tang, M., Park, S.H., and Streuli, M. 1996. The multidomain protein Trio binds the LAR transmembrane tyrosine phosphatase, contains a protein kinase domain, and has separate rac-specific and rho-specific guanine nucleotide exchange factor domains. *Proc Natl Acad Sci U S A* **93**(11): 5466-5471.

Dejana, E. 2006. The transcellular railway: insights into leukocyte diapedesis. *Nat Cell Biol* **8**(2): 105-107.

del Pozo, M.A., Alderson, N.B., Kiosses, W.B., Chiang, H.H., Anderson, R.G., and Schwartz, M.A. 2004. Integrins regulate Rac targeting by internalization of membrane domains. *Science* **303**(5659): 839-842.

Del Pozo, M.A., Kiosses, W.B., Alderson, N.B., Meller, N., Hahn, K.M., and Schwartz, M.A. 2002. Integrins regulate GTP-Rac localized effector interactions through dissociation of Rho-GDI. *Nat Cell Biol* **4**(3): 232-239.

Del Pozo, M.A., Price, L.S., Alderson, N.B., Ren, X.D., and Schwartz, M.A. 2000. Adhesion to the extracellular matrix regulates the coupling of the small GTPase Rac to its effector PAK. *Embo Journal* **19**(9): 2008-2014.

Del Pozo, M.A. and Schwartz, M.A. 2007. Rac, membrane heterogeneity, caveolin and regulation of growth by integrins. *Trends Cell Biol* **17**(5): 246-250.

Denker, S.P. and Barber, D.L. 2002. Cell migration requires both ion translocation and cytoskeletal anchoring by the Na-H exchanger NHE1. *J Cell Biol* **159**(6): 1087-1096.

Devreotes, P. and Janetopoulos, C. 2003. Eukaryotic chemotaxis: distinctions between directional sensing and polarization. *J Biol Chem* **278**(23): 20445-20448.

Dhanasekaran, D.N., Kashef, K., Lee, C.M., Xu, H., and Reddy, E.P. 2007. Scaffold proteins of MAP-kinase modules. *Oncogene* **26**(22): 3185-3202.

Dharmawardhane, S., Sanders, L.C., Martin, S.S., Daniels, R.H., and Bokoch, G.M. 1997. Localization of p21-activated kinase 1 (PAK1) to pinocytic vesicles and cortical actin structures in stimulated cells. *J Cell Biol* **138**(6): 1265-1278.

Dharmawardhane, S., Schurmann, A., Sells, M.A., Chernoff, J., Schmid, S.L., and Bokoch, G.M. 2000. Regulation of macropinocytosis by p21-activated kinase-1. *Mol Biol Cell* **11**(10): 3341-3352.

Dise, R.S., Frey, M.R., Whitehead, R.H., and Polk, D.B. 2008. Epidermal growth factor stimulates Rac activation through Src and phosphatidylinositol 3-kinase to promote colonic epithelial cell migration. *Am J Physiol Gastrointest Liver Physiol* **294**(1): G276-285.

Dransart, E., Morin, A., Cherfils, J., and Olofsson, B. 2005. RhoGDI-3, a promising system to investigate the regulatory function of rhoGDIs: uncoupling of inhibitory and shuttling functions of rhoGDIs. *Biochem Soc Trans* **33**(Pt 4): 623-626.

Dumenil, G., Sansonetti, P., and Tran Van Nhieu, G. 2000. Src tyrosine kinase activity down-regulates Rho-dependent responses during Shigella entry into epithelial cells and stress fibre formation. *J Cell Sci* **113 (Pt 1)**: 71-80.

Dunn, G.A. and Jones, G.E. 2004. Cell motility under the microscope: Vorsprung durch Technik. *Nat Rev Mol Cell Biol* **5**(8): 667-672.

Edwards, D.C., Sanders, L.C., Bokoch, G.M., and Gill, G.N. 1999. Activation of LIM-kinase by Pak1 couples Rac/Cdc42 GTPase signalling to actin cytoskeletal dynamics. *Nat Cell Biol* **1**(5): 253-259.

Efron, B. and Tibshirani, R.J. 1994. *An Introduction to the Bootstrap* Chapman & Hall/CRC.

Elfenbein, A., Rhodes, J.M., Meller, J., Schwartz, M.A., Matsuda, M., and Simons, M. 2009. Suppression of RhoG activity is mediated by a syndecan 4-synectin-RhoGDI1 complex and is reversed by PKCalpha in a Rac1 activation pathway. *J Cell Biol* **186**(1): 75-83.

Ellerbroek, S.M., Wennerberg, K., Arthur, W.T., Dunty, J.M., Bowman, D.R., DeMali, K.A., Der, C., and Burridge, K. 2004. SGEF, a RhoG guanine nucleotide exchange factor that stimulates macropinocytosis. *Mol Biol Cell* **15**(7): 3309-3319.

Engelhardt, B. and Wolburg, H. 2004. Mini-review: Transendothelial migration of leukocytes: through the front door or around the side of the house? *Eur J Immunol* **34**(11): 2955-2963.

Entman, M.L., Michael, L., Rossen, R.D., Dreyer, W.J., Anderson, D.C., Taylor, A.A., and Smith, C.W. 1991. Inflammation in the course of early myocardial ischemia. *Faseb J* **5**(11): 2529-2537.

Etienne-Manneville, S. and Hall, A. 2002. Rho GTPases in cell biology. *Nature* **420**(6916): 629-635.

-. 2003. Cell polarity: Par6, aPKC and cytoskeletal crosstalk. *Curr Opin Cell Biol* **15**(1): 67-72.

Etienne-Manneville, S., Manneville, J.B., Adamson, P., Wilbourn, B., Greenwood, J., and Couraud, P.O. 2000. ICAM-1-coupled cytoskeletal rearrangements and transendothelial lymphocyte migration involve intracellular calcium signaling in brain endothelial cell lines. *J Immunol* **165**(6): 3375-3383.

Etienne, S., Adamson, P., Greenwood, J., Strosberg, A.D., Cazaubon, S., and Couraud, P.O. 1998. ICAM-1 signaling pathways associated with Rho activation in microvascular brain endothelial cells. *J Immunol* **161**(10): 5755-5761.

Faix, J., Breitsprecher, D., Stradal, T.E., and Rottner, K. 2009. Filopodia: Complex models for simple rods. *Int J Biochem Cell Biol* **41**(8-9): 1656-1664.

Falcone, S., Cocucci, E., Podini, P., Kirchhausen, T., Clementi, E., and Meldolesi, J. 2006. Macropinocytosis: regulated coordination of endocytic and exocytic membrane traffic events. *J Cell Sci* **119**(Pt 22): 4758-4769.

Faustmann, P.M. and Dermietzel, R. 1985. Extravasation of polymorphonuclear leukocytes from the cerebral microvasculature. Inflammatory response induced by alpha-bungarotoxin. *Cell Tissue Res* **242**(2): 399-407.

Fernandez-Borja, M., van Buul, J.D., and Hordijk, P.L. 2010. The regulation of leucocyte transendothelial migration by endothelial signalling events. *Cardiovasc Res* **86**(2): 202-210.

Ford, B.J. 1995. First Steps in Experimental Microscopy, Leeuwenhoek as Practical Scientist. *The Microscope* **43**: 47-57.

Frantz, C., Barreiro, G., Dominguez, L., Chen, X., Eddy, R., Condeelis, J., Kelly, M.J., Jacobson, M.P., and Barber, D.L. 2008. Cofilin is a pH sensor for actin free barbed end formation: role of phosphoinositide binding. *J Cell Biol* **183**(5): 865-879.

Frantz, C., Karydis, A., Nalbant, P., Hahn, K.M., and Barber, D.L. 2007. Positive feedback between Cdc42 activity and H+ efflux by the Na-H exchanger NHE1 for polarity of migrating cells. *J Cell Biol* **179**(3): 403-410.

Franz, C.M., Jones, G.E., and Ridley, A.J. 2002. Cell migration in development and disease. *Dev Cell* **2**(2): 153-158.

Friedl, P. and Wolf, K. 2009. Plasticity of cell migration: a multiscale tuning model. *J Cell Biol* **188**(1): 11-19.

Gadea, G., Roger, L., Anguille, C., de Toledo, M., Gire, V., and Roux, P. 2004. TNFalpha induces sequential activation of Cdc42- and p38/p53-dependent pathways that antagonistically regulate filopodia formation. *J Cell Sci* **117**(Pt 26): 6355-6364.

Gaggioli, C., Hooper, S., Hidalgo-Carcedo, C., Grosse, R., Marshall, J.F., Harrington, K., and Sahai, E. 2007. Fibroblast-led collective invasion of carcinoma cells with differing roles for RhoGTPases in leading and following cells. *Nat Cell Biol* **9**(12): 1392-1400.

Galkina, E. and Ley, K. 2007. Vascular adhesion molecules in atherosclerosis. *Arterioscler Thromb Vasc Biol* **27**(11): 2292-2301.

Ganz, M.B., Boyarsky, G., Sterzel, R.B., and Boron, W.F. 1989. Arginine vasopressin enhances pHi regulation in the presence of HCO3- by stimulating three acid-base transport systems. *Nature* **337**(6208): 648-651.

Garrett, T.A., Van Buul, J.D., and Burridge, K. 2007. VEGF-induced Rac1 activation in endothelial cells is regulated by the guanine nucleotide exchange factor Vav2. *Exp Cell Res* **313**(15): 3285-3297.

Garrett, W.S., Chen, L.M., Kroschewski, R., Ebersold, M., Turley, S., Trombetta, S., Galan, J.E., and Mellman, I. 2000. Developmental control of endocytosis in dendritic cells by Cdc42. *Cell* **102**(3): 325-334.

Gauthier-Rouviere, C., Vignal, E., Meriane, M., Roux, P., Montcourier, P., and Fort, P. 1998. RhoG GTPase controls a pathway that independently activates Rac1 and Cdc42Hs. *Mol Biol Cell* **9**(6): 1379-1394.

Geiger, B., Spatz, J.P., and Bershadsky, A.D. 2009. Environmental sensing through focal adhesions. *Nat Rev Mol Cell Biol* **10**(1): 21-33.

Gibbs, J.B. 1995. Determination of guanine nucleotides bound to Ras in mammalian cells. *Methods Enzymol* **255**: 118-125.

Glading, A., Lauffenburger, D.A., and Wells, A. 2002. Cutting to the chase: calpain proteases in cell motility. *Trends Cell Biol* **12**(1): 46-54.

Grant, D.M., Zhang, W., McGhee, E.J., Bunney, T.D., Talbot, C.B., Kumar, S., Munro, I., Dunsby, C., Neil, M.A., Katan, M. et al. 2008. Multiplexed FRET to image multiple signaling events in live cells. *Biophys J* **95**(10): L69-71.

Greenwood, J., Amos, C.L., Walters, C.E., Couraud, P.O., Lyck, R., Engelhardt, B., and Adamson, P. 2003. Intracellular domain of brain endothelial intercellular adhesion molecule-1 is essential for T lymphocyte-mediated signaling and migration. *J Immunol* **171**(4): 2099-2108.

Greenwood, J., Howes, R., and Lightman, S. 1994. The blood-retinal barrier in experimental autoimmune uveoretinitis. Leukocyte interactions and functional damage. *Lab Invest* **70**(1): 39-52.

Grinstein, S., Cohen, S., Goetz, J.D., Rothstein, A., and Gelfand, E.W. 1985. Characterization of the activation of Na+/H+ exchange in lymphocytes by phorbol esters: change in cytoplasmic pH dependence of the antiport. *Proc Natl Acad Sci U S A* **82**(5): 1429-1433.

Grinstein, S., Rotin, D., and Mason, M.J. 1989. Na+/H+ exchange and growth factor-induced cytosolic pH changes. Role in cellular proliferation. *Biochim Biophys Acta* **988**(1): 73-97.

Gu, Z., Noss, E.H., Hsu, V.W., and Brenner, M.B. 2011. Integrins traffic rapidly via circular dorsal ruffles and macropinocytosis during stimulated cell migration. *J Cell Biol* **193**(1): 61-70.

Hakeda-Suzuki, S., Ng, J., Tzu, J., Dietzl, G., Sun, Y., Harms, M., Nardine, T., Luo, L., and Dickson, B.J. 2002. Rac function and regulation during Drosophila development. *Nature* **416**(6879): 438-442.

Hansson, G.K. and Libby, P. 2006. The immune response in atherosclerosis: a double-edged sword. *Nat Rev Immunol* **6**(7): 508-519.

Harlan, J.M. and Winn, R.K. 2002. Leukocyte-endothelial interactions: clinical trials of anti-adhesion therapy. *Crit Care Med* **30**(5 Suppl): S214-219.

Harrison, R.G. 1907. Observations on the living developing nerve fiber. *Anatomy Record* **1**: 116-118.

Hasegawa, H., Kiyokawa, E., Tanaka, S., Nagashima, K., Gotoh, N., Shibuya, M., Kurata, T., and Matsuda, M. 1996. DOCK180, a major CRK-binding protein, alters cell morphology upon translocation to the cell membrane. *Mol Cell Biol* **16**(4): 1770-1776.

Hendey, B., Klee, C.B., and Maxfield, F.R. 1992. Inhibition of neutrophil chemokinesis on vitronectin by inhibitors of calcineurin. *Science* **258**(5080): 296-299.

Henson, P.M. 2005. Engulfment: ingestion and migration with Rac, Rho and TRIO. *Curr Biol* **15**(1): R29-30.

Heuser, J. 1989. Effects of cytoplasmic acidification on clathrin lattice morphology. *J Cell Biol* **108**(2): 401-411.

Heuser, J.E. and Anderson, R.G. 1989. Hypertonic media inhibit receptor-mediated endocytosis by blocking clathrin-coated pit formation. *J Cell Biol* **108**(2): 389-400.

Hinner, M.J. and Johnsson, K. 2010. How to obtain labeled proteins and what to do with them. *Curr Opin Biotechnol* **21**(6): 766-776.

Hiraga, J., Katsumi, A., Iwasaki, T., Abe, A., Kiyoi, H., Matsushita, T., Kinoshita, T., and Naoe, T. 2007. Prognostic analysis of aberrant somatic hypermutation of RhoH gene in diffuse large B cell lymphoma. *Leukemia* **21**(8): 1846-1847.

Hiramoto-Yamaki, N., Takeuchi, S., Ueda, S., Harada, K., Fujimoto, S., Negishi, M., and Katoh, H. 2010. Ephexin4 and EphA2 mediate cell migration through a RhoG-dependent mechanism. *J Cell Biol* **190**(3): 461-477.

Hiramoto, K., Negishi, M., and Katoh, H. 2006. Dock4 is regulated by RhoG and promotes Rac-dependent cell migration. *Exp Cell Res* **312**(20): 4205-4216.

Ho, E., Irvine, T., Vilk, G.J., Lajoie, G., Ravichandran, K.S., D'Souza, S.J., and Dagnino, L. 2009. Integrin-linked kinase interactions with ELMO2 modulate cell polarity. *Mol Biol Cell* **20**(13): 3033-3043.

Ho, H.Y., Rohatgi, R., Lebensohn, A.M., Le, M., Li, J., Gygi, S.P., and Kirschner, M.W. 2004. Toca-1 mediates Cdc42-dependent actin nucleation by activating the N-WASP-WIP complex. *Cell* **118**(2): 203-216.

Hodgson, L., Nalbant, P., Shen, F., and Hahn, K. 2006. Imaging and photobleach correction of Mero-CBD, sensor of endogenous Cdc42 activation. *Methods Enzymol* **406**: 140-156.

Hodgson, L., Nalbant, P., Shen, F., and Hahn, K.M. 2005. Imaging and Photobleach Correction of Mero-CBD, Sensor of Endogenous Cdc42 Activation. in *Methods in Enzymology* (ed. A. Hall), pp. 140 - 156. Elsevier, New York.

Hodgson, L., Pertz, O., and Hahn, K.M. 2008. Design and optimization of genetically encoded fluorescent biosensors: GTPase biosensors. *Methods Cell Biol* **85**: 63-81.

Hodgson, L., Shen, F. and Hahn, K. 2009. Biosensors for characterizing the dynamics of Rho family GTPases in living cells. *Current Protocols in Cell Biology* **In Press.**

Hood, J.D. and Cheresh, D.A. 2002. Role of integrins in cell invasion and migration. *Nat Rev Cancer* **2**(2): 91-100.

Hoppe, A.D. and Swanson, J.A. 2004. Cdc42, Rac1, and Rac2 display distinct patterns of activation during phagocytosis. *Mol Biol Cell* **15**(8): 3509-3519.

Hordijk, P.L. 2006. Endothelial signalling events during leukocyte transmigration. *Febs J* **273**(19): 4408-4415.

Huang, Y.E., Iijima, M., Parent, C.A., Funamoto, S., Firtel, R.A., and Devreotes, P. 2003. Receptor-mediated regulation of PI3Ks confines PI(3,4,5)P3 to the leading edge of chemotaxing cells. *Mol Biol Cell* **14**(5): 1913-1922.

Ilina, O. and Friedl, P. 2009. Mechanisms of collective cell migration at a glance. *J Cell Sci* **122**(Pt 18): 3203-3208.

Itoh, R.E., Kiyokawa, E., Aoki, K., Nishioka, T., Akiyama, T., and Matsuda, M. 2008. Phosphorylation and activation of the Rac1 and Cdc42 GEF Asef in A431 cells stimulated by EGF. *J Cell Sci* **121**(Pt 16): 2635-2642.

Itoh, R.E., Kurokawa, K., Fujioka, A., Sharma, A., Mayer, B.J., and Matsuda, M. 2005. A FRET-based probe for epidermal growth factor receptor bound non-covalently to a pair of synthetic amphipathic helixes. *Exp Cell Res* **307**(1): 142-152.

Itoh, R.E., Kurokawa, K., Ohba, Y., Yoshizaki, H., Mochizuki, N., and Matsuda, M. 2002. Activation of rac and cdc42 video imaged by fluorescent resonance energy transfer-based single-molecule probes in the membrane of living cells. *Mol Cell Biol* **22**(18): 6582-6591.

Jaffe, A.B. and Hall, A. 2005. Rho GTPases: biochemistry and biology. *Annu Rev Cell Dev Biol* **21**: 247-269.

Jarzynka, M.J., Hu, B., Hui, K.M., Bar-Joseph, I., Gu, W., Hirose, T., Haney, L.B., Ravichandran, K.S., Nishikawa, R., and Cheng, S.Y. 2007. ELMO1 and Dock180, a bipartite Rac1 guanine nucleotide exchange factor, promote human glioma cell invasion. *Cancer Res* **67**(15): 7203-7211.

Jiang, W.G., Watkins, G., Lane, J., Cunnick, G.H., Douglas-Jones, A., Mokbel, K., and Mansel, R.E. 2003. Prognostic value of rho GTPases and rho guanine nucleotide dissociation inhibitors in human breast cancers. *Clin Cancer Res* **9**(17): 6432-6440.

Jones, M.K., Sasaki, E., Halter, F., Pai, R., Nakamura, T., Arakawa, T., Kuroki, T., and Tarnawski, A.S. 1999. HGF triggers activation of the COX-2 gene in rat gastric epithelial cells: action mediated through the ERK2 signaling pathway. *FASEB J* **13**(15): 2186-2194.

Jones, S.P. and Lefer, D.J. 2000. Myocardial Reperfusion Injury: Insights Gained from Gene-Targeted Mice. *News Physiol Sci* **15**: 303-308.

Jones, S.P., Trocha, S.D., Strange, M.B., Granger, D.N., Kevil, C.G., Bullard, D.C., and Lefer, D.J. 2000. Leukocyte and endothelial cell adhesion molecules in a chronic murine model of myocardial reperfusion injury. *Am J Physiol Heart Circ Physiol* **279**(5): H2196-2201.

Jullien, D., Prinz, J.C., Langley, R.G., Caro, I., Dummer, W., Joshi, A., Dedrick, R., and Natta, P. 2004. T-cell modulation for the treatment of chronic plaque psoriasis with efalizumab (Raptiva): mechanisms of action. *Dermatology* **208**(4): 297-306.

Kamath, R.S., Fraser, A.G., Dong, Y., Poulin, G., Durbin, R., Gotta, M., Kanapin, A., Le Bot, N., Moreno, S., Sohrmann, M. et al. 2003. Systematic functional analysis of the Caenorhabditis elegans genome using RNAi. *Nature* **421**(6920): 231-237.

Kanchanawong, P., Shtengel, G., Pasapera, A.M., Ramko, E.B., Davidson, M.W., Hess, H.F., and Waterman, C.M. 2010. Nanoscale architecture of integrin-based cell adhesions. *Nature* **468**(7323): 580-584.

Kansas, G.S. 1996. Selectins and their ligands: current concepts and controversies. *Blood* **88**(9): 3259-3287.

Katoh, H., Hiramoto, K., and Negishi, M. 2006. Activation of Rac1 by RhoG regulates cell migration. *J Cell Sci* **119**(Pt 1): 56-65.

Katoh, H. and Negishi, M. 2003. RhoG activates Rac1 by direct interaction with the Dock180-binding protein Elmo. *Nature* **424**(6947): 461-464.

Katoh, H., Yasui, H., Yamaguchi, Y., Aoki, J., Fujita, H., Mori, K., and Negishi, M. 2000. Small GTPase RhoG is a key regulator for neurite outgrowth in PC12 cells. *Mol Cell Biol* **20**(19): 7378-7387.

Kelly, M., Hwang, J.M., and Kubes, P. 2007. Modulating leukocyte recruitment in inflammation. *J Allergy Clin Immunol* **120**(1): 3-10.

Kinashi, T. 2005. Intracellular signalling controlling integrin activation in lymphocytes. *Nat Rev Immunol* **5**(7): 546-559.

Kishore, R.S. and Sundaram, M.V. 2002. ced-10 Rac and mig-2 function redundantly and act with unc-73 trio to control the orientation of vulval cell divisions and migrations in Caenorhabditis elegans. *Dev Biol* **241**(2): 339-348.

Kiyokawa, E. and Matsuda, M. 2009. Regulation of focal adhesion and cell migration by ANKRD28-DOCK180 interaction. *Cell Adh Migr* **3**(3): 281-284.

Koh, C.G., Manser, E., Zhao, Z.S., Ng, C.P., and Lim, L. 2001. Beta1PIX, the PAK-interacting exchange factor, requires localization via a coiled-coil region to

promote microvillus-like structures and membrane ruffles. *J Cell Sci* **114**(Pt 23): 4239-4251.

Koivusalo, M., Welch, C., Hayashi, H., Scott, C.C., Kim, M., Alexander, T., Touret, N., Hahn, K.M., and Grinstein, S. 2010. Amiloride inhibits macropinocytosis by lowering submembranous pH and preventing Rac1 and Cdc42 signaling. *J Cell Biol.*

Kolsch, V., Charest, P.G., and Firtel, R.A. 2008. The regulation of cell motility and chemotaxis by phospholipid signaling. *J Cell Sci* **121**(Pt 5): 551-559.

Korobova, F. and Svitkina, T. 2008. Arp2/3 complex is important for filopodia formation, growth cone motility, and neuritogenesis in neuronal cells. *Mol Biol Cell* **19**(4): 1561-1574.

Koushik, S.V., Blank, P.S., and Vogel, S.S. 2009. Anomalous surplus energy transfer observed with multiple FRET acceptors. *PLoS One* **4**(11): e8031.

Kratchmarova, I., Blagoev, B., Haack-Sorensen, M., Kassem, M., and Mann, M. 2005. Mechanism of divergent growth factor effects in mesenchymal stem cell differentiation. *Science* **308**(5727): 1472-1477.

Kraynov, V.S., Chamberlain, C., Bokoch, G.M., Schwartz, M.A., Slabaugh, S., and Hahn, K.M. 2000. Localized Rac activation dynamics visualized in living cells. *Science* **290**(5490): 333-337.

Kubes, P., Jutila, M., and Payne, D. 1995. Therapeutic potential of inhibiting leukocyte rolling in ischemia/reperfusion. *J Clin Invest* **95**(6): 2510-2519.

Kurokawa, K., Itoh, R.E., Yoshizaki, H., Nakamura, Y.O., and Matsuda, M. 2004. Coactivation of Rac1 and Cdc42 at lamellipodia and membrane ruffles induced by epidermal growth factor. *Mol Biol Cell* **15**(3): 1003-1010.

Kurokawa, K. and Matsuda, M. 2005. Localized RhoA activation as a requirement for the induction of membrane ruffling. *Mol Biol Cell* **16**(9): 4294-4303.

Kwok, S., Lee, C., Sanchez, S.A., Hazlett, T.L., Gratton, E., and Hayashi, Y. 2008. Genetically encoded probe for fluorescence lifetime imaging of CaMKII activity. *Biochem Biophys Res Commun* **369**(2): 519-525.

L'Allemain, G., Paris, S., and Pouysségur, J. 1984. Growth factor action and intracellular pH regulation in fibroblasts. Evidence for a major role of the Na+/H+ antiport. *J Biol Chem* **259**(9): 5809-5815.

-. 1985. Role of a Na+-dependent Cl-/HCO3- exchange in regulation of intracellular pH in fibroblasts. *J Biol Chem* **260**(8): 4877-4883.

Lagana, A., Vadnais, J., Le, P.U., Nguyen, T.N., Laprade, R., Nabi, I.R., and Noel, J. 2000. Regulation of the formation of tumor cell pseudopodia by the Na(+)/H(+) exchanger NHE1. *J Cell Sci* **113 (Pt 20)**: 3649-3662.

Lammers, M., Meyer, S., Kuhlmann, D., and Wittinghofer, A. 2008. Specificity of interactions between mDia isoforms and Rho proteins. *J Biol Chem* **283**(50): 35236-35246.

Lanni, F., Waggoner, A.S., and Taylor, D.L. 1985. Structural organization of interphase 3T3 fibroblasts studied by total internal reflection fluorescence microscopy. *J Cell Biol* **100**(4): 1091-1102.

Lauffenburger, D.A. and Horwitz, A.F. 1996. Cell migration: a physically integrated molecular process. *Cell* **84**(3): 359-369.

Lazarides, E. and Weber, K. 1974. Actin antibody: the specific visualization of actin filaments in non-muscle cells. *Proc Natl Acad Sci U S A* **71**(6): 2268-2272.

Lebrand, C., Dent, E.W., Strasser, G.A., Lanier, L.M., Krause, M., Svitkina, T.M., Borisy, G.G., and Gertler, F.B. 2004. Critical role of Ena/VASP proteins for filopodia formation in neurons and in function downstream of netrin-1. *Neuron* **42**(1): 37-49.

Lee, C.S., Choi, C.K., Shin, E.Y., Schwartz, M.A., and Kim, E.G. 2010a. Myosin II directly binds and inhibits Dbl family guanine nucleotide exchange factors: a possible link to Rho family GTPases. *J Cell Biol* **190**(4): 663-674.

Lee, J., Ishihara, A., Oxford, G., Johnson, B., and Jacobson, K. 1999. Regulation of cell movement is mediated by stretch-activated calcium channels. *Nature* **400**(6742): 382-386.

Lee, J.D., Hempel, N., Lee, N.Y., and Blobe, G.C. 2009. The type III TGF-beta receptor suppresses breast cancer progression through GIPC-mediated inhibition of TGF-beta signaling. *Carcinogenesis* **31**(2): 175-183.

Lee, K., Gallop, J.L., Rambani, K., and Kirschner, M.W. 2010b. Self-assembly of filopodia-like structures on supported lipid bilayers. *Science* **329**(5997): 1341-1345.

Lemmon, M.A., Ferguson, K.M., and Abrams, C.S. 2002. Pleckstrin homology domains and the cytoskeleton. *FEBS Lett* **513**(1): 71-76.

Lendvai, B., Stern, E.A., Chen, B., and Svoboda, K. 2000. Experience-dependent plasticity of dendritic spines in the developing rat barrel cortex in vivo. *Nature* **404**(6780): 876-881.

Levskaya, A., Weiner, O.D., Lim, W.A., and Voigt, C.A. 2009. Spatiotemporal control of cell signalling using a light-switchable protein interaction. *Nature* **461**(7266): 997-1001.

Ley, K., Laudanna, C., Cybulsky, M.I., and Nourshargh, S. 2007. Getting to the site of inflammation: the leukocyte adhesion cascade updated. *Nat Rev Immunol* **7**(9): 678-689.

Li, Z., Hannigan, M., Mo, Z., Liu, B., Lu, W., Wu, Y., Smrcka, A.V., Wu, G., Li, L., Liu, M. et al. 2003. Directional sensing requires G beta gamma-mediated PAK1 and PIX alpha-dependent activation of Cdc42. *Cell* **114**(2): 215-227.

Liaw, Y.S., Yang, P.C., Yu, C.J., Kuo, S.H., Luh, K.T., Lin, Y.J., and Wu, M.L. 1998. PKC activation is required by EGF-stimulated Na(+)-H+ exchanger in human pleural mesothelial cells. *Am J Physiol* **274**(5 Pt 1): L665-672.

Liberali, P., Kakkonen, E., Turacchio, G., Valente, C., Spaar, A., Perinetti, G., Bockmann, R.A., Corda, D., Colanzi, A., Marjomaki, V. et al. 2008. The closure of Pak1-dependent macropinosomes requires the phosphorylation of CtBP1/BARS. *Embo J* **27**(7): 970-981.

Lichtman, A.H., Cybulsky, M., and Luscinskas, F.W. 1996. Immunology of atherosclerosis: the promise of mouse models. *Am J Pathol* **149**(2): 351-357.

Lindmo, K. and Stenmark, H. 2006. Regulation of membrane traffic by phosphoinositide 3-kinases. *J Cell Sci* **119**(Pt 4): 605-614.

Liu, B.P. and Burridge, K. 2000. Vav2 activates Rac1, Cdc42, and RhoA downstream from growth factor receptors but not beta1 integrins. *Mol Cell Biol* **20**(19): 7160-7169.

Lutters, B.C., Leeuwenburgh, M.A., Appeldoorn, C.C., Molenaar, T.J., Van Berkel, T.J., and Biessen, E.A. 2004. Blocking endothelial adhesion molecules: a potential therapeutic strategy to combat atherogenesis. *Curr Opin Lipidol* **15**(5): 545-552.

Machacek, M. and Danuser, G. 2006. Morphodynamic profiling of protrusion phenotypes. *Biophys J* **90**(4): 1439-1452.

Machacek, M., Hodgson, L., Welch, C., Elliott, H., Pertz, O., Nalbant, P., Abell, A., Johnson, G.L., Hahn, K.M., and Danuser, G. 2009. Coordination of Rho GTPase activities during cell protrusion. *Nature* **461**(7260): 99-103.

Mahal, L.K. 2008. Glycomics: towards bioinformatic approaches to understanding glycosylation. *Anticancer Agents Med Chem* **8**(1): 37-51.

Makino, Y., Tsuda, M., Ichihara, S., Watanabe, T., Sakai, M., Sawa, H., Nagashima, K., Hatakeyama, S., and Tanaka, S. 2006. Elmo1 inhibits ubiquitylation of Dock180. *J Cell Sci* **119**(Pt 5): 923-932.

Marcoux, N. and Vuori, K. 2003. EGF receptor mediates adhesion-dependent activation of the Rac GTPase: a role for phosphatidylinositol 3-kinase and Vav2. *Oncogene* **22**(38): 6100-6106.

Marguet, D., Lenne, P.F., Rigneault, H., and He, H.T. 2006. Dynamics in the plasma membrane: how to combine fluidity and order. *Embo Journal* **25**(15): 3446-3457.

Masereel, B., Pochet, L., and Laeckmann, D. 2003. An overview of inhibitors of Na(+)/H(+) exchanger. *Eur J Med Chem* **38**(6): 547-554.

Matthews, B.D., Overby, D.R., Mannix, R., and Ingber, D.E. 2006. Cellular adaptation to mechanical stress: role of integrins, Rho, cytoskeletal tension and mechanosensitive ion channels. *J Cell Sci* **119**(Pt 3): 508-518.

Matz, M.V., Fradkov, A.F., Labas, Y.A., Savitsky, A.P., Zaraisky, A.G., Markelov, M.L., and Lukyanov, S.A. 1999. Fluorescent proteins from nonbioluminescent Anthozoa species. *Nat Biotechnol* **17**(10): 969-973.

Mazzarello, P. 1999. A unifying concept: the history of cell theory. *Nat Cell Biol* **1**(1): E13-15.

McDonald, J.A., Pinheiro, E.M., and Montell, D.J. 2003. PVF1, a PDGF/VEGF homolog, is sufficient to guide border cells and interacts genetically with Taiman. *Development* **130**(15): 3469-3478.

McMenamin, P.G., Forrester, J.V., Steptoe, R.J., and Dua, H.S. 1992. Ultrastructural pathology of experimental autoimmune uveitis. Quantitative evidence of activation and possible high endothelial venule-like changes in retinal vascular endothelium. *Lab Invest* **67**(1): 42-55.

Meier, O., Boucke, K., Hammer, S.V., Keller, S., Stidwill, R.P., Hemmi, S., and Greber, U.F. 2002. Adenovirus triggers macropinocytosis and endosomal leakage together with its clathrin-mediated uptake. *J Cell Biol* **158**(6): 1119-1131.

Meller, J., Vidali, L., and Schwartz, M.A. 2008. Endogenous RhoG is dispensable for integrin-mediated cell spreading but contributes to Rac-independent migration. *J Cell Sci* **121**(Pt 12): 1981-1989.

Mellor, H. 2009. The role of formins in filopodia formation. *Biochim Biophys Acta* **1803**(2): 191-200.

Merlot, S. and Firtel, R.A. 2003. Leading the way: Directional sensing through phosphatidylinositol 3-kinase and other signaling pathways. *J Cell Sci* **116**(Pt 17): 3471-3478.

Michaelson, D., Abidi, W., Guardavaccaro, D., Zhou, M., Ahearn, I., Pagano, M., and Philips, M.R. 2008. Rac1 accumulates in the nucleus during the G2 phase of the cell cycle and promotes cell division. *J Cell Biol* **181**(3): 485-496.

Michaelson, D., Silletti, J., Murphy, G., D'Eustachio, P., Rush, M., and Philips, M.R. 2001. Differential localization of Rho GTPases in live cells: regulation by hypervariable regions and RhoGDI binding. *J Cell Biol* **152**(1): 111-126.

Middleton, J., Neil, S., Wintle, J., Clark-Lewis, I., Moore, H., Lam, C., Auer, M., Hub, E., and Rot, A. 1997. Transcytosis and surface presentation of IL-8 by venular endothelial cells. *Cell* **91**(3): 385-395.

Millan, J., Hewlett, L., Glyn, M., Toomre, D., Clark, P., and Ridley, A.J. 2006. Lymphocyte transcellular migration occurs through recruitment of endothelial ICAM-1 to caveola- and F-actin-rich domains. *Nat Cell Biol* **8**(2): 113-123.

Miller, D.H., Khan, O.A., Sheremata, W.A., Blumhardt, L.D., Rice, G.P., Libonati, M.A., Willmer-Hulme, A.J., Dalton, C.M., Miszkiel, K.A., and O'Connor, P.W. 2003. A controlled trial of natalizumab for relapsing multiple sclerosis. *N Engl J Med* **348**(1): 15-23.

Mitra, R.D., Silva, C.M., and Youvan, D.C. 1996. Fluorescence resonance energy transfer between blue-emitting and red-shifted excitation derivatives of the green fluorescent protein. *Gene* **173**(1 Spec No): 13-17.

Miyawaki, A. 2003. Visualization of the spatial and temporal dynamics of intracellular signaling. *Developmental Cell* **4**(3): 295-305.

Mohammadi, S. and Isberg, R.R. 2009. Yersinia pseudotuberculosis virulence determinants invasin, YopE, and YopT modulate RhoG activity and localization. *Infect Immun* **77**(11): 4771-4782.

Monypenny, J., Zicha, D., Higashida, C., Oceguera-Yanez, F., Narumiya, S., and Watanabe, N. 2009. Cdc42 and Rac family GTPases regulate mode and speed but not direction of primary fibroblast migration during platelet-derived growth factor-dependent chemotaxis. *Mol Cell Biol* **29**(10): 2730-2747.

Moran, M.F., Polakis, P., McCormick, F., Pawson, T., and Ellis, C. 1991. Protein-tyrosine kinases regulate the phosphorylation, protein interactions, subcellular distribution, and activity of p21ras GTPase-activating protein. *Mol Cell Biol* **11**(4): 1804-1812.

Muders, M.H., Vohra, P.K., Dutta, S.K., Wang, E., Ikeda, Y., Wang, L., Udugamasooriya, D.G., Memic, A., Rupasinghe, C.N., Baretton, G.B. et al. 2009. Targeting GIPC/synectin in pancreatic cancer inhibits tumor growth. *Clin Cancer Res* **15**(12): 4095-4103.

Nakashima, Y., Raines, E.W., Plump, A.S., Breslow, J.L., and Ross, R. 1998. Upregulation of VCAM-1 and ICAM-1 at atherosclerosis-prone sites on the endothelium in the ApoE-deficient mouse. *Arterioscler Thromb Vasc Biol* **18**(5): 842-851.

Nakayama, M., Goto, T.M., Sugimoto, M., Nishimura, T., Shinagawa, T., Ohno, S., Amano, M., and Kaibuchi, K. 2008. Rho-kinase phosphorylates PAR-3 and disrupts PAR complex formation. *Dev Cell* **14**(2): 205-215.

Nalbant, P., Hodgson, L., Kraynov, V., Toutchkine, A., and Hahn, K.M. 2004. Activation of endogenous Cdc42 visualized in living cells. *Science (New York, NY)* **305**(5690): 1615-1619.

Narumiya, S., Ishizaki, T., and Watanabe, N. 1997. Rho effectors and reorganization of actin cytoskeleton. *FEBS Lett* **410**: 68-72

Nayal, A., Webb, D.J., Brown, C.M., Schaefer, E.M., Vicente-Manzanares, M., and Horwitz, A.R. 2006. Paxillin phosphorylation at ser273 localizes a GIT1-PIX-PAK complex and regulates adhesion and protrusion dynamics. *Journal of Cell Biology* **173**(4): 587-599.

Nethe, M., Anthony, E.C., Fernandez-Borja, M., Dee, R., Geerts, D., Hensbergen, P.J., Deelder, A.M., Schmidt, G., and Hordijk, P.L. 2010. Focal-adhesion targeting links caveolin-1 to a Rac1-degradation pathway. *J Cell Sci* **123**(Pt 11): 1948-1958.

Newman, R.H., Fosbrink, M.D., and Zhang, J. 2011. Genetically encodable fluorescent biosensors for tracking signaling dynamics in living cells. *Chem Rev* **111**(5): 3614-3666.

Newman, R.H. and Zhang, J. 2008. Visualization of phosphatase activity in living cells with a FRET-based calcineurin activity sensor. *Mol Biosyst* **4**(6): 496-501.

Nguyen, A.W. and Daugherty, P.S. 2005. Evolutionary optimization of fluorescent proteins for intracellular FRET. *Nature Biotechnology* **23**(3): 355-360.

Nieminen, M., Henttinen, T., Merinen, M., Marttila-Ichihara, F., Eriksson, J.E., and Jalkanen, S. 2006. Vimentin function in lymphocyte adhesion and transcellular migration. *Nat Cell Biol* **8**(2): 156-162.

Niino, Y., Hotta, K., and Oka, K. 2009. Simultaneous live cell imaging using dual FRET sensors with a single excitation light. *PLoS One* **4**(6): e6036.

-. 2010. Blue Fluorescent cGMP Sensor for Multiparameter Fluorescence Imaging. *PLoS One* **5**(2): e9164.

Nimnual, A.S., Taylor, L.J., and Bar-Sagi, D. 2003. Redox-dependent downregulation of Rho by Rac. *Nat Cell Biol* **5**(3): 236-241.

Nishimura, T., Yamaguchi, T., Kato, K., Yoshizawa, M., Nabeshima, Y., Ohno, S., Hoshino, M., and Kaibuchi, K. 2005. PAR-6-PAR-3 mediates Cdc42-induced Rac activation through the Rac GEFs STEF/Tiam1. *Nat Cell Biol* **7**(3): 270-277.

Nobes, C.D. and Hall, A. 1995. Rho, rac, and cdc42 GTPases regulate the assembly of multimolecular focal complexes associated with actin stress fibers, lamellipodia, and filopodia. *Cell* **81**(1): 53-62.

Nobes, C.D., Hawkins, P., Stephens, L., and Hall, A. 1995. Activation of the small GTP-binding proteins rho and rac by growth factor receptors. *J Cell Sci* **108 (Pt 1)**: 225-233.

Noren, N.K., Arthur, W.T., and Burridge, K. 2003. Cadherin engagement inhibits RhoA via p190RhoGAP. *J Biol Chem* **278**(16): 13615-13618.

Norman, M.U. and Kubes, P. 2005. Therapeutic intervention in inflammatory diseases: a time and place for anti-adhesion therapy. *Microcirculation* **12**(1): 91-98.

Nurnberg, A., Kitzing, T., and Grosse, R. 2011. Nucleating actin for invasion. *Nat Rev Cancer* **11**(3): 177-187.

O'Rourke, N.A., Meyer, T., and Chandy, G. 2005. Protein localization studies in the age of 'Omics'. *Curr Opin Chem Biol* **9**(1): 82-87.

Oda, K., Matsuoka, Y., Funahashi, A., and Kitano, H. 2005. A comprehensive pathway map of epidermal growth factor receptor signaling. *Mol Syst Biol* **1**: 2005 0010.

Ohta, Y., Hartwig, J.H., and Stossel, T.P. 2006. FilGAP, a Rho- and ROCK-regulated GAP for Rac binds filamin A to control actin remodelling. *Nature Cell Biology* **8**(8): 803-U835.

Oi, V.T., Glazer, A.N., and Stryer, L. 1982. Fluorescent phycobiliprotein conjugates for analyses of cells and molecules. *J Cell Biol* **93**(3): 981-986.

Olson, M.F. 2008. Applications for ROCK kinase inhibition. *Curr Opin Cell Biol* **20**(2): 242-248.

Orlowski, J. and Grinstein, S. 2004. Diversity of the mammalian sodium/proton exchanger SLC9 gene family. *Pflugers Arch* **447**(5): 549-565.

Osherov, N. and Levitzki, A. 1994. Epidermal-growth-factor-dependent activation of the src-family kinases. *Eur J Biochem* **225**(3): 1047-1053.

Osmani, N., Peglion, F., Chavrier, P., and Etienne-Manneville, S. 2010. Cdc42 localization and cell polarity depend on membrane traffic. *J Cell Biol* **191**(7): 1261-1269.

Ouyang, M., Huang, H., Shaner, N.C., Remacle, A.G., Shiryaev, S.A., Strongin, A.Y., Tsien, R.Y., and Wang, Y. 2010. Simultaneous visualization of protumorigenic Src and MT1-MMP activities with fluorescence resonance energy transfer. *Cancer Res* **70**(6): 2204-2212.

Palamidessi, A., Frittoli, E., Garre, M., Faretta, M., Mione, M., Testa, I., Diaspro, A., Lanzetti, L., Scita, G., and Di Fiore, P.P. 2008. Endocytic trafficking of Rac is required for the spatial restriction of signaling in cell migration. *Cell* **134**(1): 135-147.

Palazzo, A., Cook, T., Alberts, A., and Gundersen, G. 2001. mDia mediates Rho-regulated formation and orientation of stable microtubules. *Nature Cell Biology* **3**(8): 723-729.

Palmer, A.E., Qin, Y., Park, J.G., and McCombs, J.E. 2011. Design and application of genetically encoded biosensors. *Trends Biotechnol* **29**(3): 144-152.

Pandey, A., Podtelejnikov, A.V., Blagoev, B., Bustelo, X.R., Mann, M., and Lodish, H.F. 2000. Analysis of receptor signaling pathways by mass spectrometry: identification of vav-2 as a substrate of the epidermal and platelet-derived growth factor receptors. *Proc Natl Acad Sci U S A* **97**(1): 179-184.

Pankov, R., Endo, Y., Even-Ram, S., Araki, M., Clark, K., Cukierman, E., Matsumoto, K., and Yamada, K.M. 2005. A Rac switch regulates random versus directionally persistent cell migration. *J Cell Biol* **170**(5): 793-802.

Park, D., Tosello-Trampont, A.C., Elliott, M.R., Lu, M., Haney, L.B., Ma, Z., Klibanov, A.L., Mandell, J.W., and Ravichandran, K.S. 2007. BAI1 is an engulfment receptor for apoptotic cells upstream of the ELMO/Dock180/Rac module. *Nature* **450**(7168): 430-434.

Patel, V., Rosenfeldt, H.M., Lyons, R., Servitja, J.M., Bustelo, X.R., Siroff, M., and Gutkind, J.S. 2007. Persistent activation of Rac1 in squamous carcinomas of the head and neck: evidence for an EGFR/Vav2 signaling axis involved in cell invasion. *Carcinogenesis* **28**(6): 1145-1152.

Pegtel, D.M., Ellenbroek, S.I., Mertens, A.E., van der Kammen, R.A., de Rooij, J., and Collard, J.G. 2007. The Par-Tiam1 complex controls persistent migration by stabilizing microtubule-dependent front-rear polarity. *Curr Biol* **17**(19): 1623-1634.

Peng, J., Wallar, B.J., Flanders, A., Swiatek, P.J., and Alberts, A.S. 2003. Disruption of the Diaphanous-related formin Drf1 gene encoding mDia1 reveals a role for Drf3 as an effector for Cdc42. *Curr Biol* **13**(7): 534-545.

Pertz, O. and Hahn, K.M. 2004. Designing biosensors for Rho family proteins--deciphering the dynamics of Rho family GTPase activation in living cells. *Journal of Cell Science* **117**(Pt 8): 1313-1318.

Pertz, O., Hodgson, L., Klemke, R.L., and Hahn, K.M. 2006. Spatiotemporal dynamics of RhoA activity in migrating cells. *Nature* **440**(7087): 1069-1072.

Petrie, R.J., Doyle, A.D., and Yamada, K.M. 2009. Random versus directionally persistent cell migration. *Nat Rev Mol Cell Biol* **10**(8): 538-549.

Peyker, A., Rocks, O., and Bastiaens, P.I. 2005. Imaging activation of two Ras isoforms simultaneously in a single cell. *Chembiochem* **6**(1): 78-85.

Peyton, S.R. and Putnam, A.J. 2005. Extracellular matrix rigidity governs smooth muscle cell motility in a biphasic fashion. *J Cell Physiol* **204**(1): 198-209.

Piljic, A. and Schultz, C. 2008. Simultaneous recording of multiple cellular events by FRET. *ACS Chem Biol* **3**(3): 156-160.

Pouyssegur, J., Franchi, A., L'Allemain, G., and Paris, S. 1985. Cytoplasmic pH, a key determinant of growth factor-induced DNA synthesis in quiescent fibroblasts. *FEBS Lett* **190**(1): 115-119.

Prasher, D.C., Eckenrode, V.K., Ward, W.W., Prendergast, F.G., and Cormier, M.J. 1992. Primary structure of the Aequorea victoria green-fluorescent protein. *Gene* **111**(2): 229-233.

Prieto-Sanchez, R.M., Berenjeno, I.M., and Bustelo, X.R. 2006. Involvement of the Rho/Rac family member RhoG in caveolar endocytosis. *Oncogene* **25**(21): 2961-2973.

Prieto-Sanchez, R.M. and Bustelo, X.R. 2003. Structural basis for the signaling specificity of RhoG and Rac1 GTPases. *J Biol Chem* **278**(39): 37916-37925.

Prior, I.A., Harding, A., Yan, J., Sluimer, J., Parton, R.G., and Hancock, J.F. 2001. GTP-dependent segregation of H-ras from lipid rafts is required for biological activity. *Nat Cell Biol* **3**(4): 368-375.

Prosser, D.C., Tran, D., Schooley, A., Wendland, B., and Ngsee, J.K. 2010. A novel, retromer-independent role for sorting nexins 1 and 2 in RhoG-dependent membrane remodeling. *Traffic* **11**(10): 1347-1362.

Racoosin, E.L. and Swanson, J.A. 1989. Macrophage colony-stimulating factor (rM-CSF) stimulates pinocytosis in bone marrow-derived macrophages. *J Exp Med* **170**(5): 1635-1648.

Raine, C.S., Cannella, B., Duijvestijn, A.M., and Cross, A.H. 1990. Homing to central nervous system vasculature by antigen-specific lymphocytes. II. Lymphocyte/endothelial cell adhesion during the initial stages of autoimmune demyelination. *Lab Invest* **63**(4): 476-489.

Ray, R.M., Vaidya, R.J., and Johnson, L.R. 2007. MEK/ERK regulates adherens junctions and migration through Rac1. *Cell Motil Cytoskeleton* **64**(3): 143-156.

Ridley, A.J. 2004. Rho proteins and cancer. *Breast Cancer Res Treat* **84**(1): 13-19.

-. 2006. Rho GTPases and actin dynamics in membrane protrusions and vesicle trafficking. *Trends Cell Biol* **16**(10): 522-529.

Ridley, A.J., Paterson, H.F., Johnston, C.L., Diekmann, D., and Hall, A. 1992. The small GTP-binding protein rac regulates growth factor-induced membrane ruffling. *Cell* **70**(3): 401-410.

Ridley, A.J., Schwartz, M.A., Burridge, K., Firtel, R.A., Ginsberg, M.H., Borisy, G., Parsons, J.T., and Horwitz, A.R. 2003. Cell migration: integrating signals from front to back. *Science* **302**(5651): 1704-1709.

Riento, K., Guasch, R.M., Garg, R., Jin, B., and Ridley, A.J. 2003. RhoE binds to ROCK I and inhibits downstream signaling. *Mol Cell Biol* **23**(12): 4219-4229.

Rodrigues, G.A., Falasca, M., Zhang, Z., Ong, S.H., and Schlessinger, J. 2000. A novel positive feedback loop mediated by the docking protein Gab1 and phosphatidylinositol 3-kinase in epidermal growth factor receptor signaling. *Mol Cell Biol* **20**(4): 1448-1459.

Rodriguez, O.C., Schaefer, A.W., Mandato, C.A., Forscher, P., Bement, W.M., and Waterman-Storer, C.M. 2003. Conserved microtubule-actin interactions in cell movement and morphogenesis. *Nat Cell Biol* **5**(7): 599-609.

Rohatgi, R., Ma, L., Miki, H., Lopez, M., Kirchhausen, T., Takenawa, T., and Kirschner, M.W. 1999. The interaction between N-WASP and the Arp2/3 complex links Cdc42-dependent signals to actin assembly. *Cell* **97**(2): 221-231.

Rohlena, J., Volger, O.L., van Buul, J.D., Hekking, L.H., van Gils, J.M., Bonta, P.I., Fontijn, R.D., Post, J.A., Hordijk, P.L., and Horrevoets, A.J. 2009. Endothelial CD81 is a marker of early human atherosclerotic plaques and facilitates monocyte adhesion. *Cardiovasc Res* **81**(1): 187-196.

Ross, R. 1999. Atherosclerosis--an inflammatory disease. *N Engl J Med* **340**(2): 115-126.

Rossman, K.L., Der, C.J., and Sondek, J. 2005. GEF means go: turning on RHO GTPases with guanine nucleotide-exchange factors. *Nat Rev Mol Cell Biol* **6**(2): 167-180.

Rothenberg, P., Glaser, L., Schlesinger, P., and Cassel, D. 1983. Activation of Na+/H+ exchange by epidermal growth factor elevates intracellular pH in A431 cells. *J Biol Chem* **258**(20): 12644-12653.

Rottner, K., Hall, A., and Small, J.V. 1999. Interplay between Rac and Rho in the control of substrate contact dynamics. *Current Biology* **9**(12): 640-649.

Rubin, I. and Yarden, Y. 2001. The basic biology of HER2. *Ann Oncol* **12 Suppl 1**: S3-8.

Rupper, A., Lee, K., Knecht, D., and Cardelli, J. 2001. Sequential activities of phosphoinositide 3-kinase, PKB/Aakt, and Rab7 during macropinosome formation in Dictyostelium. *Mol Biol Cell* **12**(9): 2813-2824.

Sabatini, B.L. and Svoboda, K. 2000. Analysis of calcium channels in single spines using optical fluctuation analysis. *Nature* **408**(6812): 589-593.

Sahai, E. and Marshall, C.J. 2003. Differing modes of tumour cell invasion have distinct requirements for Rho/ROCK signalling and extracellular proteolysis. *Nat Cell Biol* **5**(8): 711-719.

Saito, H., Minamiya, Y., Kitamura, M., Saito, S., Enomoto, K., Terada, K., and Ogawa, J. 1998. Endothelial myosin light chain kinase regulates neutrophil migration across human umbilical vein endothelial cell monolayer. *J Immunol* **161**(3): 1533-1540.

Sallusto, F., Cella, M., Danieli, C., and Lanzavecchia, A. 1995. Dendritic cells use macropinocytosis and the mannose receptor to concentrate macromolecules in the major histocompatibility complex class II compartment: downregulation by cytokines and bacterial products. *J Exp Med* **182**(2): 389-400.

Samson, T., Welch, C., Monaghan-Benson, E., Hahn, K.M., and Burridge, K. 2010. Endogenous RhoG is rapidly activated after epidermal growth factor

stimulation through multiple guanine-nucleotide exchange factors. *Mol Biol Cell* **21**(9): 1629-1642.

Sanchez-Aguilera, A., Rattmann, I., Drew, D.Z., Muller, L.U., Summey, V., Lucas, D.M., Byrd, J.C., Croce, C.M., Gu, Y., Cancelas, J.A. et al. 2009. Involvement of RhoH GTPase in the development of B-cell chronic lymphocytic leukemia. *Leukemia* **24**(1): 97-104.

Sandborn, W.J. and Yednock, T.A. 2003. Novel approaches to treating inflammatory bowel disease: targeting alpha-4 integrin. *Am J Gastroenterol* **98**(11): 2372-2382.

Sander, E.E., ten Klooster, J.P., van Delft, S., van der Kammen, R.A., and Collard, J.G. 1999. Rac downregulates Rho activity: reciprocal balance between both GTPases determines cellular morphology and migratory behavior. *J Cell Biol* **147**(5): 1009-1022.

Sandvig, K., Olsnes, S., Petersen, O.W., and van Deurs, B. 1987. Acidification of the cytosol inhibits endocytosis from coated pits. *J Cell Biol* **105**(2): 679-689.

Sanz-Moreno, V., Gadea, G., Ahn, J., Paterson, H., Marra, P., Pinner, S., Sahai, E., and Marshall, C.J. 2008. Rac activation and inactivation control plasticity of tumor cell movement. *Cell* **135**(3): 510-523.

Sardet, C., Fafournoux, P., and Pouyssegur, J. 1991. Alpha-thrombin, epidermal growth factor, and okadaic acid activate the Na+/H+ exchanger, NHE-1, by phosphorylating a set of common sites. *J Biol Chem* **266**(29): 19166-19171.

Sasaki, A.T., Janetopoulos, C., Lee, S., Charest, P.G., Takeda, K., Sundheimer, L.W., Meili, R., Devreotes, P.N., and Firtel, R.A. 2007. G protein-independent Ras/PI3K/F-actin circuit regulates basic cell motility. *J Cell Biol* **178**(2): 185-191.

Sasaoka, T., Langlois, W.J., Leitner, J.W., Draznin, B., and Olefsky, J.M. 1994. The signaling pathway coupling epidermal growth factor receptors to activation of p21ras. *J Biol Chem* **269**(51): 32621-32625.

Schlegel, N., Burger, S., Golenhofen, N., Walter, U., Drenckhahn, D., and Waschke, J. 2008. The role of VASP in regulation of cAMP- and Rac 1-mediated endothelial barrier stabilization. *Am J Physiol Cell Physiol* **294**(1): C178-188.

Schleiden, M.M. 1838. Beiträge zur Phytogenesis. *Archives of Anatomy and Physiology Wiss Medicine* **13**: 137-176.

Schwann, T. 1839. Mikroskopische Untersuchungen über die Übereinstimmung in der Struktur und dem Wachstum der Tiere und Pflanzen.

Schwille, P., Korlach, J., and Webb, W.W. 1999. Fluorescence correlation spectroscopy with single-molecule sensitivity on cell and model membranes. *Cytometry* **36**(3): 176-182.

Scita, G., Nordstrom, J., Carbone, R., Tenca, P., Giardina, G., Gutkind, S., Bjarnegard, M., Betsholtz, C., and Di Fiore, P.P. 1999. EPS8 and E3B1 transduce signals from Ras to Rac. *Nature* **401**(6750): 290-293.

Seth, A., Otomo, T., Yin, H.L., and Rosen, M.K. 2003. Rational design of genetically encoded fluorescence resonance energy transfer-based sensors of cellular Cdc42 signaling. *Biochemistry* **42**(14): 3997-4008.

Settleman, J., Albright, C.F., Foster, L.C., and Weinberg, R.A. 1992. Association between GTPase activators for Rho and Ras families. *Nature* **359**(6391): 153-154.

Shaner, N.C., Campbell, R.E., Steinbach, P.A., Giepmans, B.N., Palmer, A.E., and Tsien, R.Y. 2004. Improved monomeric red, orange and yellow fluorescent proteins derived from Discosoma sp. red fluorescent protein. *Nat Biotechnol* **22**(12): 1567-1572.

Shaner, N.C., Lin, M.Z., McKeown, M.R., Steinbach, P.A., Hazelwood, K.L., Davidson, M.W., and Tsien, R.Y. 2008. Improving the photostability of bright monomeric orange and red fluorescent proteins. *Nat Methods* **5**(6): 545-551.

Shaner, N.C., Patterson, G.H., and Davidson, M.W. 2007. Advances in fluorescent protein technology. *J Cell Sci* **120**(Pt 24): 4247-4260.

Shaner, N.C., Steinbach, P.A., and Tsien, R.Y. 2005. A guide to choosing fluorescent proteins. *Nat Methods* **2**(12): 905-909.

Sigismund, S., Woelk, T., Puri, C., Maspero, E., Tacchetti, C., Transidico, P., Di Fiore, P.P., and Polo, S. 2005. Clathrin-independent endocytosis of ubiquitinated cargos. *Proc Natl Acad Sci U S A* **102**(8): 2760-2765.

Silver, D.L. and Montell, D.J. 2001. Paracrine signaling through the JAK/STAT pathway activates invasive behavior of ovarian epithelial cells in Drosophila. *Cell* **107**(7): 831-841.

Simoes Sde, M., Blankenship, J.T., Weitz, O., Farrell, D.L., Tamada, M., Fernandez-Gonzalez, R., and Zallen, J.A. 2010. Rho-kinase directs Bazooka/Par-3 planar polarity during Drosophila axis elongation. *Dev Cell* **19**(3): 377-388.

Simpson, K.J., Dugan, A.S., and Mercurio, A.M. 2004. Functional analysis of the contribution of RhoA and RhoC GTPases to invasive breast carcinoma. *Cancer Res* **64**(23): 8694-8701.

Simpson, K.J., Selfors, L.M., Bui, J., Reynolds, A., Leake, D., Khvorova, A., and Brugge, J.S. 2008. Identification of genes that regulate epithelial cell migration using an siRNA screening approach. *Nat Cell Biol* **10**(9): 1027-1038.

Sligh, J.E., Jr., Ballantyne, C.M., Rich, S.S., Hawkins, H.K., Smith, C.W., Bradley, A., and Beaudet, A.L. 1993. Inflammatory and immune responses are impaired in mice deficient in intercellular adhesion molecule 1. *Proc Natl Acad Sci U S A* **90**(18): 8529-8533.

Smith, C.W., Entman, M.L., Lane, C.L., Beaudet, A.L., Ty, T.I., Youker, K., Hawkins, H.K., and Anderson, D.C. 1991. Adherence of neutrophils to canine cardiac myocytes in vitro is dependent on intercellular adhesion molecule-1. *J Clin Invest* **88**(4): 1216-1223.

Springer, T.A. 1994. Traffic signals for lymphocyte recirculation and leukocyte emigration: the multistep paradigm. *Cell* **76**(2): 301-314.

St Croix, B., Rago, C., Velculescu, V., Traverso, G., Romans, K.E., Montgomery, E., Lal, A., Riggins, G.J., Lengauer, C., Vogelstein, B. et al. 2000. Genes expressed in human tumor endothelium. *Science* **289**(5482): 1197-1202.

Staite, N.D., Justen, J.M., Sly, L.M., Beaudet, A.L., and Bullard, D.C. 1996. Inhibition of delayed-type contact hypersensitivity in mice deficient in both E-selectin and P-selectin. *Blood* **88**(8): 2973-2979.

Steffen, A., Faix, J., Resch, G.P., Linkner, J., Wehland, J., Small, J.V., Rottner, K., and Stradal, T.E. 2006. Filopodia formation in the absence of functional WAVE- and Arp2/3-complexes. *Mol Biol Cell* **17**(6): 2581-2591.

Stock, C., Gassner, B., Hauck, C.R., Arnold, H., Mally, S., Eble, J.A., Dieterich, P., and Schwab, A. 2005. Migration of human melanoma cells depends on extracellular pH and Na+/H+ exchange. *J Physiol* **567**(Pt 1): 225-238.

Svitkina, T.M., Bulanova, E.A., Chaga, O.Y., Vignjevic, D.M., Kojima, S., Vasiliev, J.M., and Borisy, G.G. 2003. Mechanism of filopodia initiation by reorganization of a dendritic network. *J Cell Biol* **160**(3): 409-421.

Swanson, J.A. and Watts, C. 1995. Macropinocytosis. *Trends Cell Biol* **5**(11): 424-428.

Tachibana, M., Kiyokawa, E., Hara, S., Iemura, S., Natsume, T., Manabe, T., and Matsuda, M. 2009. Ankyrin repeat domain 28 (ANKRD28), a novel binding partner of DOCK180, promotes cell migration by regulating focal adhesion formation. *Exp Cell Res* **315**(5): 863-876.

Tamas, P., Solti, Z., Bauer, P., Illes, A., Sipeki, S., Bauer, A., Farago, A., Downward, J., and Buday, L. 2003. Mechanism of epidermal growth factor regulation of

Vav2, a guanine nucleotide exchange factor for Rac. *J Biol Chem* **278**(7): 5163-5171.

Tauber, A.I. 2003. Metchnikoff and the phagocytosis theory. *Nat Rev Mol Cell Biol* **4**(11): 897-901.

Tay, L.H., Griesbeck, O., and Yue, D.T. 2007. Live-cell transforms between Ca2+ transients and FRET responses for a troponin-C-based Ca2+ sensor. *Biophys J* **93**(11): 4031-4040.

Taylor, D.L. and Wang, Y.L. 1978. Molecular cytochemistry: incorporation of fluorescently labeled actin into living cells. *Proc Natl Acad Sci U S A* **75**(2): 857-861.

Taylor, R.J., Falconnet, D., Niemisto, A., Ramsey, S.A., Prinz, S., Shmulevich, I., Galitski, T., and Hansen, C.L. 2009. Dynamic analysis of MAPK signaling using a high-throughput microfluidic single-cell imaging platform. *Proceedings of the National Academy of Sciences of the United States of America* **106**(10): 3758-3763.

ten Klooster, J.P., Jaffer, Z.M., Chernoff, J., and Hordijk, P.L. 2006. Targeting and activation of Rac1 are mediated by the exchange factor beta-Pix. *J Cell Biol* **172**(5): 759-769.

Thompson, P.W., Randi, A.M., and Ridley, A.J. 2002. Intercellular adhesion molecule (ICAM)-1, but not ICAM-2, activates RhoA and stimulates c-fos and rhoA transcription in endothelial cells. *J Immunol* **169**(2): 1007-1013.

Tkachenko, E., Sabouri-Ghomi, M., Pertz, O., Kim, C., Gutierrez, E., Machacek, M., Groisman, A., Danuser, G., and Ginsberg, M.H. 2011. Protein kinase A governs a RhoA-RhoGDI protrusion-retraction pacemaker in migrating cells. *Nat Cell Biol* **13**(6): 661-668.

Trager, K., DeBacker, D., and Radermacher, P. 2003. Metabolic alterations in sepsis and vasoactive drug-related metabolic effects. *Curr Opin Crit Care* **9**(4): 271-278.

Trichas, G., Begbie, J., and Srinivas, S. 2008. Use of the viral 2A peptide for bicistronic expression in transgenic mice. *BMC Biol* **6**: 40.

Tsukada, Y., Aoki, K., Nakamura, T., Sakumura, Y., Matsuda, M., and Ishii, S. 2008. Quantification of local morphodynamics and local GTPase activity by edge evolution tracking. *PLoS Comput Biol* **4**(11): e1000223.

Turner, M. 2002. The role of Vav proteins in B cell responses. *Adv Exp Med Biol* **512**: 29-34.

Tzima, E., Irani-Tehrani, M., Kiosses, W.B., Dejana, E., Schultz, D.A., Engelhardt, B., Cao, G., DeLisser, H., and Schwartz, M.A. 2005. A mechanosensory complex that mediates the endothelial cell response to fluid shear stress. *Nature* **437**(7057): 426-431.

Tzima, E., Kiosses, W.B., del Pozo, M.A., and Schwartz, M.A. 2003. Localized cdc42 activation, detected using a novel assay, mediates microtubule organizing center positioning in endothelial cells in response to fluid shear stress. *J Biol Chem* **278**(33): 31020-31023.

Valiente, M. and Marin, O. 2010. Neuronal migration mechanisms in development and disease. *Curr Opin Neurobiol* **20**(1): 68-78.

van Buul, J.D., Allingham, M.J., Samson, T., Meller, J., Boulter, E., Garcia-Mata, R., and Burridge, K. 2007a. RhoG regulates endothelial apical cup assembly downstream from ICAM1 engagement and is involved in leukocyte trans-endothelial migration. *J Cell Biol* **178**(7): 1279-1293.

van Buul, J.D. and Hordijk, P.L. 2009. Endothelial adapter proteins in leukocyte transmigration. *Thromb Haemost* **101**(4): 649-655.

van Buul, J.D., Kanters, E., and Hordijk, P.L. 2007b. Endothelial signaling by Ig-like cell adhesion molecules. *Arterioscler Thromb Vasc Biol* **27**(9): 1870-1876.

Van Obberghen-Schilling, E., Chambard, J.C., Paris, S., L'Allemain, G., and Pouyssegur, J. 1985. alpha-Thrombin-induced early mitogenic signalling events and G0 to S-phase transition of fibroblasts require continual external stimulation. *Embo J* **4**(11): 2927-2932.

van Wetering, S., van Buul, J.D., Quik, S., Mul, F.P., Anthony, E.C., ten Klooster, J.P., Collard, J.G., and Hordijk, P.L. 2002. Reactive oxygen species mediate Rac-induced loss of cell-cell adhesion in primary human endothelial cells. *J Cell Sci* **115**(Pt 9): 1837-1846.

van Wetering, S., van den Berk, N., van Buul, J.D., Mul, F.P., Lommerse, I., Mous, R., ten Klooster, J.P., Zwaginga, J.J., and Hordijk, P.L. 2003. VCAM-1-mediated Rac signaling controls endothelial cell-cell contacts and leukocyte transmigration. *Am J Physiol Cell Physiol* **285**(2): C343-352.

VanEngelenburg, S.B. and Palmer, A.E. 2008. Fluorescent biosensors of protein function. *Curr Opin Chem Biol* **12**(1): 60-65.

Vega, F.M. and Ridley, A.J. 2008. Rho GTPases in cancer cell biology. *FEBS Lett* **582**(14): 2093-2101.

Veithen, A., Cupers, P., Baudhuin, P., and Courtoy, P.J. 1996. v-Src induces constitutive macropinocytosis in rat fibroblasts. *J Cell Sci* **109 (Pt 8)**: 2005-2012.

Vidali, L., Chen, F., Cicchetti, G., Ohta, Y., and Kwiatkowski, D.J. 2006. Rac1-null mouse embryonic fibroblasts are motile and respond to platelet-derived growth factor. *Mol Biol Cell* **17**(5): 2377-2390.

Vignal, E., Blangy, A., Martin, M., Gauthier-Rouviere, C., and Fort, P. 2001. Kinectin is a key effector of RhoG microtubule-dependent cellular activity. *Mol Cell Biol* **21**(23): 8022-8034.

Vigorito, E., Bell, S., Hebeis, B.J., Reynolds, H., McAdam, S., Emson, P.C., McKenzie, A., and Turner, M. 2004. Immunological function in mice lacking the Rac-related GTPase RhoG. *Mol Cell Biol* **24**(2): 719-729.

Wallar, B.J., Stropich, B.N., Schoenherr, J.A., Holman, H.A., Kitchen, S.M., and Alberts, A.S. 2006. The basic region of the diaphanous-autoregulatory domain (DAD) is required for autoregulatory interactions with the diaphanous-related formin inhibitory domain. *J Biol Chem* **281**(7): 4300-4307.

Wang, L., Lau, J.S., Patra, C.R., Cao, Y., Bhattacharya, S., Dutta, S., Nandy, D., Wang, E., Rupasinghe, C.N., Vohra, P. et al. 2010. RGS-GAIP-interacting protein controls breast cancer progression. *Mol Cancer Res* **8**(12): 1591-1600.

Wang, W., Eddy, R., and Condeelis, J. 2007. The cofilin pathway in breast cancer invasion and metastasis. *Nat Rev Cancer* **7**(6): 429-440.

Wang, Y., Botvinick, E.L., Zhao, Y., Berns, M.W., Usami, S., Tsien, R.Y., and Chien, S. 2005. Visualizing the mechanical activation of Src. *Nature* **434**(7036): 1040-1045.

Waschke, J., Drenckhahn, D., Adamson, R.H., Barth, H., and Curry, F.E. 2004. cAMP protects endothelial barrier functions by preventing Rac-1 inhibition. *Am J Physiol Heart Circ Physiol* **287**(6): H2427-2433.

Wekerle, H., Engelhardt, B., Risau, W., and Meyermann, R. 1991. Interaction of T lymphocytes with cerebral endothelial cells in vitro. *Brain Pathol* **1**(2): 107-114.

Welch, H.C., Coadwell, W.J., Stephens, L.R., and Hawkins, P.T. 2003. Phosphoinositide 3-kinase-dependent activation of Rac. *FEBS Lett* **546**(1): 93-97.

Wennerberg, K., Ellerbroek, S.M., Liu, R.Y., Karnoub, A.E., Burridge, K., and Der, C.J. 2002. RhoG signals in parallel with Rac1 and Cdc42. *J Biol Chem* **277**(49): 47810-47817.

Wennerberg, K., Rossman, K.L., and Der, C.J. 2005. The Ras superfamily at a glance. *J Cell Sci* **118**(Pt 5): 843-846.

Wertheimer, S.J., Myers, C.L., Wallace, R.W., and Parks, T.P. 1992. Intercellular adhesion molecule-1 gene expression in human endothelial cells. Differential regulation by tumor necrosis factor-alpha and phorbol myristate acetate. *J Biol Chem* **267**(17): 12030-12035.

Wessels, D., Lusche, D.F., Kuhl, S., Heid, P., and Soll, D.R. 2007. PTEN plays a role in the suppression of lateral pseudopod formation during Dictyostelium motility and chemotaxis. *J Cell Sci* **120**(Pt 15): 2517-2531.

West, M.A., Bretscher, M.S., and Watts, C. 1989. Distinct endocytotic pathways in epidermal growth factor-stimulated human carcinoma A431 cells. *J Cell Biol* **109**(6 Pt 1): 2731-2739.

West, M.A., Prescott, A.R., Eskelinen, E.L., Ridley, A.J., and Watts, C. 2000. Rac is required for constitutive macropinocytosis by dendritic cells but does not control its downregulation. *Curr Biol* **10**(14): 839-848.

Wherlock, M. and Mellor, H. 2002. The Rho GTPase family: a Racs to Wrchs story. *J Cell Sci* **115**(Pt 2): 239-240.

White, C.D., Brown, M.D., and Sacks, D.B. 2009. IQGAPs in cancer: a family of scaffold proteins underlying tumorigenesis. *FEBS Lett* **583**(12): 1817-1824.

Williamson, J.R. and Grisham, J.W. 1961. Electron microscopy of leukocytic margination and emigration in acute inflammation in dog pancreas. *Am J Pathol* **39**: 239-256.

Wojciak-Stothard, B., Williams, L., and Ridley, A.J. 1999. Monocyte adhesion and spreading on human endothelial cells is dependent on Rho-regulated receptor clustering. *J Cell Biol* **145**(6): 1293-1307.

Wolf, K., Alexander, S., Schacht, V., Coussens, L.M., von Andrian, U.H., van Rheenen, J., Deryugina, E., and Friedl, P. 2009. Collagen-based cell migration models in vitro and in vivo. *Semin Cell Dev Biol* **20**(8): 931-941.

Wolf, K. and Friedl, P. 2006. Molecular mechanisms of cancer cell invasion and plasticity. *Br J Dermatol* **154 Suppl 1**: 11-15.

Worthylake, R.A. and Burridge, K. 2001. Leukocyte transendothelial migration: orchestrating the underlying molecular machinery. *Curr Opin Cell Biol* **13**(5): 569-577.

Worthylake, R.A., Lemoine, S., Watson, J.M., and Burridge, K. 2001. RhoA is required for monocyte tail retraction during transendothelial migration. *J Cell Biol* **154**(1): 147-160.

Wu, Y.I., Frey, D., Lungu, O.I., Jaehrig, A., Schlichting, I., Kuhlman, B., and Hahn, K.M. 2009. A genetically encoded photoactivatable Rac controls the motility of living cells. *Nature* **461**(7260): 104-108.

Xu, J., Wang, F., Van Keymeulen, A., Herzmark, P., Straight, A., Kelly, K., Takuwa, Y., Sugimoto, N., Mitchison, T., and Bourne, H.R. 2003. Divergent signals and cytoskeletal assemblies regulate self-organizing polarity in neutrophils. *Cell* **114**(2): 201-214.

Yamaki, N., Negishi, M., and Katoh, H. 2007. RhoG regulates anoikis through a phosphatidylinositol 3-kinase-dependent mechanism. *Exp Cell Res* **313**(13): 2821-2832.

Yamana, N., Arakawa, Y., Nishino, T., Kurokawa, K., Tanji, M., Itoh, R.E., Monypenny, J., Ishizaki, T., Bito, H., Nozaki, K. et al. 2006. The Rho-mDia1 pathway regulates cell polarity and focal adhesion turnover in migrating cells through mobilizing Apc and c-Src. *Mol Cell Biol* **26**(18): 6844-6858.

Yanaka, A., Suzuki, H., Shibahara, T., Matsui, H., Nakahara, A., and Tanaka, N. 2002. EGF promotes gastric mucosal restitution by activating Na(+)/H(+) exchange of epithelial cells. *Am J Physiol Gastrointest Liver Physiol* **282**(5): G866-876.

Yang, L., Froio, R.M., Sciuto, T.E., Dvorak, A.M., Alon, R., and Luscinskas, F.W. 2005. ICAM-1 regulates neutrophil adhesion and transcellular migration of TNF-alpha-activated vascular endothelium under flow. *Blood* **106**(2): 584-592.

Yarden, Y. and Sliwkowski, M.X. 2001. Untangling the ErbB signalling network. *Nat Rev Mol Cell Biol* **2**(2): 127-137.

Yilmaz, M. and Christofori, G. 2009. EMT, the cytoskeleton, and cancer cell invasion. *Cancer Metastasis Rev* **28**(1-2): 15-33.

Yuan, B.Z., Zhou, X., Durkin, M.E., Zimonjic, D.B., Gumundsdottir, K., Eyfjord, J.E., Thorgeirsson, S.S., and Popescu, N.C. 2003. DLC-1 gene inhibits human breast cancer cell growth and in vivo tumorigenicity. *Oncogene* **22**(3): 445-450.

Zaidel-Bar, R., Ballestrem, C., Kam, Z., and Geiger, B. 2003. Early molecular events in the assembly of matrix adhesions at the leading edge of migrating cells. *J Cell Sci* **116**(22): 4605-4613.

Zaidel-Bar, R., Itzkovitz, S., Ma'ayan, A., Iyengar, R., and Geiger, B. 2007. Functional atlas of the integrin adhesome. *Nat Cell Biol* **9**(8): 858-867.

Zalcman, G., Closson, V., Camonis, J., Honore, N., Rousseau-Merck, M.F., Tavitian, A., and Olofsson, B. 1996. RhoGDI-3 is a new GDP dissociation inhibitor (GDI). Identification of a non-cytosolic GDI protein interacting with the small GTP-binding proteins RhoB and RhoG. *J Biol Chem* **271**(48): 30366-30374.

Zeng, L., Sachdev, P., Yan, L., Chan, J.L., Trenkle, T., McClelland, M., Welsh, J., and Wang, L.H. 2000. Vav3 mediates receptor protein tyrosine kinase signaling, regulates GTPase activity, modulates cell morphology, and induces cell transformation. *Mol Cell Biol* **20**(24): 9212-9224.

Zipfel, W.R., Williams, R.M., and Webb, W.W. 2003. Nonlinear magic: multiphoton microscopy in the biosciences. *Nat Biotechnol* **21**(11): 1369-1377.